Single and collective fiber dynamics in confined microflows

Hélène Berthet

UNIVERSITÉ PIERRE ET MARIE CURIE (Paris 6)

ÉCOLE DOCTORALE 389
LA PHYSIQUE, DE LA PARTICULE À LA MATIÈRE CONDENSÉE

THÈSE DE DOCTORAT

PHYSIQUE DES FLUIDES

HÉLÈNE BERTHET

SINGLE AND COLLECTIVE FIBER DYNAMICS IN CONFINED MICROFLOWS

Soutenue le 9 mars 2012

JURY

Mme Isabelle Cantat	Rapportrice
M. Eric Climent	Rapporteur
Mme Elisabeth Guazzelli	Examinatrice
Mme Elise Lorenceau	Examinatrice
M. Harold Auradou	Examinateur
M. Alfred Crosby	Examinateur
Mme Anke Lindner	Directrice de Thèse
M. Gérard Daccord	Directeur de Thèse

THÈSE EFFECTUÉE CONJOINTEMENT AU

LABORATOIRE DE PHYSIQUE ET MÉCANIQUE DES MILIEUX HÉTÉROGÈNES (PMMH)
UMR CNRS 7636

École Supérieure de Physique et de Chimie Industrielles de la Ville de Paris (ESPCI)

10, rue Vauquelin
75231 Paris Cedex 05

ET

ÉTUDES ET PRODUCTIONS SCHLUMBERGER

WELL SERVICES INTEGRITY

1 rue Henri Becquerel
92140 Clamart, France

Schlumberger

Merci

I am very grateful to Anke Lindner, my supervisor and guidance along these three years, for believing in the experiments and pushing me towards the first results, and for her always pertinent advice. It was a truly scientifically-enriching adventure in a positive, open-minded environment. Thank you!

I would also like to express my gratitude to Schlumberger for supporting my PhD, in particular Gerard, Jean, Jean-Philippe, Paul, Benoit, Bernard for their scientific support. I thank WIT for understanding the fundamental aspects of my research and balancing them with the industry-side challenges and fast responses which are their everyday jobs.

Thank you Katia, Eve, Amandine, Tullio, for the great fun, encouragements and help in the "and now, what?" question.

Thank you Michael for your support. Cambridge has been a big part of this work.

A lot of thanks to the PMMH lab, in particular: Olivia for her huge help with the experiments; Marc for his scientific guidance, for launching the simulation side of my work and help me in making it a significant part; Julien; Fabrice, Hervé from MMN. Thank you Yoann, Dylan and Pierre who interned with me at the lab, for their hard work and good company. Thank you Sophie for lending me some of your CPU, many results in this manuscript would not have seen the light of day without your super-powerful computer!

Merci to Nawal, Sophie, Cathy, Nais for the best office of pmmh, to my dear Frederique and Amina for the other best office in pmmh, for the morning hello and so nice "thé à la menthe toutes ensembles". Merci to Anne, Denis, Ramiro, José, Pierre-Brice, Olivier, Thibaut, Alain, Chelsea, Baptiste, Jeremie, Etienne, Patrice, Evelyne, Bertrand , Gaston, Khanh-Dang, Annie, Eduardo, Joseph, Raphaele, Dan, Caroline et Philippe.

Merci beaucoup to Marc Schneider for our Parisian and Clamartisian discussions and for your support.

Thank you Nais for your drawing for the PhD cover. It is perfect, and keeps on reminding me I have a pile of post-it notes with dinosaurs in my drawer.

Shoukran Claudio for your Egyptian painting. A memory that a lot of this manuscript was written in Egypt, and for the best reason possible. Thank you also for your help with the data processing, for your enthusiasm for the little fiber and the long hours at the lab when it seemed writing would never end.

Thank you Lionel and Claudio for reading the manuscript and providing insightful comments.

And thank you to my family and numerous friends for being there, every step of the way.

RÉSUMÉ

Cette thèse porte sur le transport de fibres isolées et de suspensions de fibres dans des géométries microfluidiques. L'utilisation de fibres dans les fluides de forage et ciments pour réduire les pertes de circulation dans les puits de pétrole est à l'origine de cette collaboration entre Schlumberger et l'ESPCI-PMMH. Dans ce contexte industriel où les fibres en écoulement interagissent avec les roches frontières du puits et des fractures, il est nécessaire de comprendre le rôle de la géometrie des fibres, leurs propriétés mécaniques et leur concentration, ainsi que la géométrie d'écoulement.

Nous avons créé un système microfluidique modèle qui intègre dans la même expérience la fabrication et la mise en écoulement de fibres, implémentant deux techniques différentes. Ce système nous permet d'étudier indépendamment l'effet de tous les paramètres d'écoulement. Nous proposons une méthode de mesure in situ des propriétés mécaniques des fibres. Nous étudions expérimentalement et numériquement le transport de fibres isolées dans un écoulement de Darcy, en fonction de l'orientation et du confinement de la fibre. Lorsque la largeur du canal microfluidique diminue, des interactions entre la fibre et les bords latéraux du canal apparaissent. Elles mènent à un mouvement oscillatoire et régulier de la fibre entre les bords dont nous étudions la dynamique. Nous nous intéressons enfin aux effets collectifs de fibres en suspensions qui s'écoulent à travers une restriction. Nous étudions en particulier le rôle joué par leur orientation sur le blocage des restrictions, et la formation de flocs en amont de celles-ci.

MOTS-CLÉS

FIBRES, MICROFLUIDIQUE, MICROFABRICATION, ÉCOULEMENTS VISQUEUX, HELE-SHAW, EFFETS COLLECTIFS, ÉCOULEMENT ÉLONGATIONNELS, PERTE DE CIRCULATION

Abstract

In this thesis, we studied the transport of single fibers and suspensions of fibers in microfluidic geometries. This collaboration work between Schlumberger and ESPCI-PMMH was motivated by the use of fibers in lost-circulation curing fluids in the oil industry. In this context where fibers are closely interacting with the flow boundaries, the roles of the geometry, flexibility and concentration of fibers as well as the flow geometry need to be understood. We created a microfluidic model system, integrating in a single experiment the fabrication and the flow of tailor-made fibers, using two different techniques. This new experimental system allows us to independently investigate the effect of all flow parameters. An *in situ* measurement of their mechanical properties is developed. Experimental and numerical work aims at understanding the transport of an isolated fiber in the Darcy flow, depending on its orientation and confinement. We show that the interactions of the fiber with the lateral borders of the microfluidic channel can lead to regular oscillations of the fiber. The collective dynamics of higher concentration of fibers is investigated when forcing them through a restriction in the microchannel. In particular, we address the question of the role of the orientation of the fibers on the clogging of the restrictions and the formation of fiber clusters upstream of the restriction.

Keywords

fibers, microfluidics, microfabrication, viscous flows, Hele-Shaw cell, collective effects, extensional flows, lost circulation

CONTENTS

Contents 11

Introduction 15

1 State-of-the-art review 21
- 1.1 Flow of one fiber . . . 21
  - 1.1.1 Slender-body theory . . . 22
  - 1.1.2 Fiber in a simple shear flow in an unbounded medium . . . 22
  - 1.1.3 Fiber flow near a wall . . . 23
  - 1.1.4 Sedimentation near a wall . . . 24
- 1.2 Fibers in confined geometries . . . 25
- 1.3 Collective dynamics of fibers in suspensions . . . 27
- 1.4 *In situ* particle microfabrication techniques . . . 30
  - 1.4.1 Lithography method of particle fabrication . . . 30
  - 1.4.2 Self-assembling colloids to fabricate filaments . . . 32

2 Lithography fabrication of fibers 37
- 2.1 Fabrication principle . . . 38
- 2.2 Experimental protocol . . . 39
  - 2.2.1 Experimental set-up . . . 39
  - 2.2.2 Microfluidic channel . . . 39
  - 2.2.3 Oligomer solutions . . . 39
  - 2.2.4 Lithography mask design . . . 39
  - 2.2.5 Light shutter . . . 40
  - 2.2.6 Protocol . . . 40
- 2.3 Fiber characteristics . . . 42
  - 2.3.1 Geometrical design: from the mask to the fiber . . . 42
  - 2.3.2 Inhibition layer and consequence on the fiber geometry . . . 43
  - 2.3.3 Enhancing the fiber surface roughness . . . 43
  - 2.3.4 Mechanical characterization . . . 44
- 2.4 Fabrication and flow . . . 46
  - 2.4.1 Fabrication with the fluid at rest . . . 46
  - 2.4.2 Fabrication during continuous flow . . . 46
- 2.5 Fabrication of fibers suspensions . . . 47
- 2.6 Data processing . . . 48

3 Fabrication of fibers by colloids self-assembly 51

3.1 Principle of fabrication . . . 52
3.2 Experimental protocol . . . 52
3.2.1 Solution of colloids in water . . . 52
3.2.2 Microscope set-up and channel . . . 52
3.2.3 Protocol . . . 53
3.3 Fibers suspension characteristics . . . 53
3.3.1 Fiber geometry . . . 53
3.3.2 Concentration . . . 54
3.3.3 Elasticity . . . 54

4 *In situ* measurement of fiber mechanical properties: bending-fiber experiments 57
4.1 Experimental . . . 58
4.2 Numerical simulations . . . 60
4.2.1 Design . . . 60
4.2.2 Results . . . 61
4.3 Modeling in the lubrication limit . . . 62
4.4 Computation of Young's modulus . . . 65
4.5 Conclusion . . . 66

5 Flow dynamics of a single fiber away from the lateral flow boundaries 67
5.1 Experimental results . . . 68
5.1.1 Velocity of a fiber parallel to the flow direction . . . 68
5.1.2 Effect of confinement . . . 69
5.1.3 Effect of the initial orientation . . . 70
5.1.4 Streakline visualization . . . 72
5.1.5 Conclusions of the experimental study . . . 74
5.2 Flow equations . . . 74
5.3 Numerical study . . . 76
5.3.1 2D simulation of a parallel fiber (infinite fiber length) . . . 76
5.3.2 2D simulation of a perpendicular fiber . . . 78
5.3.3 Velocity results with fiber confinement . . . 80
5.3.4 3D simulations: fiber with finite length . . . 81
5.3.5 Perturbation of the flow profiles . . . 88
5.3.6 Conclusion of the simulations . . . 92
5.4 Conclusion . . . 94

6 Single fiber interacting with the lateral flow boundaries 95
6.1 Introduction . . . 96
6.1.1 Observation of oscillating fibers . . . 96
6.1.2 Experimental set-up . . . 97
6.1.3 Regime decomposition . . . 98
6.2 Fiber in the contact phase . . . 100
6.2.1 Observations . . . 100
6.2.2 Regime characteristics . . . 101
6.3 Fiber in the rotation phase . . . 103
6.3.1 Fiber angle and distance to the walls . . . 103

6.3.2 Angular velocity . . . 104
6.3.3 Influence of the flow velocity . . . 105
6.4 Fiber in the drift phase . . . 105
6.4.1 Drift towards a lateral wall . . . 105
6.4.2 Comparison with simulation . . . 107
6.4.3 Influence of the mean flow velocity . . . 108
6.5 Summary . . . 109
6.6 Conclusion . . . 109

7 Collective dynamics of fibers flowing through a restriction 111
7.1 Flow dynamics of dilute fiber suspensions in confined two-dimensional geometries 111
7.1.1 Gallery of experimental flow configurations . . . 111
7.1.2 Protocol for the three configurations . . . 112
7.1.3 Fibers in pseudo-random initial position . . . 113
7.1.4 Fibers all parallel to the restriction . . . 113
7.1.5 Fibers perpendicular to the restriction . . . 119
7.2 Flow dynamics of a concentrated fiber suspension in three-dimensional flow geometries . . . 124
7.2.1 Experimental protocol . . . 124
7.2.2 Experimental observations . . . 125
7.2.3 Image processing . . . 133
7.3 Summary . . . 133
7.4 Conclusion . . . 133

8 Conclusion 135

A Microfluidic device fabrication 139
A.1 Preparation of channel mold . . . 139
A.2 All-PDMS channels . . . 139
A.3 PDMS-glass channels . . . 140

B Simulations of a single fiber flow 141
B.1 Two-dimensional simulations in FreeFem++ . . . 141
B.1.1 Fiber parallel to the flow direction . . . 141
B.1.2 Fiber perpendicular to the flow direction . . . 145
B.2 Three-dimensional simulations in COMSOL . . . 151
B.2.1 MATLAB code for a typical flow simulation in COMSOL . . . 151
B.2.2 Determination of the fiber velocity . . . 155
B.2.3 Mesh convergence study . . . 156

C Data Processing Methods 159
C.1 Data processing for the flow experiments of single confined fibers . . . 159
C.1.1 Objectives . . . 159
C.1.2 Reference frame . . . 159
C.1.3 Enhancing the contrast . . . 161
C.1.4 Algorithm of detection . . . 163
C.2 Image processing for the experiment of fiber suspensions at high concentration . 165

C.2.1 Algorithm principles 165
C.2.2 First results 166

D Particle Tracking Velocimetry Methods **169**

E Collaborations **173**
E.1 Bending of elastic fibers in viscous flow: Jason Wexler, Princeton University . . . 173
E.2 Active suspensions: Gaston Mino, ESPCI 174

Bibliography **177**

INTRODUCTION

Fibers and flow of fiber suspensions have attracted the interest of physicists for many decades, motivated by several industrial applications where these suspensions are used. The oldest of them is the paper industry. Several thousand years ago, the Egyptian *papyrus* industry consisted in extracting stems of the papyrus plant to eventually form sheets. Paper in the form that we know today has existed since 200 B.C.: a small fragment of paper made of linen fibers was found and dated in China. Figure 0.1 shows the entangled structure of fibers of a paper sheet observed with scanning electron microscopy.
Fibers have also been widely used in the oil and gas industry for applications of stimulation and lost-circulation curing [1]. Stimulating a well can be done using hydraulic fracturing: pressurized water is injected to create new flow paths for hydrocarbons. In this application, fibers are added to proppant fluid to be used as a stabilizing agent to maintain the flow channels open. In applications of lost circulation, fibers are used to seal leak paths and prevent the loss of drilling fluid and cement slurries into the rock formations. Little is known about the fractures geometry and size downhole. Therefore it remains a challenge to systematically cure the losses when they occur.

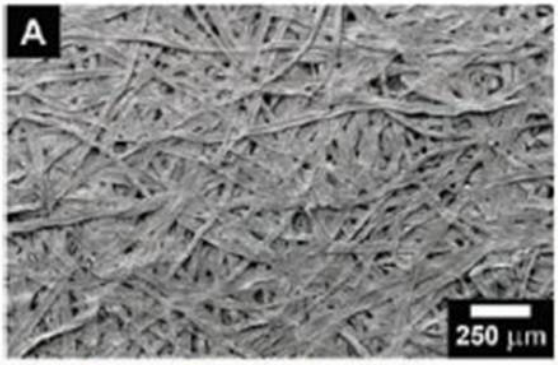

Figure 0.1: *Scanning electron micrograph of ordinary paper made from wood pulp fibre, Science.*

Suspensions of fibers under shear flocculate. Fiber flocculation is the aggregation process of fibers into entangled networks whose size can be several fiber lengths. Paper manufacturers avoid it as it is responsible for heterogeneities of paper sheets leading to weak regions and unaesthetic features. In the oil industry however, flocculation was identified as a possible mechanism to cure circulation losses. Fiber flocs would form in the suspension upstream of the fracture, then would act like a flow plug at its entrance. Mason in the fifties [2],[3] was the first to address the question of flocculation, define it scientifically and propose an understanding of the formation mechanisms. He identified the large numbers of parameters acting in favor or

against flocculation in experiments inspired by the different industrial steps of paper making. Today, the physics of flocculation is still not fully understood and the paper industry still a driving element of the research.

Other fiber collective effects develop in fiber suspensions under flow. For example, clustering in sedimenting fiber suspensions has been recently the object of many experimental, numerical and theoretical studies [4]. As the concentration of fibers is increased, aggregation of fibers is observed leading to a highly heterogeneous distribution of particles in the fluid. Back-flow regions with very low concentration of fibers develop, and as the concentration increases furthermore a semi-rigid network of fiber forms. The transition to jamming in suspension of anisotropic particles has also attracted recent attention. The presence of a flow constriction was found responsible for a filtration process downstream [5].

The investigation on the flow of isolated fibers started with Jeffery in 1922 [6]. He mathematically described the equations of motion of an ellipsoid freely transported in a simple shear flow. Such body (later generalized to all bodies of revolution [7]) is translated with its center's velocity flowing at the velocity of the fluid. It also experiences a periodic rotation along a "Jeffery orbit" as illustrated in figure 0.2. Experimental studies [8] confirmed these results in the case of unbounded flows and later on in increasingly complex flow geometries. For example, the free transport of isolated fibers in shear flows or Poiseuille flows near a boundary were studied [9][10]. Jeffery orbits were recovered when the fiber is away from the wall at least of a fiber-length. Closer to the border, interactions with the wall start to occur and perturb the rotating motion. The deformation of an elastic slender-body transported in a viscous flow has recently been investigated, both experimentally [11] and numerically [12] showing the ability of such bodies to buckle near hyperbolic stagnation points in the flow. Studies on the transport of isolated fibers in Stokes flow have largely benefited from the development of the slender-body theory [13]. This technique is used to approximate the flow field around an elongated body and the force exerted by the fluid using a distribution of Stokeslet on its surface.

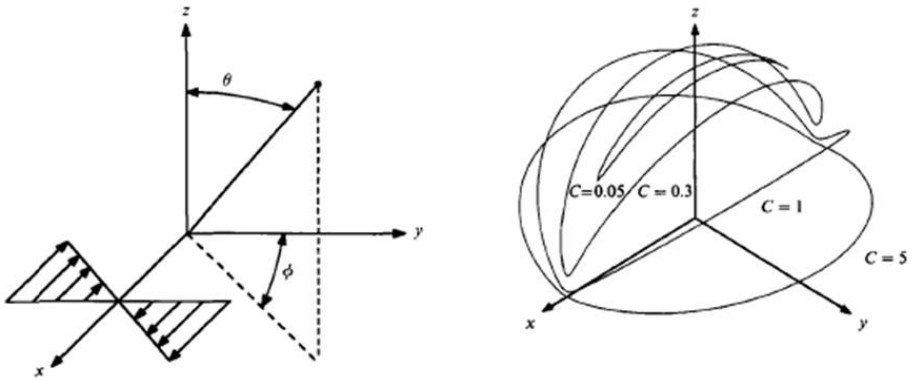

Figure 0.2: *Drawings extracted from Stover et al. [14] illustrating the Jeffery orbits. One fiber tip is centered while the other one rotates along a closed orbit as represented on the right drawing. Coefficients C correspond to different possible orbital trajectories.*

Little is known on the tranport of suspensions of fibers and isolated fibers in confined geome-

tries. Yet, such flows are important in injection processes, in biological applications [15] or in problems of flow through rock fractures and pores [16]. Semin *et al.* studied the interactions of a cylindrical fiber confined between two parallel walls focusing in particular on the calculation of the drag force and its dependence with the fiber orientation in the flow [17][18]. The case of a cylindrical fiber freely transported in the fluid was investigated with numerical computations by Champmartin *et al.* [19]. Both of these works stress the importance of the fiber confinement and its orientation with the flow direction. The fiber confinement needs to be understood in two ways, firstly as the confinement of the geometry itself. Typically, flows are two-dimensional similarly to flows in Hele-Shaw cells. Then the fiber is confined between the flow boundaries, such as two parallel walls in these two studies.

The mechanisms of lost-circulation curing in rock fractures are complex. They require the understanding of the behaviour of fiber suspensions flows near a restriction, and the role of the fiber geometry, mechanical properties, in their collective dynamics. Understanding the interactions of the fibers with the boundaries in such confined flow geometries is also necessary. In this Ph.D. study in collaboration between Schlumberger and ESPCI-PMMH, we aim at understanding the role of the nature of the flow, of its geometry and of the fiber characteristics in the single and collective fiber dynamics in confined flows. In an effort to manipulate each of these parameters independently, we built an experimental microfluidic model system characterized by three features. Firstly, flow geometries are controllable and can be modified with today's techniques of microfabrication. Then, the flow at such microscales is laminar. Finally, we fabricate the fibers directly inside the microchannels using two complementary techniques. It is in fact difficult to find commercially-available microfibers of controlled dimensions and properties. Also, injecting them into microfluidic channels would likely block connections. Using the fabrication techniques that we implemented, we control very well the fibers geometry, concentration and mechanical properties.

The first chapter of this manuscript reviews past studies on the flow of single fibers and fibers suspensions. Literature on fibers is very rich. The aim of our study is to understand the single and collective dynamics of fibers under flow at low concentrations. These information will also be useful to understand the macroscopic properties of flowing suspensions, such as, for example, their viscosity. Linking the microscopic structure to the macroscopic properties is however outside the scope of this work. We will thus restrict the review of previous work on the flow dynamics of individual and collective fibers. In the last section, we will focus on two techniques of particle microfabrication on which our experimental methods are based. The first one, developed by Dendukuri *et al.* [20], uses *in situ* photo-polymerization. This technique ensures control of many aspects of the particle: geometry, orientation and initial position in the channel. We also take advantage of the development at the PMMH of a microfilament fabrication method based on self-assembly of superparamagnetic particles [21].

The second and third chapters are dedicated to the two fabrication techniques we implemented in our microfluidic channels. The principle of the techniques and the experimental protocols are detailed, followed by the characteristics of the isolated fibers and fiber suspensions we obtained. They are complementary techniques, the polymerization one allowing us to fabricate isolated fibers and fiber suspensions confined in the microchannel. Figure 0.3-A shows a fabrication example of a single fiber and a suspension of fibers all perpendicular to the flow direction. The colloidal-assembly method is used to fabricate fiber suspensions at high concentrations flowing

as illustrated in picture B. The flow geometries also differ between the two methods: in the first one, channels are Hele-Shaw cells where a two-dimensional flow develops. In the second method, the flow is three-dimensional.

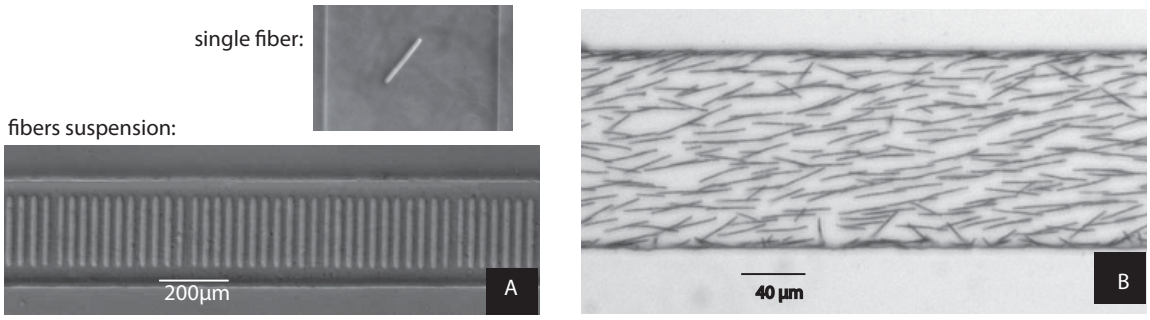

Figure 0.3: *Micrographs of fibers fabricated directly in the microchannels. A: we use a photo-polymerization technique to fabricate an isolated fiber (top picture) and a suspension of fibers all perpendicular to the flow direction. B: high-concentration fiber suspension fabricated with the colloidal self-assembly technique.*

The fourth chapter presents an experiment to mechanically characterize the fibers fabricated with the photo-polymerization method. Even though this fabrication technique is used in many experimental investigations, there is no mechanical characterization method available yet. Here we fabricate a single fiber fixed across a microchannel subjected to the fluid drag force, similar to a "bending-beam" test. Using our experimental data of fiber deflection and results from a lubrication analysis, we obtain the fiber's Youngs modulus. Figure 0.4 shows the successive deflections of the fiber.

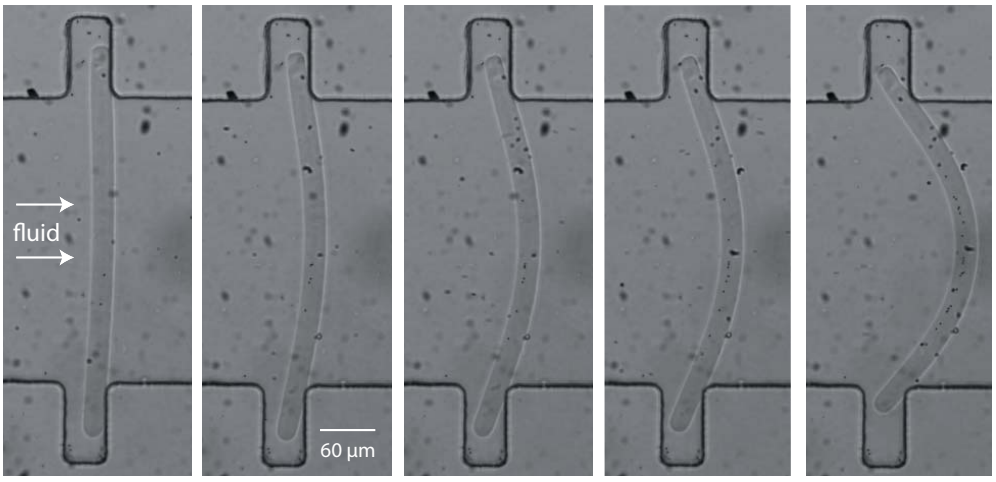

Figure 0.4: *Snapshot of pictures showing the fiber bending as the fluid flowrate is increased, increasing the drag force on the fiber. This experiment was designed to provide us with a mechanical characterization of the fiber fabricated with the polymerization technique.*

We study in the fifth chapter the free transport of an isolated fiber confined in a Hele-Shaw geometry flowing far from the lateral walls. Experimental data complemented with 2D and

3D numerical simulations are used to investigate the fiber velocity with respect to the flow velocity, depending on its confinement and its angle with the flow direction. We also quantify the perturbation on the flow profile caused by the presence of a fiber. An example of this study is shown in figure 0.5 with a chronograph of a fiber flowing perpendicular to the flow direction.

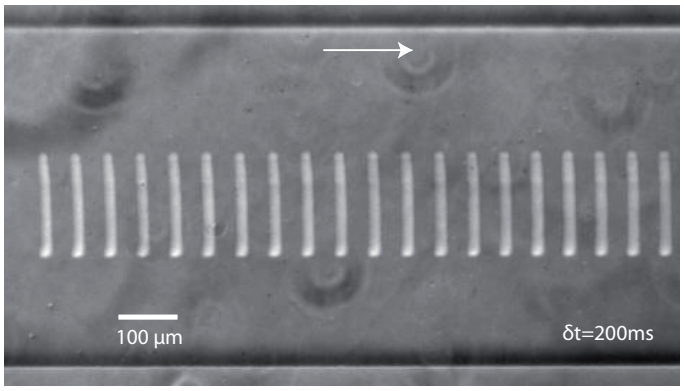

Figure 0.5: *Chronograph of a fiber flowing freely in a confined microchannel away from the lateral boundaries. The fiber is fabricated perpendicular to the flow direction (first position on the left). We study the fiber velocity and trajectory depending on its initial orientation with the flow.*

In the sixth chapter we modify the fiber and channel geometry of the previous study to make the channel width comparable to the fiber length. Interactions between the fiber and the lateral walls start to occur, leading to a beautiful oscillatory motion of the fiber as illustrated in figure 0.6. We describe the fiber oscillations as a sequence of three phases occuring in each oscillation period. We use the fiber's angle to define a criterion to determine the occurence of each regime. We characterize the three phases in terms of fiber position, velocity along the flow direction and perpendicular to it, and in terms of angular velocity.

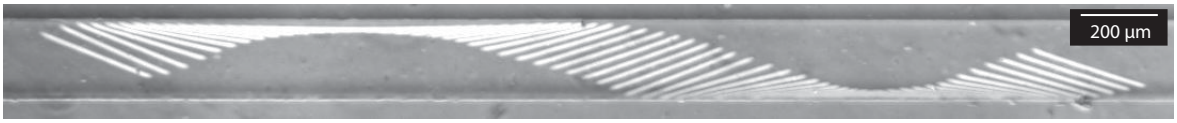

Figure 0.6: *Successive positions of a fiber oscillating between the two channel lateral walls. We observe such robust oscillations when the channel width is reduced to the fiber length, triggering interactions between the fiber and the walls. The motion is decomposed in a sequence of three regimes that we analyze in terms of position, velocity and angle.*

The seventh chapter presents our first results of flow of fiber suspensions in microfluidic geometries going through a flow restriction. Taking advantage of the two fabrication techniques, we study fiber suspensions in two regimes. The first one concerns dilute suspensions of fibers fabricated with the photo-polymerization method where the initial state (position, orientation) of fibers is controlled. Figure 0.7-A shows the example of a suspension where all fibers are fabricated parallel to the flow direction upstream of the restriction. In this regime, the fibers are

confined in a two-dimensional flow geometry. The second fabrication technique corresponds to more concentrated suspensions where the fibers are randomly positionned at the initial state and flow through a three-dimensional flow geometry. Figure 0.7-B shows an example of 3D suspension flowing through a restriction. At such concentrations we observe the development of a heterogeneous distribution of fiber and the formation of flocs.

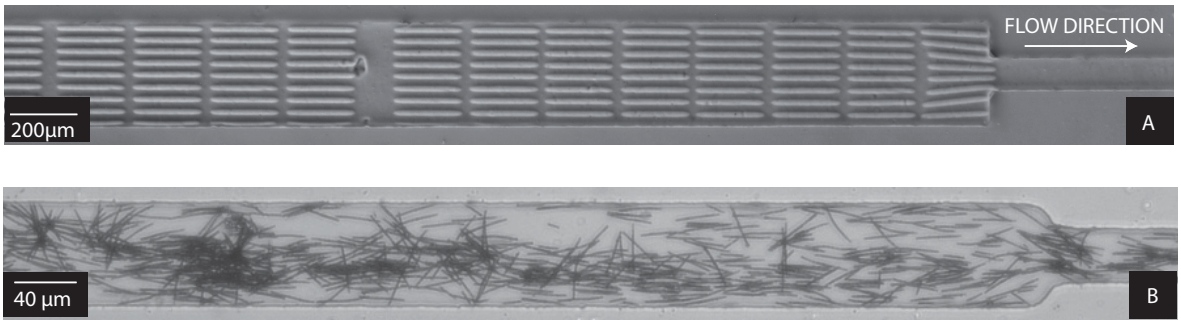

Figure 0.7: *Two pictures showing the flow of a fiber suspension through a restriction in the channel. The top picture (A) shows the initial state of a suspension of fibers fabricated with the photo-polymerization technique all parallel to the flow direction, upstream of the restriction. The bottom picture (B) illustrates the case of a 3D flow where the fibers are fabricated using the super-paramagnetic-particle-assembly technique, leading to more concentrated suspensions. The fiber spatial distribution is heterogeneous, we observe the formation of flocs. Such collective dynamics will be studied in chapter seven.*

The last chapter concludes this thesis. Experimental and numerical methods are detailed in the first four appendices. In the last appendix, I summarize other projects I participated in during my Ph.D. work.

CHAPTER 1

STATE-OF-THE-ART REVIEW

In this first chapter we propose a review of some important studies in the literature on flow of fibers and fiber suspensions that are relevant for our study. Then, in a second part, we review recent technical achievements on fabrication techniques developed to produce particles in small flow geometries. We will focus on the photo-polymerization method [20] and the magnetic colloidal self-assembly method [22] that we implemented in our channels to fabricate *in situ* microfluidic fibers.

We start this review with studies on the flow of isolated fibers, first in an unbounded medium then in interaction with a boundary. The principle of the slender-body theory is explained through the example of a sedimenting fiber. Then we focus on the case of confined fibers: the flow of a fiber perpendicular to the flow direction and confined between two walls is described as well as the interactions between a fixed fiber and the boundaries in similar geometries. As the fiber concentration is increased, collective effects start to occur in flowing suspensions of fibers. We will present in particular effects of clogging, sedimentation and flocculation. Exhaustive reviews are available on fiber suspensions as well as particle microfabrication: see in particular Hubbe *et al.*[23], Guazzelli *et al.* [4] and Dendukuri *et al.* [24].

1.1 Flow of one fiber

The word "fiber" describes an elongated solid body. Its geometry is fully characterized by its section shape and aspect ratio: ratio of fiber length to diameter or thickness. Fibers can be found in many applications: paper, fiber-reinforced composite materials, wellbore-completion fluids in the oil industry. In such examples, fiber suspensions are carefully designed in terms of concentration, stiffness, roughness and interactions, among other parameters.

We focus in this first section on the viscous flow of isolated fibers. The cases of simple shear flows and Poiseuille flows are presented for unbounded media and flow near boundaries at small Reynolds numbers. We start with the principle of the slender-body theory which made

possible many theoretical and numerical work on flows of isolated fibers. We mention in particular the case of a sedimenting fiber in an unbounded fluid.

1.1.1 Slender-body theory

Slender-body theory is an asymptotic technique to approximate the Stokes flow field around a body using its slenderness [13]. It allows to compute the force exerted by the fluid on the body. The principle of the method is to consider the slender body as a distribution of Stokeslets on its surface. The velocity on each little domain is given by the force per unit length exerted by the fluid on that point.
The slender-body theory can be applied for example to the case of a rigid cylindrical fiber translating in an unbounded fluid of viscosity η at a constant velocity U. Calling a the fiber's radius, l its length and $\varepsilon = (ln(l/a))^{-1}$, the force exerted on the fiber when its axis is parallel to the flow direction $F_{\parallel}$ and the force when it is perpendicular $F_{\perp}$ are given by [25]:

$$F_{\parallel} \approx -2\pi\eta l\varepsilon U \tag{1.1}$$

$$F_{\perp} \approx -4\pi\eta\varepsilon l U \tag{1.2}$$

The drag for the perpendicular motion is almost twice larger than the drag when the fiber is parallel. An important consequence of this result is found for the sedimentation of a fiber away from the flow boundaries. A fiber parallel to the vertical direction will sediment at a velocity twice larger than a perpendicular fiber. When the fiber is initially at an angle different from 0° or 90°, this velocity difference between parallel and perpendicular motions will result in a drift of the fiber. Figure 1.1 illustrates the direction of the drift compared to the orientation of the fiber.

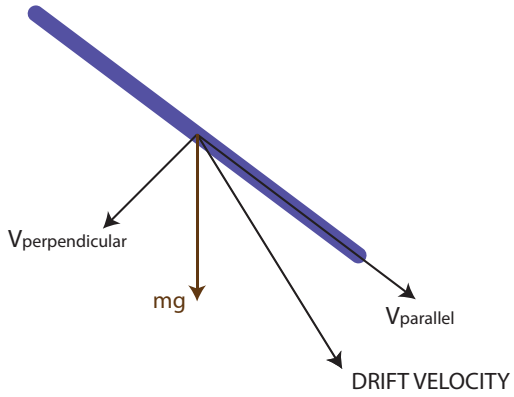

Figure 1.1: *Drawing illustrating the drift of a fiber sedimenting with a non-zero angle with the vertical direction.*

1.1.2 Fiber in a simple shear flow in an unbounded medium

Jeffery published in 1922 his work on the free transport of ellipsoids in simple shear flows [6]. He found two characteristic features. First, the particle's centroid flows at the velocity of the fluid at that same location. He also showed that the ellipsoid experiences a periodic rotation

depending only on the shear rate $\dot{\gamma}$ and the particle's aspect ratio r. Figure 1.2 shows a view of such ellipsoid in polar coordinates.

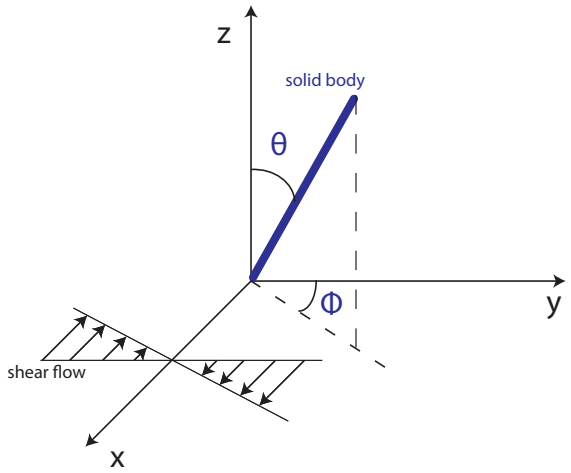

Figure 1.2: *Representation of an elongated body in a simple shear flow in polar coordinates.*

Jeffery's equation describing the angular velocity with the ellipsoid's aspect ratio r is [6]:

$$\dot{\phi} = -\frac{\dot{\gamma}}{r^2+1}(r^2 cos^2\phi + sin^2\phi) \tag{1.3}$$

The integration of his equations leads to a family of curves described by the ellipsoid angle θ:

$$tan\theta = \frac{C_r}{(r^2 cos^2\phi + sin^2\phi)^{\frac{1}{2}}} \tag{1.4}$$

C_r is a constant of integration called the orbit constant . In the absence of external forces or interactions, the ellipsoid will flow indefinitely in a unique orbit. The maximal angular velocity $\dot{\phi}$ is obtained when the ellipsoid is perpendicular to the flow direction and minimal when it is parallel ($\theta = 0$). As a result, most of the flow is done when the ellipsoid is almost parallel to the flow direction. Every half period it flips rapidly (sometimes referred to as a "tumbling motion"). These results were generalized later on for the case of rigid bodies of revolution by Bretherton given a modification of r [7].

1.1.3 Fiber flow near a wall

The flow of a fiber near a solid boundary was investigated experimentally and numerically in simple shear flows and Poiseuille flows [9][10][26]. Questions addressed concerned the fiber's velocity, orientation, and position relative to the boundary.

The case of a fiber transported in a Poiseuille flow near the boundary was investigated in a Hele-Shaw cell of aspect ratio 30 with a cell height much larger than the fiber length: ratio of 3 to 20 [10]. The fiber trajectory is observed in two planes of view and in particular within the channel height where the flow develops into a Poiseuille flow. Two fiber flow regimes are found, depending on the initial position of the fiber. At a distance to the wall δ larger than the fiber length l, fibers rotate periodically with a period of rotation in agreement with previous studies

in unbounded fluids. The presence of the wall does not have any influence on the motion. As the distance δ decreases but stays above $l/2$, the rotation period is higher than the value predicted with the shear rate, regardless of the fiber orbit constant.
In the regime where $\delta/l < 1/2$, interactions with the wall perturb the motion of the fiber. For fibers of high orbit constants, a "pole-vaulting" motion is observed (*in French: saut à la perche*) as illustrated in figure 1.3. The reference to the pole-vaulting discipline should not only be understood in terms of the successive angles of the fiber but also in terms of distance to the wall: the fiber systematically flows away from the wall to a distance comparable to half its length ($l/2$). As this position is reached, the fiber continues to periodically rotate but stays at the same distance. The principles of reversibility and symmetry of Stokes flow are not verified during a pole-vault motion, leading the authors to suggest that non-hydrodynamic forces such as mechanical contact are taking place. Low orbit constant fibers experience a similar motion but stay at constant distance to the wall.

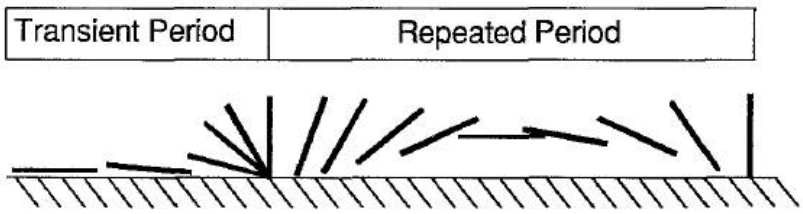

Figure 1.3: *Pole-vaulting trajectory of a fiber placed close to a boundary in a Poiseuille flow. Figure extracted from [10].*

Similarly, in the case of a fiber near a wall in simple shear flow [9], a fiber initially perpendicular to the boundary will rotate. In the regime far from the wall ($\delta > l$) the angular velocity is in agreement with the Jeffery equations. At a closer distance to the boundary, the fiber will rotate at a higher velocity (in agreement with Jeffery using a correction on the shear rate) until it is aligned with the flow direction. No further rotation is observed within the field of view.

1.1.4 Sedimentation near a wall

A third example of a fiber interacting with a solid boundary is the case of sedimentation near a wall. Experiments supported with the slender-body theory report results on the position, orientation and velocity of a single rod inclined with the vertical direction sedimenting near a wall [27].

We recall that an inclined fiber in an unbounded fluid drifts during sedimentation. No rotation is observed, following the principle of reversibility of Stokes flows. As the fiber is approaching a wall, a rotation will occur in two different regimes depending on its initial angle with the vertical direction. Figure 1.4 illustrates the trajectory observed in the two regimes: glancing and reversing.

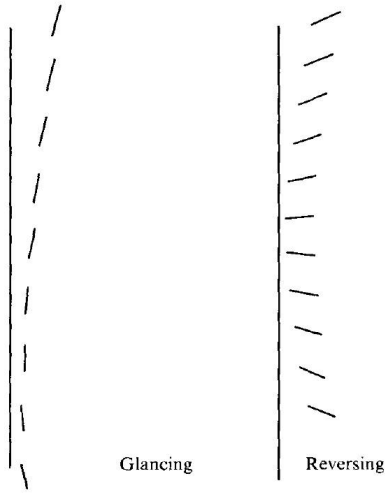

Figure 1.4: *Drawing extracted from [27] showing two possible trajectories of a rod sedimenting near a vertical wall.*

1.2 Fibers in confined geometries

We saw in the previous examples that the presence of a boundary perturbs the flow of an advected fiber. The case of a further interaction, when a fiber is confined between two flow boundaries, was recently investigated experimentally and numerically in the Ph.D. work of B. Semin (2010, [18]). In this study, a single fiber is placed parallel or perpendicular to the flow direction between two parallel walls. Figure 1.5 illustrates the flow geometry.

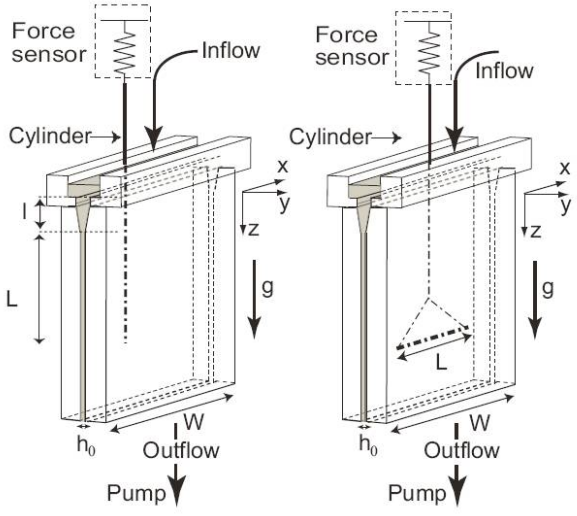

Figure 1.5: *Experimental set-up for the study of a confined fiber between two parallel walls. The left drawing shows the configuration where the fiber is parallel to the flow direction. The right one is the perpendicular configuration. The parameters of particular interest are the fiber length L compared with the aperture width h_0 and the channel width W. (Figure extracted from [17])*

The experimental investigation of the parallel orientation is supported with 2D numerical simulations considering an infinitely-long fiber. In the perpendicular case however, 3D calculations are necessary to take into account the flow circulation around the fiber tips.

The drag force is proportional to the fluid velocity and viscosity as expected in Stokes flows. Drag coefficients for both orientations are found to linearly increase with the confinement however their behaviour differ towards the limit of high confinements (fiber diameter $\approx h_0$). In the parallel case, the drag coefficient increases with the confinement but does not diverge. The drag coefficient of the perpendicular configuration increases faster with confinement and eventually diverges due to the restricted flow path. Figure 1.6 shows the evolution of both drag coefficients.

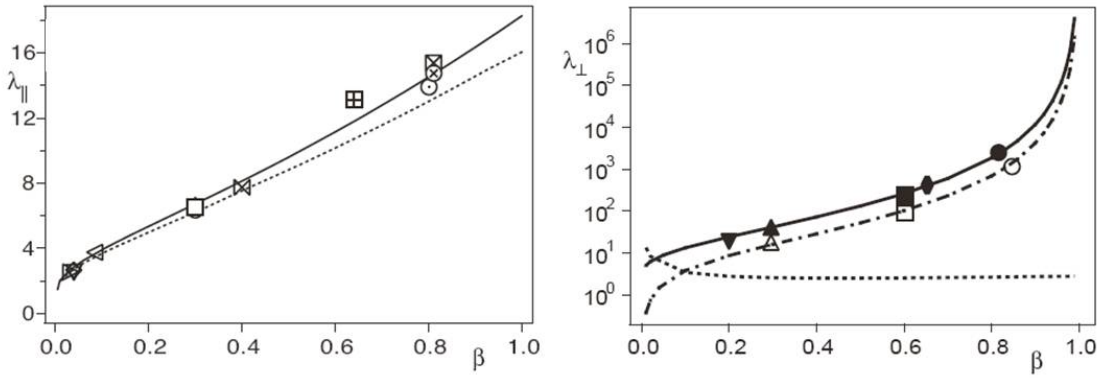

Figure 1.6: *Experimental (symbols) and numerical results (lines) of drag coefficients for the parallel (left) and perpendicular (right) orientations of the fiber reported with the degree of confinement β. β is defined as d/h_0 where d is the fiber diameter. In both cases, drag coefficients increases linearly with the confinement, diverging in the limit of high confinements $\beta = 1$ only in the perpendicular case. Figure extracted from [17].*

At Reynolds number higher than 20, the central position of the fiber between the two walls becomes unstable. The fiber starts to oscillate between them. These experimental observations are supported with modeling work.

The free transport of a unique fiber in a similar geometry was numerically investigated by Champmartin *et al.* [19] and supported with asymptotic developments. The flow geometry is an infinitely-long cylindrical particle positioned perpendicularly to the flow direction and freely transported between two boundaries. The calculation is therefore two-dimensional. The position of the particle relative to the boundaries as well as the effect of confinement on its velocity is explored. The authors found in particular that in the limit of small confinements, the particle flows at the maximal velocity of the fluid in the Poiseuille profile. Towards high confinements, the particle flows at the mean flow velocity. Figure 1.7 illustrates these results of the particle's velocity.

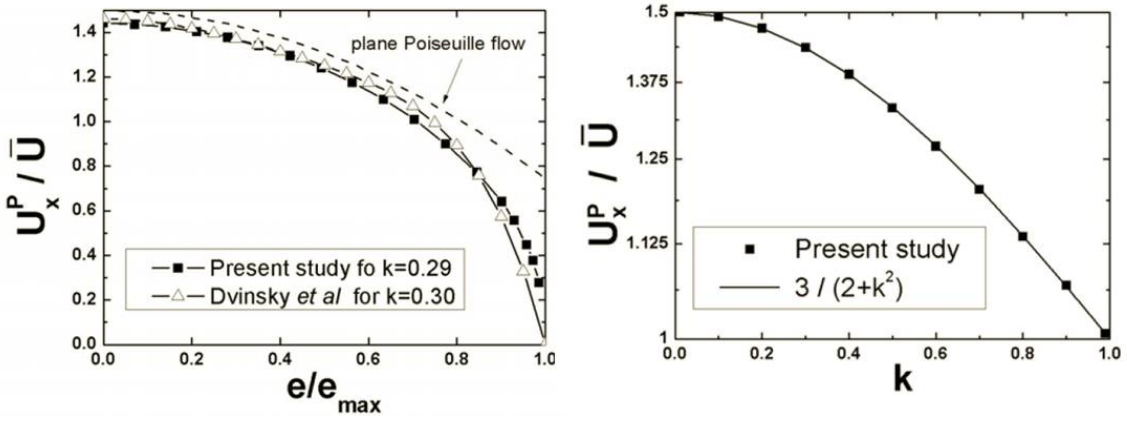

Figure 1.7: *Results of particle velocity (divided with the mean flow velocity $\overline{U}$) reported with the transverse position e and the particle confinement k. e=0 corresponds to the center of the channel, e_{max} to the position of the boundaries. Figures extracted from [19]*

Contrary to fibers, the free transport of spherical particles in confined geometries has recently been investigated experimentally [28]. The development of microfabrication techniques allows to design flow geometries with obstacles, confinement, in a controlled way.

1.3 Collective dynamics of fibers in suspensions

We present in this section some examples of fiber collective dynamics observed in flowing suspensions of fibers.

Clustering

Spontaneous aggregation of fibers in supensions occur in several different physical situations. The first example is a suspension of sedimenting fibers. As recalled earlier in the chapter, a unique fiber inclined with the vertical direction sediments with a drift. Then, as it approaches a solid boundary, its motion is perturbed and the fiber rotates. When many of such fibers are dispersed in a fluid with random orientations, collisions will occur between drifting fibers at a probability increasing with their concentration.
Recent theoretical studies predict that the sedimentation of dilute monodisperse fiber suspensions is an unstable flow, leading to the formation of fiber clusters [29]. Heterogeneities in the distribution of fibers and in their velocity increase as the clusters sediment faster than isolated fibers. Recent experimental and numerical work agreed with these theoretical predictions and showed results dependent on the fiber concentration in suspension. The case of dilute suspensions was for example investigated by Butler & Shaqfeh [30] at low Reynolds numbers (10^{-2}). They observe the continuous formation and deformation of fiber clusters, agreeing with the experimental observation [31]. Such clusters obtained experimentally [31] are shown in figure 1.8. Fiber clusters flow faster than isolated fibers and occasionally flip due to back flow of regions of fluid with less fibers. Strong orientation in the direction of gravity is also observed.
In the semi-dilute regime, at higher concentrations, fibers entangle to form a semi-rigid network hindering the sedimentation motion. The orientation of fibers however was found not to depend on the concentration regime [4].

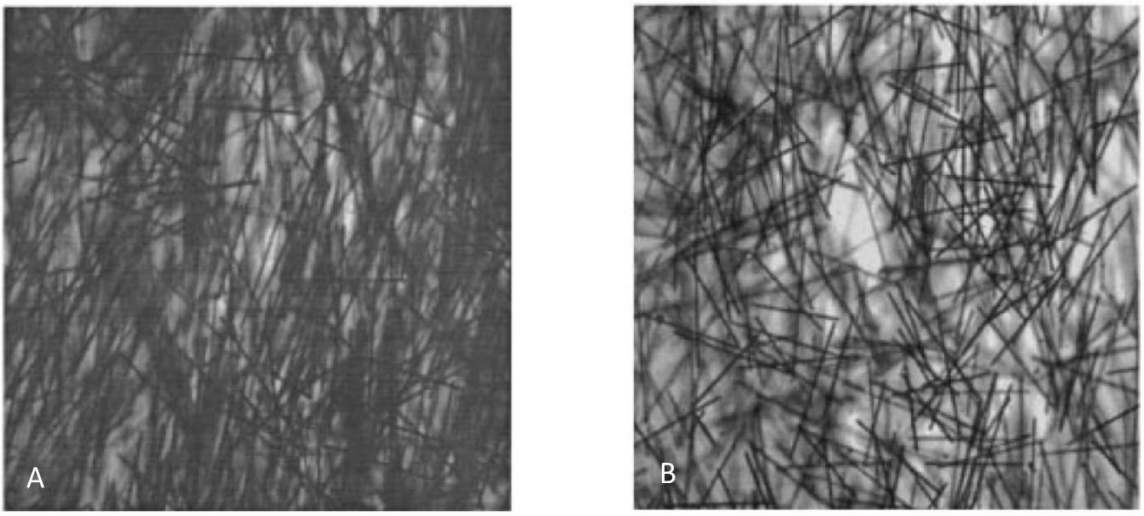

Figure 1.8: *Experimental pictures of the sedimentation of a fiber suspension at two different time steps, extracted from [31]. The suspension is homogeneous initially. Time is made dimensionless by the time taken by an isolated fiber to fall half its length. In photograph A, time t=5, in photograph B t=60. The second picture shows the apparition of fiber aggregates, leading to fast-sedimenting clusters in the suspension.*

Clustering of fibers is also observed in sheared suspensions and called in this situation **flocculation**.
Flocculation-related issues in papermaking has actually been a driving element for research on fiber suspensions for many decades [32]. Flocculation describes the aggregation of fibers into clumps when a highly-concentrated suspension of fibers is sheared. Figure 1.9 presents an example of flocs obtained from industrial fibers suspended in a water-based fluid. Paper manufacturers try to avoid flocculation as flocs in the cellulose fiber suspensions are responsible for heterogeneities on the final paper sheets. Heterogeneities imply that there will be weak regions in the paper, leading to mechanical fragility. They are also responsible for unaesthetic features.

Figure 1.9: *Pictures of fibers flocculated in suspensions. Initially dry fibers (left) are dispersed in a water-based fluid (middle). Entangled fibers form a network structure (right). Pictures extracted from CemNET Schlumberger documentation[33].*

When many of fibers are suspended in a sheared fluid, their rotating motions will cause collisions unless their concentration is too small [6]. Fibers collisions are the first cause of the formation of flocs, leading Mason [2][3] to propose a concentration threshold for a given suspension. He introduced the "critical fiber concentration" based on the idea that a rotating fiber describes a spherical volume whose diameter is given by the fiber length. Then, in order to compute a probability of collisions and of inter-fiber contacts, Kerekes introduced a crowding factor [34] [35]. This parameter characterizes a suspension by the number of fibers in the spherical volume corresponding to the rotation volume of one fiber.

In this mechanical point of view, flocs can form and deform continuously. A mechanism explaining their persistence in flow was proposed based on the idea that fibers temporarily bend under shear [23]. Fibers collide and entangle with their neighbouring particles, blocked in bent configurations. Friction between fibers and elastic energy stored in the bending give flocs their strength and persistence through flow.

The main factors enhancing flocculation are typically high flow velocities, low viscosities, high fiber aspect ratio and stiffness [23][35][36]. Such results obtained with experimental studies are largely complemented with literature on numerical work where the technical difficulties associated with fibers experiments are overcome. For example, simulations are used to tune inter-fiber friction without modifying other fibers parameters or taking into account other forces [37]. Similarly, many numerical studies can be found on sedimentation of fibers [30] and flows of fiber suspensions interacting with boundaries [38].

The mechanism proposed for the formation of flocs, often referred to as "bend, straighten and lock" [23] suggests that flocs can break when subjected to forces higher than the friction and stored elastic forces holding them together. Shear flows will tend to make them rotate [39]. However, extensional flows have been shown to efficiently break them [40] [41] [42]. This behavior is of particular interest in this collaboration work between Schlumberger and the ESPCI-PMMH. In applications of lost-circulation curing introduced in the previous chapter, fibers are mixed with drilling fluids to block flow through natural or induced fractures, fissures or highly porous zones [1]. The presence of flocs in the suspensions downhole is believed to be one of the mechanisms of sealing. Depending on fracture sizes, pressure, flocs may however be broken at the entrance of the fracture where maximal extensional stresses occur. Typically wellbore diameter is of the order of 20 cm, to be compared with typical fracture sizes of a few millimeters.

Jamming

Another mechanism proposed for the clogging of flow restrictions in lost-circulation curing is jamming of fiber suspensions. Particle suspensions jam when their volume fraction is high enough. Recent rheological studies showed that this jamming threshold is however reduced when the suspension experiences shear [43], with an increased effect observed for suspensions of anisotropic particles. In extensional flows of jammed suspensions such as flows through restrictions, particles concentration is reduced downstream of the restriction [5].

1.4 *In situ* particle microfabrication techniques

We now present recent technical achievements in the production of particles in microchannels. The two techniques reviewed here were implemented in our micromodel investigation.

1.4.1 Lithography method of particle fabrication

1.4.1.1 Fabrication principle

A technique to fabricate microparticles directly into microfluidic channels has been recently developped in Patrick Doyle's research group at MIT [44]. The fabrication uses the principle of microscope-based projection photolithography. Initially invented and developped for the microelectronics industry [45], this technique would enable the fabrication of micrometric and submicrometric features in photo-sensitive resins by means of projecting a mask onto a silicon wafer with an optical microscope objective. It was then succesfully applied to soft-lithography techniques as an alternative to the now-traditionnal clean room fabrication method and its expensive costs [46]. A few years later, Dendukuri *et al.* applied the same principle to mass-fabricate micrometric-shaped particles directly inside microfluidic channels where they can then flow [20].

Similarly to its microelectronics precursor, the fabrication set-up only requires a microscope, a lithography mask, a UV-light source and an all-PDMS (polydimethylsiloxane, Sigma, see Appendix A) microfluidic channel. The channel is placed on an inverted microscope and filled with a solution of oligomer and photo-initiator. A photolithography mask of the particle shape is placed in the field-stop position of the microscope. We expose the channel to a pulse of UV-light through the lithography mask; the particle shape gets projected into the microchannel and focused in its center where the exposed portion of fluid crosslinks within tens of microseconds. A schematic drawing of the process is described in figure 1.10.
The polymerization process is a free-radical reaction taking place in four steps: photolysis, chain initiation, propagation and termination. During the photolysis, the photo-initiator reacts with UV-light to produce two free radical species as illustrated in figure 1.12 with the commercial photo-initiator Darocur 1173 (2-Hydroxy-2-Methylpropiophenone, Sigma, 1.11). The radicals react with an acrylate group of the oligomer to form a reactive alkyl monomer radical, initiating the reaction. Crosslinking occurs during the propagation step where the radicals react in chain with other oligomer molecules. The termination step happens as radicals interact or recombine to give neutral species. These four steps are described for the case of acrylate-monomers in figure 1.13.

1.4.1.2 Particle characteristics

The particles fabricated using projection photolithography have a rectangular or square cross-section due to the geometry of the channel. Particle length and width are proportionnal to the dimensions on the lithography mask modulo a factor given both by the magnification of the objective and a constant from the microscope itself.

The particle height is given by the channel height, since the projection of UV-light is done through the fluid along this direction. The method takes advantage of the permeability of PDMS to dioxygen so that the fabricated particle doesn't stick to the channel walls and flows

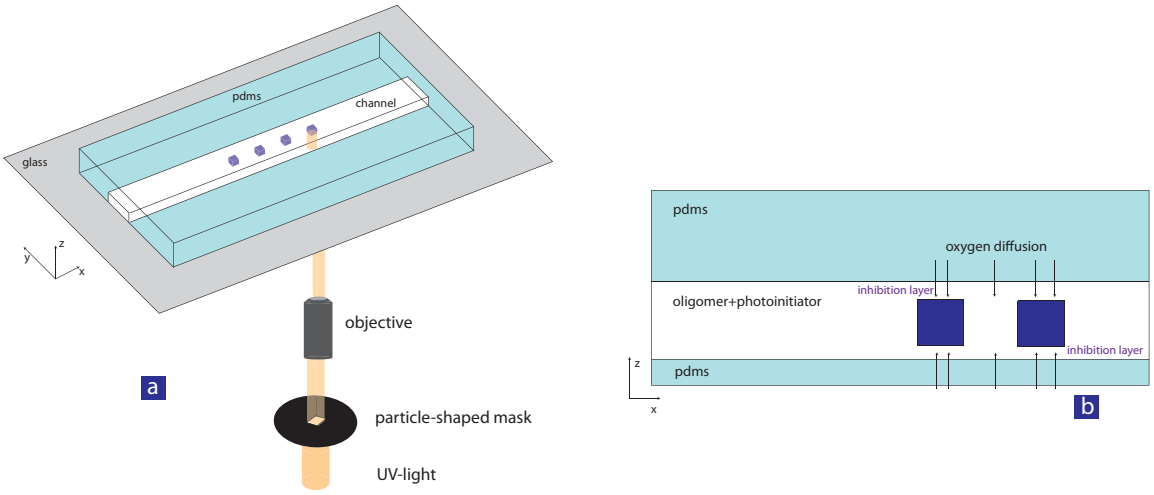

Figure 1.10: *Schematic drawing of the fabrication method (a): a particle-shaped mask (here, square shape) is projected into an oligomer solution containing some photo-initiator, by means of a UV light source and through a microscope objective. The right drawing (b) shows the inhibition layers where the presence of dioxygen terminates the polymerization. The particles can then flow in the fluid downstream of the microchannel.*

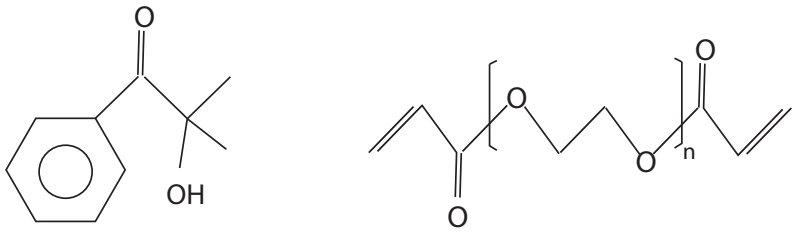

Figure 1.11: *Photo-initator Darocur 1173 (Sigma)*

downstream. Dioxygen inhibits the polymerization reaction as it reacts with radicals to form an oxygen-oxygen link (see in eq. 1.5 the chemical reaction: R designing the radical, M the monomer).

$$RM_n^{\cdot} + O_2 -> RM_nOO \tag{1.5}$$

A thin layer of fluid along all the channel walls contains dioxygen that has diffused through the PDMS. Consequently, the portion of fluid polymerizing along the channel height is reduced by these so-called inhibition layers (right drawing of 1.10). The layer thickness is independent of the channel height [47]. It was characterized by a one-dimensional model of light penetration and reaction kinetics to study the influence of the concentration of photo-initiator, the light intensity and channel height. In conclusion, the three dimensions of the particle are determined by the optical properties of the system (microscope+objective+mask dimensions) as well as by

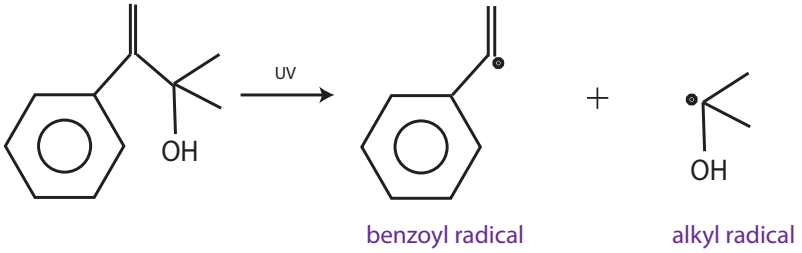

Figure 1.12: *initiation*

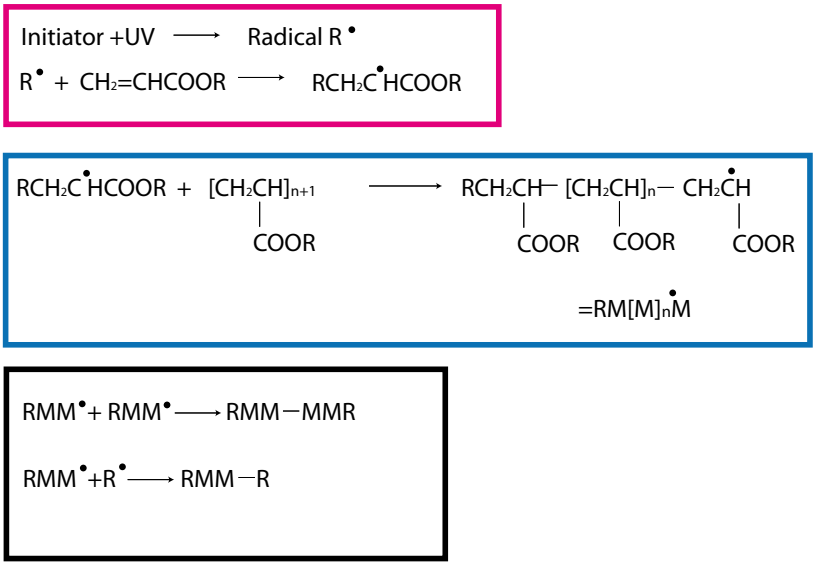

Figure 1.13: *radical photopolymerization reaction*

the channel height and chemistry.

The mechanical properties of the particles are governed by the nature of the polymer used for the fabrication. It can play a major role in the targeted flow application. For example Attia et al [48] developed a flow sensor using the *in situ* polymerization of a spring-like structure fixed inside the channel. In this case, the elongational properties of the sensor depend on the nature of the polymerised network.

1.4.2 Self-assembling colloids to fabricate filaments

1.4.2.1 Fabrication principle

We introduce a second fabrication method which was originally developed experimentally during the PhD work of C. Goubault at ESPCI (2004, [22]) to fabricate elastic filaments in microchannels. These filaments are made of self-assembled super-paramagnetic colloids which are bridged together by polymer chains. Initially developed to provide micromechanical sensors [21], they have been used as a basis for active micro-swimmers [49]. Babataheri *et al.* demonstrated that they could be anchored on a surface to form carpets of cilia, driven by a

variable magnetic field [50]. They studied the collective beating dynamics for such structures while Coq *et al.* [51] reported on beating regimes of isolated filaments actuated by a magnetic field.

Super-paramagnetic particles are freely suspended in solution and subject to Brownian motion. When a magnetic field is applied, each colloidal particle acquires a magnetic moment **m** parallel to the magnetic field **B** and of intensity $v\chi B$ where v is the particle volume, χ its magnetic susceptibility and B the magnetic field intensity. Dipolar interactions induce self-assembly in one-dimensional structures aligned with **B**.

The magnetic interaction energy between two dipoles depends as $1-3cos^2\theta$ with the angle θ formed by the two moments and the direction of the magnetic field. Figure 1.14 gives its full expression with μ_0 the vacuum permeability. The minimal energy is obtained when the two dipoles are aligned, however if the angle is maintained below: $\theta < arccos(1/\sqrt{3})$ the interaction stays attractive. The dipoles are in the "attractive region" as illustrated in figure 1.14 and can come in close contact. The formation of chains with more than one array of colloids is therefore possible.

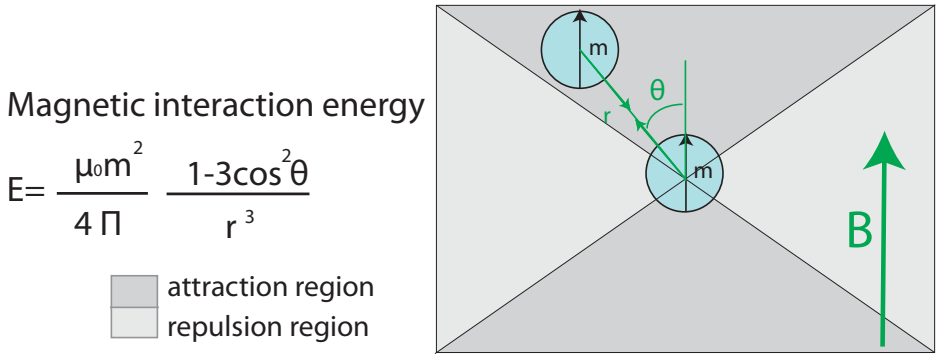

Figure 1.14: *Dipole dipole magnetic interactions*

Since the particles are super-paramagnetic, the filaments are not permanently formed. Once the magnetic field is removed the colloids move freely and independently in the solution due to brownian motion. One way to bridge the colloids and form permanent filaments is to use polymer chains bridging colloids together when they are aligned in chains in very close contact [52]. This mechanism has a threshold: it can only work when the distance separating the two colloids is very small, meaning that the intensity of the magnetic field should be high enough to bring colloids to close contact. Other methods are possible, for instance using biological linkers like antibodies and antigenes [22].

The set-up requires a microscope equipped with a coil to produce a vertical magnetic field, a microchannel and super-paramagnetic particles. The fabrication takes place in three steps as described in figure 1.15. The solution of superparamagnetic colloidal particles and polymer in water is introduced in a microchannel or capillary tube. The flow is stopped and a vertical magnetic field is applied. During this step, the attractive magnetic interactions cause the colloids to self-assemble as chains along the vertical direction. When two colloids get close to each other, polyelectrolyte binding cause the polymer chains adsorbed on their surface to

bridge them permanently together, acting like linkers [53]. In the last step, the magnetic field is removed causing the colloidal particles to loose their magnetic moment though they are still held together by the polymer. The filaments are permanently formed and sediment in the channel with random directions.

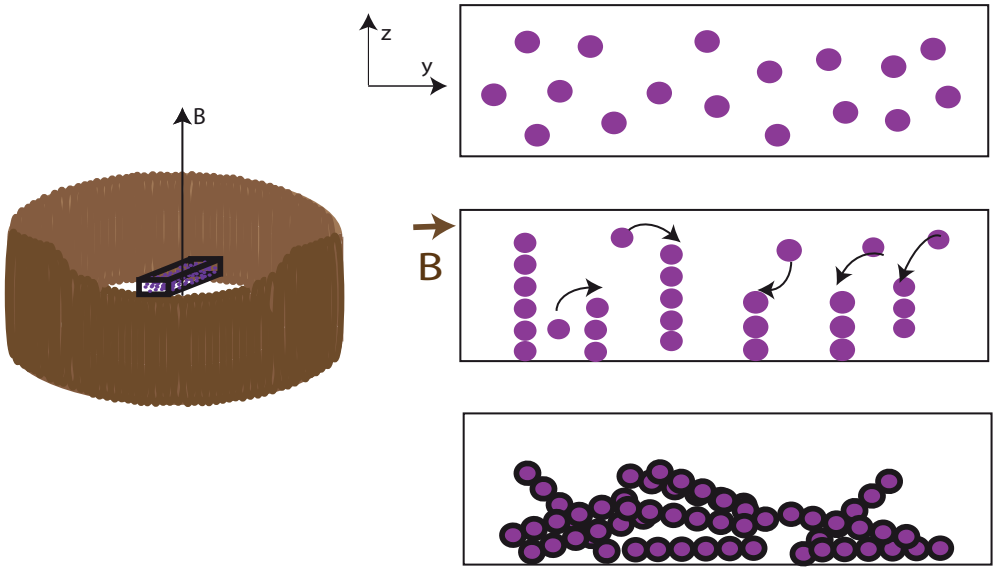

Figure 1.15: *Principle of fabrication of fibers using super-paramagnetic particles*

1.4.2.2 Filaments characteristics

The filaments are characterized by a cylindrical shape: their diameter is given by the diameter of the colloidal particles. Their aspect ratio can be very large: the fiber length is only governed by the channel height and the volume fraction of particles available. Babataheri *et al.* typically obtained $200\mu m$-long filaments. Since the colloidal particles contain nanoscopic grains of iron oxyde (Fe_2O_3), they are denser than the aqueous solution. During the application of the vertical magnetic field, their density will tend to make them sediment to the bottom of the channel, competing with the magnetic attractive forces between two particles along the vertical direction. This property can be used to get filaments much shorter than the channel height by adding a sedimentation step before the application of the magnetic field [51].

The concentration of filaments in solution depends on the initial volume fraction of colloids for a given channel geometry. When applying the magnetic field, the columns formed by the assembled colloids show a strong ordering: the dipolar magnetic interactions between columns are responsible for a constant separation distance between them. Liu *et al.* [54] characterized this ordering and showed that the separation distance follows a relation with the chain length: $d = 1.33L^{0.37}$. It also means that there is a maximum concentration of filaments which depends on the channel height. At constant volume fraction, the higher a channel the longer the chains forms, which in return decreases the distance between filaments.

Filament elasticity depends on the nature of the polymer bridging the particles together. A bending modulus of $10^{-23} J.m$ was measured [22] for filaments obtained with the same particles

and polymer chains as in our experiments. As they are formed as chains of spherical particles, their surface roughness is given by the particles radius and cannot be easily modified.

CHAPTER 2

LITHOGRAPHY FABRICATION OF FIBERS

The motivation of this work is to study the flow dynamics of isolated fiber and suspensions of fibers in confined flow geometries. Our objective is to use microfluidics to set up an experimental model system where we can observe the flow and vary parameters associated with the flow geometry and with the fibers. Experiments of fiber flow at the microfluidic scale requires the introduction of fibers inside the channel. However microsized fibers of controlled geometry are not commercially available. Another technical difficulty comes from the flow restrictions inside all the microfluidic connections where the fibers could accumulate and create flow blockage. A solution is to use modern techniques of micro fabrication to produce fibers *in situ*. We present in this chapter how we adapted the microparticle fabrication method based on photolithography which was introduced in the first chapter of this manuscript (1.4.1.1) for the fabrication of microscale fibers. This technique enables the fabrication of fiber-shaped particles with an excellent control of their geometry, directly inside the microchannel preventing risks of flow plugs. This way we can tune the mechanical properties of the fibers as well as their surface state. We will describe the fabrication of both isolated fibers and fiber suspensions with an excellent control over their initial state: orientation of the fiber, placement inside the microfluidic geometry.

2.1 Fabrication principle

The method uses the principle of microscope-based projection lithography which was introduced in the first chapter of this thesis (1.4.1.1). The idea is to project UV-light through a fiber-shaped mask into the channel where one wants to make the fiber. The channel is filled with a solution of oligomer and photo-initiator chosen for the properties of its polymerized phase. The solution crosslinks under UV-light: the illumination of the target fluid region makes it polymerize within tens of milliseconds. A schematic drawing of the method is presented in Figure 2.1.

Since we are projecting a two-dimensional fiber shape through the height of the channel, we create fibers of typically rectangular cross-sections. The fabricated particles are able to flow inside the channel because thin layers of fluid along the channel top and bottom walls remain unpolymerized. This inhibition property of such layers is taken advantage of for the design of the fiber geometry as we will see later in this chapter.

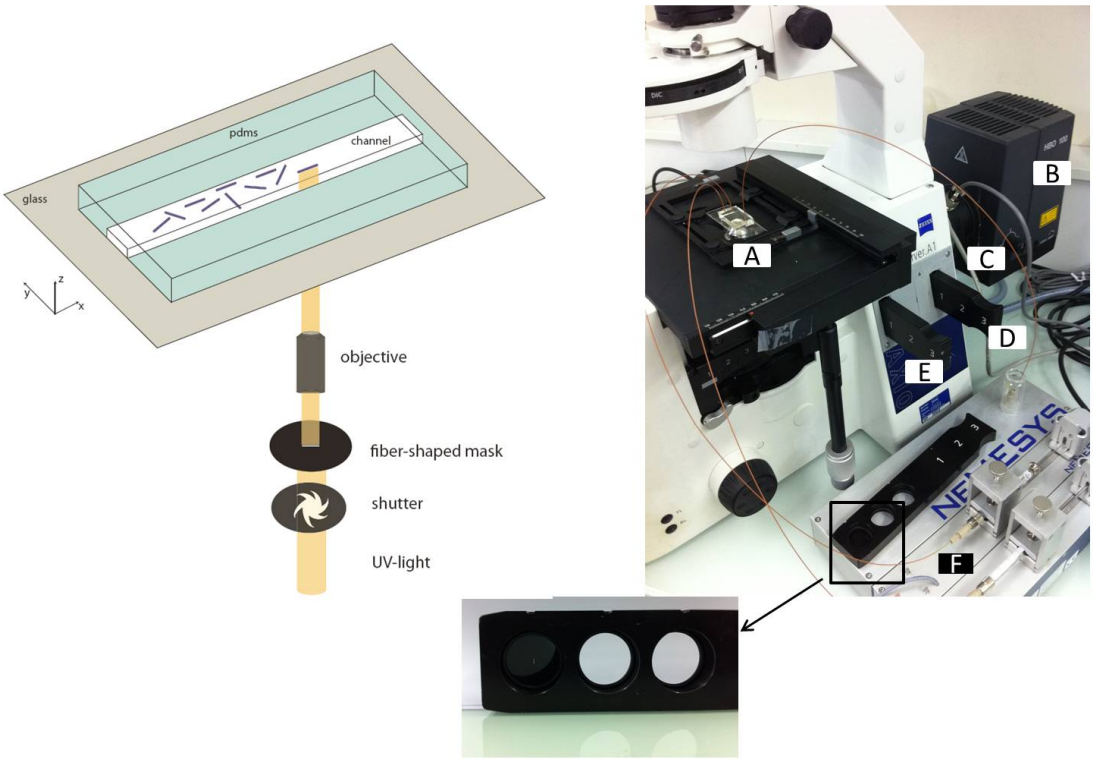

Figure 2.1: *In situ fabrication of fibers using a projection method. The left drawing shows all the elements necessary for the projection on the microscope. They are indicated on the picture of the experimental set-up (right): A: channel filled with oligomer and photo-initiator solution, placed on the microscope. B: UV-light source C: shutter D: filter E: fiber-shaped mask and F: syringe pump. The bottom picture shows the mask holder with an actual mask in place in the left slot. A white fiber shape is drawn in its center.*

2.2 Experimental protocol

2.2.1 Experimental set-up

We build a fabrication and flow platform in a single set-up as illustrated in 2.1. A transparent microchannel is made with traditionnal soft-lithography techniques in polydimethylsiloxane (PDMS, Sylgard 184, Corning). Details of the microfabrication can be found in Appendix A. It is then placed on the stage of an inverted microscope (Zeiss Axio Observer) equipped with a UV-light source, a shutter and a fiber-shaped mask (Shutter Uniblitz V25, Lamp HBO 130W). The UV light is filtered through a narrow-UV-excitation filter set (11004v2 Chroma) with an emission peak at λ >390 nm.

Anti-UV coated tubings are used to connect the inlet and outlet of the microchannel to a syringe or fluid reservoir. We use two methods to start and stop the flow: the first one consists in varying the vertical distance between the inlet and outlet fluid levels to induce a pressure-imposed flow. The second method consists in imposing a constant flowrate with a syringe pump delivering fluid into the inlet tubing. Our geometries require a small flowrate of the order of $nL.s^{-1}$. We use a NeMESYS (Cetoni) syringe pump capable of delivering such small flow in a stable continuous manner.

2.2.2 Microfluidic channel

We work with rectangular-section channels where the width is typically ten times larger than the height. Orders of magnitude of channel dimensions are: width $100\mu m$, height $10\mu m$, length several centimeters. Such confinement is required by the fabrication technique because of the constraint imposed by the channel height on the fiber dimension. As we explained in the introduction chapter 1.4.1.1, fiber width and length are independent of the channel geometry however its height is given by the channel height. We will develop this aspect in more details in the section dedicated to fiber geometrical design 2.3.1.

2.2.3 Oligomer solutions

The choice of the oligomer solution and the concentration of photo-initiator should be made in regards with the targeted mechanical properties of the fabricated fiber. The nature of the photo-initiator is also important from a technical point of view: its excitation wavelength should be matched with the light source available and the set-up constraints. We worked with a solution of polyethyleneglycoldiacrylate (PEGDA, Mw=575, Sigma) with Darocur 1173 photo-initiator (PI) (2-hydroxy-2-methylpropiophenone, Sigma) at 10 wt%.

The density of the oligomer/PI solution is 1.12 $g.cm^{-3}$ and its kinematic viscosity 52.2 $mm^2.s^{-1}$ (experimentally measured using capillary rheometers and densitometer).

2.2.4 Lithography mask design

A fiber shape is projected into the channel using a lithography mask specifically designed for a given fiber geometry. We place this mask in the field stop position of the microscope to get it focused into the objective image plane (see picture of the set-up in 2.1-E). The mask is designed with AUTOCAD 2009 and printed at a resolution of 50800 dpi at SELBA S.A (Switzerland). It

consists of a transparent-fiber shape drawn in the center part of a 25mm-diameter black disk to be conveniently placed in the microscope holder. The highest printing resolution available was used to limit defects on the border line and black spots inside the fiber shape. Examples of fiber masks are presented in figure 2.2. Figure 2.3 shows pictures of two masks, one printed with a poor resolution and one with the highest one.

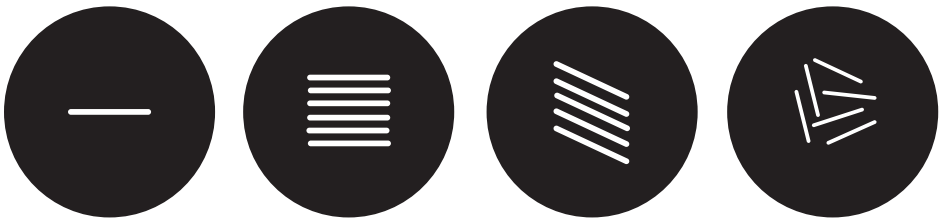

Figure 2.2: *Possible designs of fiber-shaped lithography masks. The first one is used for a single fiber, the three others are used for fabrication of groups of fibers with a given orientation.*

2.2.5 Light shutter

We equipped the Zeiss microscope with an electronic shutter (V25, Uniblitz) capable of a minimum window time of 10 ms (from pulse sent to opening and closing of the shutter). The shutter is mounted between the microscope and the UV-light source (HBO lamp) as illustrated in picture 2.1. Its blades are treated to resist to high temperature from UV-exposure. We control the opening time (=duration of the light pulse for the fabrication) and the opening frequency (for the fabrication of several fibers in the channel) using a computer-based Labview programme. We wrote the programme to dialogue directly from the PC to the shutter driver (VCM-D1 Single Channel, Uniblitz). This will be particularly useful in the future as a single Labview programme can be used to control several pieces of equipment of the set-up simultaneously: shutter, camera, electronic microscope stage.

2.2.6 Protocol

2.2.6.1 Workflow

We describe here the typical work flow of a fabrication experiment. The preparation prior to the experiment should involve the design of the mask for the desired fiber geometry, the design and fabrication of the microchannel accordingly, and placement of the channel and mask on the microscope. A camera is used for direct observation of the channel. The first step is the optical focusing of the fiber-shape mask. It consists in making sure that the microscope is set with the mask placed in the image plane of the lens. This step is described in the next section. The second step is to get a stable continuous flow or stop the flow, according to the need. As mentioned above, either a syringe pump or pressure-imposed flow will be used. Then

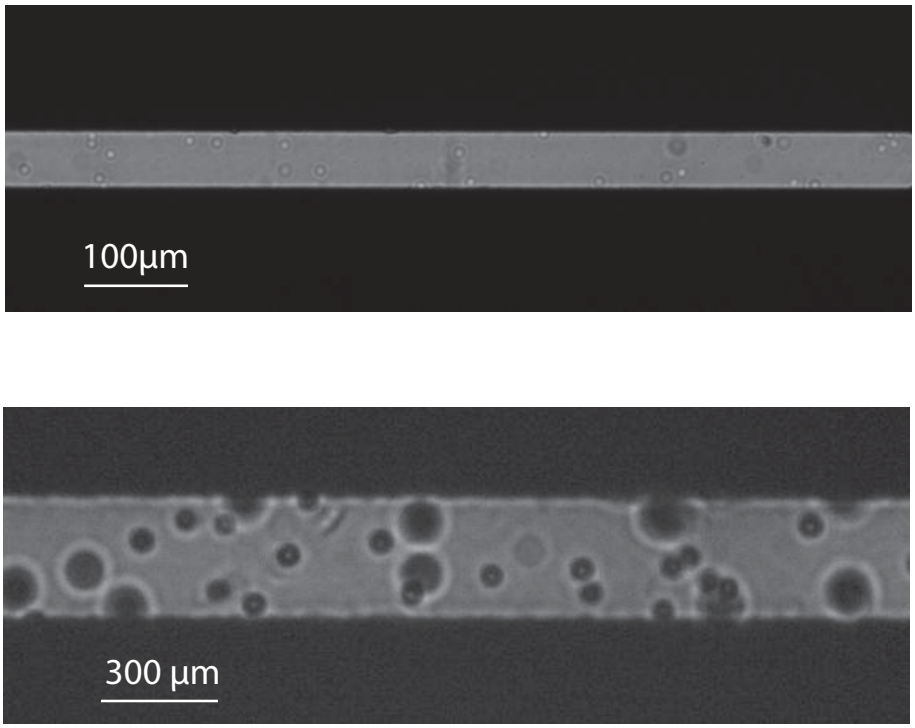

Figure 2.3: *Examples of two printing resolutions of lithography masks. The top micrograph shows a fiber-shaped mask printed at 50800 dpi. The bottom micrograph shows a channel designed with a restriction, printed at 10000 dpi.*

the user positions the channel using the stage so that the fiber shape will be projected at the right location inside the channel. Finally, the user programs the shutter via the computer to illuminate the channel for a given duration. All these steps are described in a workflow diagramme presented in figure 2.4.

2.2.6.2 Optical focusing

The fabrication requires the user to carefully focus the projected mask structure into the channel. Microscope objectives are typically corrected in visible light for achromatic aberrations. These aberrations are caused by the dispersion of the lense refractive properties with wavelength. A calibration of the optical system is necessary prior to fabrication since it requires UV-light: an object focused with visible light will not be focused anymore with UV-light in the channel. This is particularly true of high-magnification objectives which have a short depth of field.

For an objective 10X, a preliminary focusing of the fiber-shaped mask is realized with visible light and no shift is applied. For objectives 20X and higher, the distance of "defocusing" is determined in a test channel and applied before each fabrication, following the focus settings. On our microscope, for the X40 objective the defocusing was a quarter of full knob rotation.

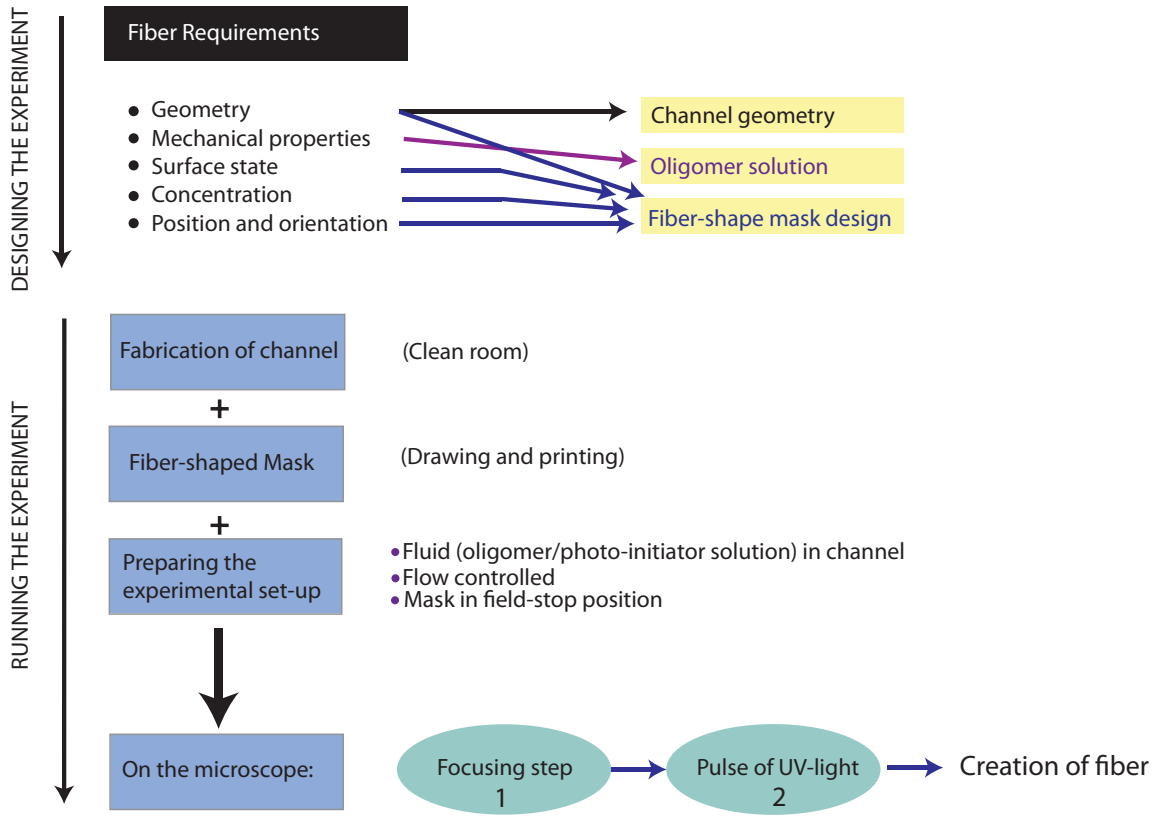

Figure 2.4: *A to Z steps for designing and running a fiber fabrication experiment with the lithography technique*

The resolution of our optical system can be similarly characterized based on the type of objectives used for the fabrication. We call resolution the smallest distance between two object structures at which these objects are imaged separately. A theoretical resolution limit was first introduced by Abbe (1880) and can be computed using the numerical aperture of the objectives. Table 2.1 gives the theoretical resolutions for all the objectives used in our experimental tests.

Note that microscope objectives have vary different optical transmission in UV-light wavelengths. A "good" objective for other microscopy applications may not be useful at all for the photopolymerization method.

2.3 Fiber characteristics

2.3.1 Geometrical design: from the mask to the fiber

As the fabrication technique relies on the 2D projection of a fiber-shape through the channel height, we cannot fabricate cylindrical fibers but rectangular cross-section fibers and in our particular approach, square cross-section fibers.

We characterized our optical system to obtain the linear relation between mask dimensions and

the actual particle dimensions in the channel. The reduction factor corresponds to the magnification of the objective corrected by a factor from the tube lens. In most optical microscopes, the objective forms the object images at infinity and this supplementary lens in the microscope tube is used to project this image into the focal plane of the camera. We found that the tube lens factor was 2.2. The reduction factor for an αX objective is $\alpha/2.2$. Table 2.1 gives the different reduction factors depending on the microscope objectives. Low-magnification objectives are easier to work with for the fabrication as they have a larger depth of field.
For very small-height channels, the use of high-magnification objectives may become an issue when the depth of field gets smaller than the channel height.

Objectives	5X	10X	20X	40X
Reduction factor	2.27	4.54	9.1	18.2
Depth of field(μm)	230	60.26	25.98	7.92
Numerical aperture	0.13	0.25	0.3	0.5
Theoretical resolution(μm)	1.5	0.78	0.65	0.39

Table 2.1: *Properties of the different objectives used in the fabrication of fibers by projection lithography. The wavelength (λ) used for the calculation of the resolution and depth of field is 390 nm. Depth of field is computed using the equation provided by the microscope objectives manufacturer (Zeiss): $DOF = \frac{1000}{7NA} + \frac{\lambda}{2*NA^2}$ with NA being the numerical aperture of the lens.*

2.3.2 Inhibition layer and consequence on the fiber geometry

Portions of fluid along the channel walls stay unpolymerized due to diffused oxygen through the PDMS walls as illustrated in figure 2.5. Oxygen inhibits the chemical reaction of polymerization as it reacts with free radicals to form an oxygen-oxygen bond (1.5). We measure for each channel the inhibition layer thickness to fine tune the height dimension of the fiber. The measurement method consists of hypothysizing an inhibition layer thickness of around $5\mu m$ then fabricating a fiber with a much smaller width. When the fiber starts flowing it turns on its side and shows its height that one can then easily measure. Figure 2.6 shows a top view of the fiber flowing in the channel. The first picture (a) shows the fiber as it appears upon fabrication. As it turns on its side, its height becomes sharp in the observation plane as illustrated in picture b.
Another calibration method consists in taking advantage of PDMS structures inside the channel. One can crosslink a particle around such feature and measure the distance separating it to the particle.
We will present in the next chapters results of fibers fabricated in channels of different heights. The inhibition layer thickness was found to be 6 μm regardless of the channel height. The corresponding measurements are given in table 2.2. We tried to reduce chemically the inhibition layers by performing initial rinsing of the channel with a solution of ethanol and photo-initiator (10 w%) prior to fabrication. The polymerized fibers were stuck inside the channel as if the inhibition layer had completely disappeared.

2.3.3 Enhancing the fiber surface roughness

In order to enhance the roughness in a controlled way, it is possible to modify the borders of the lithography-mask fiber from straight to sawtooth lines. Picture of such mask and the resulted

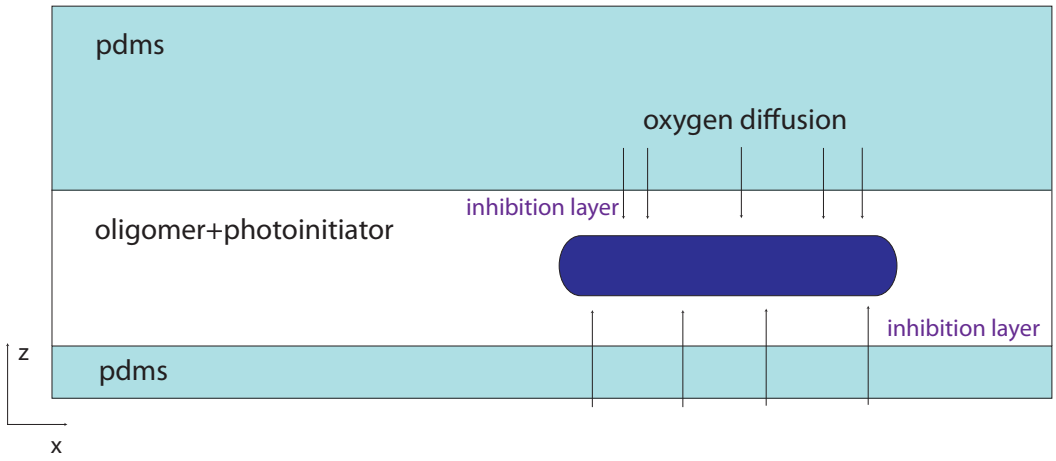

Figure 2.5: *Schematic drawing of inhibition layers above and below a fiber fabricated with projection photo-lithography.*

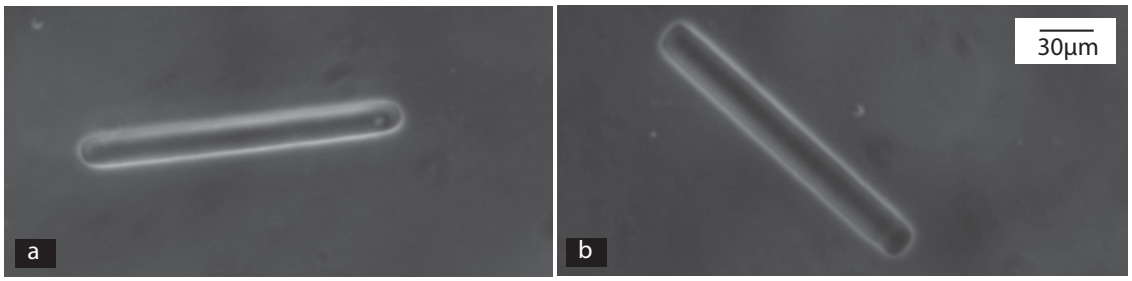

Figure 2.6: *Two pictures of the same fiber, (a) upon fabrication and (b) as it turned on its side. We adjusted the dimensions of the fiber-shaped mask to the channel height so that the fiber height would be significantly larger than the fiber width. This method of channel calibration is used to measure the inhibition layer thickness.*

fiber are presented in figure 2.7. The same strategy can also be adopted when designing the channel geometry for the soft-lithography fabrication. This way, we can increase mechanical interactions between fibers or fibers with the lateral flow boundaries.

2.3.4 Mechanical characterization

The fiber mechanical properties are governed by the nature of the polymer used for the fabrication. The degree of cross-linking that we obtain inside the microchannel using our experimental protocol cannot be easily upscaled to do a macroscopic mechanical caracterization. In order to have a measurement of the fiber's Young's modulus, we developped an independent experiment where we fabricate a fiber which interacts with the flow similarly to a bending beam test. The

Channel height (μm)	Fiber height (μm)	Inhibition layer thickness (μm)
20 ±0.5	8±2	6±1
32±0.5	20±2	6±1

Table 2.2: *Fiber height obtained in two channels of different height.*

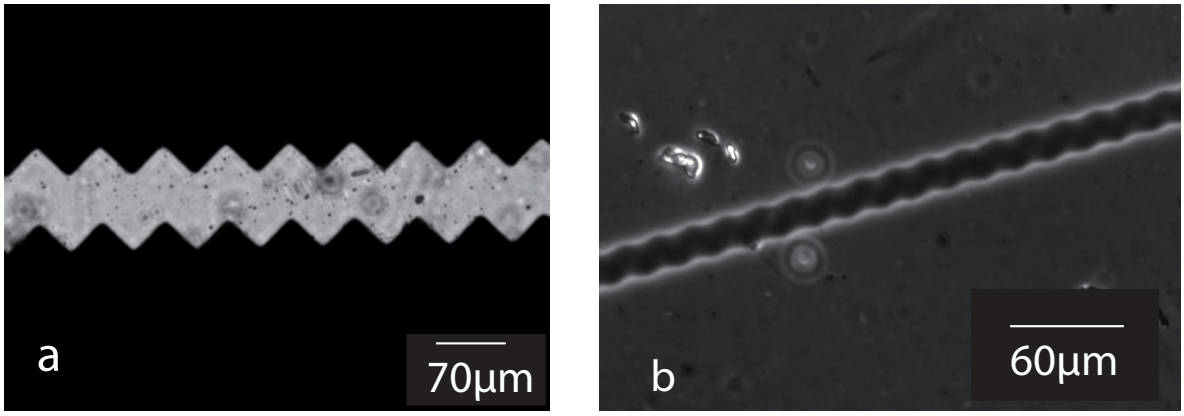

Figure 2.7: *One way to artificially enhance the surface roughness of the fibers is to draw its borders with saw-tooth lines instead of straight ones on the fiber-shaped lithography mask. We illustrate this with a picture of the mask (a) taken on the microscope and the corresponding fiber flowing in the channel (b). Phase contrast is used to enhance the fiber visibility and is responsible for the white region around the fiber.*

deformation of the fiber coupled with numerical simulations lead to a reproducible measurement of its Young's modulus as detailed in chapter 4 of this manuscript. We found a modulus of 1.054 $MPa \pm 3.2$.[1]

We also present in Appendix E a collaboration work with Jason Wexler and Howard Stone (Princeton University) where the deformation of a fiber fixed in a confined microchannel is investigated. Characterization of the fiber mechanical properties is required to analize its bending under drag force.

The same solution of PEGDA with photoinitiator was used throughout this work. Note that the flexibility of the fibers can be changed by acting on the chemical nature of the polymerizing solution: using PEGDA of different chain lengths, using monoacrylate polymers rather than diacrylate ones.

[1] The Young's modulus is obtained from a set of experiments with three different geometries. The average value and its uncertainty are obtained aggregating the results of all the experiments. More detail is provided in chapter 4, table 4.2.

2.4 Fabrication and flow

2.4.1 Fabrication with the fluid at rest

Fibers can be made inside the microchannel at zero flowrate. We typically use pressure-driven flows to instantaneously stop and start the flow by controlling hydrostatic pressure between the inlet and the outlet of the channel. This way, we obtain very well-resolved fibers. However we do not control the transient regime as the flow is restarted after fabrication.

2.4.2 Fabrication during continuous flow

The fabrication step can also be performed during continuous flow, for example when the flow is imposed at the syringe pump. However the resolution of the fiber will be reduced when the fabrication is done at high flowrates as the portion of fluid illuminated with UV-light will be moving downstream on a significant length compared to the fiber size. For example, for a $200\mu m$-wide $20\mu m$-high channel at a $200nL.s^{-1}$-flowrate, a portion of fluid illuminated during 100 ms will have moved downstream by 20 μm, which is the order of magnitude of the fiber width in our typical experiments. We illustrate this smearing in figure 2.8 where a fiber made during continuous flow is compared to one fabricated at zero-flow.

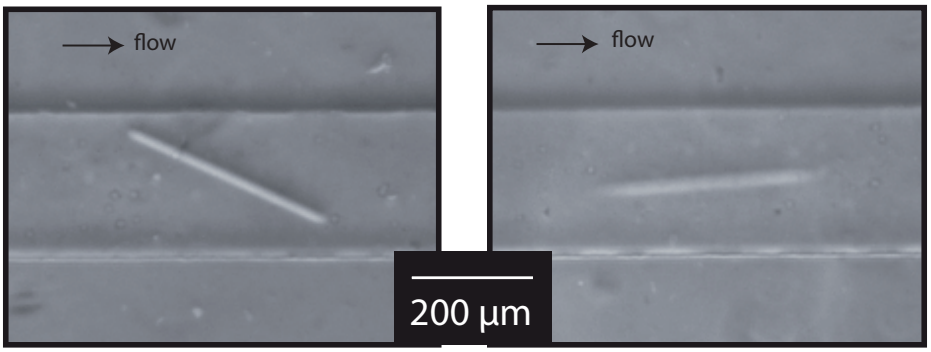

Figure 2.8: *Loss of resolution when the fiber is fabricated during a fast continuous flow. The left picture shows a fiber made at 2.5 $nL.s^{-1}$, corresponding to a velocity of 625 $\mu m.s^{-1}$. The right picture shows the same fiber fabricated at 4 $nL.s^{-1}$, hence 1 $mm.s^{-1}$. Its shape is much less resolved and it presents a blurry surface.*

The continuous-flow fabrication is therefore restricted to small velocities. Making fibers while the flowrate is low and gradually change it at the syringe pump may be a problem because of the transient regime of the pump before the target velocity is obtained. A long stabilization time would cause the channel length to be a limiting experimental factor. To overcome this difficulty, we design a Y-shaped-inlet microchannel for flow applications with fibers flowing at high flowrates. The idea is to impose a slow flowrate in the branch where the fiber is fabricated. The flowrate in the second branch is high, leading to a high-velocity flow in the main part of the channel. To illustrate this idea, we show in figure 2.9 the successive positions of a fiber from its fabrication to its flow into the main channel. The channel length is not a limiting parameter anymore, the fabrication resolution is good, but we lose control over the initial orientation and position of the fiber as it flows into the faster branch.

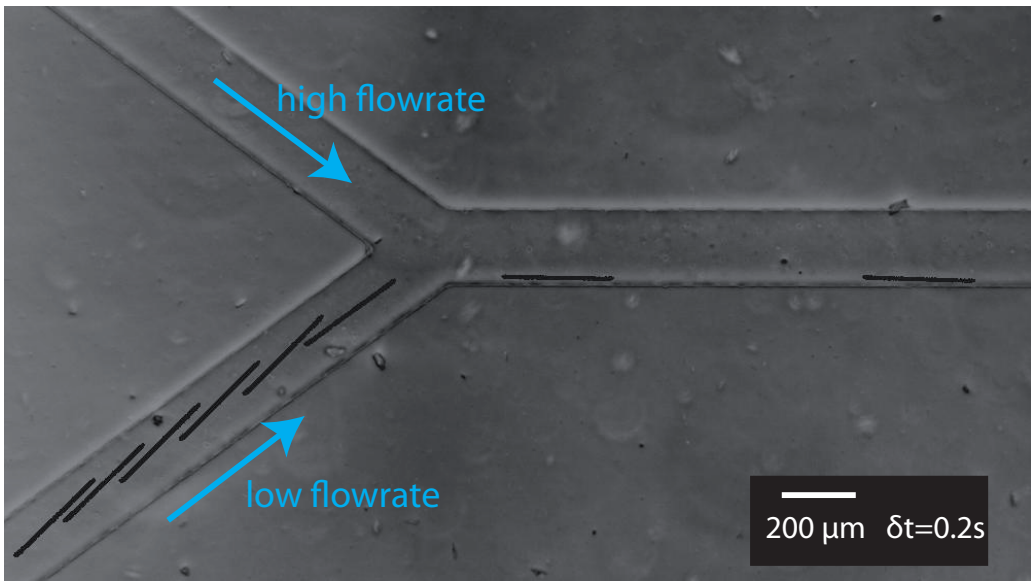

Figure 2.9: *Chronograph showing successive positions of a fiber flowing into the straight portion of the channel. In order to fabricate fibers with a high resolution and have them flow at a constant stable fast flow, we design a channel with a y-shaped inlet. The high flowrate (here, 1.5 $nL.s^{-1}$) is imposed in the top branch using a syringe pump, and a slow one (here, 0.5 $nL.s^{-1}$ corresponding to 125 $\mu m.s^{-1}$) is imposed in the bottom one where the fabrication will take place. The difference in flowrate is shown by the increased distance separating two successive positions (time interval of 200 ms). It is also responsible for the fiber to be flowing along the wall in the main channel portion, a feature used later to study the interactions with the lateral walls (see 6).*

2.5 Fabrication of fibers suspensions

The lithography technique provides a way to create an isolated fiber with a given initial orientation and precise position inside the channel whether the flow is continuous or stopped. Modifying the initial orientation is done solely via controlling the position of the fiber-shape lithography mask. Controlling the position of the particle to fabricate requires to use the microscope stage in relation with the position of the projected lithography mask.

The same idea is used to fabricate fibers suspension. Firstly, the lithography mask can be designed with several fibers, with a large freedom over the distance between them, their individual orientation and dimension. Figure 2.3 shows four examples of fiber configurations on the lithography mask. Upon one pulse of UV-light one could obtain a group of fibers of different lengths (hence different mechanical properties), different roughness (see 2.3.3) etc. Then, moving the microscope stage either by hand (for us) or by computer (in a coming future, using an electronic stage), one can fill up the channel with many times the same group of fibers. A snapshot of pictures taken during the fabrication of suspended perpendicular fibers upstream of a channel restriction is shown in 2.10.

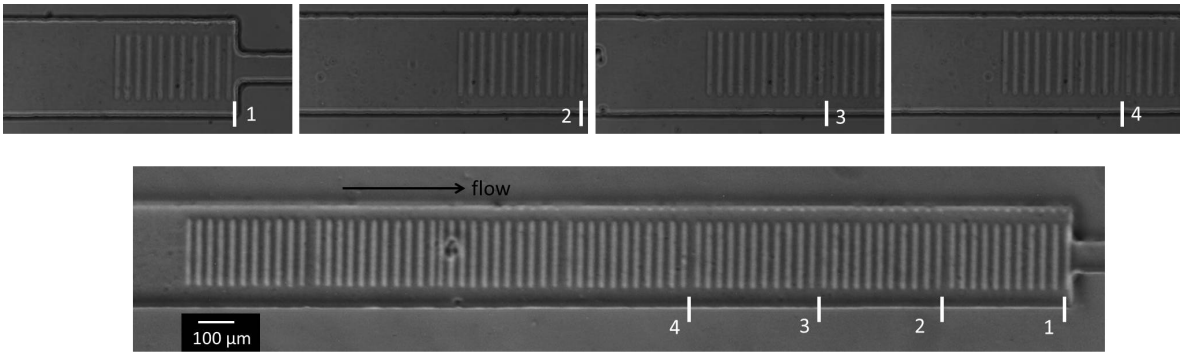

Figure 2.10: *Fabrication of a suspension of fibers all perpendicular to the streamwise direction. The four top pictures show the fabrication going upstream of the restriction (positions 1,2,3,4 etc), each group corresponding to the 11 fibers on the lithography mask. The images are blurry since we are defocused to correct the chromatic aberrations modifications of the objectives at visible light. The larger channel-view on the bottom picture shows the suspension before flow through the restriction.*

There is however a limitation towards the high concentrations of fibers[2]. When two neighbouring particles are fabricated, the region separating them which should remain unpolymerized does crosslink if they are made too close. We believe this is due to a limited control of the polymerization termination leading to a region of partially cured fluid.

2.6 Data processing

We developed a tracking and processing platform in MATLAB to extract the position of the fiber, its geometrical features and its orientation with the flow direction for all the images of a given experiment. We describe here the main steps of the processing, and detail the techniques in Appendix C.

The first feature of the platform consists in linking all the successive frames of the experiment in a single reference system. In fact, we use long channels to observe fiber dynamics over significant distances. Following the fiber as it moves out of the field of view is simply done by translating the microscope stage, however this translation needs to be quantified to correct for the position of the fiber within the flow direction. We use fixed elements of the channel geometry or dust particles on the frames to quantify the shift caused by this motion from a flow sequence to the next.

Then, the frames' contrast is enhanced using background substraction. Then a threshold is applied and the region around the fiber is automatically selected. Within this selection, the programme scans for a region of bright pixels covering an area comparable to the fiber's surface. This step is the fiber detection. When such a region is found, it is fitted with an ellipsoid. Its center of mass position is extracted along with its geometry and orientation with the flow direction. A picture of the fitted fiber is shown for each time steps for control purposes. Figure

[2]To determine a two-dimensional concentration of the fiber suspension, we measure the minimal distance separating two fibers during fabrication (α). For fibers of width ω the surface fraction is given by: $\phi = \frac{\omega}{\omega+\alpha}$

2.11 illustrates these steps showing the motion of a fiber over a sequence of 27 frames and the result of the detection.

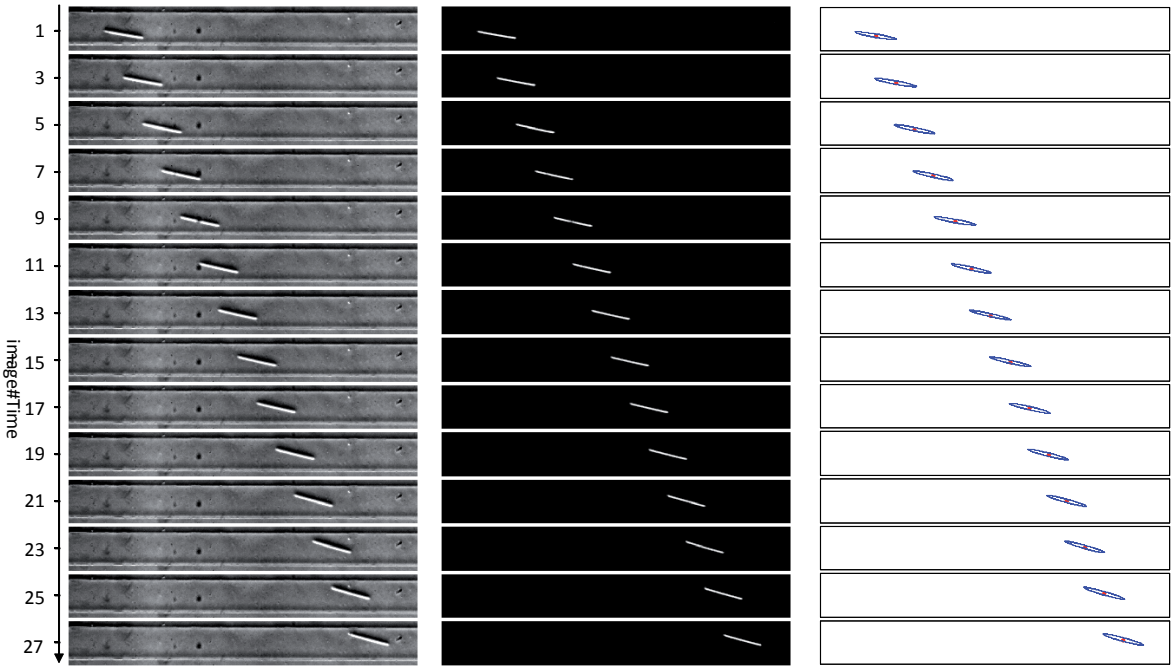

Figure 2.11: *Successive positions of a fiber flow in a microchannel. The left panel shows the original frames, the middle one the corresponding thresholded ones. The right panel displays the result of detected and ellipse-fitted fibers with our data-processing technique.*

CHAPTER 3

FABRICATION OF FIBERS BY COLLOIDS SELF-ASSEMBLY

We introduced in 1.4.2 a fabrication method based on magnetic colloidal self-assembly to make filaments directly inside microchannels. We adapted this technique to have a complementary way of making fibers compared to the lithography technique. The fibers have a different but still well-controllable geometry, they can also interact using their super-paramagnetic properties. Moreover, we are now able to fabricate them in much higher concentrated suspensions.

We recall the basics of the fabrication principle and detail the adapted experimental protocol necessary for the fabrication of fibers. We will show that we can play on many aspects of the suspension and that the flow profile can vary from a confined flow to a three-dimensional one. This work was done in collaboration with O. du Roure.

3.1 Principle of fabrication

The fabrication technique is based on the property of super-paramagnetic colloidal particles to self-assemble when a magnetic field is applied. Figure 1.15 in the background section shows the three main steps of the technique: the introduction of an aqueous solution of these colloids suspended with surfactant and polyacrylic acid (PAA) chains into a microchannel, the application of a vertical magnetic field causing the particles to self-assemble, and a sedimentation step when the magnetic field is removed, causing the newly formed fibers to fall in the channel due to their high density.

The fibers are permanently formed even when the magnetic field is removed thanks to polymer chains of PAA which bridge the colloids together.

3.2 Experimental protocol

3.2.1 Solution of colloids in water

The super-paramagnetic particles are provided by Ademtech (V2G colloids). They have a radius of 375 nm and a magnetic susceptibility of χ=1.3. Initially dispersed in an aqueous solution of nonylphenolethoxylate surfactant (NP10, Sigma) at 1 wt%, we disperse them at a volume fraction of 2.5 % in water containing NP10 at 0.1 wt% and polyacrylic acid (PAA, M_w = 250000, Sigma) at 0.1 wt%.

3.2.2 Microscope set-up and channel

The microscope is a Nikon inverted one equipped with a large coil placed around the microscope stage delivering a vertical magnetic field. The microchannel is placed in the center of the coil on the microscope stage.

We worked with microchannels made in PDMS bonded to a microscope glass slide. We vary the channel height from 15 to 40 μm to obtain different fiber lengths. The channel width typically ranges from 30 to 200 μm leading to some confined flow geometries where the flow is mostly two-dimensional, and some three-dimensional ones. The inlet and outlet are connected[1] to tubings whose ends are attached to a micrometric displacement system. This way, hydrostatic pressure is used to impose a constant pressure-controlled flow in the channel. The pressure difference needs to be carefully and instantaneously adjusted during the different steps of the fabrication: introducing the solution inside the channel, possibly locally in a portion of the channel, and stopping it during the application of the magnetic field to avoid perturbation of the chains formation.

[1] Small metallic tubes were used to place the connecting tubings into the holes in the PDMS channels. They got magnetised during the application of the magnetic field, and introduced a small horizontal magnetic gradient. The super-paramagnetic colloids were sensitive to the gradient, inducing a small flow in the channel. The quality of the fibers: single chains, very small dispersion in length, requires to stop the flow completely during the application of the magnetic field when the fibers are forming. All the set-up equipment needs therefore to be checked to avoid such issues.

3.2.3 Protocol

The channel is initially rinsed with a solution of NP10 in water (0.1 wt%). A small volume (smaller than a μL) of colloids is taken out of their initial solution and placed inside an eppendorf container. We rinse them three times successively with the solution of NP10 by mixing them with a vortex and removing the supernatant using a small magnet held against the bottom of the eppendorf container to get all the colloids at the bottom. Once the solution of colloids and NP10 in water is ready, the set up should be prepared with a no-flow condition. PAA is introduced into the colloidal solution and mixed carefully by pushing/pulling the solution kept inside the micropipette tip. Immediately after, the solution is flowed through the channel, ready to start the fiber fabrication. This careful preparation is required to ensure a good colloidal stability of the mixture.

The magnetic field intensity was 25 mT (5A) applied for 35 minutes for an optimum fabrication.

The fabrication step must be performed at zero flow. If a small flow remains, the fabrication quality is reduced. Chains made of more than one array of particles are obtained, the dispersion in the chain lengths can be high. Combining a short fabrication step with a small flow may often make the fabrication fail.

3.3 Fibers suspension characteristics

3.3.1 Fiber geometry

Fibers have a disk-shape cross-section due to the spherical geometry of the super-paramagnetic particles. When they assemble as a single chain, the fibers have a diameter of 750 nm and a length close to the channel height (tens of μm). We represent the geometry of a single-chain fiber in figure 3.1 showing how the polymer chains of PAA adhere to the surface of the colloids and bridge them together.

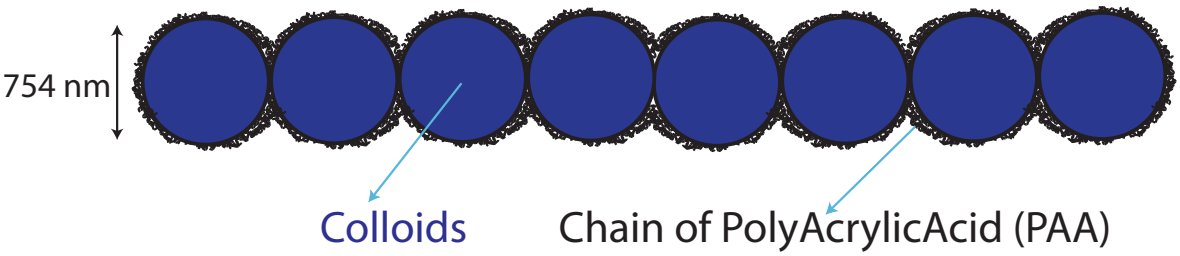

Figure 3.1: *Drawing of a fiber fabricated with the super-paramagnetic colloids. The long chains of PAA polymer adsorbed on the colloids surface bridge them together when the colloids are in close contact during the application of the magnetic field.*

The colloidal particles sediment at a vertical velocity of around 1 $\mu m.s^{-1}$, competing with the magnetic dipolar attractive forces during the fabrication phase. Since we apply the magnetic field for a duration of thirty minutes, some sedimentation occurs and the fiber length is slightly smaller than the channel height. We illustrate this effect in figure 3.2 with three pictures of the channel after the fabrication step. The fibers have sedimented to the bottom of the channel.

The three pictures correspond to three channel heights from 15 to 30 μm, resulting in fiber length between 12 and 27 μm.

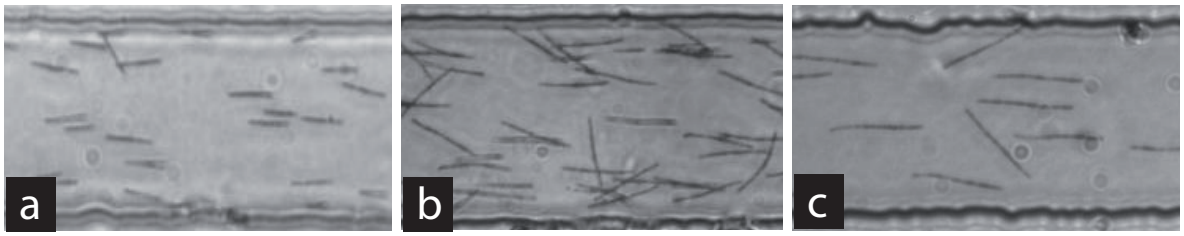

Figure 3.2: *Top view of the sedimented fibers fabricated in three channels of varying heights. The channel height and fiber length are: (a) 15 µm and 12 µm, (b) 27 µm and 23 µm and (c) 30 µm and 27 µm*

3.3.2 Concentration

As we mentioned in the background section, the concentration of fibers depends on the initial volume fraction of colloids introduced in the channel (1.4.2.2). Figure 3.3 shows pictures of fiber suspensions fabricated at three different concentrations. We also show the suspensions during the application of the magnetic field when the fibers are being formed along the channel height. One can see the strong ordering of the filaments, showing a constant distance between chains. The channel used for the fabrication is the same for all three top pictures with a height of 24 μm.

3.3.3 Elasticity

The elasticity of the fibers is governed by the nature of the polymer briging the colloids together. The fibers we obtained with PAA chains are very flexible. Isolated fibers deform under flow, they also easily bend to penetrate the flow restriction in geometries where their length is larger than the channel width. Figure 3.4 illustrates these two cases with fibers of aspect ratio 36. We show also the case of very long fibers (several centimeters long) that we obtain from the colloids present in the tubings connecting the inlet reservoir to the channel entrance. Figure 3.5 shows a unique fiber folded in many locations. It is capable of flowing through the restriction.

It is possible to modify the aspect ratio without reducing the fiber length drastically in order to form more rigid fibers. At high concentrations of colloids in the channel, fibers form with more than one chain of bridged colloids as illustrated in figure 3.6. The dispersity in width is larger than for unique chains.

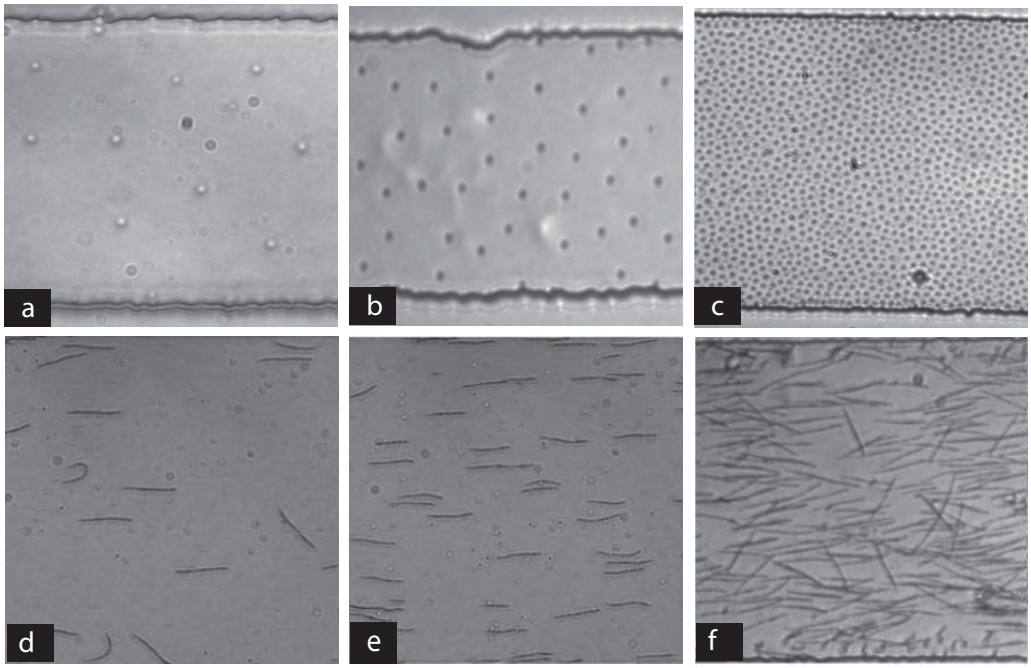

Figure 3.3: *Variations of fiber concentration with the initial volume fraction of colloids in a given channel. The top three pictures show three colloidal suspensions during the fabrication phase at increasing volume fraction from a to c. Fibers are forming in the direction perpendicular to the plane of view. suspensions of increasing concentration. Pictures (d), (e) and (f) show three suspensions as they sedimented to the channel bottom after the fabrication. Increasing volume concentration lead to higher-concentrations of fibers in suspensions.*

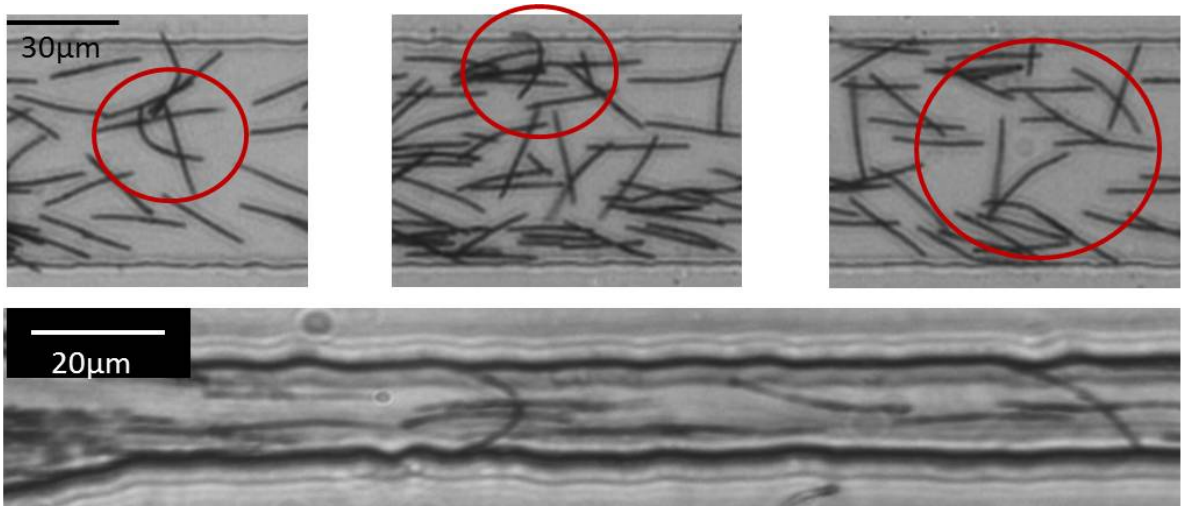

Figure 3.4: *Examples of fibers of aspect ratio* ≈ 36 *deforming in the flow. The three top pictures show fibers in the bulk or blocked with the boundary. The bottom picture shows a restriction of width 20 µm, smaller than the fiber length (27 µm). We observe fibers bridging the restriction and bending under drag.*

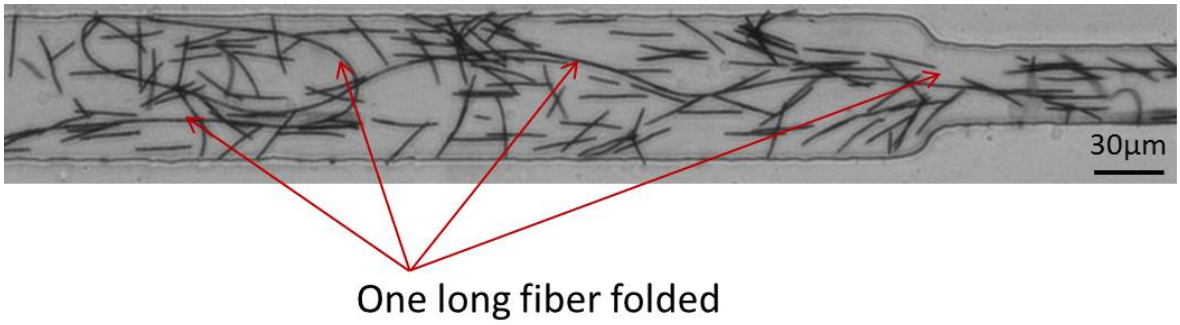

Figure 3.5: *Case of a very long fiber (several centimeters) fabricated in the connecting tubings used to introduce the solutions and flowing inside the channel. The long fiber bends and folds, interacting with the flow boundaries, and flow through the restriction.*

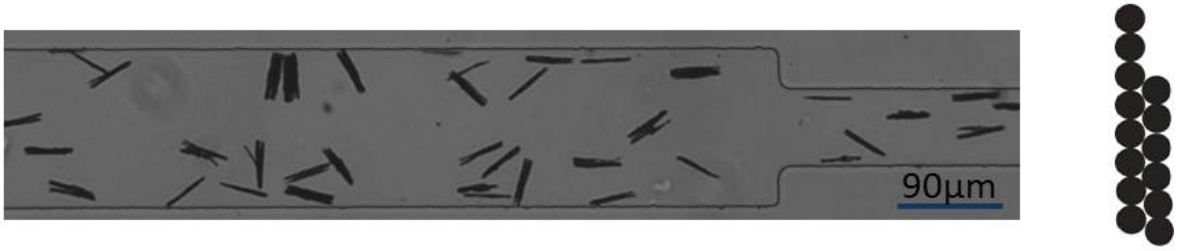

Figure 3.6: *Fibers can form with several chains of colloids bridged together, as illustrated in the right-side drawing., when the volume fraction of colloids is high. This way, one can obtain more rigid fibers without reducing the fiber length.*

CHAPTER 4

In situ MEASUREMENT OF FIBER MECHANICAL PROPERTIES: BENDING-FIBER EXPERIMENTS

We presented in the previous chapters how we adapted the photo-polymerization technique for the fabrication of microfibers directly inside microfluidic channels. The control of the particle geometry is excellent, as well as their placement in the channel and their initial state. Once the particles are made, it becomes important to characterize them mechanically. Here we are interested in measuring their Young's modulus. An *in situ* measurement is required for two main reasons. First, upscaling the fabrication to a millimeter-size sample requires to upscale the degree of crosslinking achieved during the polymerization in the channel, which is unknown. Also, the particles are made inside the microfluidic channels where they stay in contact with the fluid at all times. We expect their mechanical properties to vary if they are taken out of the channels in a dry environment.

Thus we propose here an *in situ* measurement of the fiber Young's modulus using an adapted "bending beam" test based on experiments and numerical simulations. The microfluidic experiments provide deformation data of the fiber in a controlled flow geometry for varying fiber geometry. Flow simulations provide the force exerted on the fiber through the computation of drag coefficients. We compare our numerical results with analytical drag coefficients obtained with the lubrication theory ([17],[18]). As a result, we are able to measure the fiber Young's modulus for different geometries. This is the first measurement ever obtained for particles fabricated *in situ*, with the photo-polymerization method. Note that the analytical approach we use is done in collaboration with Jason Wexler and Howard Stone (Princeton University) in relation to our joint study on the deformation of a fixed fiber in confined micro flows (Appendix E).

4.1 Experimental

We build an experiment where the fiber is kept fixed in the microchannel but can deform under the drag force exerted by the flow. The flow geometry consists of a rectangular cross-section channel with a small height compared to the other dimensions (Hele-Shaw geometry). A slot is designed in the channel walls where we fabricate the fiber using the photo-polymerization method. This is illustrated in figure 4.1.

A top view of the channel on the microscope in figure 4.1 shows the fiber under flow. The fiber is fabricated in the slot without contact with the boundaries because of the inhibition layers along the PDMS walls. Immediately after polymerization, it moves and sits on the slot boundaries as a small constant flowrate is imposed to the inlet via a syringe pump during the fabrication step. Then, we increase the flowrate by steps, wait for its stabilization, and capture images of the deflected fiber over time. Direct optical measurement of the deflection is done using the ImageJ software.

The Hele-Shaw geometry creates a plug flow making the fiber experience an almost constant velocity on its side. Tracer particles were added to the fluid to verify the flow velocity during the experiment, allowing for a visualization of the streamlines going above and below the fiber. Figure 4.2-a shows superimposed images of the fiber as the particles flow past it. Figure 4.2-b shows the successive positions of the fiber during a typical experiment. Imaging is done using phase contrast objectives on the microscope to increase the contrast between the fiber, the fluid and channel walls. Therefore fiber edges appear brighter than the background. Although deformations can be large, we will use data corresponding to a maximal deflection of twice the fiber width in order to derive the Young's modulus from a small deformation approximation.

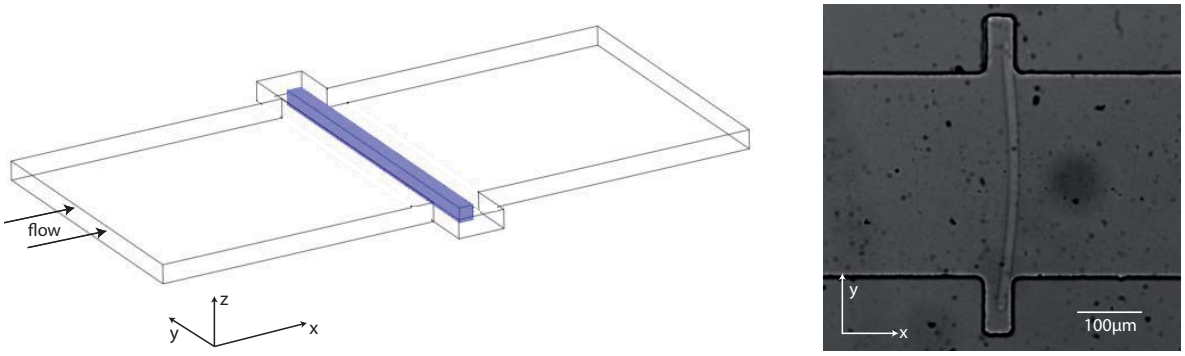

Figure 4.1: *Left: schematic drawing of the channel and fiber geometry for the bending experiment. The channel has a Hele-Shaw cell-like geometry, with a slot where the fiber is made using the photo-polymerization method. The fiber is suspended in the flow but sits on the channel slot walls, as showed on the top-view micrograph (right).*

We tested three geometries varying the fiber length (via the channel width), as well as the fiber height and width. These dimensions are given in table 4.1. Fiber dimensions directly affect the mechanical properties of the fiber. In particular, its bending rigidity EI depends on the fiber cross-section dimensions from the second inertia moment I. (E is the Young's modulus of the fiber)

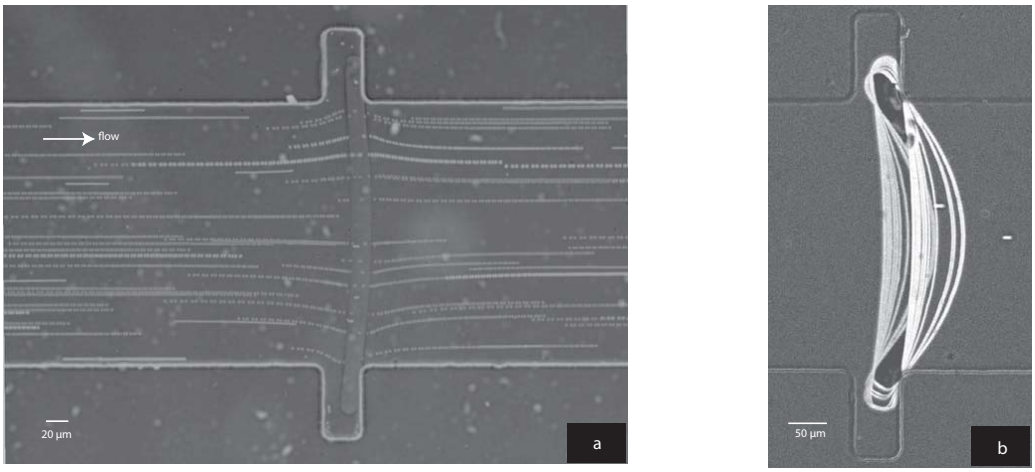

Figure 4.2: *Superposition of images at constant flowrate when the fluid is filled with tracer particles (picture a). This view shows the streamlines going above and below the fiber. In picture b we superimpose the view of the fiber as we increase the flowrate. By phase contrast we can see well the fiber edge deflecting.*

Geometry	Channel height (μm) *(H)*	Fiber length (μm) *(l)*	Fiber width (μm) *(ω)*	Fiber height (μm) *(h)*
A	42 ± 1	300 ± 2	29 ± 2	34 ± 2
B	42 ± 1	350 ± 2	23 ± 2	30 ± 2
C	42 ± 1	350 ± 2	21 ± 2	32 ± 2

Table 4.1: *Channel and fiber dimensions for the three bending experiments tested.*

Fiber deflection is the distance of the fiber edge to its position at zero-flow. For practical reasons, we always maintain a flow in the channel, even during the fiber fabrication where it is kept very low. Consequently we don't know the zero-flow position of the fiber. We chose to measure the deflection as the fiber distance to the slot position. Two deflection data sets of the Geometry A test are showed in graph 4.3 along with a picture of a bending fiber illustrating this data collection process. Since the slot position is only approximately the zero-flow fiber position, our measurement process is responsible for the fact that the data points intercept the vertical axis at a positive value.

Vertical error bars on the deflection data correspond to an instability of the imposed flowrate making the fiber oscillate at each position of the syringe pump. For each flowrate, we measure a minimal and maximal deflection and compute the average value. The linear fit is done using the averaged deflection data for each channel/fiber geometry and correcting the slot position. Specifying a fit of the form $\delta = \alpha U_{mean} + \delta_{zeroflowrate}$, we solve for α, which will then be used in the computation of the Young's modulus as detailed in section 4.4.

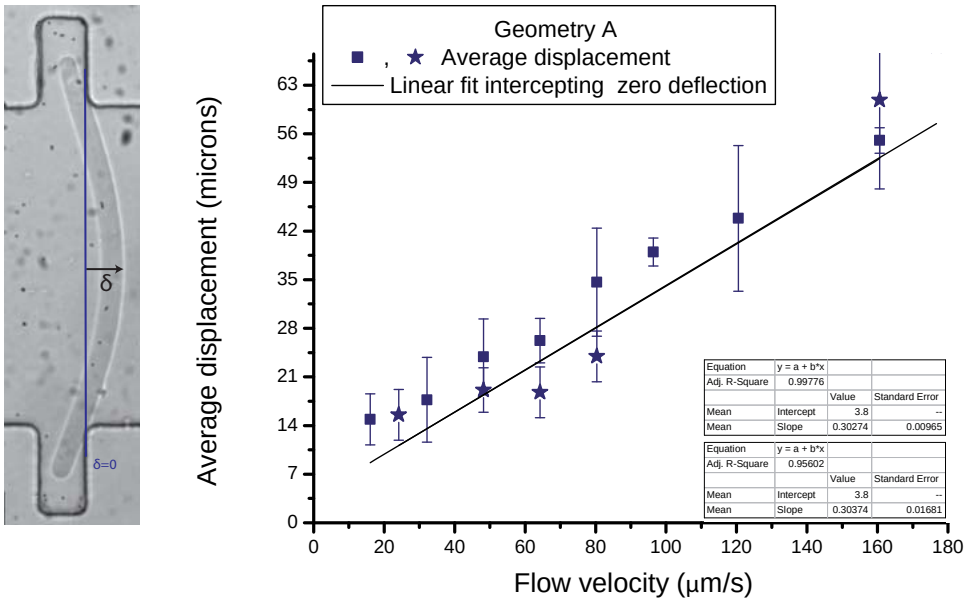

Figure 4.3: *Results of fiber deflection reported versus mean flow velocity . Two sets of data points (square and stars) correspond to two different experiments done with the same fiber geometry. They are both linearly fitted with a curve going through the zero deflection point. We find a slope of 0.3 with a 0.3% difference between the two experiments. A picture of a bending fiber is shown left of the graph illustrating how we obtain the deflection data and where the zero is taken.*

4.2 Numerical simulations

4.2.1 Design

We use three-dimensional flow simulations to compute the drag coefficient on the fiber for each geometry tested experimentally. The simulations are set in COMSOL. Since the experimental Reynolds number remains below 10^{-2} for all geometries tested, we used the 3D Stokes flow module (more details are given in the next chapter).

The flow geometry consists of a channel of rectangular cross-section with an imposed constant velocity on the entry face so that the flow develops parallel to the channel length. At mid-length, the volume corresponding to a rigid fiber perpendicular to the flow direction is substracted from the channel so that we only simulate the fluid domain. Figure 4.4 shows a perspective view of this design along with the meshed channel.

COMSOL enables the calculation of the force exerted on the fluid boundaries. Summing the forces exerted on each fiber face provides with the total drag force and the drag coefficient.

Channel and fiber dimensions are set to match the experimental tests. The fluid properties also correspond to the oligomer solution used in the experiments. We use a dynamic viscosity η of $0.057 Pa.s$ and a density of $1120 kg.m^{-3}$ for the fluid, a constant velocity on the inlet face of $100 \mu m.s^{-1}$, a zero pressure on the outlet face and a no-slip condition on all other boundaries.

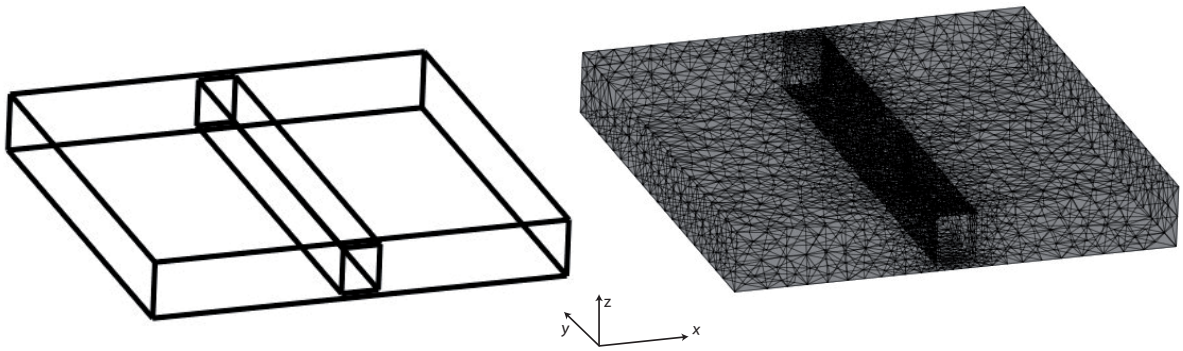

Figure 4.4: *Design of the channel for the 3D-simulations of the flow in Geometry A. We show the fluid domain and its mesh obtained in Comsol.*

The domain is meshed with a density of 5 nodes on channel height edges, 30 on its width and 50 on its length edges (tetrahedral elements). The fiber mesh is made with 5 nodes on its heights and widths and 50 on its lengths. (e.g 245426 elements used to mesh Geometry A)

4.2.2 Results

We obtain a parabolic flow profile within the channel height as expected for such confined flows. This is illustrated in figures 4.5 and 4.6. As we impose a no-slip condition on the fiber faces, the fluid accelerates above and under the fiber as showed in the velocity profiles. Using Comsol post-processing, we obtain the total force exerted from the fluid on the fiber faces for each geometry tested. Using force F, mean flow velocity U_{mean}, fluid viscosity η and fiber length l, we can compute the drag coefficient: $\lambda = F/(\eta * l * U_{mean})$. We report the computed values of drag coefficients in table 4.2 for the three experimental flow configurations.

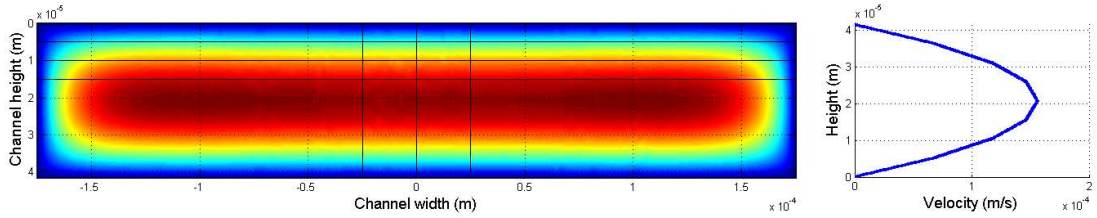

Figure 4.5: *Colour map of velocity in the channel cross-section upstream of the fiber. The right-side graph shows the typical parabolic velocity profile along the channel height.*

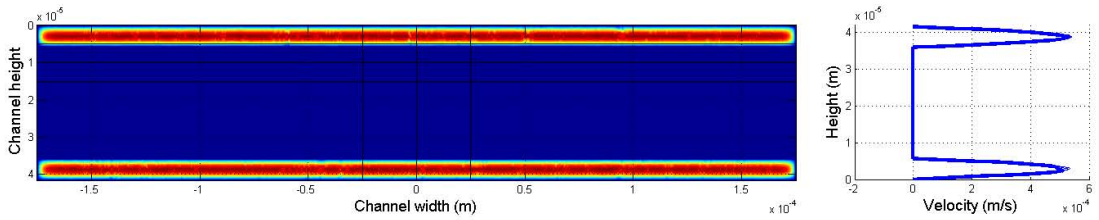

Figure 4.6: *Colour map of velocity in the channel cross-section on the fiber: the blue region (zero velocity) corresponds to the fiber. The fluid accelerates as it flows above and below the fiber as illustrated in the right hand-side graph.*

Geometry	U_{mean} $(m.s^{-1})$	Drag force (N)	**Drag coefficient** λ
A	$9.96 \cdot 10^{-5}$	$8.74 \cdot 10^{-6}$	**5132**
B	$9.78 \cdot 10^{-5}$	$2.75 \cdot 10^{-6}$	**1410**
C	$9.78 \cdot 10^{-5}$	$3.89 \cdot 10^{-6}$	**1994**

Table 4.2: *Simulation results of drag force F and mean flow velocity for the three experimental geometries. The drag coefficient λ is computed as: $\lambda = F/(\eta * l * U_{mean})$ with l the fiber length. Computed values of mean flow velocity differ from the boundary-imposed velocity (100 $\mu m/s$) due to numerical errors.*

4.3 Modeling in the lubrication limit

The analytical resolution of the flow equations leading to the drag coefficient may be done in the lubrication approximation [55]. There is no flow around the fiber tips but only above and below the fiber, leading to a 2D problem. Let's consider a section of the channel along its length and height, cutting the fiber along its cross section. The schematic drawing in figure 4.7 recalls the notations that we will use for the analytical solution.

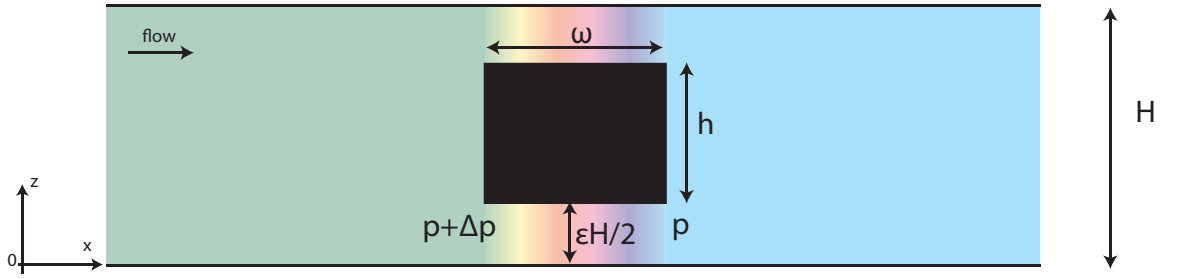

Figure 4.7: *Channel plane along its length and height, showing the fiber cross-section. The colour gradient represents the variations of pressure. For clarity purposes, we represented a geometry where the fiber is not very confined in the channel, though the experimental and numerical cases solved were with a confinement higher than 0.7.*

In the lubrication approximation, the flow equation in the gap below the fiber is given by: (5.2)

$$U(x,z) = \frac{1}{2\eta}\frac{dp}{dx} z(z - d(x)) \tag{4.1}$$

$d(x)$ corresponds to the position of the fiber edge along the channel height.
By conservation of the flowrate per unit length q, we obtain:

$$\frac{q}{2} = \int_0^{d(x)} U(x,z)dz \tag{4.2}$$

$$= \frac{-1}{12\eta}\frac{dp}{dx}d^3(x) \tag{4.3}$$

We extract now the pressure difference upstream and downstream of the fiber using $\varepsilon = (H - h)/H$

$$\frac{dp}{dx} = \frac{-6\eta q}{d^3(x)} \tag{4.4}$$

$$\int_0^{\omega}\frac{dp}{dx}dx = \int_0^{\omega}\frac{-6\eta q}{d^2(x)}dx \tag{4.5}$$

$$\Delta p = \int_0^{\omega}\frac{-6\eta q}{(\frac{\varepsilon H}{2})^3}dx \tag{4.6}$$

$$= \frac{48\eta q\omega}{(H-h)^3} \tag{4.7}$$

The viscous stress due to the term in $\frac{\partial U}{\partial x}$ can be neglected against the variations in z and the pressure terms. We get the viscous stress on the fiber sides:

$$\frac{\partial U}{\partial z} = \frac{1}{\eta}\frac{dp}{dx}z - \frac{1}{2\eta}\frac{dp}{dx}d(x) \tag{4.8}$$

$$= \frac{1}{2\eta}\frac{dp}{dx}d(x) \tag{4.9}$$

$$\sigma_{xz} = \eta\frac{\partial U}{\partial z} = \frac{1}{4}\frac{\Delta p\varepsilon H}{\omega} \tag{4.10}$$

Using the pressure difference Δp and the viscous stress σ_{xz}, we can now compute the force per unit length acting on the fiber:

$$f_p = \Delta p h = \frac{48\eta q\omega h}{(H-h)^3} \tag{4.11}$$

$$f_v = \sigma_{xz}2\omega = \frac{24\eta q\omega}{(H-h)^2} \tag{4.12}$$

$$f_{total} = 24\eta q\omega\frac{H+h}{(H-h)^3} \tag{4.13}$$

Drag coefficients λ are proportionnal to the force per unit length: $f = \lambda\eta U_{mean}$. Rewriting the flowrate per unit length q with the velocity: $q = U_{mean}H$, we obtain:

$$\lambda_p = \frac{48Hh\omega}{(H-h)^3} \tag{4.14}$$

$$\lambda_v = \frac{24\omega H}{(H-h)^2} \tag{4.15}$$

$$\lambda_{total} = \frac{24\omega H(H+h)}{(H-h)^3} \tag{4.16}$$

We report the values of the drag coefficients calculated using the lubrication approximation in table 4.3 for the three experimental geometries[1].

Geometry	λ_{lub}	λ_{num}
A	4339 ±1795	5132
B	966±260	1410
C	1566 ±510	1994

Table 4.3: *Drag coefficients calculated in the lubrication approximation compared with the coefficients obtained from flow simulations* .

There is a deviation of up to twenty percent between the simulations results and the drag coefficients computed analytically in the lubrication approximation. This deviation is not reduced when going to even more confined situations. We believe that the deviation is mainly caused by a numerical error in the computation of the pressure field around the fiber vertices. To illustrate this assumption, we show results of the calculated pressure field in the channel in figure 4.8 where we zoomed on two opposite vertices of the fiber. Non-physical variations of pressure are present around the edges, where we compute the viscous and pressure forces on the fiber. They could be responsible for the deviation with the analytical estimations of the drag coefficients.

[1]The uncertainty of the drag coefficient is estimated propagating the uncertainty of the different parameters via Monte Carlo simulation. Due to the nonlinearity of the eq. 4.16 the distribution is positively skewed. The error is estimated using the median absolute deviation.

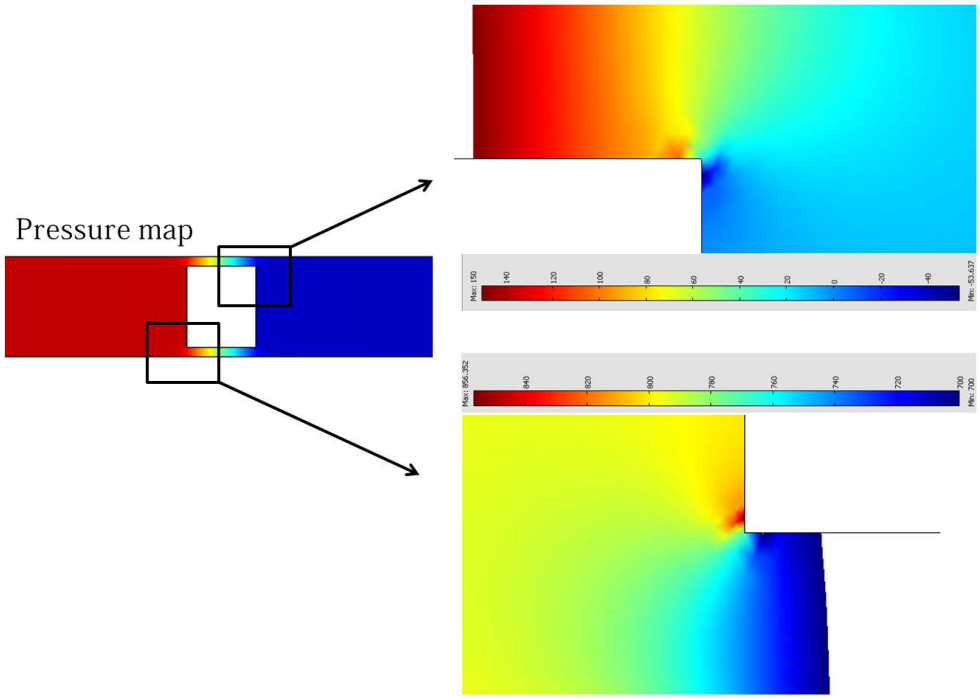

Figure 4.8: *Colour map of pressure in the channel from COMSOL simulations. We zoom on two opposite fiber vortices where the pressure field gives non-physical variations (the insets colours are coded independently). They could explain an error in the estimation of the drag force on the fiber.*

4.4 Computation of Young's modulus

In the case of small deformation, the deflection δ of the fiber can be written with the drag force per unit length, f, the fiber length, l, the Young's modulus, E and the second inertia moment, I as [56]:

$$\delta = \frac{5fl^4}{384IE} \quad \text{with} \begin{cases} I = \dfrac{\omega^3 h}{12} \\ f = \lambda \eta U_{mean} \end{cases} \tag{4.17}$$

The parameters ω and h are the fiber width and height. We extract from the experimental tests the fiber deflection as a function of the imposed flow velocity. Fitting with a linear curve these results, we obtain the factor α as $\delta = \alpha U_{mean}$. Rewriting the deflection with the flow velocity and the Young's modulus, we get:

$$\delta = \frac{5fl^4}{384IE} = \frac{5\lambda\eta U_{mean} l^4}{384IE} \tag{4.18}$$

$$= \frac{5\lambda\eta U_{mean} l^4}{32\omega^3 hE} \tag{4.19}$$

$$\alpha = \frac{5\lambda\eta l^4}{32\omega^3 hE} \tag{4.20}$$

We get the fiber Young's modulus:

$$E = \frac{5\lambda\eta l^4}{32\alpha\omega^3 h} \tag{4.21}$$

Finally, we report in table 4.4 the values of Young's modulus computed for each one of the tested geometries using the drag coefficients from the lubrication analysis[2].

Geometry	α	**E (Pa)**
A	0.3 ±0.0009	$1.258 \cdot 10^6$ ±$4.82 \cdot 10^5$
B	0.4 ±0.071	$0.884 \cdot 10^6$ ±$2.12 \cdot 10^5$
C	0.67 ±0.039	$1.054 \cdot 10^6$ ±$3.12 \cdot 10^5$

Table 4.4: *Computed values of the fiber Young's modulus for each experimental geometry, using the simulation results of drag coefficient and the deflection results from the experiments.*

4.5 Conclusion

We presented in this chapter an experimental method to characterize mechanically the fibers we fabricate using the photo-polymerization method. It is the first measurement of the Young's modulus of *in situ* photopolymerized particles published. The experiment consists in bending a fiber confined in a microchannel with an imposed constant flow similarly to the well-known flexion tests in solid mechanics. We extract the experimental data of fiber deflection as a function of the flowrate while numerical simulations provide a computation of the drag force exerted on the fiber. We obtained consistent results for three different channel and fiber geometries, with a Young's modulus of the order of megapascals (MPa). Deviations between analytical results from lubrication theory and simulations are attributed to numerical error on the fiber vertices where the pressure field results are inaccurate.

This method can be used in the future to systematically characterize the fibers used in flow experiments. As explained before, the fabrication technique provides some freedom over the flexibility of the particle via the use of different oligomer solutions or quantity of crosslinker used in the solution. The bending test only requires to fill the channel, make the fiber and proceed with the analysis supported with numerical simulations. Finally, our measurement method provides a way to determine the optimal fiber dimensions to obtain given mechanical properties.

[2]The uncertainty of the modulus is estimated propagating the uncertainty of the different parameters via Monte Carlo simulation. Due to the nonlinearity of eq, 4.21, the distribution is positively skewed. The error is estimated using the median absolute deviation.

CHAPTER 5

FLOW DYNAMICS OF A SINGLE FIBER AWAY FROM THE LATERAL FLOW BOUNDARIES

The first question we adress concerns the transport of a single fiber in a Hele-Shaw flow. Contrary to fibers in three-dimensional flows ([6], [13], [57]), confined flows of fibers have been scarcely studied [18]. Their importance has increased with the development of microfluidics and manipulation of particles in microchannels. Champmartin *et al.*[19] studied the transport of an infinitely long cylindrical particle in a plane Poiseuille flow moving perpendicular to the flow direction. In this chapter, we experimentally and numerically address the question of the confined-fiber motion in a situation where the lateral walls are far from the fiber. We are interested in characterizing the fiber velocity depending on its geometry and its orientation with the flow direction. The influence of fibre confinement and fiber length is explored experimentally and numerically. This work was done in collaboration with Marc Fermigier.

5.1 Experimental results

In this section, we report on the experimental flow of a fiber confined between the top and bottom walls but several lengths away from the lateral walls as illustrated in figure 5.1. We use photopolymerization to fabricate the fiber and vary its position, orientation and confinement. These parameters are extracted with the detection techniques presented in the previous chapter C to study the flow dynamics.

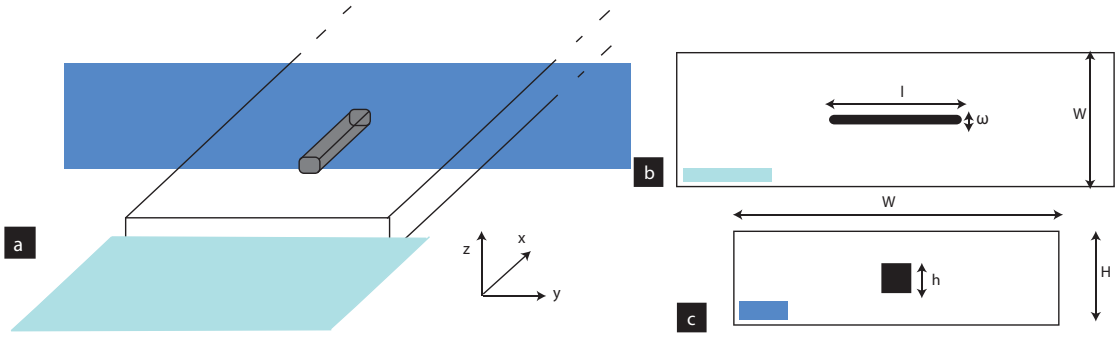

Figure 5.1: *Schematic drawing of the microchannel geometry with a suspended fiber moving parallel to the flow direction (a). Two sections are shown with the names of the different dimensions used in our experiments and simulations. (b) corresponds to a plane cut at channel mid-height, showing the streamwise and spanwise directions. (c) corresponds to a cross-section of the channel at fiber mid-length. The fiber has a square cross-section with rounded edges due to the lithography fabrication technique.*

5.1.1 Velocity of a fiber parallel to the flow direction

We start with comparing the velocity of a fiber parallel with the imposed flow velocity. We use a microchannel of constant width and height W_{max} = 400 μm and H=20 μm. The inlet is connected to a glass syringe on the syringe pump where a constant flowrate is imposed. Fluid velocity ranges from 200 to 1000 $\mu m/s$, leading to a maximal Reynolds number of 10^{-3}. The outlet is connected to a fluid reservoir. We wait five minutes upon changing the flowrate to work at a stable velocity in the channel. The fiber is fabricated at continuous flow in the middle of the channel and parallel to the flow direction using the photopolymerization technique. We used two masks to get different particle lengths: first type has l=200 μm, ω=11 μm, h=8 μm and the second type of particles: l=300 μm, ω=11 μm and h=8 μm. The fiber position is extracted as a function of time. Figure 5.2 shows velocity results for both fiber types along with an example of data of detected positions.

As we fabricate the fiber at continuous flow, high velocities decrease the resolution of the fabrication and we get some smearing effect (see 2.4.2 in chapter 2). For the first type of fiber, we measure a fiber length l=200 μm at 250 $\mu m.s^{-1}$ increasing to 241 μm at 875 $\mu m.s^{-1}$ but with a stable width. The same effect was found for the longer type of fibers: l=300 μm at 180 $\mu m.s^{-1}$ leading to 333 μm at 625 $\mu m.s^{-1}$. All length measurements have a precision of 2 μm.

We calculate the imposed flow velocity (or mean velocity) using the flowrate Q and the channel cross-section S: $V_{mean} = \frac{Q}{S}$. Fiber velocity increases linearly with the flow velocity (eq. 5.1).

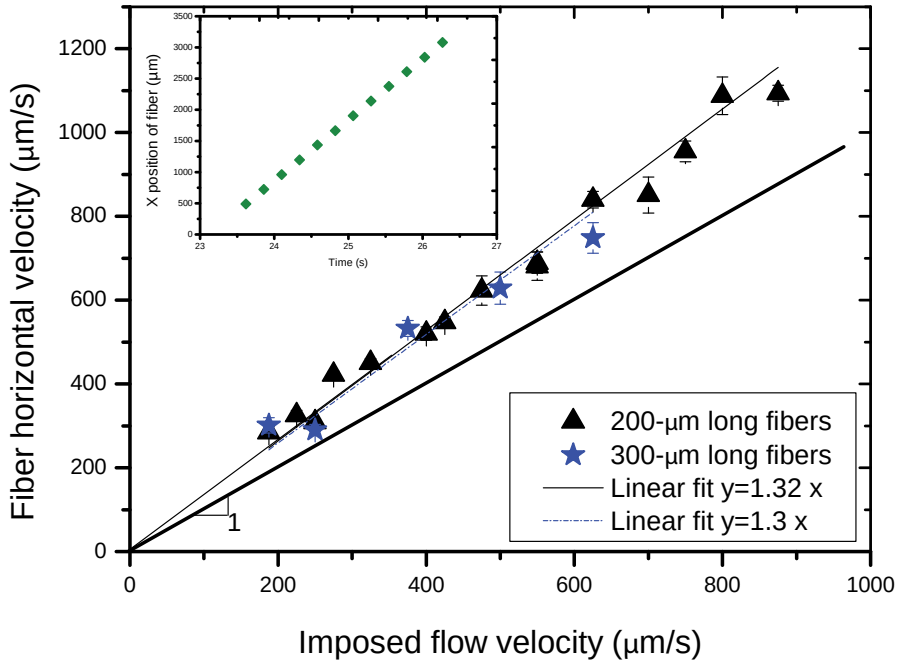

Figure 5.2: *Experimental results of velocity for a fiber made parallel to the flow and away from the lateral walls. Each data point corresponds to an experiment. The error bars correspond to the error on the detection of fiber positions. The inset graph shows an example of detected fiber positions (x) in time within one sequence of the flow. We compute the velocity from fitting linearly such data.*

$$V_{fiber} = 1.3 V_{mean} \quad ; \quad R^2 = 0.995 \tag{5.1}$$

The fiber moves faster than the mean flow velocity with a ratio of 1.3, independently of the fiber length (200 μm or 300 μm).

5.1.2 Effect of confinement

We now modify the fiber geometry to test different degrees of confinement. Confinement is defined as the ratio of fiber height with channel height. In order to modify the fiber height, we use channels of different heights taking advantage of the fact that the polymerization inhibition layer thickness remains constant. We present results obtained with three different channels. Their dimensions are given in figure 5.3.

We compare fiber and flow velocity in table 5.1. The fiber slows down from Geometry A to Geometry B and C as the confinement increases. There is however no significant difference between the two more confined tests. To obtain a larger range of confinements, we also do a numerical study where we can artificially vary the confinement and explore more easily its effect than with experiments. These results are presented in the section 5.3.

Dimensions (μm)	Geometry A	Geometry B	Geometry C
L	$>10^4$	$>10^4$	$>10^4$
W	200	600	190
H	20	26	32
l	200	192	243
ω	11	18	18
h	8	16	20
Confinement	0.4	0.61	0.63

(a) Table of geometries

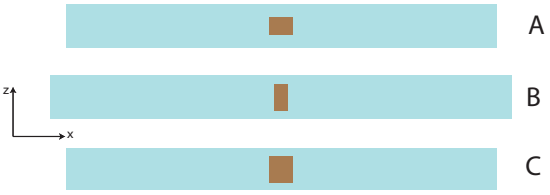

(b) Section views of geometries

Figure 5.3: *5.3a: dimensions of channel and fiber for the three cases studied. All distance measurements have a precision of 2 µm. 5.3b: Schematic drawing of the channel cross-section showing the three geometries. The scale is the same for all of them (channel width not accurate for B) illustrating the increasing confinement from A to C.*

	Geometry A	Geometry B	Geometry C
Confinement	0.4	0.61	0.63
V_{fiber}/V_{mean}	1.3	0.78	0.84

Table 5.1: *Effect of fiber confinement on the velocity of the fiber. With an error of 2 µm on the fiber position and mean flow velocity larger than 200 µm/s we have a maximal error of the order of* 10^{-2}.

5.1.3 Effect of the initial orientation

We are now interested in the variations of fiber velocity with its initial orientation. Each experiment consists in fabricating a fiber with a given orientation and following its motion downstream. Several tests are done for the same angle before modifying it. The channel geometry is modified to account for the case of a perpendicular fiber remaining without interactions with the lateral walls. Channel dimensions are W=600 μm and H=26 μm. Fiber dimensions are l=192 μm, ω=18 μm and h=16 μm leading to a confinement of 0.62. A constant flowrate (0.5 to 2 $nL.s^{-1}$) is imposed at the syringe pump before the fabrication of the fiber. This flowrate is slow enough to ensure a good quality of fabrication and constant dimensions independent of the orientation of the fiber. We tested the following four initial angles with the flow direction: 0°, 90°, −45° and 45°, respectively picture (a), (b), (c) and (d) in figure 5.4.

5.1.3.1 Fiber velocity

First we investigate the question of velocities along the channel length V_x and width V_y for a parallel or perpendicular fiber. Table 5.2 shows results of velocities for independent tests at different imposed flowrates. V_y velocity remains very small, at the order of magnitude of the detection error for both orientations (the detection error is computed with the error on the position of the fiber and the duration of the experiment over which we fit these positions. The detection error is therefore lower than 0.7 $\mu m/s$). In conclusion, parallel and perpendicular fibers do not drift towards the walls in a Hele-Shaw channel. We couldn't compare the Vx velocities from a parallel test to a perpendicular test because of the instability of the imposed flowrate between experiments.
When the fiber is fabricated with an angle of ±45°, we observe a drift of the fiber towards one

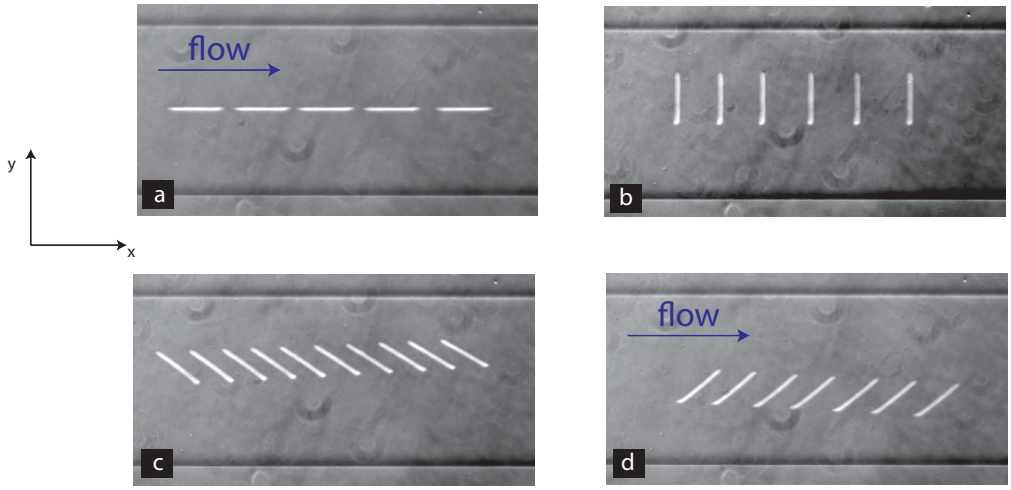

Figure 5.4: *Flow of a confined fiber away from the lateral boundaries with different initial orientations with the flow direction. For each case we show the successive positions of the fiber in time. The fiber is fabricated using the lithography technique at continuous stable flow (flowrate imposed by the syringe pump). For clarity we show the successive positions with an increment of 5 images for a, 3 images for b, 5 images for c and d.*

Angle (degrees)	$V_x(\mu m/s)$	$V_y(\mu m/s)$
0	71.4	0.4
0	99.5	0.6
0	82.4	0.5
90	41.8	0.3
90	37.3	0.3
90	55	0.4

Table 5.2: *Velocities along the channel length and width for a fiber created either parallel or perpendicular to the flow direction. V_x is two orders of magnitude larger than V_y which is of the order of our detection error.*

of the lateral walls. This drift is due to the apparition of a velocity component V_y which cannot be neglected anymore. Reporting values of V_y with respect to V_x, we find that their ratio is constant for different experiments and imposed flowrates. Graph 5.5 shows results of velocities V_x and V_y measured in five distinct series of experiments (each experiment repeating the test 3 to 10 times) with a linear fit of : $V_y = 0.058V_x$ ($R^2 = 0.999$ for the black-square data points). Fiber confinement is still 0.62 for all data sets.

We are not confident in the value of the mean flow velocity in these drift experiments as we repeated the test of a parallel fiber regularly and measured a decreasing fiber velocity. The time scales during a test are small enough not to be affected by this uncertainty. In other

words, the measured velocities Vx and Vy can be trusted but we are not able to provide with their ratio to the mean flow velocity.

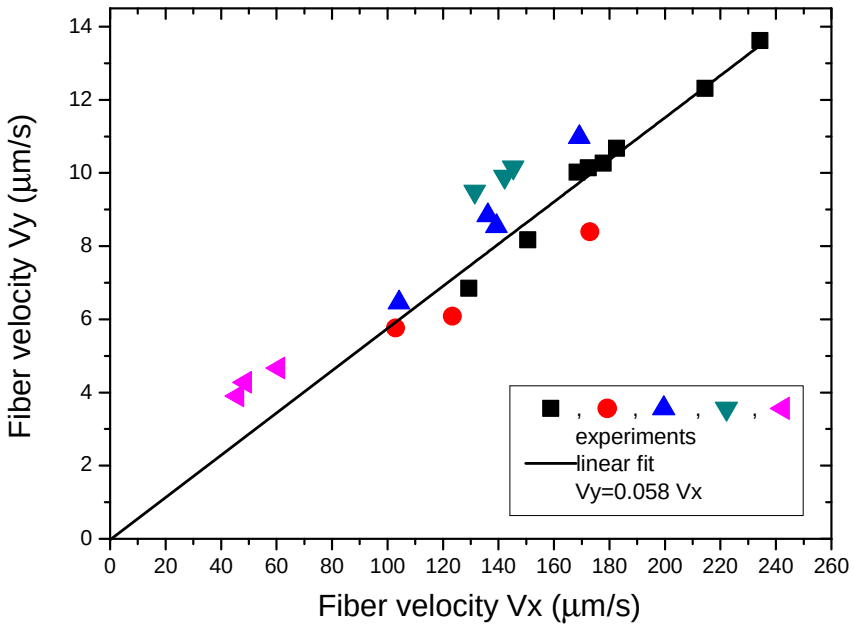

Figure 5.5: *Measurement of fiber velocities along the channel length (V_x) and channel width (V_y) for a fiber fabricated with an angle of ±45° with the flow direction. Each colour (symbol) corresponds to an experiment series for which the same test was repeated several times. The data are fitted with a linear curve going through the origin: we find that the velocity V_y is 0.06 times V_x.*

5.1.3.2 Fiber angle

We now investigate the question of the angle evolution when the fiber is advected at a constant imposed flowrate. No rotation is observed for a fiber flowing parallel, perpendicular or with an angle of ±45° to the flow direction. We report values of the angle for the parallel and perpendicular configurations measured in two distinct experiments in graph 5.6. Variations of less than $2°/s$ are observed without reproducibility from one test to the next. We illustrate these results with a picture of superimposed successive positions of the fiber, next to each graph. When the fiber is parallel to the flow direction, we obtain a continuous line. Similarly, the perpendicular fiber keeps its orientation.

5.1.4 Streakline visualization

Particle Image Velocimetry (PIV) experiments are done to map the velocity profile around the fiber. Details of the image processing are given in Appendix D. The objective of the PIV tests is to get an instantaneous picture of the streamlines in the channel and the perturbation caused

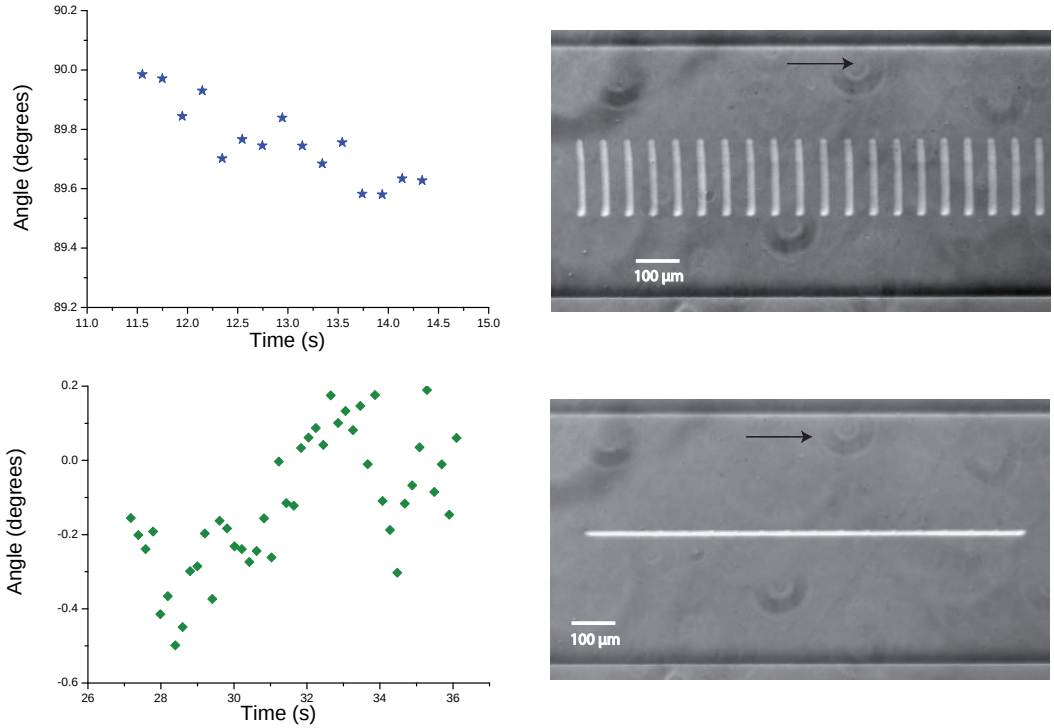

Figure 5.6: *Variations of the fiber angle with time. Top: case of a fiber made perpendicular to the flow direction. The right hand-side picture shows superimposed successive positions of the fiber. Bottom: case of a fiber made parallel to the flow direction. The superimposed positions show a continuous line.*

by the fiber advected in the flow. The fabrication is done with the lithography method at zero flowrate. The channel was initially filled with a high concentration suspension of micrometric particles in the oligomer/photo-initiator mixture. We start the flow by imposing a constant pressure difference between the inlet and outlet connections to obtain a fast response. Results of the image processing are shown in figure 5.7 for a $20\mu m$-wide $300\mu m$-long parallel fiber of confinement 0.4. The microchannel height is 20 μm. This reconstructed image is built from processing several successive image captures of the flow. They are then superimposed while keeping the fiber in the center immobile: in other words, we stack the successive frames to show a representation of the flow in the fiber reference system. As a consequence, all pixels inside the fiber area are still: the particles in this area appear sharp. Looking at the rest of the image, we obtain an instantaneous picture of the streamlines around the fiber. No flow perturbation can be detected around the fiber sides. However the streamlines are deviating in front of the fiber on a distance slightly larger than the fiber width as represented with the red bar.

Figure 5.7: *Particle paths around a fiber flowing parallel to the flow direction at a confinement of 0,4. The image is built from successive frames of the flow superimposed in the reference system of the fiber. Particles flowing above the fiber appear as still particles when others leave a trace corresponding to streamlines. We can visualize the flow around the fiber and the perturbed streamlines downstream of its edge. The perturbation extends over a distance comparable to the fiber width (and channel height).*

5.1.5 Conclusions of the experimental study

Using the photo-lithography technique, we set up an experimental study of a single fiber transported in a Hele-Shaw channel away from the lateral boundaries. We varied the dimensions of the fiber as well as its initial orientation with the flow direction for several imposed flow velocities. We observed that the fiber velocity depends on its degree of confinement in the channel. A fiber parallel to the flow direction at a confinement of 0.4 flows faster than the mean flow velocity, with a ratio of 1.3, independently of the fiber length. For a given fluid velocity, the fiber speed decreases as its confinement increases. When the fiber is parallel or perpendicular to the flow direction, it keeps its orientation and flows only in the direction of the fluid. We observed a small drift when the fiber was initially made at $\pm 45^\circ$ to the flow direction, with $V_y = 0.058 V_x$ for a confinement of 0.62. This small drift indicates a small difference in a parallel fiber velocity $V_\parallel$ and the perpendicular one $V_\perp$ even though we don't have a measurement of $V_\perp$ so far.

5.2 Flow equations

So far, we have only considered the imposed fluid velocity, V_{mean}. To understand the transport of the fiber, we need to establish the equations governing the flow in a Hele-Shaw cell with the appropriate boundary conditions applied on the fiber. This section recalls some basic knowledge of hydrodynamics in confined geometries without considering the presence of a fiber. The particular case of a fiber will be studied analytically in the following sections in a

two-dimensionnal approach based on the fiber orientation to the flow.

Flow dynamics of isolated fibers in our geometries are caracterized by a low Reynolds number, where the inertia is negligible and viscous forces predominent. The experiments presented in this section were designed using a syringe pump imposing a mean flow velocity below 2.5 $mm.s^{-1}$. The Reynolds number built with the channel width as a characteristic length is given in equation 5.2. The kinematic viscosity of the solution of PEGDA with photo-initiator is measured with a capillary viscometer. The Reynolds number associated to the fiber is 10^{-2} since the fiber length is three times smaller than the channel width.

$$Re = \frac{V.L}{\nu} = \frac{2.5 * 0.6}{52.17} \approx 3 \times 10^{-2} \tag{5.2}$$

Since the inertial forces are negligible compared to the viscous ones (Re<<1), the Navier-Stokes equations describing the flow dynamics are reduced to the Stokes equation written in Eq. 5.3, where p and $\mathbf{V}$ are respectively the pressure and velocity fields. The velocity field also respects the incompressibility equation 5.4.

$$-\nabla p + \eta \nabla^2 \mathbf{V} = 0 \tag{5.3}$$

$$\nabla . \mathbf{V} = 0 \tag{5.4}$$

We call x the coordinate along the direction of the flow (and channel length), y along the direction of the channel width and z the channel height. The symmetry of the geometry imposes that the velocity field $\mathbf{V}$ is invariant with x. When a constant pressure gradient along x or a constant flowrate is imposed, $\mathbf{V}$ is parallel to the x direction: $\mathbf{V}$=V(y,z) $\mathbf{e}_x$ ($\mathbf{e}_x$ unit vector).

We can write the projection of Eq. 5.3 along the x direction to obtain the governing flow equation:

$$\boxed{-\frac{\partial p}{\partial x} + \eta \left(\frac{\partial^2 v}{\partial y^2} + \frac{\partial^2 v}{\partial^2 z} \right) = 0} \tag{5.5}$$

In order to obtain the variation of the velocity field with y and z, we solve Eq. 5.5 taking advantage of the invariance of the pressure with z. Separating the parts with variations in z to the ones varying in the Oxy plane, we can write the velocity field as([58]):

$$\mathbf{V}(y,z) = \mathbf{V}(y,0) * f(z) \tag{5.6}$$

Solving equation 5.5 with 5.6, using a no-slip condition on the horizontal walls of the channel (placed at $z = -h$ and $z = h$), we get:

$$f(z) = 1 - \frac{z^2}{h^2} \tag{5.7}$$

$$\mathbf{V}_{Oxy} = \frac{h^2}{2\eta} * \nabla p \tag{5.8}$$

Let's consider the two sections of the channel as represented in figure 5.1. The result obtained in equation 5.8 shows that the flow profile in the streamwise/spanwise section is a **plug flow**, this latter equation can be seen as the Darcy equivalent of the Hele-Shaw cell flow velocity. This section corresponds to the top view captured with the camera during the experiments with some averaging within the channel height. We will characterize the flow of the fluid and the fiber in this observation plane with experimental results, PIV measurements as well as two-dimensional simulations. The other section (channel cross-section) will be solely characterized with simulations since no direct observation is possible. There, the flow profile away from the fiber is **parabolic** as found in equation 5.7, typical of Hele-Shaw cells. In this section, fluid velocity can be explicitely written as a development in Fourier series where the development coefficients only depend on the ratio of the channel width with channel height [59]. We will use it to approximate the ratio of the mean flow velocity and the maximal velocity within the channel height depending on the channel geometry.

The flow velocity follows the no-slip condition on the lateral, top and bottom walls of the channel. The fiber is advected by the fluid, without force or torque exerted on it. Velocity boundary conditions on the fiber then correspond to a continuity condition.

5.3 Numerical study

In this section, we present numerical simulations in both 2D and 3D to provide comparison with the experimental data and explore the dependence of our parameters of fiber position, confinement and orientation in a wider range. The two-dimensional simulations corresponding to a fiber of infinite length are done with the CFD (computational fluid dynamics) programme FreeFem++ [60]. Written in C++, this software can numerically solve partial differential equations such as the Stokes equations in a two or three-dimensionnal meshed object. We chose it to get an excellent control of the different steps of the simulations: designing the geometry and modifying it easily, generating a mesh and most importantly writing the flow equations.

We complemented these calculations with three-dimensional simulations done with COMSOL. They provide a way to study fibers of finite length, modifying in particular the results of a fiber perpendicular to the flow direction. COMSOL is a commercial software widely used in industry as well as in research laboratories. Its graphics interface eases the preparation of the simulation and offers clarity in the choice of the governing flow equations but it doesn't require to write them in variationnal form. We mainly used it coupled with Matlab to run parameter-dependent simulations in 3D. The programming itself is detailed in Appendix B for FreeFem and COMSOL.

All simulations are designed to have the lateral flow boundaries away from the fiber and prevent any interaction, similarly to the experiments previously described.

5.3.1 2D simulation of a parallel fiber (infinite fiber length)

We study first the case of a fiber flowing with its axis parallel to the flow direction along the channel length. The simulations are two-dimensional in the Oyz plane corresponding to the channel cross-section. We will assume that the fiber is infinitely long along the channel direc-

tion (Ox).

The geometry is illustrated in schematic 5.8 with the notations used in the computations. We also show the mesh Th generated by FreeFem. The flow domain is called Ω, with the lateral boundaries Ω_c and the boundaries corresponding to the fiber Ω_f. A no-slip condition is imposed on Ω_c and a fixed velocity is imposed on Ω_f. All lengths are made dimensionless with the channel height: the fiber is characterized by its confinement and we keep its width constant. In the simulation code, viscosity is made dimensionless with the oligomer viscosity 57mPa.s.

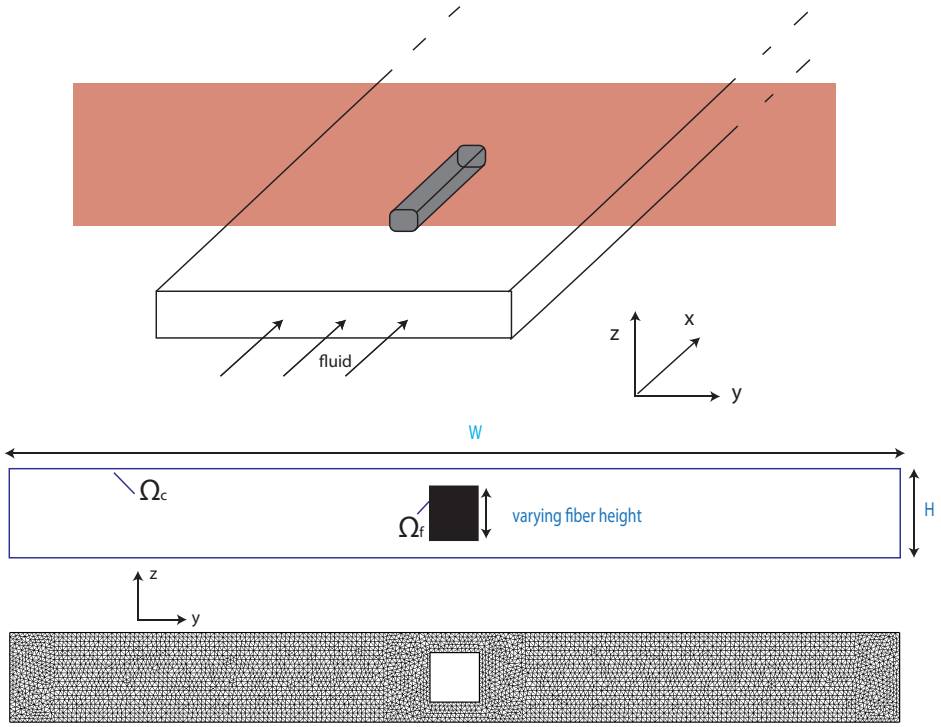

Figure 5.8: *Simulations in Oyz plane*

The Stokes equation (Eq.5.3) governs the motion of the fluid. We consider a constant pressure gradient G along Ox. We are now solving the following problem P with a velocity field $\mathbf{u}$ with a single velocity component along the channel length which depends on both coordinates y and z. The Dirichlet boundary conditions of no-slip are imposed on Ω_c and Ω_f.

$$\Delta u = \frac{G}{\eta} \quad \begin{cases} u = u_x(y,z) \\ u \in H^2(\Omega) \\ u_{\Omega_c} = 0 \\ u_{\Omega_f} = v_{fiber} \end{cases} \tag{P}$$

We also consider the incompressibility condition:

$$\nabla . \mathbf{u} = 0 \tag{5.9}$$

We write the equation in its variationnal form. If u solves the problem P then for any smooth function v which satisfies the boundary conditions $v_{|\Omega_c \cup \Omega_f} = 0$, we have:

$$\int_\Omega \{ \frac{\partial^2 u}{\partial y^2} * v + \frac{\partial^2 u}{\partial z^2} * v = \frac{G * v}{\eta} \} d\Omega \tag{5.10}$$

We integrate by parts:

$$\int_y \int_z \frac{\partial^2 u}{\partial y^2} * v dy dz + \int_y \int_z \frac{\partial^2 u}{\partial y^2} * v dy dz = \int_y \int_z \frac{G * v}{\eta} dy dz \tag{5.11}$$

$$\int_y \int_z \frac{\partial^2 u}{\partial y^2} * v dy dz = \int_y \int_z -\frac{\partial v}{\partial y} \frac{\partial u}{\partial y} dy dz \tag{5.12}$$

$$\int_y \int_z \frac{\partial^2 u}{\partial z^2} * v dy dz = \int_y \int_z -\frac{\partial v}{\partial z} \frac{\partial u}{\partial z} dy dz \tag{5.13}$$

The variational form of the Stokes equation to solve in the Oyz plane is:

$$\boxed{\int_\Omega \nabla u . \nabla v d\Omega + \int_\Omega \frac{G.v}{\eta} = 0} \tag{5.14}$$

The hydrodynamic force per unit length exerted on the fiber can be computed using the stress tensor.

$$F = \int_{\Omega_f} \sigma_{xy} n_y + \sigma_{xz} n_z + G\omega h \tag{5.15}$$

$$= \int_{\Omega_f} \eta * \frac{\partial u}{\partial y} n_y + \eta * \frac{\partial u}{\partial z} n_z + G\omega h \tag{5.16}$$

We solve the flow equation in its variational form 5.14 imposing a constant pressure gradient in a given geometry (channel dimensions, fiber dimensions). We run first the simulation with a low fiber velocity and compute the resulted force exerted on the fiber from the flow. We iterate the fiber velocity until we find a zero force: this corresponds to our physical situation of a fiber advected by the flow. We obtain the correct fiber velocity v_{fiber} from this iteration. We can then extract the velocity u on all the nodes and process it into different flow profiles.
Both programmes are reproduced in Appendix B.

5.3.2 2D simulation of a perpendicular fiber

We also study numerically the flow of a fiber perpendicular to the flow direction in the same confined microchannel. The fiber is considered infinitely long along the width direction of the channel. This means that there is no flow around the fiber edges. The simulation is computed in the channel height and channel length plane (cross-section of the fiber). The equivalent two-dimensional geometry is illustrated in figure 5.9 along with the meshing generated by FreeFem. The equation of motion in this plane is the Stokes equation (P') but with some significant modifications as we need to consider now two components of the velocity. The boundary conditions must also be adapted since we are simulating the inlet and outlet lines.

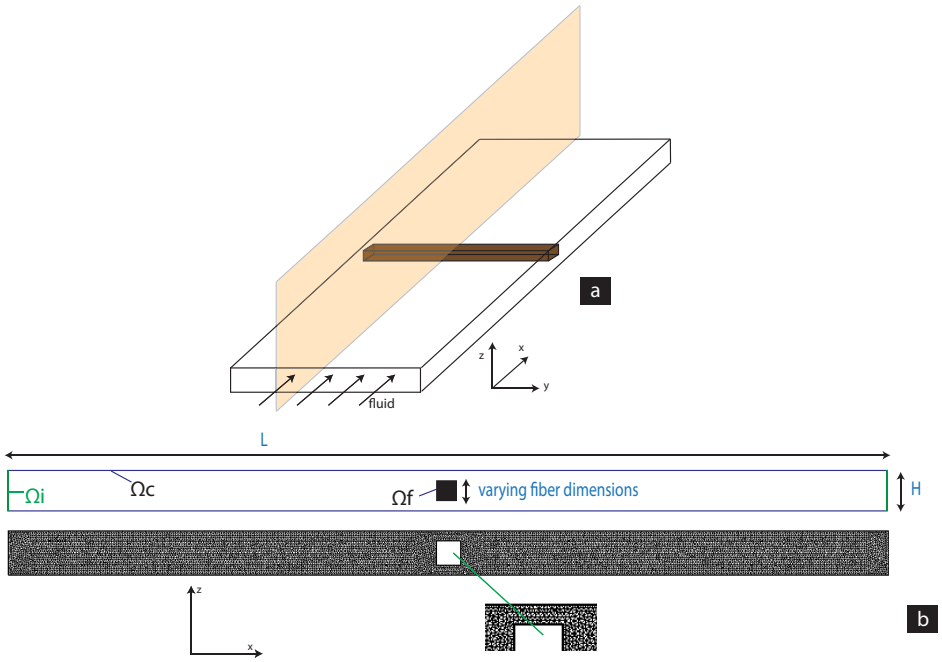

Figure 5.9: *Simulations of a fiber advected by the flow with an orientation perpendicular to the flow direction and infinitely long (a). The yellow surface shows the section plane where the computation will be done (Oxz plane). In (b) we draw the corresponding two-dimensional geometry of the flow with the typical dimensions used in the calculation. The mesh is reproduced as generated by FreeFem for a fiber width and height of half the channel height.*

$$\Delta \mathbf{u} = \frac{\nabla p}{\eta} \quad \begin{cases} \mathbf{u} = u_x(x,z)\mathbf{e}_x + u_z(x,z)\mathbf{e}_z \\ u \in H^2(\Omega) \\ u_{\Omega_c} = 0 \\ u_{\Omega_f} = v_{fiber} \\ u_{\Omega_i} = -\dfrac{4}{h^2} * (z^2 - h * z) \end{cases} \tag{P'}$$

We also consider the incompressibility condition:

$$\nabla . \mathbf{u} = 0 \tag{5.17}$$

If $\mathbf{u}$ solves problem P' then for any smooth functions uu, vv satisfying the no-slip condition on Ω_c and Ω_f we have:

$$\int_\Omega \{ \frac{\partial^2 u}{\partial x^2} * uu + \frac{\partial^2 u}{\partial z^2} * uu = \frac{1}{\eta} \frac{\partial p}{\partial x} * uu \; \} d\Omega \tag{5.18}$$

$$\int_\Omega \{ \frac{\partial^2 v}{\partial x^2} * vv + \frac{\partial^2 v}{\partial z^2} * vv = \frac{1}{\eta} \frac{\partial p}{\partial z} * vv \; \} d\Omega \tag{5.19}$$

We can integrate once again by parts the two terms of the left element, leading to the flow equation variational form:

$$\boxed{\int_\Omega \nabla u.\nabla uu + \nabla v.\nabla vv \;\; d\Omega + \int_\Omega \frac{1}{\eta}(\frac{\partial p}{\partial x} * uu + \frac{\partial p}{\partial z} * vv) \;\; d\Omega = 0} \tag{5.20}$$

The incompressibility condition is also integrated into the programme using a smooth function pp and adding a stabilizing term for the pressure.The programme is available in Appendix B. The hydrodynamic force per unit length exerted on the fiber is computed using the stress tensor. Since the geometry is symmetric in z, we simply consider the x component of the force.

$$F_x = \int_{\Omega_f} \sigma_{xi} n_i \tag{5.21}$$

$$= \int_{\Omega_f} (-p + 2 * \eta * \frac{\partial u}{\partial x} n_x) + \eta * (\frac{\partial u}{\partial z} + \frac{\partial v}{\partial x}) n_z \tag{5.22}$$

where **n** is the vector normal to the surface of the fiber with component n_i along the i direction.

The computation approach is similar to the simulations of the parallel fiber. The velocity on the inlet line is a parabolic function of the height z with its maximum of 1 at $z = \frac{h}{2}$. We run the simulation with a low fiber velocity first to get the flow profile and the force exerted by the fluid on the fiber. We iterate the fiber velocity until we find that the force is zero which corresponds to a fiber advected by the flow. We compute the full flow profile which is extracted from the simulation and analyzed in Matlab.

5.3.3 Velocity results with fiber confinement

Fiber confinement (β) is defined as the ratio of the fiber height with the channel height. Varying experimentally the confinement requires to modify the channel height, since the inhibition layer thickness is difficult to change. Numerically though, it becomes much easier as the fiber dimension is specified at the beginning of the computation. We present results of simulations of the flow in the width/height section of the channel keeping the channel height constant and varying the fiber confinement from 0.1 to 0.95. Fiber velocity is reported versus its confinement in figure 5.10 for the configurations of a parallel and perpendicular fiber. Experimental points are added to the graph for comparison with numerical results.
At low confinements, the velocity ratio goes towards 1.5 which corresponds to the analytical result for the maximal velocity in our channel geometry. The fiber is like a point particle flowing at the maximal speed. As the confinement increases, the two curves tend to different limits. The parallel fiber velocity tends to zero: as its height increases towards the channel height, viscous dissipation slows it down. We expect the fluid to flow around its tips within the channel width. The perpendicular fiber simulation is different as the 2D approach is much more restrictive: the fluid can only flow above and below the fiber. At very high confinements, the fluid pushes the fiber at the mean velocity (mass conservation principle). This limit doesn't reflect the experimental situation where the fiber length is finite and we would expect the fluid to flow aroung its sides.

The experimental results of fiber velocity are in excellent agreement with the simulation results. The data is corrected with the error on both the confinement (horizontal error bar) and the velocity (vertical). The confinement error is computed from the measurement error on the fiber height. For the velocity, we take into account the detection error on the fiber position,

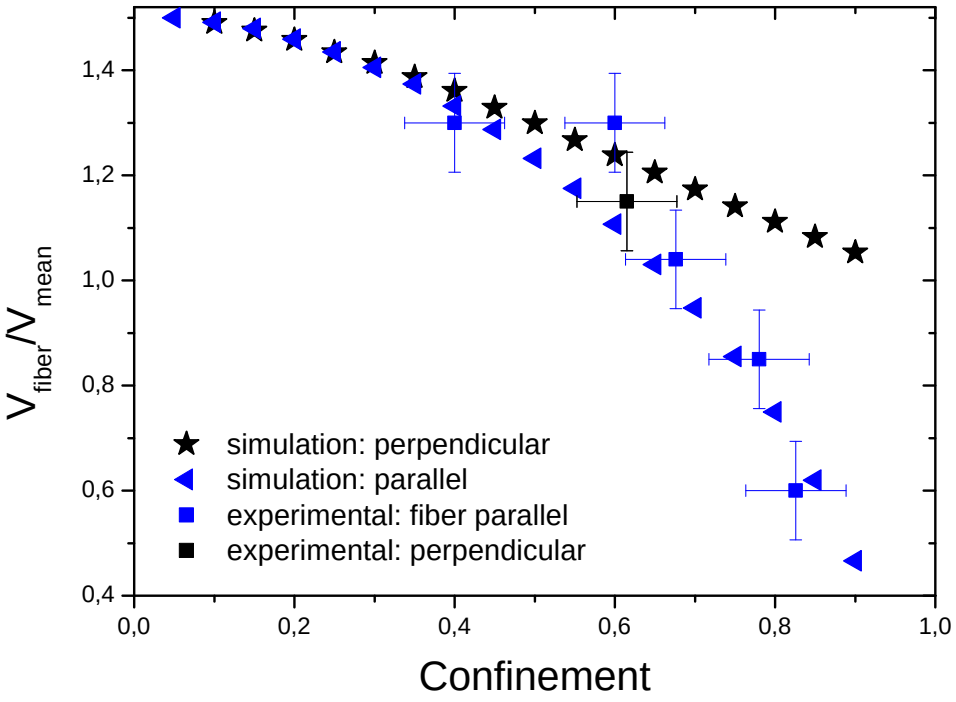

Figure 5.10: *Fiber velocity variations with confinement obtained with 2D simulations. Blue triangles correspond to a fiber parallel to the flow direction, black stars to a perpendicular fiber. Experimental results are compared to the simulations for both fiber orientations.*

during its extraction using the image processing algorithms. The experimental point corresponding to the fiber perpendicular to the flow is slightly lower than the 2D simulations: at this confinement of 0.6, we need to take into account three-dimensional flow around the fiber tips.

We compare our results with 2D numerical simulations proposed by Champmartin *et al.* [19] in figure 5.11. They studied the free-flow of a cylindrical fiber confined between two parallel walls, perpendicular to the flow direction and looked in particular at the effect of its confinement on the velocity. Both simulations are in good agreement (20% maximal difference) considering the slightly different cross-section shapes.
In conclusion, we need three-dimensional simulations to get an accurate picture of the high confinement effect for fibers perpendicular to the flow direction.

5.3.4 3D simulations: fiber with finite length

5.3.4.1 Numerical protocol

The 3D-steady state simulations are done using the commercial CFD software COMSOL. We design the microchannel as a rectangular-section channel. Its width/height ratio is chosen to

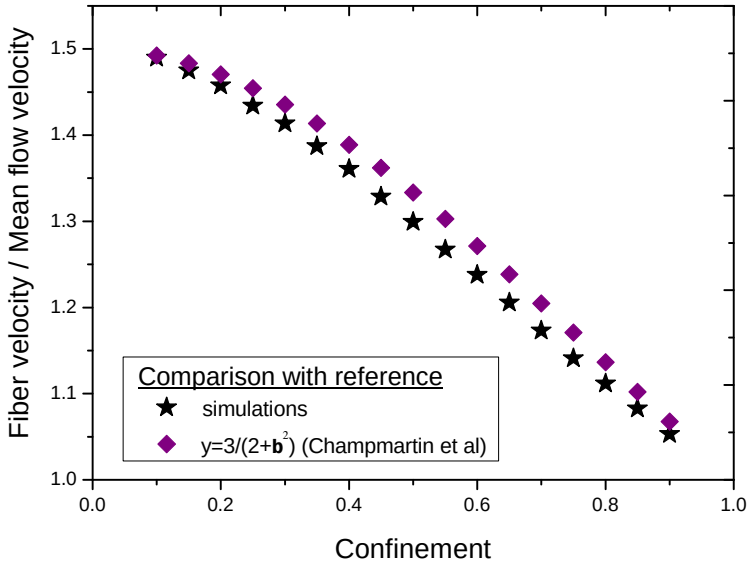

Figure 5.11: *Comparison of our 2D simulation with the results of Champmartin et al [19] for the perpendicular fiber. In their configuration, a cylindrical fiber is freely advected by the flow between two parallel walls. We compare their result of confinement effect on the fiber velocity. In the limit of high confinements (β going to 1), we obtain the same limit of* $V_{fiber} = V_{mean}$.

correspond to the confinement used in the experiments. 3D calculations are costly in computer resources so we always reduced the channel width or length as much as possible, depending on the orientation of the channel and the establishment of a fully developed flow. Details of geometries are given in Appendix B. Similarly, we design the fiber immersed in the fluid. The fiber volume is substracted from the fluid volume, leaving us with a single domain where the flow equations are solved along with the appropriate boundary conditions. This strategy simplifies the problem to solve, the number of nodes of the problem and the solid-fluid interactions that we don't need to simulate. The design is illustrated by the drawing 5.12 along with the mesh used for a simulation of a perpendicular fiber confined at 60%.

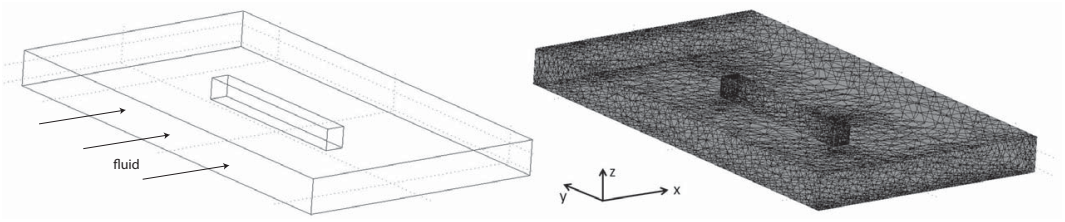

Figure 5.12: *Design and mesh of a rectangular-section microchannel for the simulation of fiber perpendicular to the flow direction (x axis). The simulation volume corresponds to the fluid only. We mesh with 5 nodes on each vertical channel edge in order to have several elements within the height in the middle of the channel. The mesh is refined around the fiber as we need to compute the drag force on its faces.*

The flow equations are the Stokes equation and the incompressibility condition (see eq. 5.3). We impose a constant velocity on the inlet face and a constant pressure condition on the outlet face. A no-slip condition is applied on the channel walls and a continuous velocity condition on the fiber faces.

We control the mesh by imposing a number of nodes on each edge and refining it using the COMSOL refinement tool. Our CPU is unfortunately limited: we adapted the mesh for each geometry to get several nodes within the channel height far away from the fiber and obtain a very fine mesh around the fiber. The maximal number of tetrahedral elements that we could use was around 1 million.

In order to compare 2D and 3D simulation results we make dimensionless all lengths with the channel height. Fiber velocities will be compared to the mean flow velocity imposed on the inlet boundary.

5.3.4.2 Finding the fiber velocity

Similarly to the 2D simulations, we need to know the fiber velocity to set up correctly the boundary conditions on the fiber faces. A procedure with MATLAB launches COMSOL automatically and extracts the simulation results to compute the force exerted on the fiber for a given fiber velocity. We use the linearity between force and velocity to determine the velocity of the fiber, at zero force. Details of the procedure are available in Appendix B.

5.3.4.3 Fiber confinement effect on velocity

We investigate the effect of fiber confinement on its velocity for the two configurations: parallel and perpendicular to the flow direction. The flow is now fully 3D: fluid can flow around the fiber ends, above and below the fiber. For each confinement, we impose a mean flow velocity on the inlet and extract the fiber velocity. Variations of the geometry and mesh density cause the flowrate to vary slightly between confinement cases. We compute the case of a zero confinement to obtain the maximal velocity when the flow is fully developped in the microchannel. We compute the ratio of V_{fiber} over the mean velocity along the channel height to compare the parallel and perpendicular orientations. Results are reported in graph 5.13. The limit towards zero confinement is 1.5 as the fiber velocity goes to the maximal speed. For small confinements (remaining under 0.5) a parallel fiber and a perpendicular one flow at the same velocity as we saw in the experiments. As the fiber gets more confined, the deviation between the two curves increases. The parallel fiber flows slower than the perpendicular one.

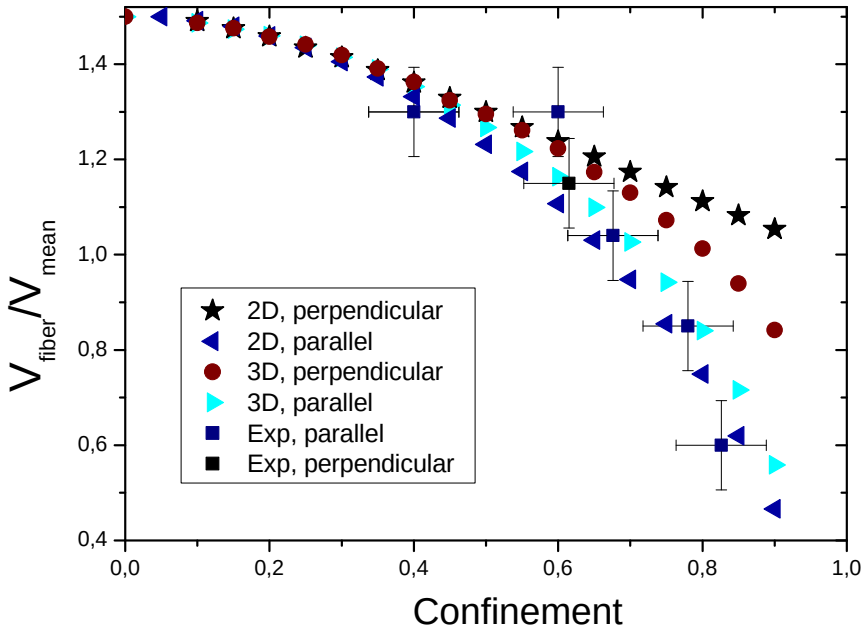

Figure 5.13: *3D and 2D simulation results of fiber velocity when it is parallel or perpendicular to the flow direction compared with experimental results. The fiber velocity is made dimensionless with the mean flow velocity along the channel height.*

We also added the 2D velocity results to compare both simulations. Black stars and red dots are respectively the 2D and 3D results of a perpendicular fiber. In the 2D case, the fiber is considered with an infinite length which makes its velocity tend to the mean flow velocity in the limit of high confinements. Taking into account the flow around fiber tips in the 3D computations, we find that the limit at high confinements decreases towards the parallel limit. The blue (dark and light) triangles compare the case of a parallel fiber. Both curves tend to the same limit at high confinements but the 3D results are higher. The difference in 3D computations between the parallel and perpendicular results can be discussed in terms of fiber length. As the length is reduced while keeping a high confinement, we should find velocity results ranging between the purple triangles and red dots. It would be interesting to vary the fiber length in the 3D computations to confirm that parallel and perpendicular curves tend to the same limit towards very small lengths at high confinement.
Finally, one should note that the experimental data point corresponding to the perpendicular fiber is in excellent agreement with the computation results.

5.3.4.4 Variations of velocity with fiber orientation

We saw in the previous section that under certain confinement conditions, we obtained a difference between the fiber velocities $V \parallel$ and $V \perp$. This difference should be responsible for a drift for fibers at an angle different from $0°$ and $90°$ with the flow direction as we have already observed experimentally. We will now study this numerically. 3D simulations are run similarly

to the parallel and perpendicular case, with an angle varying from $-90°$ to $+45°$. We extract for each case the fiber velocity along the channel length (V_x) and its velocity along the channel width (V_y). Results for two confinements are shown in figure 5.14. Variations of V_y are very small for the low confinement case (0.5), ten times smaller than in the confinement case of 0.75. This corresponds to the results presented in figure 5.13.

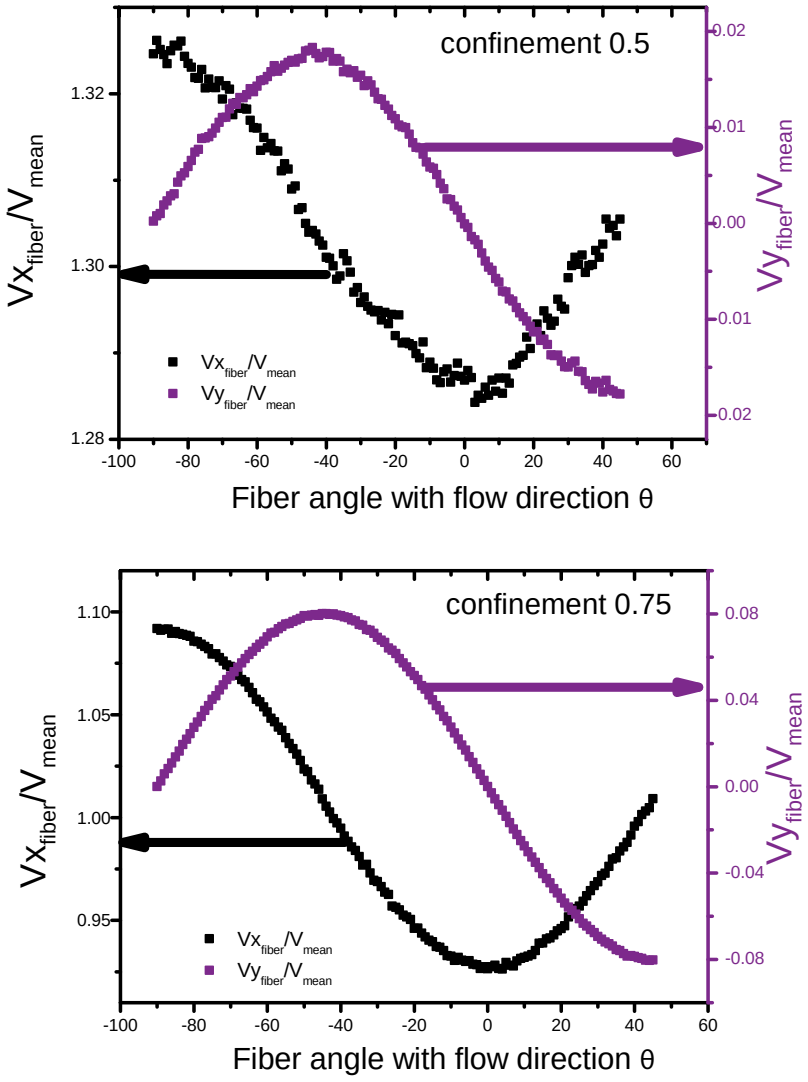

Figure 5.14: *Results of velocity for a fiber flowing at any angle ranging from $-90°$ to $+45°$ for two confinements. a: confinement of 0.5.b: confinement of 0.75. We recover the results of a parallel fiber ($\theta = 0°$) and a perpendicular fiber ($\theta = 90°$).*

We propose an understanding of the drift through a model solely based on the fiber orientation and the imposed fluid velocity. Let's consider the system { fiber and flow } in the channel. The flow is constant and imposed along the direction of the channel length. The fiber is oriented with an angle θ with the flow direction as illustrated in 5.15. The idea is to represent both flow and fiber velocities in the reference systems of the laboratory (refered to Oxy earlier) and of the

fiber. The reference system of the fiber is based on two unit vectors parallel and perpendicular to the fiber length $\mathbf{e}_{\parallel}$ and $\mathbf{e}_{\perp}$.

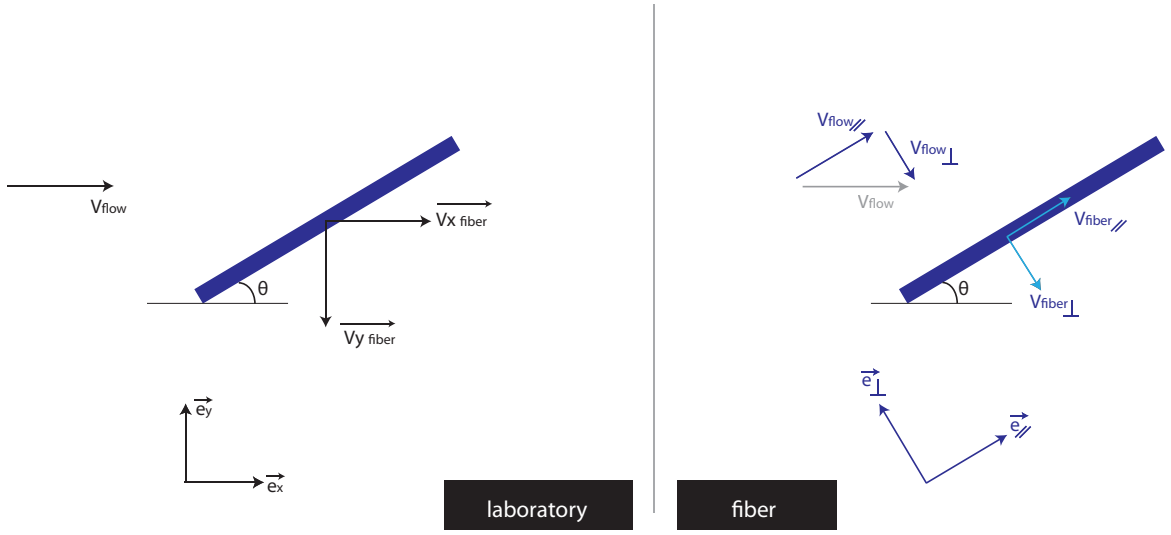

Figure 5.15: *Representation of the fluid velocity vector in the reference system of the laboratory and in the system of the fiber. Similarly we decompose the fiber velocity vector into two components parallel and perpendicular to the fiber length.*

We start by decomposing the **flow** velocity vector in the fiber reference system:

$$\mathbf{V}_{flow} = \mathbf{V}_{flow\parallel} + \mathbf{V}_{flow\perp} \tag{5.23}$$

We can write each component using the velocity and the fiber angle:

$$V_{flow\parallel} = V_{flow} cos(\theta) \tag{5.24}$$

$$V_{flow\perp} = V_{flow} sin(\theta) \tag{5.25}$$

We showed experimentally and numerically that a fiber initially parallel to the flow direction would keep this orientation and have a velocity proportionnal to the flow velocity. At a given confinement, we have: $V_{fiber\parallel} = \gamma_{\parallel}.V_{flow\parallel}$ Similarly, a fiber perpendicular to the flow direction flows at a constant velocity: $V_{fiber\perp} = \gamma_{\perp}.V_{flow\perp}$
Now we write the **fiber** velocity in the reference frame of the laboratory:

$$Vx_{fiber} = V_{fiber\parallel} cos(\theta) - V_{fiber\perp} sin(\theta) \tag{5.26}$$

$$Vy_{fiber} = V_{fiber\parallel} sin(\theta) + V_{fiber\perp} cos(\theta) \tag{5.27}$$

Finally, replacing $V_{fiber\parallel}$ and $V_{fiber\perp}$ with their equivalent with the flow velocity, we obtain:

$$\frac{Vx_{fiber}}{V_{flow}} = \gamma_{\parallel} cos^2(\theta) + \gamma_{\perp} sin^2(\theta) \tag{5.28}$$

$$\frac{Vy_{fiber}}{V_{flow}} = (\gamma_{\parallel} - \gamma_{\perp}) cos(\theta) sin(\theta) \tag{5.29}$$

Comparison of velocity results obtained in the simulations with their analytical expressions from equations B.1 and 5.29 are given in figures 5.16 and 5.17 for the same two confinements presented before (0.5 and 0.75). The values of $\gamma_{\parallel}$ and $\gamma_{\perp}$ are extracted from the simulations at an angle respectively 0 and -90°. They show an excellent agreement of the model with the simulations.

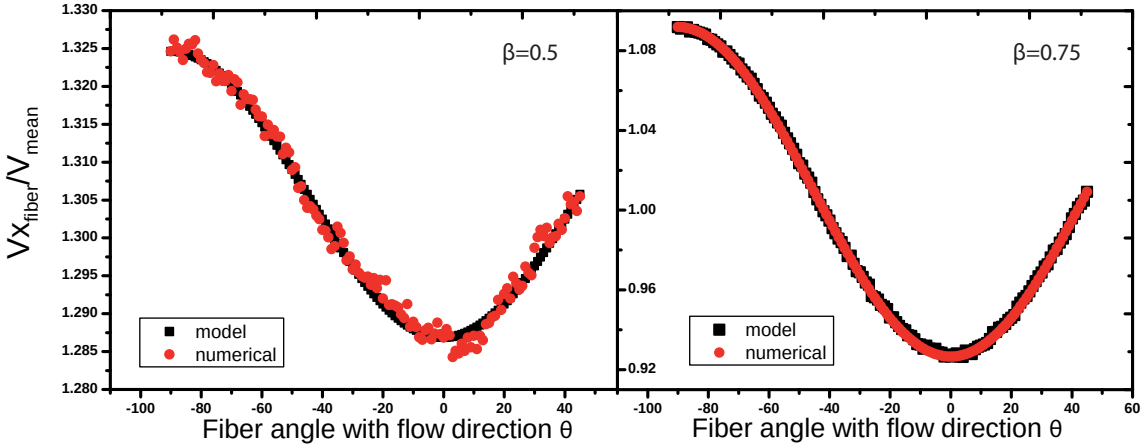

Figure 5.16: *Comparison of velocity V_x computed in the 3D simulations with its analytical expression $V_{fiber_x} = (\gamma_{\parallel} cos^2(\theta) + \gamma_{\perp} sin^2(\theta)) * V_{flow}$. The γ coefficients are extracted from simulations with $\theta = 0^{\circ}$ and $\theta = -90^{\circ}$. Simulations are in excellent agreement with the analytical model.*

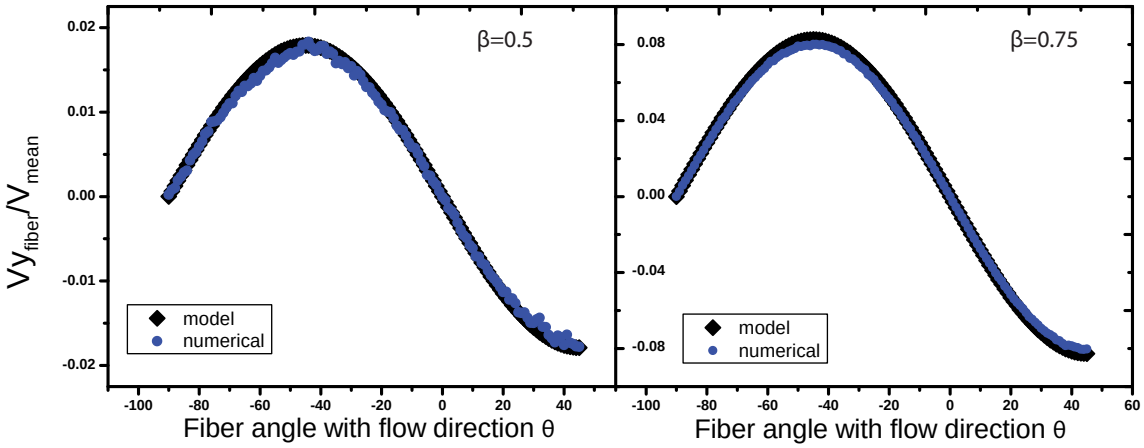

Figure 5.17: *Comparison of velocity V_y computed in the 3D simulations with its analytical expression $V_{fiber_y} = ((\gamma_{\parallel} - \gamma_{\perp}) cos(\theta) sin(\theta)) * V_{flow}$. The γ coefficients are extracted from simulations with $\theta = 0^{\circ}$ and $\theta = -90^{\circ}$. Simulations are in excellent agreement with the analytical model.*

To conclude this section, we compare our numerical predictions with the experiments described earlier in 5.1.3.1. At a confinement of 0.61 we observed a drift of fibers flowing at an angle of 45° with the flow direction. The ratio of velocity Vy/Vx was 0.058. We compare it with results

obtained for a sligtly larger confinement of 0.65. We computed $\gamma_{\parallel}$=1.104 and $\gamma_{\perp}$=1.2 leading to a velocity ratio of 0.042. We obtain a good agreement between the experiments and the simulations: the small sidewise drift is due to the small difference between drag coefficients $\lambda_{\parallel}$ and $\lambda_{\perp}$ at the experimental confinement of 0.6.

5.3.5 Perturbation of the flow profiles

In the previous sections we investigated the transport velocity of a fiber at different orientations and confinements in the microchannel. We are now interested in the perturbation of the flow caused by the presence of a fiber, depending on these parameters. The first question we address is the case of a fiber parallel to the flow direction. 2D flow simulations are used to extract velocity profiles along the channel width and height at different positions. Figure 5.18 illustrates the case of a parallel fiber (aspect ratio ω/h = 1.375) in a channel of aspect ratio W/H=10.

The top sketches indicate the position of the profile: at channel mid-height, we obtain a plug-flow profile as predicted by the flow equations (5.8). The parabolic flow profile within the channel height is also changing to adjust to the fiber velocity on its edge. The right-side graph shows velocity profiles at several distance from the fiber. The perturbation extends over a distance comparable to the channel height.

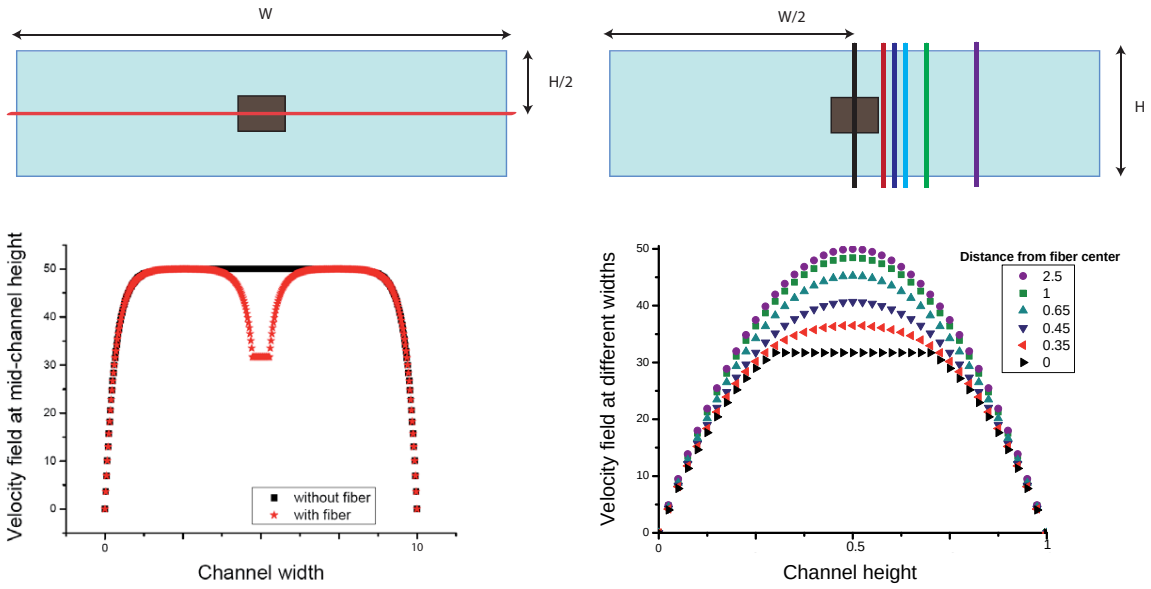

Figure 5.18: *Cross-section view of channel with the location of flow profiles along the width and length for a parallel fiber. Velocity profiles are plotted under each schematic drawing with the corresponding colour code. The location of profiles is determined by the distance to the fiber center made dimensionless with the channel height. We find that the flow profile is recovered at a distance comparable to the channel height.*

To study the effect of confinement on the perturbation magnitude, we compare the flow profiles along the channel width for seven degrees of confinement from 0.1 to 1. Fiber velocity varies

with confinement: in order to compare the different profile plots, we compute the dimensionless quantity $\frac{V_{flow}-V_{fiber}}{V_{max}-V_{fiber}}$ which varies between 0 and 1. V_{flow} is the mean velocity of the flow, V_{fiber} the fiber velocity and V_{max} the maximal velocity in the fluid flow profile. The different profiles are presented in figure 5.19. There is no strong difference between all the confinement cases, as shown in the inset of the figure (14% deviation).

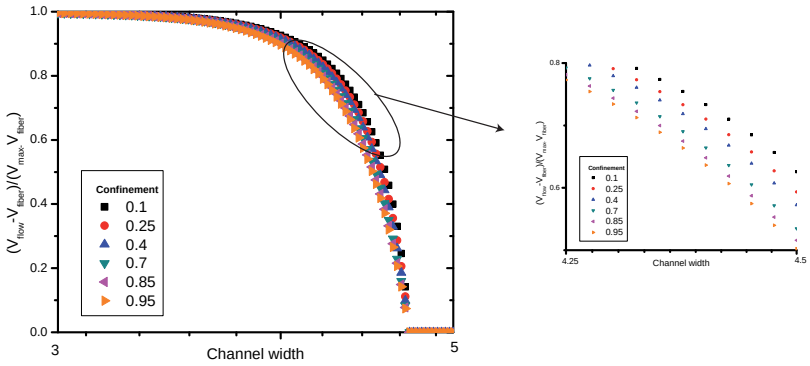

Figure 5.19: *Comparison of the velocity profiles at varying fiber confinements for the case of a parallel fiber. The inset shows a difference of around* 14% *between the extreme curves.*

Keeping the fiber confinement at 0.4, we now vary the channel height from 10 to 30 and plot the same dimensionless number. A larger difference is found between the different profiles, which we characterize by the mid-height distance. Profiles are plotted in Figure 5.20. The perturbation of the flow near the fiber scales very well with the channel height. We expected this result as the fiber behaves like a wall: the velocity profile varies only along a distance equivalent to the channel height, smallest length of the geometry.

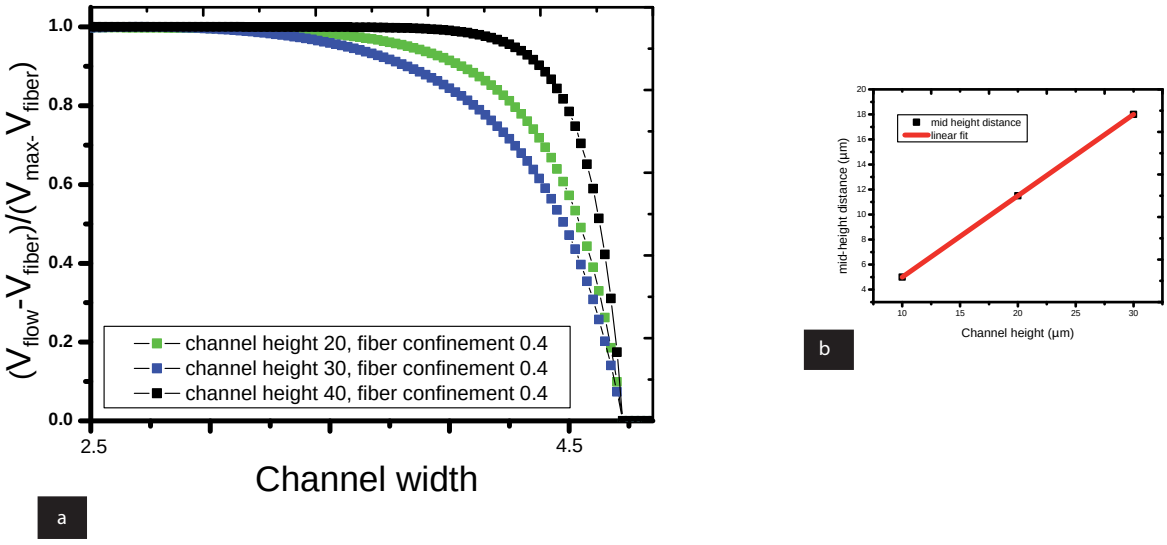

Figure 5.20: *Comparison of the velocity profiles for different channel heights, keeping the fiber confinement constant (parallel fiber). a: dimensionless flow profiles along the channel width. b: mid-height distance of flow profiles versus the channel height. The flow perturbation caused by the fiber scales well with the channel height.*

The 2D simulations do not take into account the finite length of the fiber. We supplement the results of flow perturbation with data from the 3D computations. Fluid velocity values are extracted from planes parallel to the channel width/height section downstream of the fiber for a low confinement (0.4) and a high one (0.8). A drawing in 5.21 shows a typical extracted section and its relative position to the parallel fiber. The same process is applied for the perpendicular fiber case.

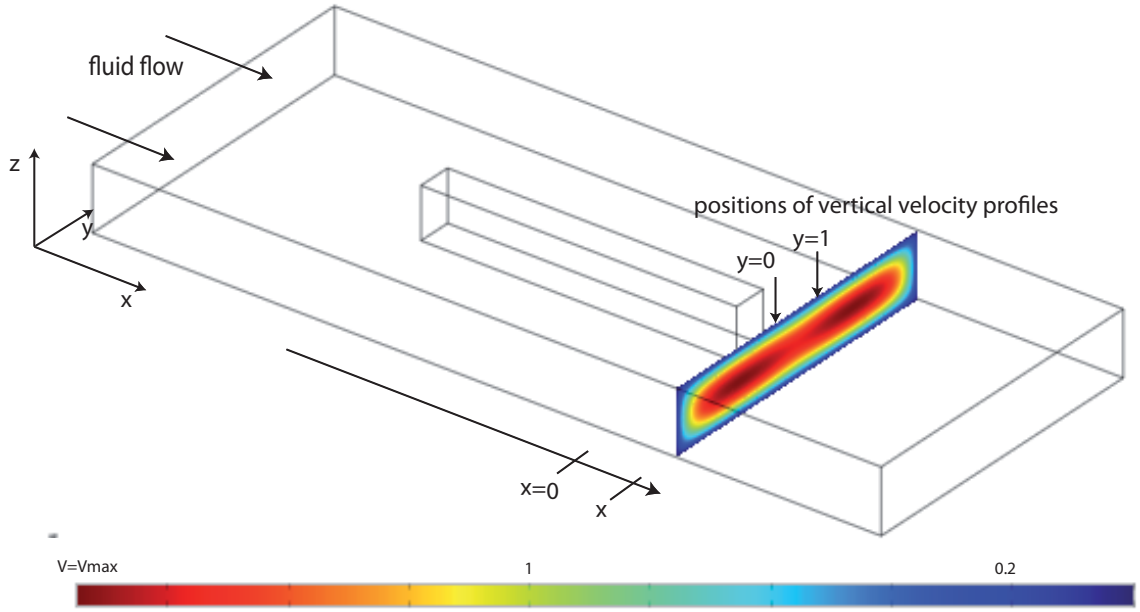

Figure 5.21: *Drawing of a fiber parallel to the flow direction centered in the channel. The color-coded section illustrates the planes from which we extract velocity values. Planes are positioned at different values of x downstream of the fiber to measure the extension of the flow perturbation induced by it. Velocity profiles in the channel height are then extracted from these selected sections at two positions y=0 and y=1 indicated with the arrows. Comparing them will provide with an indicator of the perturbation amplitude. Positions in x and y are made dimensionless with the channel height.*

First we show results of velocity for the parallel fiber in the section planes downstream of its tip edge. For each section we extract velocity along the channel height at a constant location along the channel width: y=0 and y=1. The first one corresponds to the center of the channel, exactly in front of the fiber edge. The second one corresponds to a position on the side of the fiber at a channel-height distance from the fiber. Figure 5.22 compares the case of high confinement (top panel) with low confinement (bottom panel). We see the fluid acceleration around the fiber sides. In front of the fiber, on the other hand, it significantly slows down. The first graph at $x = 0.5$ shows in fact very different profiles. Then as we move downstream of the fiber and the perturbation effect decreases, the two profiles are brought closer to finally be the same at x=1.5. At **high confinement**, the unperturbed profile is recovered at a position of x=1.5 which corresponds to a distance of **1.5 times the channel height** from the fiber edge. When the **confinement is low**, the perturbation extends only over **one channel-height distance** from the fiber edge. We find a good agreement with the experimental results presented earlier in this chapter 5.1.4. The flow perturbation extends over a distance close to the channel height,

as we would expect if we consider the highly-confined fiber as a fixed wall in the channel.

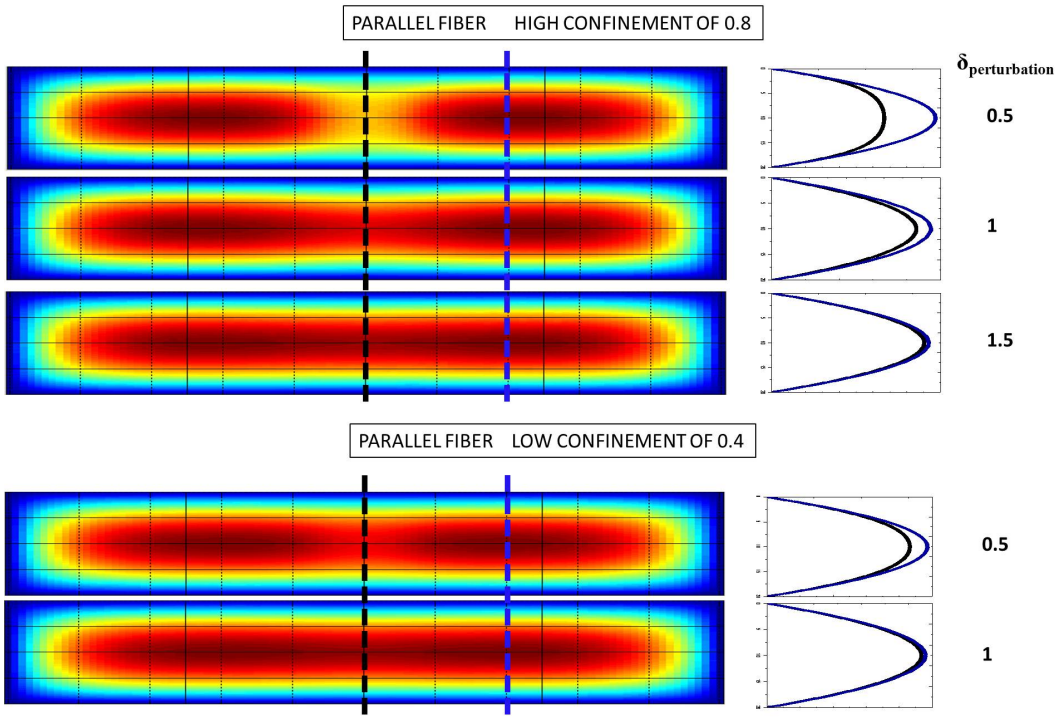

Figure 5.22: *Results of velocity on channel sections at different positions downstream of the parallel fiber for two confinements. Velocity is colour-coded at each time step, from blue to red. Velocity results on the right graphs are taken along the channel height, at two positions in the channel width as indicated with the black and blue dotted lines (vertical axis is position along channel height, horizontal axis is the velocity). The difference between the two velocity profiles is an indicator of the flow perturbation caused by the fiber*

Now we address the question of the perturbation caused by a perpendicular fiber at different confinements. Similarly to the parallel case, we extract velocity results in planes parallel to a channel width and height section as illustrated in previous figure 5.21. We also plot the velocity profiles along the channel height for two given positions along the width: one in front of the fiber edge, one translated laterally closer to the wall. Figure 5.23 shows result of **high confinement** $\beta = 0.8$ (left panel). The unperturbed profile is recovered at a distance of 2.75 times the channel height, corresponding in our geometry to **half the fiber length**.
We can compare these results to the streamlines of the flow past a fence oriented at 90° visualized by Taneda[61]. A picture of his experimental results is reproduced in figure 5.24. At a Reynolds number of $1.4 \cdot 10^{-2}$ he found that the distance between the vortex center and the corner point is 0.54 times the fence height. It is interesting to note that the perturbation in our case extends over half this distance. The confinement is lower: 0.8 instead of 1 and our fiber is flowing freely in the channel.
When the confinement is **low**, the perturbation doesn't appear on the velocity sections as represented in figure 5.23. They are already too distant from the fiber. We propose another view to easily see the distance over which the perturbation extends. The section is now extracted at channel mid-height where we extract the fluid velocity as shown in figure 5.25-A. Velocity

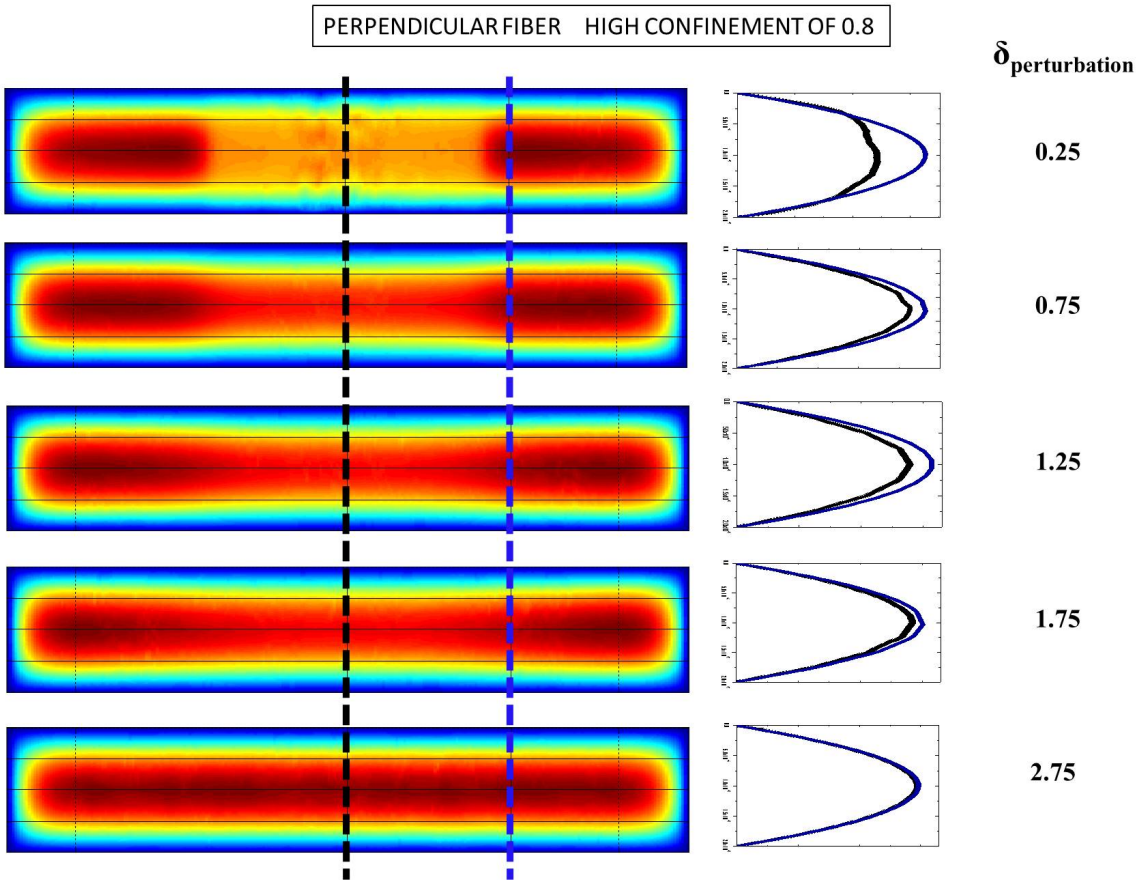

Figure 5.23: *Results of velocity on channel sections at different positions downstream of the perpendicular fiber for a confinement of 0.8. Velocity is colour-coded at each time step, from blue to red. Velocity results on the right graphs are taken along the channel height, at two positions in the channel width as indicated with the black and blue dotted lines (vertical axis is position along channel height, horizontal axis is the velocity). The difference between the two velocity profiles is an indicator of the flow perturbation caused by the fiber*

values are selected along the middle line, and plotted with their position along the channel length. Results are presented in figure 5.25-B with positions made dimensionless with the channel height. The flow perturbation extends over a distance of 0.45 times the channel height which corresponds in this case to the **fiber height**.

5.3.6 Conclusion of the simulations

We ran 2D and 3D numerical simulations to confirm experimental observations of the flow dynamics of a single fiber away from the lateral boundaries. We first addressed the question of the fiber velocity and its dependence on confinement. We were able to extend the range of confinement and study the effect of the fiber initial orientation. The slight drift oberved in the experiment was numerically reproduced and explained from the difference of fiber velocity between the two reference cases of a parallel and perpendicular fiber. We also used the simulations to investigate the fluid flow perturbation caused by the fiber. Highly-confined fibers

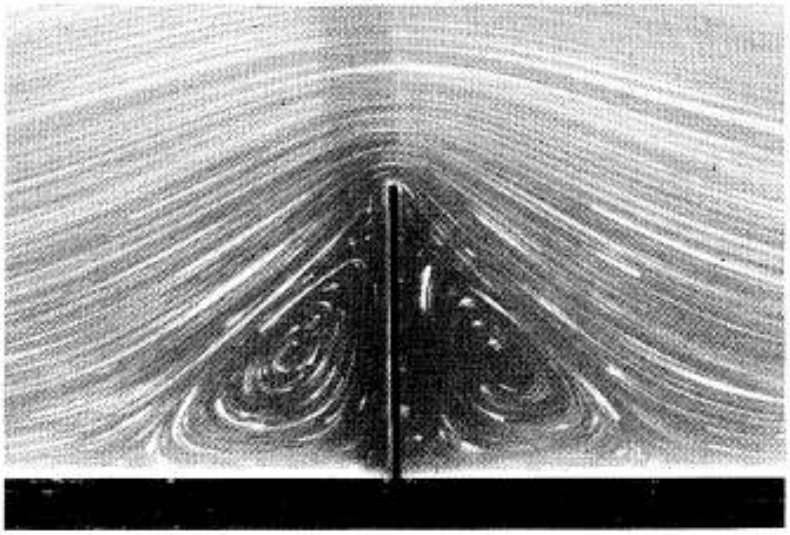

Figure 5.24: *Streamlines visualization of the flow past a fixed fence perpendicular to the flow direction. This picture was extracted from the work of Taneda[61].*

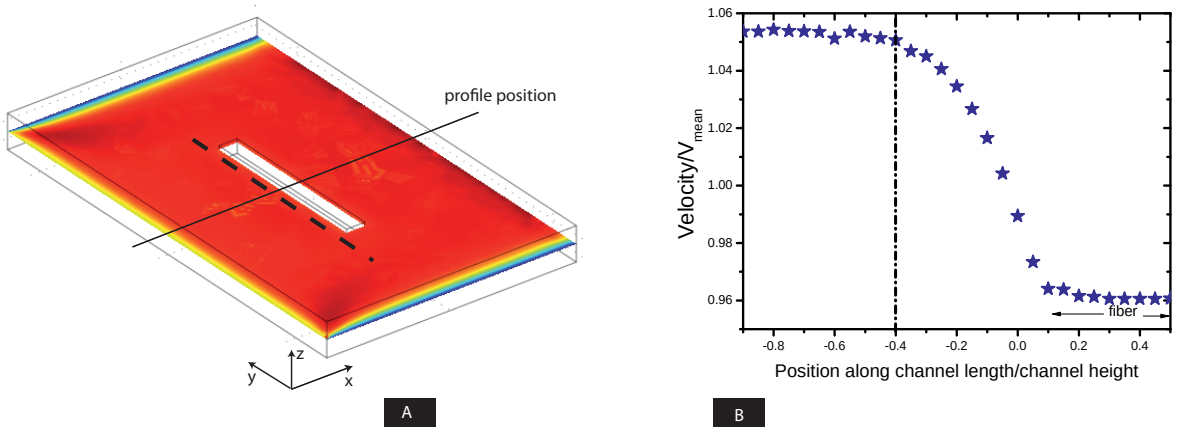

Figure 5.25: *Velocity results extracted for a plane cutting the channel at mid-height for a fiber perpendicular to the flow direction at a low confinement of 0.4. A illustrates the location of the plane and the line selected to study the velocity profile. In B are reported the velocity values along this line around one fiber's edge. The dotted line shows where the profile recovers the maximal fluid velocity: the fluid perturbation caused by the fiber extends over a distance of 0.45 times the channel height, equivalent to the fiber height.*

are responsible for a perturbation of the fluid extending over more than the channel height. It decays faster in the case of a parallel fiber than a perpendicular one. At low confinements we find that the perturbation caused by a parallel fiber is of the order of the channel height when the one caused by a perpendicular fiber is of the order of the fiber height. These results are summarized in table 5.3 for clarity.

Confinement	Parallel fiber	Perpendicular fiber
0.8	1.5× channel height	0.55× fiber length
0.4	channel height	fiber height

Table 5.3: *Distance downstream of the fiber where the perturbation decays to zero.*

5.4 Conclusion

We studied in this chapter the question of transport of a single fiber in a confined flow geometry where the lateral walls are far. We propose an original experimental approach in microfluidics complemented with numerical simulations to investigate in particular the importance of flow geometry, fiber confinement and length as well as its orientation with the flow. We found that the variations of fiber velocity with confinement were small towards the small confinement limit. As the fiber becomes more confined, its perturbation on the flow increases and its velocity starts varying with its orientation with the flow. In the limit of high confinements and for a given length, a perpendicular fiber is transported faster than a parallel one. A consequence of this orientation dependence is the apparition of a velocity component perpendicular to the flow direction leading to the drift of the fiber towards the channel lateral walls. We confirmed our experimental observation of such biased transport with numerical simulations based on the determination of the fiber velocity. Most of the experiments described here were done at an intermediate or low confinement: it gave us the flavor of these confinement-dependent features of fiber transport well described in our simulations. More experimental work will be done using highly confined fibers in microchannels to observe higher levels of drift, explore the role of the fiber length and confirm the strong slow-down obtained numerically.

As the distance to the lateral walls decreases, hydrodynamic interactions develop between the fiber and the flow boundaries, changing its transport dynamics. We will adress this question in the next chapter using some results of fiber transport studied here.

CHAPTER 6

SINGLE FIBER INTERACTING WITH THE LATERAL FLOW BOUNDARIES

In the previous chapter, we studied experimentally and numerically the flow of isolated fibers confined in a microchannel when the lateral boundaries are far. As the channel width becomes of the size of the fiber length, hydrodynamic interactions between the fiber and the lateral walls start to occur and modify its flow dynamics. We observe an established and robust oscillatory movement of the fiber from a wall to the other. Such oscillations could be used as an efficient tool to enhance mixing in microfluidic channels where the typical Reynolds numbers are too small to have small diffusion times. In this chapter, we describe our experimental observations of the fiber oscillation identifying key parameters associated with the flow and the fiber characteristics. We propose an understanding of the periodic flow as three successive regimes, with support from numerical and modeling work.

6.1 Introduction

6.1.1 Observation of oscillating fibers

We start this chapter with experimental observations of a fiber oscillating under flow. The experiments are very similar to the drift tests described in the previous chapter: a single fiber flows in a confined microchannel but now the lateral walls are much closer to the fiber. Typically, the channel width is of the order of the fiber length, constraining the angle at which the fiber can flow. The image in figure 6.1 shows successive positions of the fiber in time (time lapse between two positions: 200 ms). What we call oscillations is this continuous movement of such a fiber flowing from one lateral wall to the other, changing its orientation periodically.

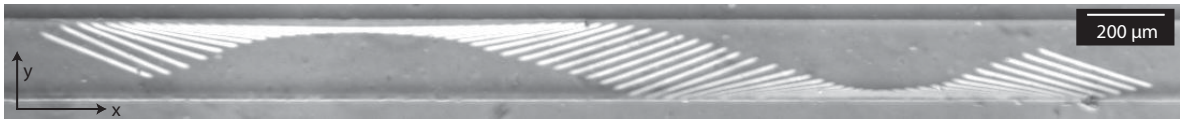

Figure 6.1: *Chronograph of fiber flowing in the channel. 200 ms separate two successive positions. Channel width is 200 µm, fiber length 290 µm.*

The simplest way to look at the fiber oscillatory dynamics is to represent its position in time. Such data are shown in figure 6.2. Fiber x position (=along the flow direction, left plot) varies smoothly, showing at first order its advection by the flow. We will see in the developed analysis that instantaneous variations provide with more information than a direct linear fit. The y position of the fiber center of mass can be represented as its distance to one of the two lateral walls. Such graph in 6.2 (right plot) shows the remarkable oscillations of the fiber. The evolution of the fiber's orientation is shown in figure 6.3.

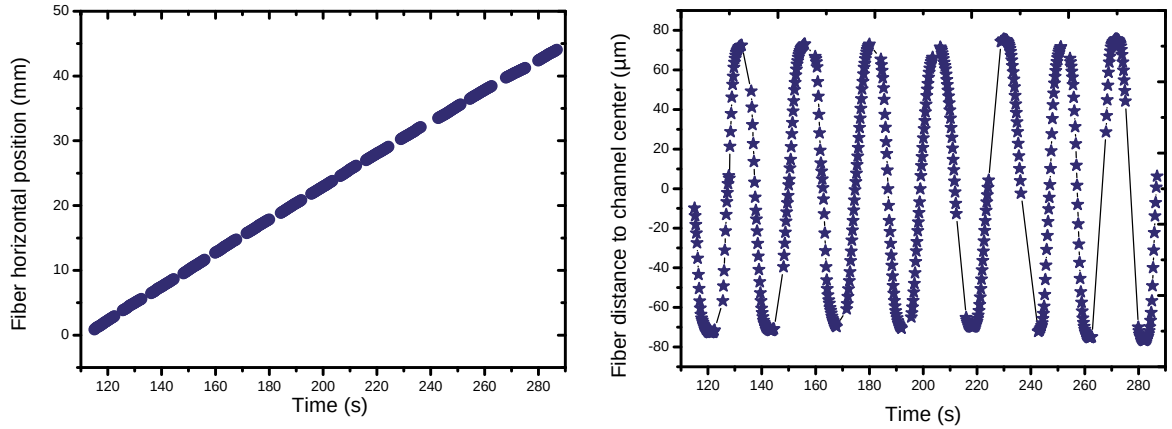

Figure 6.2: *Experimental results of fiber's center of mass position in time. One can clearly see the oscillatory movement of the fiber between the two lateral walls on the right graph. Areas with missing data correspond to the stage movement on the microscope to follow the fiber in the frame of view. Using our image processing method (see C) we reconstruct the fiber trajectory in the laboratory system.*

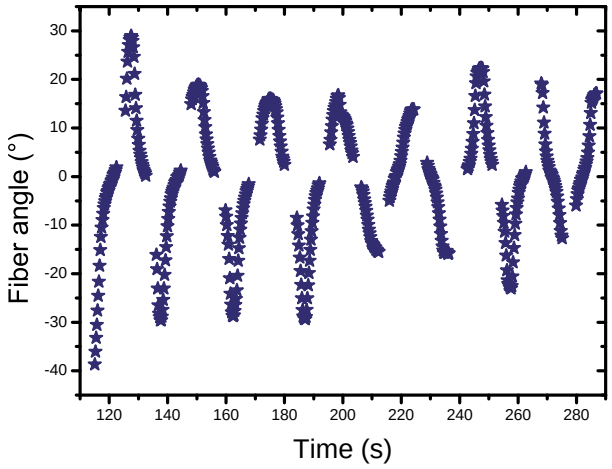

Figure 6.3: *Experimental results of fiber's angle with the flow direction over time during a full oscillation experiment. Successive data points are separated by 200 ms.*

6.1.2 Experimental set-up

The flow geometry is a confined microchannel with a Y-shaped inlet as illustrated in figure 6.4 (aspect ratio 0.1). Both branches of the inlet are connected to a syringe pump delivering the oligomer solution used for the fabrication and flow of the fiber. We use this geometry to get a good fabrication resolution of the fiber while flowing at well-controlled high or low flowrates (refer to 2.4.2 for more details).

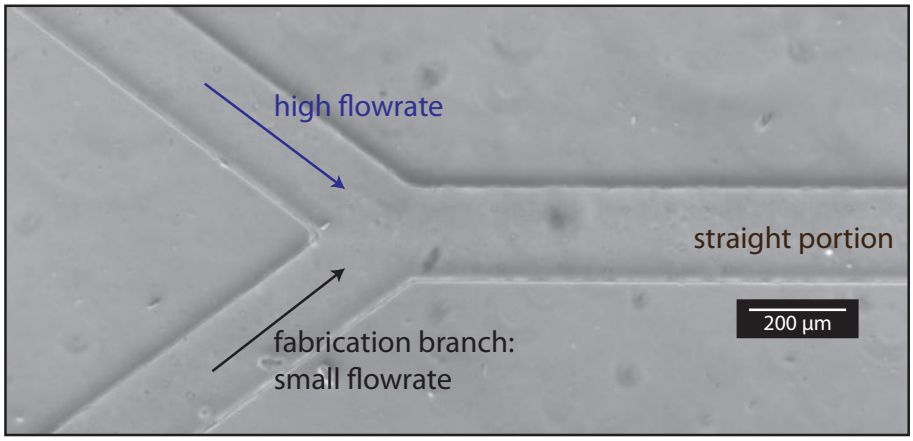

Figure 6.4: *Top-view of a microchannel typically used for the experimental study of the fiber oscillations. The Y-shaped inlet is designed to be able to impose a constant high flowrate while fabricating the fiber under flow without loss of resolution.*

All microchannels used in the oscillation experiments reported here are of the same width: 200 μm and two heights: 20 and 27 μm, leading to two fiber confinements β of 0.5 and 0.63. Fiber width was kept constant at around 15 μm, with a length of 290 μm. Oscillations are systematically observed when the fiber length is slightly larger than the channel width (ratio

of 0.7). Flow velocity in the main channel ranged from 200 to 1000 $\mu m/s$. Maximal Reynolds number is 4×10^{-4}.

The experimental workflow consists in setting the flowrates at the syringe pump, waiting for their stabilization and fabricating the fiber in the low-flowrate branch with the photo-polymerization technique. The fiber is fabricated along the lateral wall to trigger the apparition of the oscillation in the main portion of the channel. Once started, the oscillations are robust and continue until the fiber reaches the outlet. Its flow down the straight portion of the channel is captured with a video camera using the method explained in the fabrication chapter C. This way, we can use our detection algorithms to extract the fiber position and orientation in each frame of a flow experiment.

6.1.3 Regime decomposition

Our first strategy of processing the experimental data was to extract temporal or spatial periods characterizing the fiber cyclic behavior in the flow over a full experiment. The channels lengths are large in order to observe many periods of oscillations and lower the error associated with the measurement of a global frequency. More than sixty experiments leading to robust oscillations were done, varying the channel geometry, the fiber length and the imposed flow velocity. However a direct temporal or spatial analysis did not give clear answers on the understanding of the oscillations and its dependence on these parameters. While some experiments show very regular oscillations, for others the time spent by the fiber along the wall can be very different for subsequent oscillations. This situation is illustrated in figure 6.5 where the distance of the fiber's center to the channel center is reported over time. This irregular behaviour led to the idea that some features of the flow during an oscillation period are regular, deterministic, while others are stochastic and bring random irregularities in the flow pattern. In other words, a global analysis where we try to extract a single oscillation frequency does not capture the local fluctuations of the fiber flow which characterized the phenomenon.

Comparing oscillation experiments, we systematically observe the same variations in time of its angle. In this chapter, we propose an understanding of the oscillatory flow as the succession of three regimes using the fiber's angle as a criterion. As a first illustration, a chronograph in figure 6.6 shows successive positions of a fiber transported from one wall to the other. The flow is divided in colors corresponding to the three regimes. First, the fiber flows parallel to the flow direction keeping an angle of zero. We call this regime the **contact** phase. Then the fiber rotates, its angle is increasing: we call this phase a **rotation** regime. In the third regime called **drift** its angle is constant, but not zero. From one wall to the other, the fiber experiences contact, rotation, drift, rotation and contact.

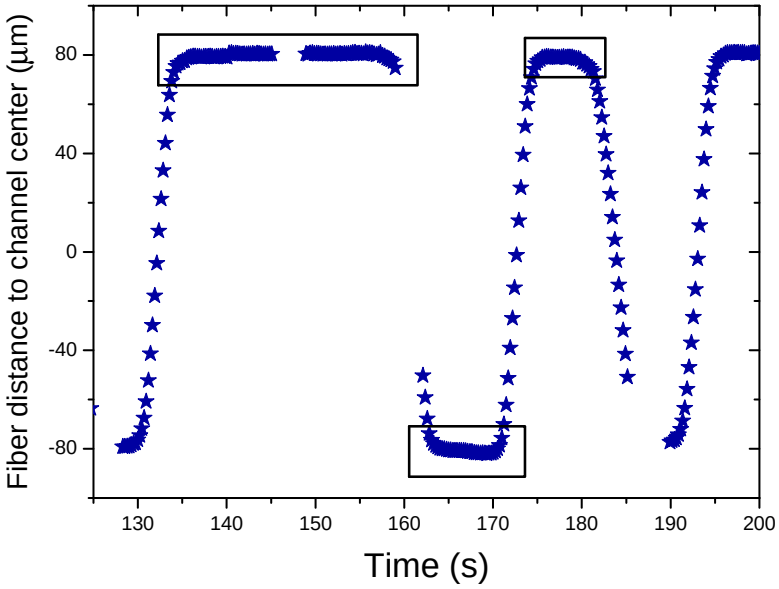

Figure 6.5: *Fiber position in the channel with time during an oscillation experiment. The fiber stays for long periods of time along a lateral wall as indicated by the black boxes.*

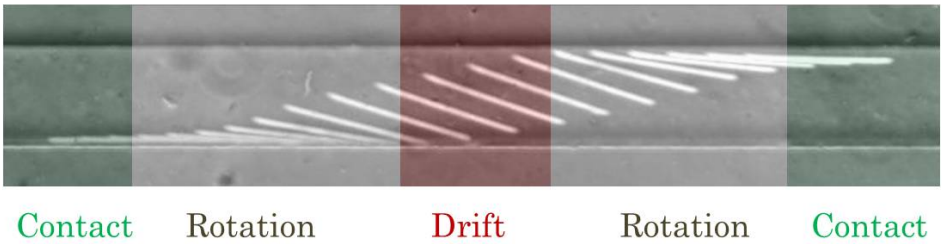

Figure 6.6: *Fiber successive positions during its flow from one lateral wall to the other. Time separating two positions: 400 ms. We divide the picture in colors corresponding to the three flow regimes.*

We show in figure 6.7 the extracted values of fiber's angle over a full oscillation experiment. The angle is plotted versus the distance of the fiber's center of mass to the channel center. This data set was obtained from the analysis of a single experimental test (one imposed flow velocity) with data from seven oscillation periods. Around the center of the channel, (corresponding to the central part of the graph), the angle remains constant, non zero. This part corresponds to the drift regime. Then as the fiber approaches the wall the angle goes towards zero: rotation regime. At a distance comparable to $\pm 80\ \mu m$, the angle is $0^\circ \pm 1.5$ corresponding to the contact phase.

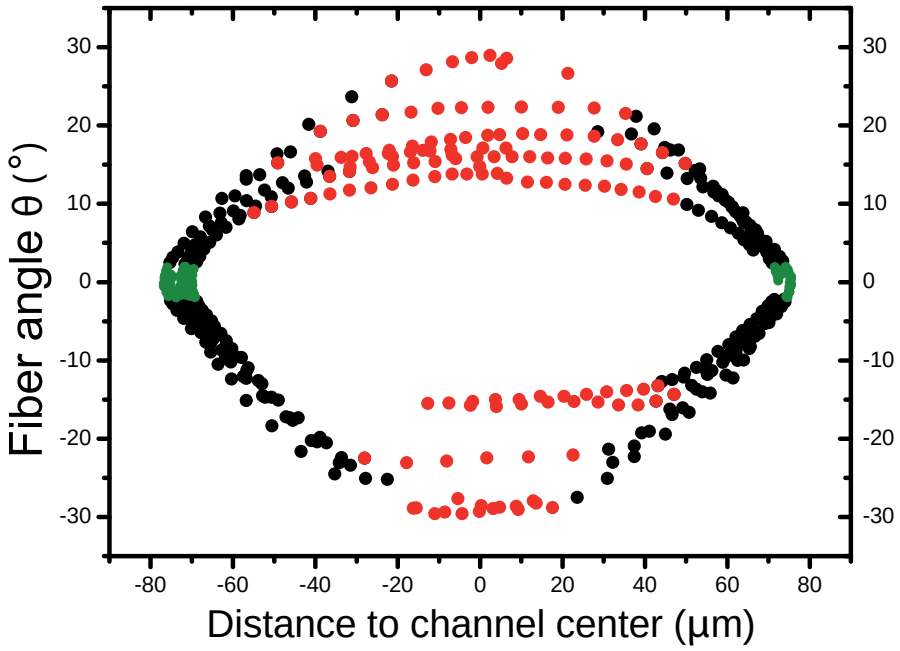

Figure 6.7: *Evolution of fiber angle with its distance to the channel center (experimental data taken over seven oscillation periods). The angle is taken with the flow direction (x). Colors correspond to the different regimes: green for a zero angle, black for a varying angle, red for a constant non zero angle.*

In the following sections, we describe each flow regime in terms of the fiber position relative to the channel center and fiber spatial and angular velocities, supported with experimental results all done with a unique geometry described in the set-up section 6.1.2. Note that the maximal distance of the fiber to the channel center is $\pm 80\ \mu m$ for a channel width of 200 μm. The 20-μm difference is partly due to the non-zero fiber width as we use the position of its center of mass. Also, the lateral walls appear as thick regions of a given width and not as clear lines, introducing the extra offset. To determine the channel center we measure the distance separating the two walls and find the middle line.

6.2 Fiber in the contact phase

6.2.1 Observations

We define a "contact" regime when the fiber's angle is zero during its oscillatory flow downstream of the channel. In figure 6.8 we report the variations of the fiber's distance to the channel center with time highlighting in red the points corresponding to the fiber angle $\theta = 0^\circ \pm 1.5$. The corresponding images of the flow during one of the cycles are shown on the chronograph of figure 6.9. Only the three central positions (purple, red and orange) correspond to a contact regime, the others show a rotation of the fiber. In this regime the fiber remains close to the lateral wall with a minimal separating distance of 65 μm from the channel center.

The regime is called "contact" however it does not necessarily mean that we observe an actual contact between the fiber and the wall. It is important to note that the regime criterion is solely a fiber angle of zero. Variations of the fiber distance to the channel center during contact phases occur as illustrated in figure 6.9.

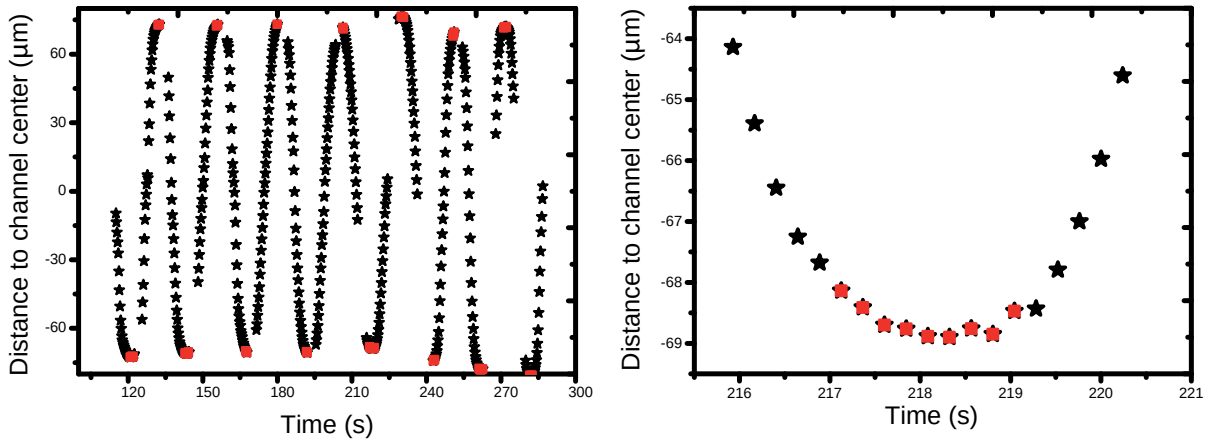

Figure 6.8: *Position of fiber's center of mass relative to the channel center in time showing in red the positions where its angle is* $0° \pm 1.5$*, in the contact phase.*

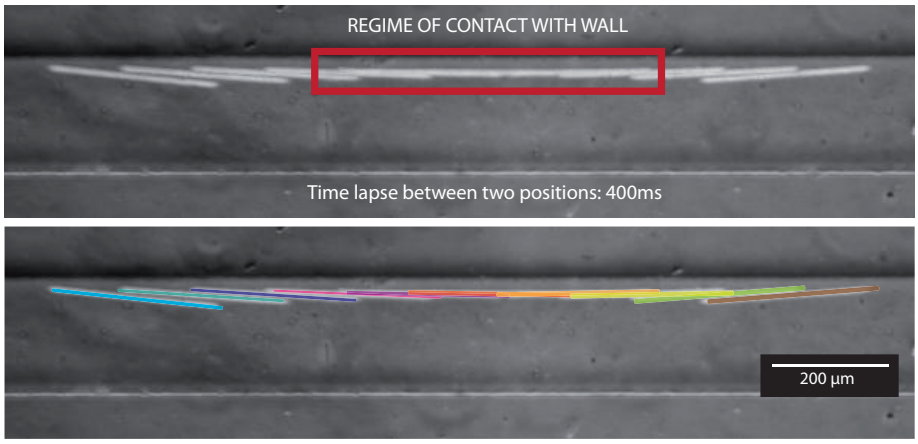

Figure 6.9: *Chronograph of fiber positions during contact phase. We color each position in the bottom picture for clarity.*

6.2.2 Regime characteristics

In the contact regime the fiber flows parallel to a lateral wall along the flow direction. We measure its velocity Vx during each occurence of the regime within an oscillation test and compare several experiments done at different mean flow velocites. Table 6.1 reports values of Vx for each experiment averaging it over all analysed contact regimes. To compare values of Vx within one experiment, the maximal and minimal Vx are also reported as well as the mean

flow velocity of each test. First, we observe that the fiber's velocity varies within the same oscillation test during contact. We also find that the fiber's velocity is lower than the mean flow velocity in all five compared experiments, as expected. The fiber flows close to the wall where the velocity is reduced, and may also be slowed down by interactions with the wall.

Mean flow velocity $\mu m/s$	Vx_{mean} $\mu m/s$	Vx_{max} $\mu m/s$	Vx_{min} $\mu m/s$	Vx_{mean}/V_{flow}
250	152	173	123	0.6
500	250	266	204	0.5
625	200	342	109	0.3
750	271	392	228	0.4
875	261	376	176	0.3

Table 6.1: *Experimental values of fiber's velocity Vx during the contact regimes, measured in five different oscillation experiments. For each of them, we average Vx among all contact regimes and report its extremal values. We compare Vx to the mean flow velocity V_{flow}: the fiber flows slower than the mean flow. Precision on measured Vx is* $\pm 3\mu m/s$.

We measure the contact times, corresponding to the duration of the contact regimes occuring in one experiment. Variations are observed within the same experiment. Figure 6.10 reports such measurements versus the flow velocity. At a given flow velocity, the vertical extension of the data illustrates the variations of times. The high value (9.1s at 750 $\mu m/s$) corresponds to the test shown previously in figure 6.5. Contact times do not seem well defined and may be linked to roughness on the walls triggering the rotation of the fiber. The maximal value of each series of experiment seems to increase with the flow velocity. There is no clear effect of the mean flow velocity on the mean contact times.

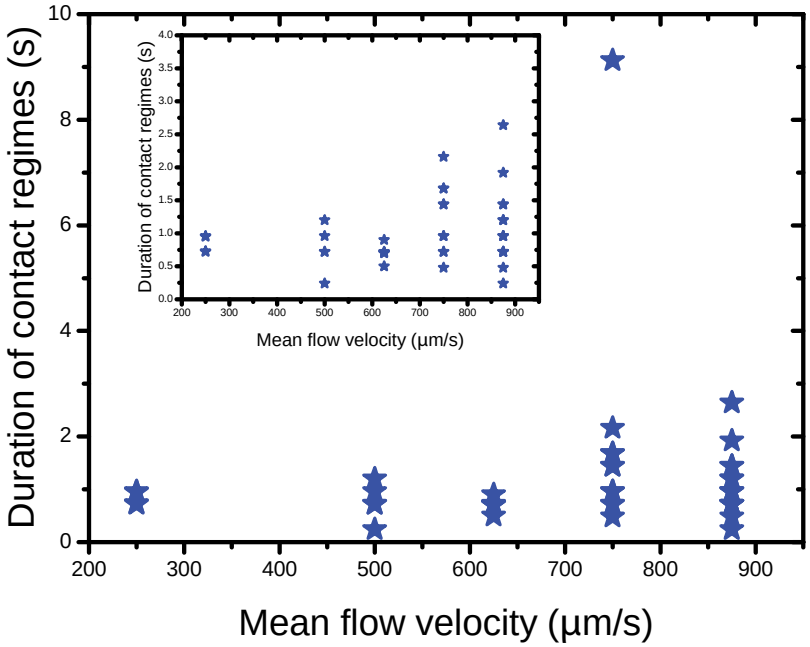

Figure 6.10: *Duration of contact regimes measured for each experiment and reported versus the mean flow velocity. Within one experiment, contact times are not constant. They do not depend on the flow velocity.*

6.3 Fiber in the rotation phase

6.3.1 Fiber angle and distance to the walls

As the fiber leaves the wall-contact phase, it enters a rotation regime where its angle is varying. Successive positions of a fiber during the rotation regime are shown in the chronograph of figure 6.11. The fiber rotates while being advected by the flow. We can also observe that it has one tip staying in close contact with the lateral wall during the motion. We measure values of the fiber angle (its sine) with its center's distance to the channel center. As recalled by the drawing in 6.11, the relationship should be linear if the fiber stays close to the wall.

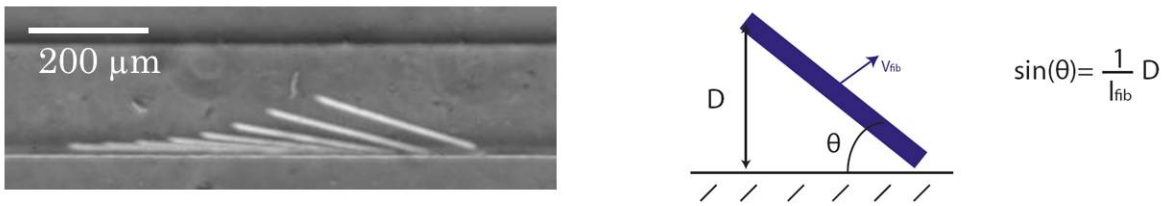

Figure 6.11: *Left: chronograph of fiber during a rotation phase. 400 ms separate successive positions. Right: drawing representing the fiber during the rotation phase in the hypothesis that its tip stays in close contact with the lateral wall during its transport downstream.*

Variations of the angle's sine with distance are shown in figure 6.12. We confirm the linear relationship, showing that one of the fiber's tip stays in close contact with the wall during the rotation phase. This behaviour could also be seen on the graph of fiber's angle with distance presented in the introduction section of this chapter (see figure 6.7). The data corresponding to all the rotation regimes of one oscillation experiment (black data points) collapse onto parallel lines either decreasing or increasing with the distance.

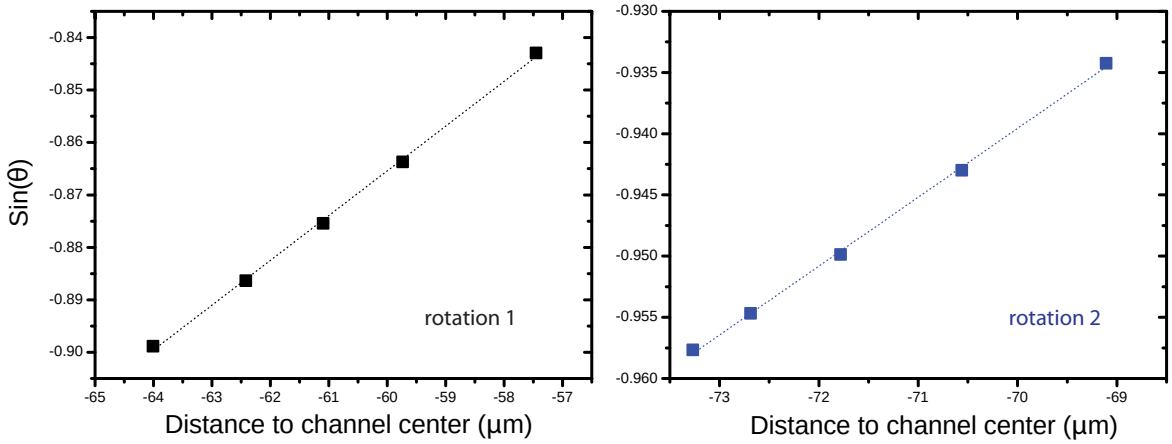

Figure 6.12: *Evolution of fiber's angle's sine with the fiber's distance to the channel center. The two graphs correspond to two different rotation regimes observed during the same oscillation experiment. The linear relationship confirms that one of the fiber's tip stays in close contact with the wall during the rotation regime, without drifting to the other wall.*

6.3.2 Angular velocity

We present in figure 6.13 the evolution of the fiber angle with time for these regions of interest. One can extract an angular velocity for each of the rotation sequence. Within an experiment however, this velocity varies. Values of velocities range from 4 to $14°/s$ during an oscillation test with large variations. The error in calculating an average velocity for a single rotation sequence varies between 0.2 and $3°/s$.

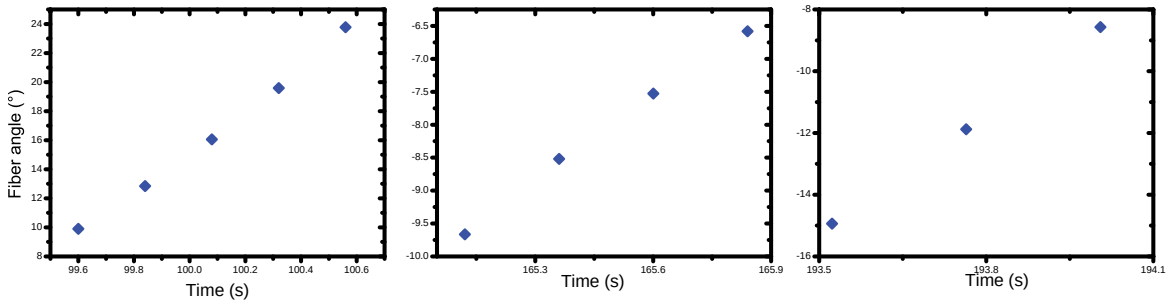

Figure 6.13: *Three rotation sequences extracted from different oscillation experiments, showing the variations of the fiber's angle with time. The relationship is linear, allowing for a computation of an angular velocity for each sequence.*

6.3.3 Influence of the flow velocity

We extract angular velocity for each rotation regime of seven oscillation experiments done at different mean flow velocity. Figure 6.14 compares their values, using the standard deviation to the average velocity as a vertical error bar. There is a small dependence of the angular velocity with the flow velocity which are both increasing from the low to the high velocities. We can understand it looking at the positions of both fiber tips. One is in close contact with the wall in the boundary layer where the fluid velocity is small. The other one experiences a higher velocity being closer to the channel center. The velocity difference should create a rotation of the fiber at a constant angular velocity if the fiber tips are experiencing constant flow velocities. The angular velocity should then depend on the mean flow velocity. More analysis is required to propose a complete model.

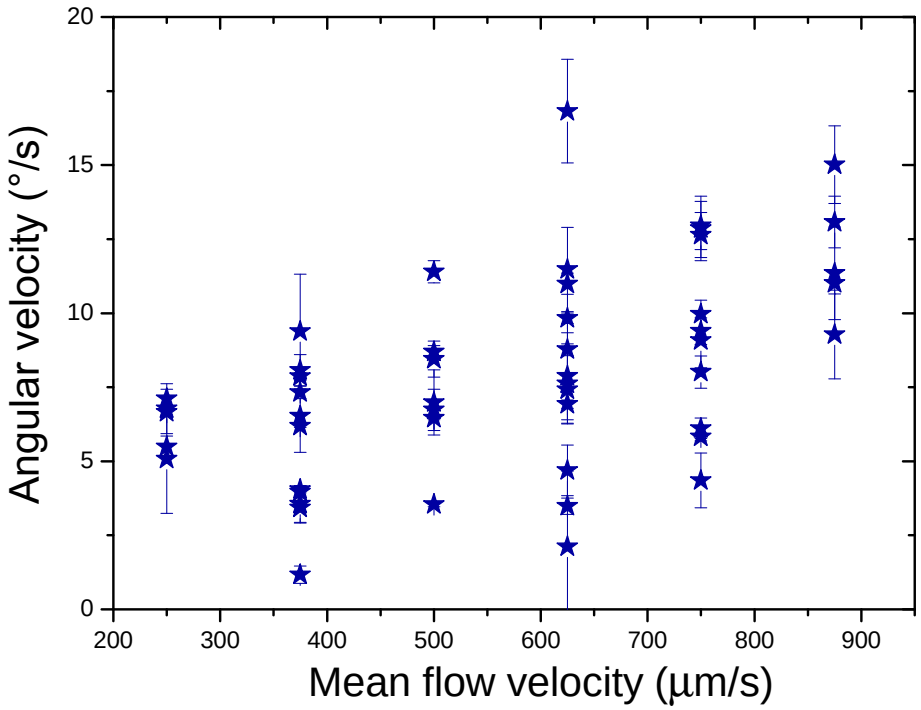

Figure 6.14: *Computed values of angular velocities in each rotation sequence for six oscillation experiments. We observe an increasing trend for the angular velocity following the increased of flow velocity.*

6.4 Fiber in the drift phase

6.4.1 Drift towards a lateral wall

The oscillating fiber leaving the "rotation regime" flows at a constant non zero angle in the "drift" phase. Most of its actual transport downstream is done during this regime at a constant

angle with the flow direction. We extract values of the fiber's angle during drift sequences for different experiments, reported in table 6.2. They vary a lot within the same experiment, ranging from 10 to 30°.

	Exp 1	Exp 2	Exp 3	Exp 4
θ_{drift}	13	-15	-14	21
	-16	-22	-28	19
	21	23	22	-12
	9	18	18	-18
		22	16	-17

Table 6.2: *Experimental values of fiber's angle during drift sequences of four different oscillation tests. Angles vary within a given experiment.*

We showed in the previous chapter that a confined fiber isolated from the lateral boundaries drifts when it is not parallel or perpendicular to the flow direction. The drift comes from the velocity difference between a parallel fiber and a perpendicular one when its confinement is larger than 0.5. A characteristic feature of this drift is that the fiber's angle is constant in the constant flow profile (plug flow regime) we have analyzed.

Channels used in the oscillation experiments have a cross-section of 200 μm by 20 μm. The fiber length is 290 μm. The flow profile in the observation plane corresponds to a plug flow with boundary layers where velocity decreases to zero. In such Hele-Shaw geometries, these shear layers extend over a distance of the channel height, the smallest dimension of the geometry. In order to see a constant flow profile, the fiber needs to remain in the central part of the channel, at least away from the lateral boundaries by 20 μm on each side (see drawing 6.15). A quick calculation shows that the fiber angle has to remain below $\arcsin(160/290) = 33.5°$ which corresponds to our experimental results. In conclusion, the drift regime of an oscillating fiber when its angle is constant and non zero corresponds to a fiber close to the channel center experiencing a plug velocity profile.

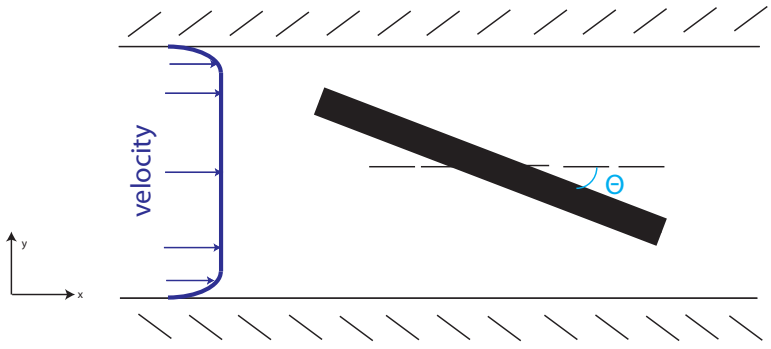

Figure 6.15: *Drawing of a fiber during the oscillatory flow downstream a microchannel. Using the fiber angle and its center distance to the boundary layers, one can compute the maximal angle possible for a drift at constant angle:* 33.5°.

6.4.2 Comparison with simulation

In the following, we call a "sequence" the successive positions of a fiber drifting at a given angle during an oscillation experiment. If the movement is perfectly periodic, we should be able to detect 2× sequences in an experiment with n oscillation periods.

We measure for each sequence a velocity in the x direction (along the channel length) and a perpendicular velocity Vy. We find a ratio Vx/Vy varying from 6 to 17. We illustrate these first results in figure 6.16 extracted from one same oscillation test, taking the absolute value of drift angles and velocities. Each data point corresponds to a drift sequence. We compute their mean value and standard deviations, the latter used to construct horizontal and vertical error bars. We find that Vx/Vy varies within a sequence. Also, it varies with the angle, between sequences. We expect it to decrease as the angle increases from 12 to 22° which corresponds to the trend here.

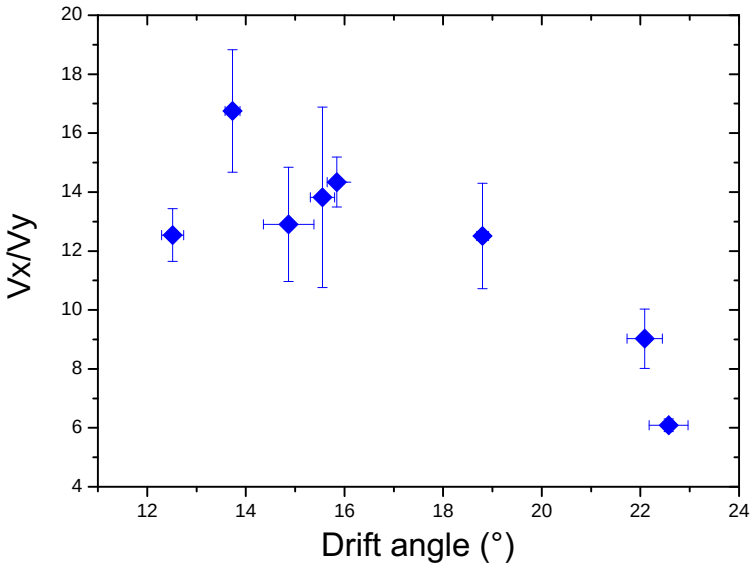

Figure 6.16: *Variations of velocity and angle during drift sequences in one oscillation experiment. Each data point corresponds to the mean value of the velocity ratio Vx/Vy, plotted versus the mean value of the drift angle. Standard deviations of both parameters are used to make horizontal and vertical error bars.*

We compute numerically the velocity ratio Vx/Vy for a fiber's confinement of 0.5 flowing away from the lateral walls at any angle between 10 and 30° (3D numerical simulations, see figure 5.14 in previous chapter). Vx/Vy is found between 80 to 200. Our numerical results were of the same order of magnitude of the numerical computations. Here, the experimental values extracted from the oscillation tests are systematically smaller than the simulation value at a given angle. In other words, the drift is enhanced by the geometry where the lateral boundaries are much closer to the fiber.

6.4.3 Influence of the mean flow velocity

We use the seven oscillation experiments to compare drift angle and velocity with the imposed flow velocity. The drift experiment of a fiber away from the lateral boundaries made at 45° with the flow direction 5.1.3.1 showed that the velocity ratio was constant for any of the fluid velocity tested. It is confirmed analytically as the fluid velocity drops out of the expression of Vx/Vy, which depends only on the angle and the fiber confinement (see eq. B.1 and eq. 5.29). In figure 6.17 we report values of angles and velocity ratio Vx/Vy with the imposed flow velocity. There is no clear effect of the imposed velocity.

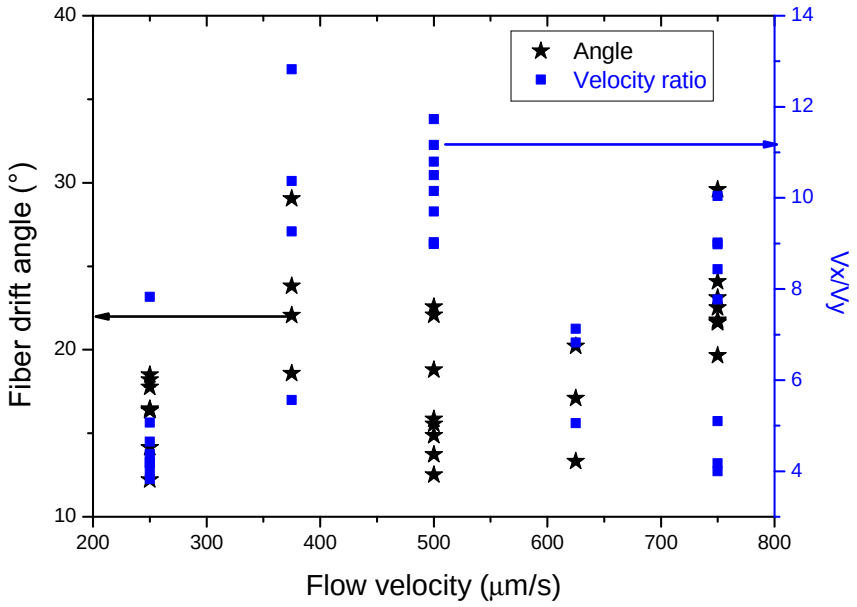

Figure 6.17: *Comparison of fiber drift angle and velocity with the imposed fluid velocity using seven oscillation experiments. As we were expecting from our analysis of the drift, no clear effect of the flow velocity can be seen.*

6.5 Summary

We summarize the characteristics of the three flow regimes in table 6.18 in terms of fiber angle, position, velocities Vx and Vy and angular velocity.

Regime	Distance to wall	Angle	Vx	Vy	Vangle
CONTACT	Constant close to 0	0	Constant	0	0
ROTATION	Increasing one tip in close contact	Varying	Constant	Constant	Constant
DRIFT	Varying	Constant	Constant	Constant	0
			Vx/Vy smaller than in drift tests		

Figure 6.18: *Table of characteristics of the three regimes for a fiber oscillating downstream a microchannel.*

6.6 Conclusion

We studied in this chapter the flow of a fiber confined in a microchannel oscillating between the lateral walls. We proposed a description of this oscillation motion as a sequence of three regimes always observed: contact, rotation and drift. The information on fiber's orientation and its temporal variations is used as a criterion of the regime.
We characterized the contact, rotation and drift phases in terms of fiber's position in the channel, velocities along the flow direction and perpendicular to it, and angular velocity. We found that only the rotation phase parameters (angular velocity) depends on the mean flow velocity. Some features of the flow were interpreted using simple flow arguments and knowledge developed in the previous chapter. In the drift phase for example, we observed a stronger drift than in the equivalent problem of a fiber away from the lateral wall flowing at the same angle and confinement.

The interaction with the walls during all three regimes is complex and is not fully understood. We have done more oscillation experiments varying both fiber and channel geometries that have not yet been analyzed. The additional results might give more insight on the interaction with the wall and dependence of the oscillation with the fiber and channel geometry. It might also be interesting to couple the experimental observations with numerical simulations of fibers in narrow channels.

We observed a number of other interesting phenomena. Figure 6.19 shows an example where the interaction of the fiber with the wall is strong enough to completely stop its advection

during the contact phase. Another interesting behaviour to investigate will be the influence of the fiber's bending modulus on the oscillation as we observed bending during the rotation phase of longer fibers, illustrated in figure 6.20.

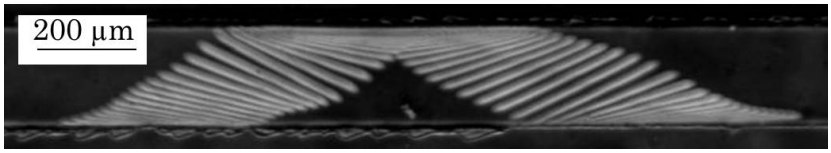

Figure 6.19: *Chronograph during an oscillation experiment showing the strong interaction acting between the fiber and the wall. The fiber does not flow when it is in contact with the wall. (Time separating two successive positions: 200 ms)*

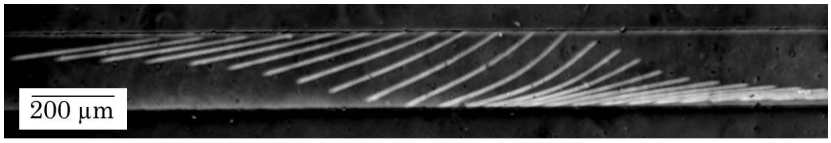

Figure 6.20: *Chronograph of fiber flow oscillating and bending during the rotation regime. Its aspect ratio is larger than the fibers considered in the chapter.*

CHAPTER 7

COLLECTIVE DYNAMICS OF FIBERS FLOWING THROUGH A RESTRICTION

We describe in this chapter the flow of suspensions of fibers in microfluidic geometries going through a flow restriction. Taking advantage of the two fiber microfabrication techniques, we study fiber suspensions in two regimes. The first one concerns dilute suspensions of fibers fabricated with the photo-polymerization method where the initial state (position, orientation) of fibers is controlled. In this regime, they are confined in a two-dimensional flow geometry. The second one corresponds to more concentrated suspensions where the fibers are randomly positionned at the initial state and flow through a three-dimensional flow geometry.

For each regime, we focus on three questions: fiber arrangements, variation of permeability, and fiber clustering. These first flow results obtained with our micromodel system are mostly qualitative. They show the potential of our method and possible future studies, in particular for the physics of fracture-bridging with fibers.

7.1 Flow dynamics of dilute fiber suspensions in confined two-dimensional geometries

In this section we investigate some flow behaviour of dilute fiber suspensions as they flow through a restriction in a microfluidic channel. We will consider three configurations of the initial state before the flow is started: fibers randomly oriented in the channel, fibers all parallel to the flow direction and fibers all perpendicular. A characteristic feature of this series of experiment is that the fibers are all positioned upstream of the restriction before the flow is started, with the whole channel filled with the same suspension.

7.1.1 Gallery of experimental flow configurations

We present in figure 7.1 a picture of the first flow configuration. The fibers are fabricated using a mask of nine fiber shapes positionned at different angles, while the flow is stopped. They

have a length of 85 $\mu m \pm 2$, a width of 9 $\mu m \pm 2$ and a height of 6 $\mu m \pm 2$ (aspect-ratio of 9). The channel has a height of 20 $\mu m \pm 1$ and a width going from 260 $\mu m \pm 2$ into 40 $\mu m \pm 2$ at the restriction. We fabricate the first group of fibers upstream of the restriction and continue with the following groups further upstream. The "first" group always refers to the fibers made the closest to the restriction.

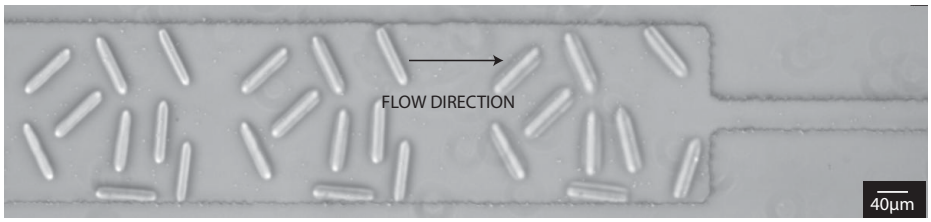

Figure 7.1: *Top view of the microchannel in the first flow configuration at the initial state. The fibers are fabricated by groups of nine, at different positions and orientations upstream of the channel. One can note that the fibers from the first group are a bit larger than the other ones. This is due to a change in the focal distance of the objective during the fabrication step, improved after the fabrication of the first group.*

Fabrication of ordered suspensions (for example, fibers all parallel with the flow direction) is more reliable and leads to higher concentrations in the channel. Therefore we chose to focus on ordered systems. The second flow configuration consists of having in the initial state all the fibers parallel to the flow direction. The mask is made of eight shapes of parallel fibers. It is carefully aligned with the channel to fabricate all fibers inside the channel, then the stage is moved manually to place the mask upstream and fabricate more fibers. A picture of this configuration is presented in figure 7.2.

Figure 7.2: *Top view of the microchannel in the second flow configuration at the initial state. The fibers are fabricated by groups of eight, all parallel to the flow direction.*

The third configuration tested consists of having all the fibers perpendicular to the flow direction, using a mask of eleven fiber shapes (figure 7.3). In both the parallel and the perpendicular configurations, the channel width changes from 300 μm to 100 μm at the restriction, at a constant height of 20 μm. The fiber dimensions are 190 μm by 12 μm with a height of 10 μm. In this chapter, all fiber and channel dimensions have a precision of 2 μm and channel height a precision of 1 μm unless stated otherwise.

7.1.2 Protocol for the three configurations

The three flow configurations differ by the initial position and orientation of the fibers upstream of the restriction, but many aspects of the flow are the same. The geometry of the channel is

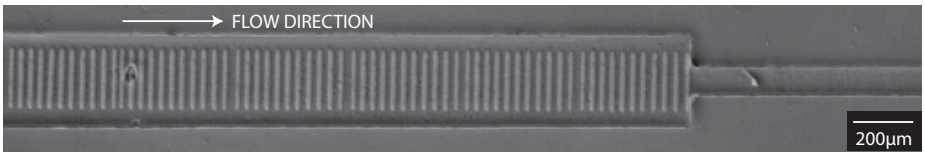

Figure 7.3: *Top view of the microchannel in the third flow configuration at the initial state. We fill the channel with fibers all perpendicular to the flow direction upstream of the restriction.*

always confined: the channel height is at least twelve times smaller than the channel width and five times smaller within the restriction. The velocity profile is parabolic along the channel height and resembles a plug flow within the width.
Fibers cannot flow on top of each other. As the inhibition layer thickness controlling their height is around 5 μm and the channel height smaller than $20\mu m$, the fibers height is larger than half of the channel height.
Hydrostatic pressure is used to control the flow via the microchannel inlet and outlet connected to fluid reservoirs. During the fabrication step, we maintain the two reservoirs at the same height to stop the flow. Once all the channel upstream of the restriction is filled with fibers, we slowly impose a constant height difference to start the flow.
We will describe mostly qualitatively the fibers flow dynamics but some quantitative analysis is reported here using the detection algorithm developed in MATLAB for the study of the isolated fiber.

7.1.3 Fibers in pseudo-random initial position

We describe in this section the flow behaviour of a dilute suspension of fibers with different initial positions. We observe strong rearrangements of the fibers as they arrive at the restriction. This dynamics is due to the elongational flow localized at the restriction as well as the flow of new fibers into those already blocked there. The fluid flowing above and below the blocked fibers as well as their close contact with neighbouring particles makes them flip frequently. We can easily detect these events by monitoring their dimensions, as their width is 1.5 times larger than their height. Figure 7.4 illustrates the fiber rearrangements and contact with a snapshot of the suspension captured over a few seconds.
Temporary bridging of the restriction can be obtained. Such event is visible on the snapshot of figure 7.4: the group of eight fibers at the restriction remains still though fibers continuously flow upstream of the bridge. As the pressure-difference is increased, fibers begin to flow through the restriction. The only experiment where we observed a permanent bridge is a limit case where the concentration of fibers is high enough to prevent any rearrangement.

7.1.4 Fibers all parallel to the restriction

7.1.4.1 Qualitative observations of the flow

We now study the case of a channel with fibers all parallel to the flow direction filling the channel upstream of the restriction.

Figure 7.4: *Pictures of successive time steps during the flow of a dilute suspension of fibers. Initially the fibers are all oriented differently. They flip and rearrange as they flow towards the restriction.*

Fibers closest to the lateral walls have a different flow dynamics than the other ones. They interact with the walls, slow down and get stuck at the restriction, reducing the channel volume available for the other fibers. In such confined geometries, only these fibers are flowing in the boundary layers along the channel walls where the velocity is reduced. Figure 7.5 shows a snapshot of two successive pictures of the parallel suspension.

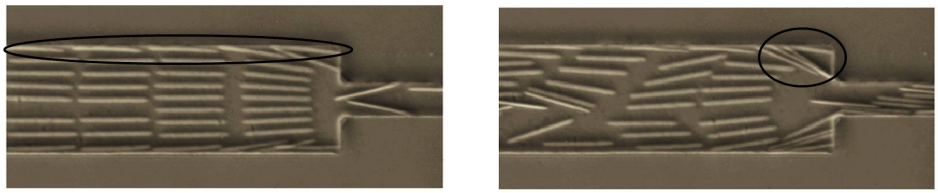

Figure 7.5: *Picture of the channel as the fibers flow parallel to the flow restriction. We show here the behaviour of the lateral fibers flowing slower than the ones in the middle of the channel and getting blocked at the restriction. The channel width is* $300\mu m$ *restricted to* $100\mu m$.

Fibers enter the restriction altogether rather than one by one with a small sliding motion between each other. At the restriction, the flow is accelerated because of the reduced channel width. However we observe a slow-down of fibers: as they enter the restriction and block the

flow path, the fluid velocity drops.

The group shape changes as the fibers flow downstream. They adopt an "inverse" parabolic profile as we show in figure 7.6. The center fiber is slower than the ones closer to the walls. This dynamics may be interpreted as a propagating effect of the restriction: there, fibers accumulating and slowing down the flow cause a perturbation propagating upstream slowing down more and more the center fiber of each group upstream. The pictures of the figure 7.6 taken at different time steps show that it is a time-dependent event. We will mention this effect again in the next section.

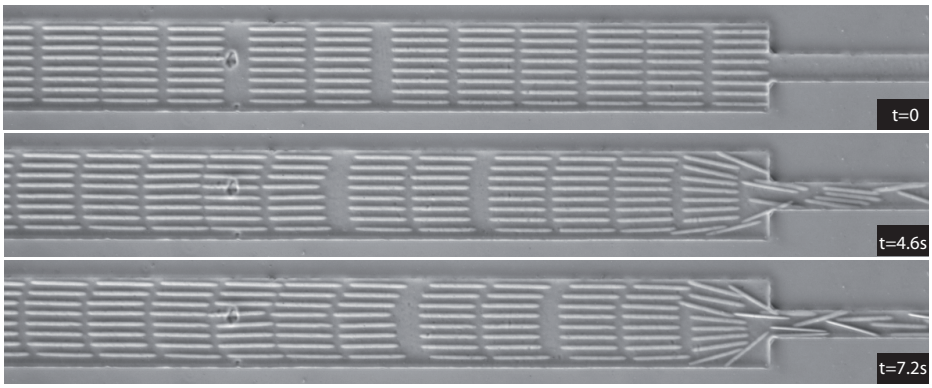

Figure 7.6: *Snapshot showing the formation of an inverse-poiseuille velocity profile upstream of the restriction. Fibers are flowing from left to right, stay organised in their initial group.*

We monitor the position of a group of fibers as they enter the restriction. Flow velocity inside the restriction is increased by a factor of 3 as given by the channel geometry. We compare the velocity of the different fibers of this first group in figure 7.7. Inside the restriction, the channel aspect ratio is 5: we still have a plug flow along the channel width which is coherent with the result that middle fibers flow at comparable velocities. The center fiber is slightly faster. Lateral ones are initially blocked on the sides of the restriction as illustrated by figure 7.7. As they flow downstream they stay in the boundary layers close to the lateral walls, where the velocity is reduced.
Later in this experiment, a bridge starts to form at the restriction from blocked and reduced flow velocity. At the time scale of our experiment, the bridge is permanent. A large enough increase of the pressure difference across the channel would be able to break it apart. A picture of this bridging state is showed in figure 7.8. Note that the channels are made of PDMS. When increasing the pressure difference across the channel to break a bridge, we can sometimes observe a local deformation of the lateral walls where one or several fibers are pushed against them. Though this was a rare event, it is important for later studies to keep in mind this possible deformation of the channel walls.

7.1.4.2 Tracing the flow through the restriction

In order to investigate more precisely the flow dynamics of these groups of fibers as they enter the restriction, we designed an experiment studying a single group and a flow tracer. The flow geometry consists of a large confined channel with a portion of smaller width. We fabricate a tracer particle upstream of the fibers with a large separating distance (more than two fiber

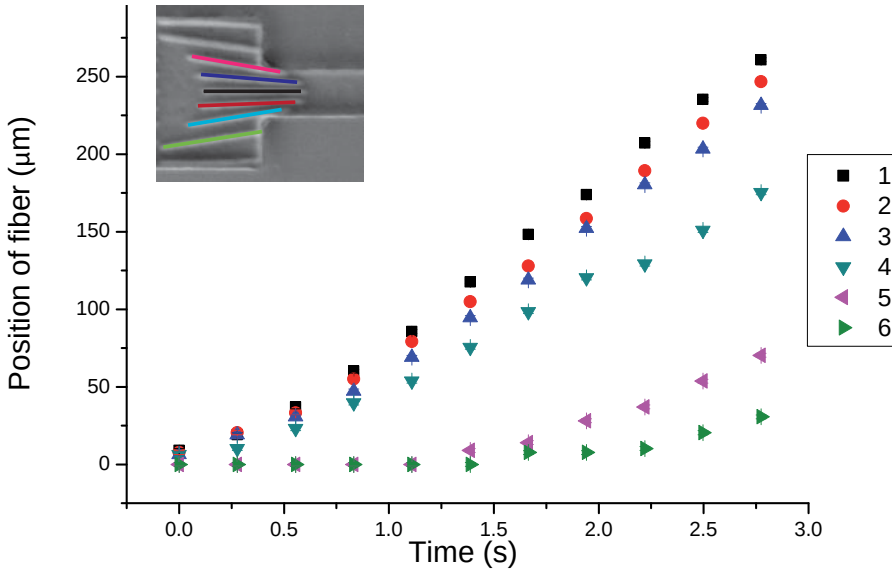

Figure 7.7: *Position of fibers of the first group as they enter and flow down the restriction. The three middle fibers flow at the same speed while the closest to the walls slow down with friction.*

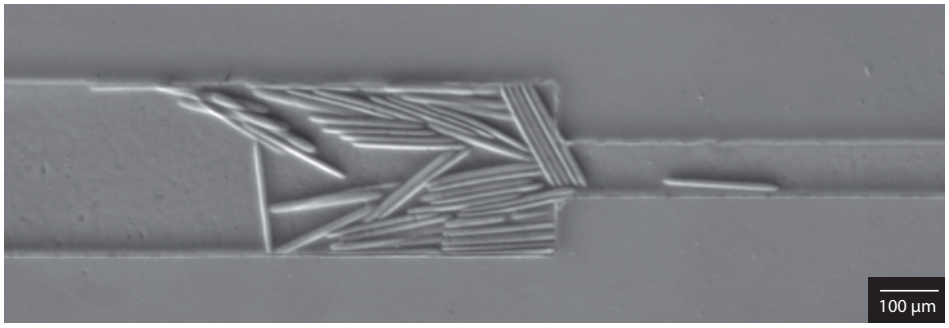

Figure 7.8: *Permanent bridging forming at the entrance of the restriction with a suspension of initially parallel fibers.*

lengths). The idea is to use our detection technique to monitor the position of the tracer particle in time and try to detect certain events such as the entrance and exit of the fibers into and from the restriction.

The initial state of the experiment is showed on picture **a** of figure 7.9. Pictures **b** and **c** show the trajectories of small tracer particles as well as our tracer disk over time. We tested three fiber lengths (180, 280 and 370μm, width and height of 11μm) for a unique channel geometry (width 400μm reduced to 150μm, height 21μm). The tracer disk has a diameter of 33μm with a height of 11μm. We also varied the imposed pressure difference at the channel inlet and outlet. First we run the test without fibers and extract the position of the tracer disk. For the three flow velocities tested (different imposed pressure differences), the tracer's velocity increases with a factor of around 4, then decreases back to its original value.

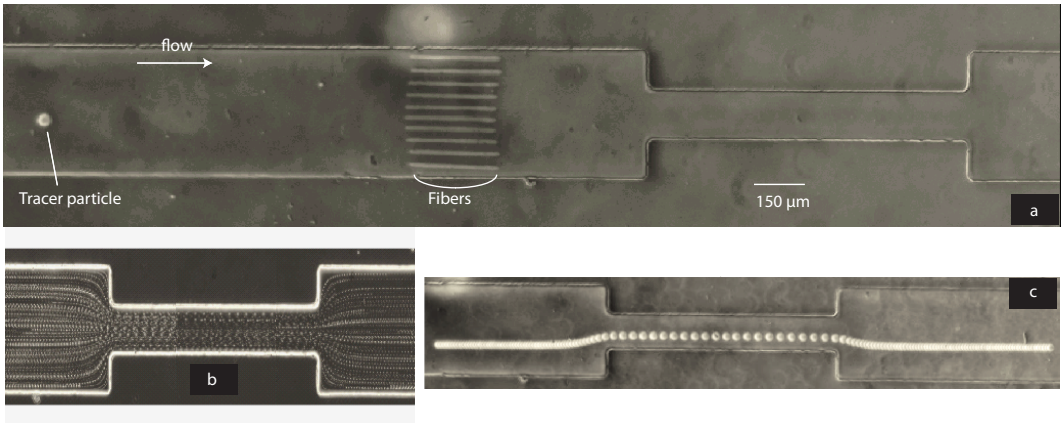

Figure 7.9: *a: initial position of fibers and tracer particle in the microchannel. b: streamlines obtained by superimposing the successive images of micron-size particles flow. c: chronophotography of the tracer showing the acceleration inside the restriction.*

As we repeat the experiment with a group of fibers upstream of the restriction, additional variations of tracer's velocity can be observed, related to the position of fibers in the channel. As they enter the restriction, the tracer's velocity is reduced by a factor close to 0.75. When they flow out of the restriction downstream, the ratio increases back to 0.95 and not 1. The increase of velocity when the tracer flows into the restriction is always less than the value obtained without fibers. Finally it is interesting to note that we systematically do not recover the original velocity of the tracer when it is flowing downstream far outside from the restriction: the ratio of velocity varies between 0.7 and 0.8. We summarize all these results in the graph 7.10.

The fibers are well aligned on the photolithography mask used for their fabrication. They are positionned regularly along the channel width at the same position along the flow direction. As the flow develops, the middle fiber is the slowest and the fibers along the wall the fastest, leading to an "inverse Poiseuille profile" as mentionned earlier when the channel was filled with fibers (see 7.1.4.1). We suggested that it was caused by the aggregation of fibers at the restriction resulting in a reduced velocity in the channel center. Here however this explanation is not satisfactory. This flow behaviour was only observed for the largest channels tested: width of 400 μm for a height of 20 μm. This high aspect ratio may cause a local bent of the channel top wall at the center, as explained in figure 7.11. We observed systematically this flow behaviour for different independent channels. Later studies will be carried out to clarify this point. For example, the channels can be fabricated with a different polymer, more rigid, to see whether the same effect is observed.

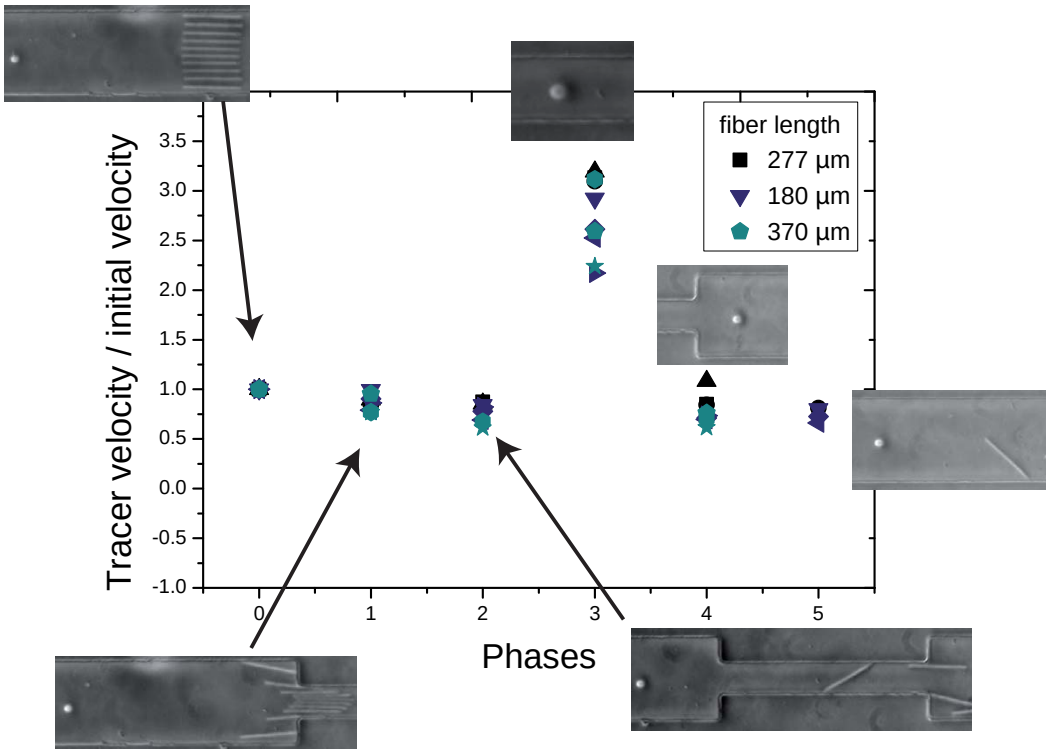

Figure 7.10: *Tracer's horizontal velocity measured for each phase of the experiment non-dimensionalized with the initial velocity. A picture of the channel (flow from left to right) illustrates each phase. Phase 0: particle and fibers are upstream of the restriction. 1: fibers are inside the restriction. 2: fibers flow downstream of the restriction. 3: the particle is inside. 4: the particle flows out. 5: particle and fibers are further downstream. No clear behavior is seen with the fiber length.*

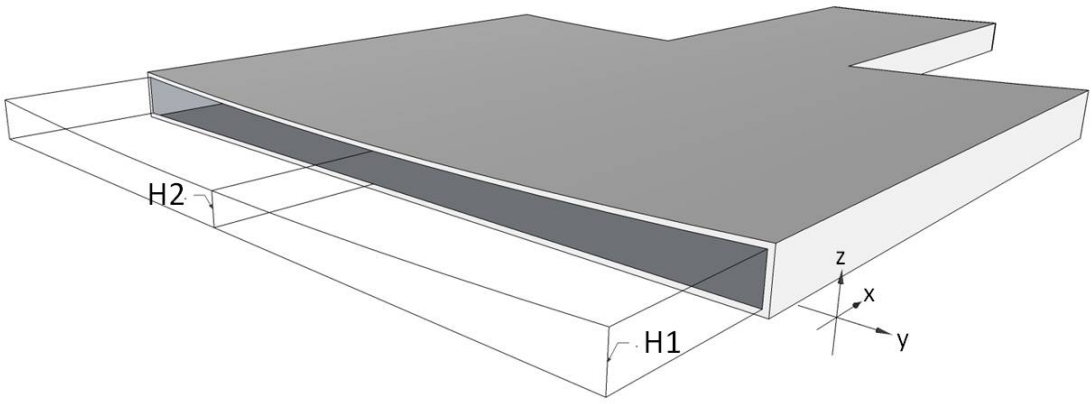

Figure 7.11: *View of the channel with the top wall bending due to the high aspect-ratio. Channel height H2 in the middle is reduced compared to the height H1 along the lateral walls.*

7.1.5 Fibers perpendicular to the restriction

7.1.5.1 Channel geometries

The flow geometries tested are rectangular cross-section microchannels of height 20 μm restricted in width: 200 to 100 μm, 300 to 100 μm, 400 to 200 μm. We designed three geometries of fibers, their dimensions are given in table 7.1.

Geometry	length (μm)	width (μm)	height (μm)
A	175	8	9
B	190	11	10
C	280	11	10

Table 7.1: *Fiber dimensions used in the third flow configuration, with a precision of ±2 μm.*

7.1.5.2 Bridging the restriction

In all experiments the fibers are longer than the restricted channel width: between 1.4 and 1.9 times longer. However we never obtained a permanent bridging event.

We observe that the perpendicular orientation of the fibers is stable. Upstream of the restriction where they would be able to rotate, they remain perpendicular. The only varying parameter is the distance between fibers which implies that they flow at different velocities.

The stability of the perpendicular orientation is illustrated in figure 7.12 with successive pictures of the channel at the restriction. From top to bottom, we observe the flow of fibers through the restriction. The red arrows divide the fiber suspensions into the original groups of fibers upon fabrication (eleven fibers on the mask). The relative position of these groups during flow show the variations of velocity: for example one fiber getting closer to the next one.

Downstream of the restriction, we can observe that the fibers are flowing preferentially towards one of the lateral boundaries. This apparent affinity with the wall is caused by their asymmetric flow past the restriction as explained in figure 7.13 . Each fiber bends with a longer portion along the "top" lateral wall where its tip experiences friction and slows down, making it rotate towards the boundary. This motion is shown with a purple arrow on figure 7.12.

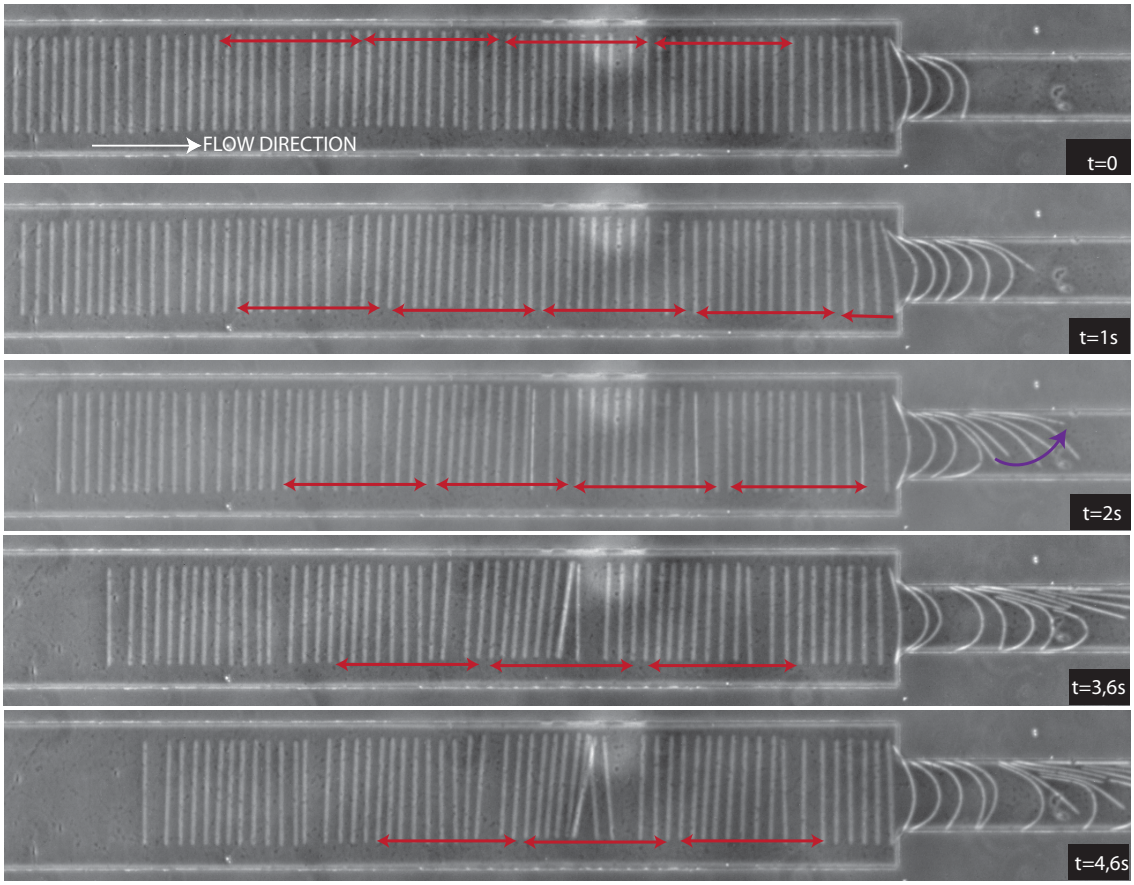

Figure 7.12: *Flow dynamics of a suspension of perpendicular fibers. Pictures from top to bottom show successive time steps of the experiment. They remain perpendicular to the flow direction until they reach the restriction and bend through. Red arrows indicate where the initial groups of fibers from the mask are: small variations of velocity can be detected as the distance separating them is not constant. As they flow through the restriction, they are not centered in the channel width but closer to the "top" lateral wall. The fiber part in close contact to the wall slows down, forcing the fiber to rotate and align along the wall. (see purple arrow).*

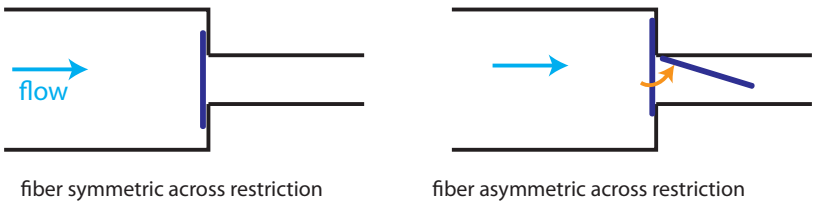

Figure 7.13: *Drawing illustrating the position of the fibers as they flow through the restriction. In the experiments presented above, the fibers are not suspended in the center of the channel but closer to the "top" lateral boundary, similar to the right drawing. This assymetry makes them rotate as they flow through the restriction and move towards this boundary.*

We observe two flow behaviours for the fibers made closest to the restriction, corresponding to their stiffness. In one case they flow onto the restriction walls, bend under the drag force and flow through (see figure 7.14). Alternatively they can accumulate at the restriction where they

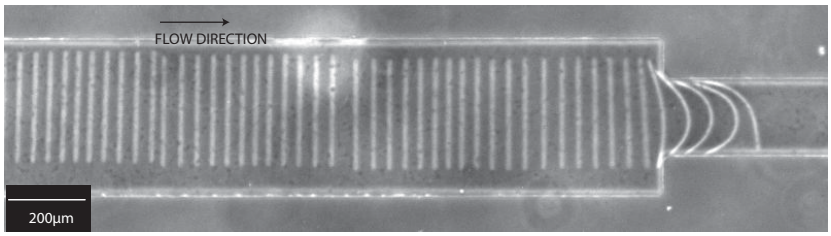

Figure 7.14: *Bending fibers as they flow perpendicular to the restriction.*

form a temporary bridge. In this case, the packed fibers move towards the top wall and rotate, enabling their flow through the restriction. The different steps of their motion can be seen on picture 7.15.

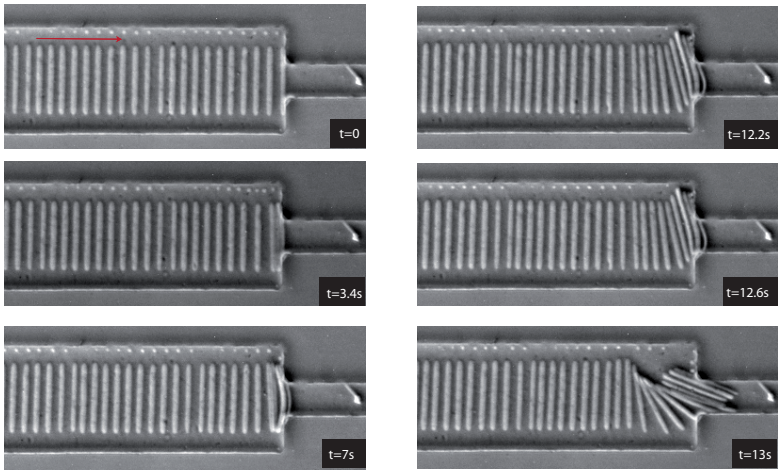

Figure 7.15: *Successive time steps showing the accumulation of fibers at the restriction.*

7.1.5.3 Cluster formation

The different snapshots in the previous illustrations showed a rather homogeneous suspension of perpendicular fibers upstream of the restriction. In most experiments, we observe a transition to a clustered state where fibers group together. Within a given group, the distance between fibers is significantly reduced from the homogeneous state as they seem to be in very close contact (given our optical resolution through the microscope). This transition occurs once fibers start to flow in the restriction and, as we interpret it, reduce the fluid velocity. When fibers accumulate at the restriction similarly to figure 7.15, clusters form systematically. At first, we observe a succession of long and short clusters. Short ones are made of 3 to 4 fibers for each geometry tested. Later, fibers flow from one group to another, resulting in clusters composed of comparable numbers of fibers. Clustering is a fast process taking place within a

few seconds. The snapshot in figure 7.16 shows an example of such transition to a clustering suspension.

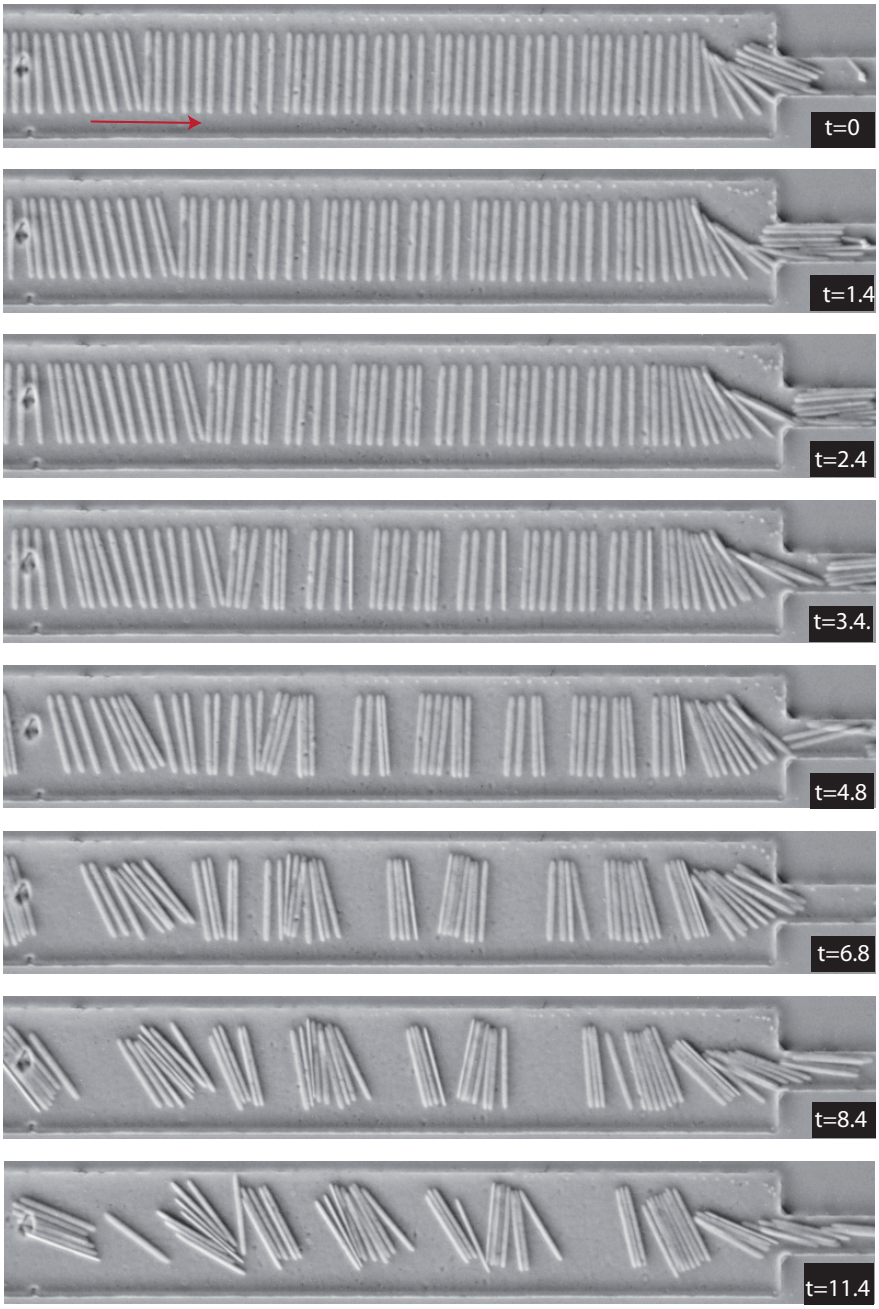

Figure 7.16: *From top to bottom pictures: spontaneous transition from homogeneous suspension of perpendicular fibers to a clustered state where fibers group together. Each picture is taken at a time step mentioned in seconds in the bottom right corner black box.*

We varied the channel and fibers dimensions to confirm these first observations. The formation of clusters always happens. However, as we vary the ratio between fiber length and restriction

width, the number of fibers in each cluster varies. Pictures of the three geometries are given in figure 7.17. We also report in table 7.2 for each geometry the number of fibers in clusters and their average dimension measured as the distance separating the first from the last one.

Geometry	Channel reduced width (μm)	Fiber length (μm)	Cluster length (μm)	Number of fibers
A	100	175	100	4 to 8
B	100	190	100	4 to 9
C	200	280	200	11 to 13

Table 7.2: *Dimensions of clusters and the number of fibers they contain for each geometry tested. Precision on measurements: 2 µm*

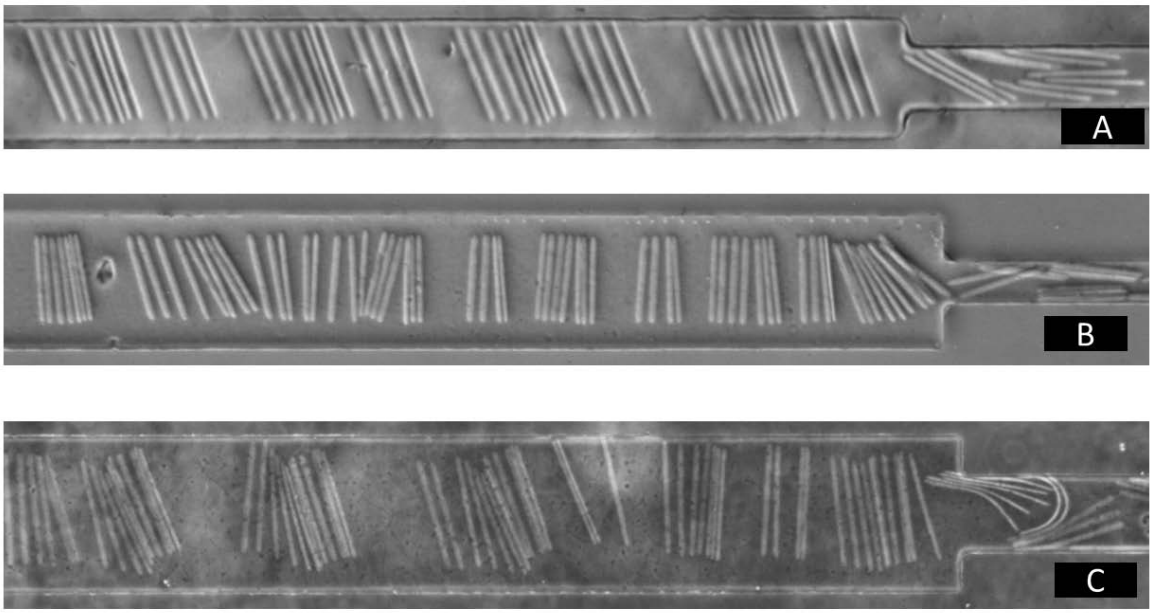

Figure 7.17: *Picture of clusters formed upstream of the restriction in each channel and fiber geometry tested.*

Finally we should note that clusters tend to move towards the apparent "top" lateral boundary similarly to the fibers inside the restriction. This behaviour seems triggered by contact started between the boundary and one fiber, likely to happen as the fibers are initially slightly closer to that boundary than to the other one.

These preliminary results have shown original collective effects of the fiber suspensions, opening several studies. When fibers are made parallel along the channel direction, their flow through the restriction lead to non trivial variations of the fluid velocity at constant imposed pressure difference. States of bridging were observed. As the fibers are made perpendicular to the flow, two configurations for their flow through the restriction can occur, based on their flexibility. As they aggregate at the restriction, a clustering effect is observed: fibers form regular packs which can not flow through without rotating and breaking at the restriction. Tests

were performed with different fiber lengths. Sizes of clusters systematically changed and may be linked with the fiber length variations.

7.2 Flow dynamics of a concentrated fiber suspension in three-dimensional flow geometries

The results presented in this section are obtained using the second method of fabrication of fibers. This method is based on the self-assembling property of super-paramagnetic particles. We implemented this technique in order to fabricate suspensions of fibers at high concentrations in microchannels that are not confined. We will show some examples of collective behaviour of fibers as they flow downstream through a restriction. First results of the image processing method we developed are also mentioned. This work was done with Yoann Maurin during his internship in the laboratory.

7.2.1 Experimental protocol

7.2.1.1 Flow geometries

All microchannels have rectangular or square cross-section of lower aspect ratio than the geometries used for the ordered suspensions presented in the previous section. Their geometry consist in a straight channel with a portion at a reduced width. The variation in width can be with inclined boundaries ("smooth") or with boundaries perpendicular to the flow direction ("abrupt") as illustrated in figure 7.18. Their length is of the order of a centimeter, typically enough to have in one field of view a portion of the channel upstream and downstream of the restriction. We use channels of different width: 200 μm reduced into 100μm, 120 μm into 60 μm, 100 μm into 50 μm and 60 μm into 30 μm. Channel heights varied from 15 μm to 30 μm.

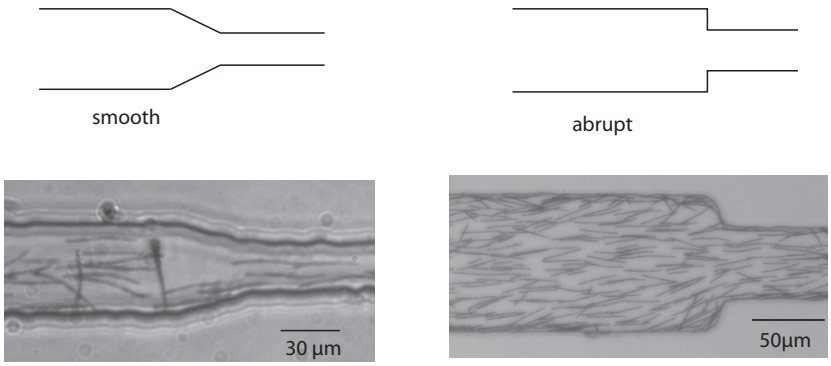

Figure 7.18: *Two channel geometries used in the flow experiment. The left drawing and picture correspond to a smooth variation of the channel width, the right ones to an abrupt change of width.*

7.2.1.2 Fiber suspensions

The suspensions of fibers are fabricated following the experimental protocal detailed previously in 3.1. Fiber length depends on the channel height. We obtained fibers with length ranging

from 10 $\mu m \pm 3$ to 28 $\mu m \pm 2$.

The concentration of fibers depends on the volume fraction of colloids in the solution introduced in the channel prior to fabrication. We used solution of volume fractions ranging from 1.5% to 3.5% in water containing surfactant and PAA. We will see that the concentrations of fabricated fibers can be high enough to observe collective effects such as fiber aggregation.

7.2.1.3 Velocity field inside the channel

The fabrication method requires to have a channel height of the order of the desired fiber length. In our experiments of flow through a restriction, we typically use fibers slightly shorter than the reduced width. Therefore the channel aspect-ratio (width/height) in the restriction is usually lower than in the confined experiments presented earlier in this chapter. The flow develops into a three-dimensional Poiseuille flow (parabolic profile along the height and width).

As we already mentioned, fibers are denser than the fluid and they tend to sediment to the bottom of the channel. As a result, they effectively experience a shear flow rather than a Poiseuille flow. They can however rotate in the three directions, in particular along the channel height.

7.2.2 Experimental observations

7.2.2.1 Orientation before flow

As the magnetic field is removed at the end of the fabrication process, fibers sediment in the channel and adopt random orientations. Figure 7.19 shows a snapshot of the sedimenting fibers starting when the magnetic field is removed.
If we prefer to flow a more ordered system, we can take advantage of the super-paramagnetic property of the filaments: using an external magnet, we can align all fibers along a given direction. We illustrate this possibility with figure 7.20.

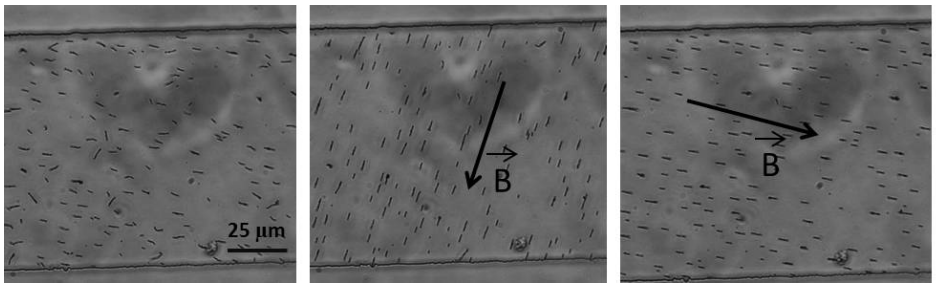

Figure 7.20: *Photographs of suspensions of short fibers as we imposed different orientations of the fibers using as an external magnet. The left picture shows the sedimented state with fibers randomly oriented. The orientation of the magnetic field is indicaded with the black arrows on the two other pictures.*

7.2.2.2 Orientation during flow

As the flow starts, fibers initially at random orientations tend to align with the flow direction. In order to illustrate this alignment, we superimpose successive frames of the flowing suspen-

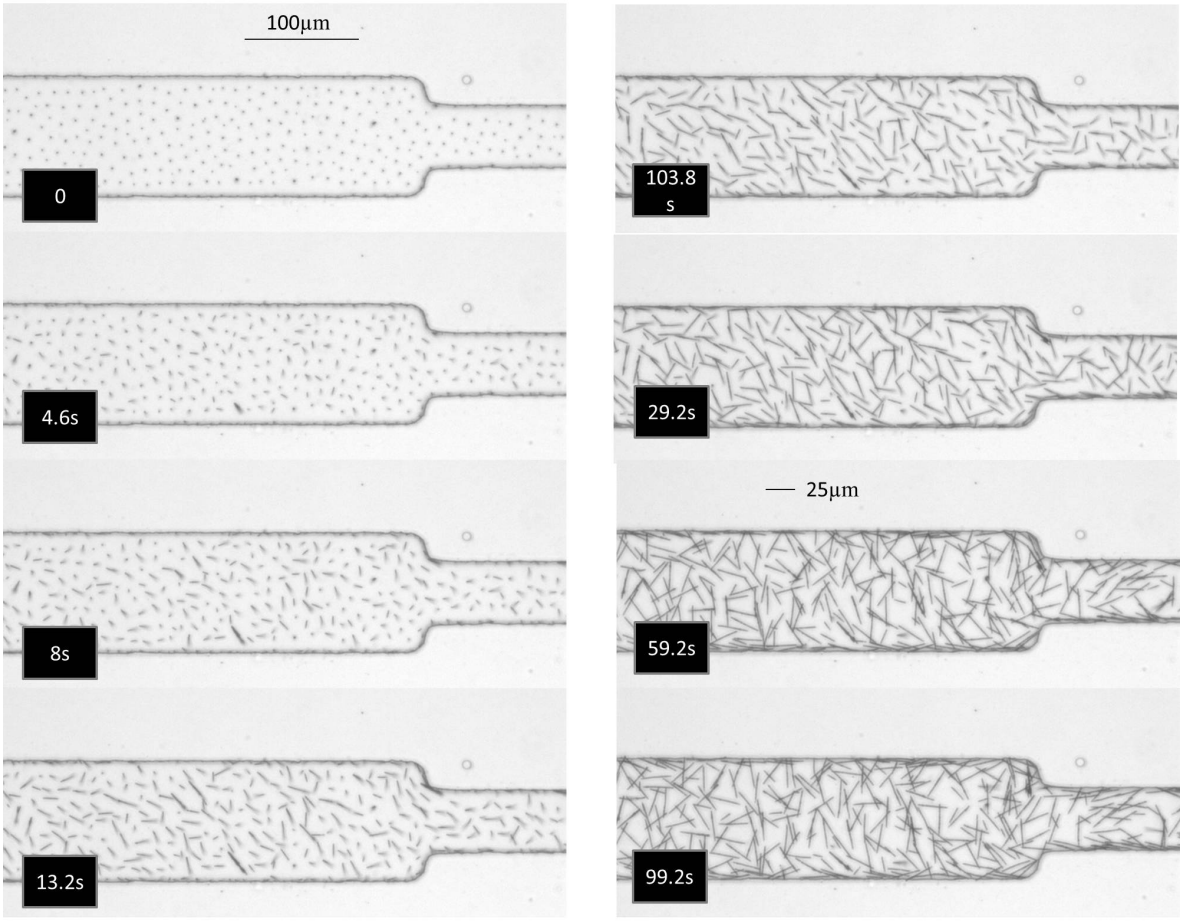

Figure 7.19: *Successive photographs of the channel from the time when the magnetic field is removed until the end of the sedimentation of fibers down in the channel. The channel width is reduced from 100 µm into 50 µm. Its height is 28 µm.*

sion. If a fiber is aligned with the flow, it will appear as a line on the stack. If it is flowing inclined with the flow direction, it will appear as successive lines on the stack. We construct such images at two times during the experiment: the first one is made as the flow is started. The second one is made with frames extracted twenty minutes later, when the flow is fully developped and stable. Both stacks are shown in figure 7.21. The alignment is clear on the bottom stack, however we can see some fibers rotating. The elongational flow at the restriction is also very clear when the flow is fully established.

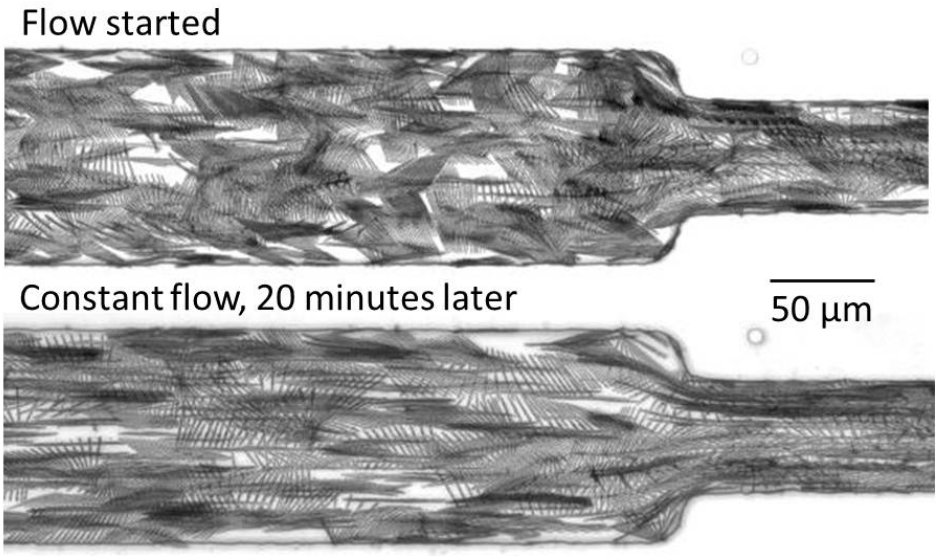

Figure 7.21: *Illustrations of rotating and aligning fibers as they flow downstream. Both pictures are constructed from the stack of 20 flow images over eight seconds. The top one corresponds to the starting time of the flow. As they are initially randomly oriented, they rotate to align: such particle traces fill the channel. The bottom stack is similarly constructed however the first frame used for the stack is chosen at twenty minutes after the flow starts. At that time, most fibers are aligned. Comparing the two pictures, it is clear that many more horizontal traces are present in the bottom picture. Note the elongational flow at the restriction forcing the fibers to align.*

The experiment is repeated in the same channel with a higher concentration of fibers. Two types of fibers do not align with the flow direction: fibers blocked along the lateral walls with a tip in contact, and aggregates of fibers. A photograph of this experiment is shown in figure 7.22.

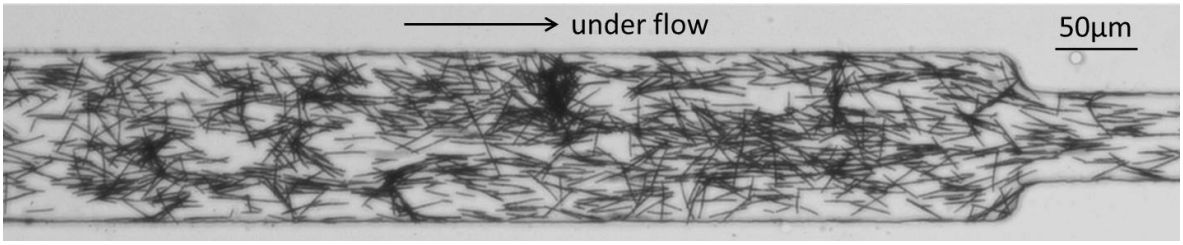

Figure 7.22: *Photograph of the same channel during a second experiment with a higher concentration of fibers. Aggregates of fibers start to form in the bulk, and some fibers are blocked with a tip in contact with the lateral wall: these fibers do not align with the flow direction. Other ones flowing freely without interacting with neighbouring particles stay aligned as previously seen in the lower concentration test.*

7.2.2.3 Velocity of fibers

In the dilute regime where most fibers flow without colliding into others, we observe small variations of velocities which are due to small variations of the fibers position within the channel

height. An illustration is given in figure 7.23 with a picture made of two captures of the flow separated by 4 seconds. Both captures are superimposed onto one image. Colors were inverted on the first frame to distinguish the first position (bright) to the second position (dark) of fibers. We indicate with arrows the displacement found between successive images. Different colors correspond to different velocities. Their values range in this example from 3.4 to 7 $\mu m/s \pm 0.8$.

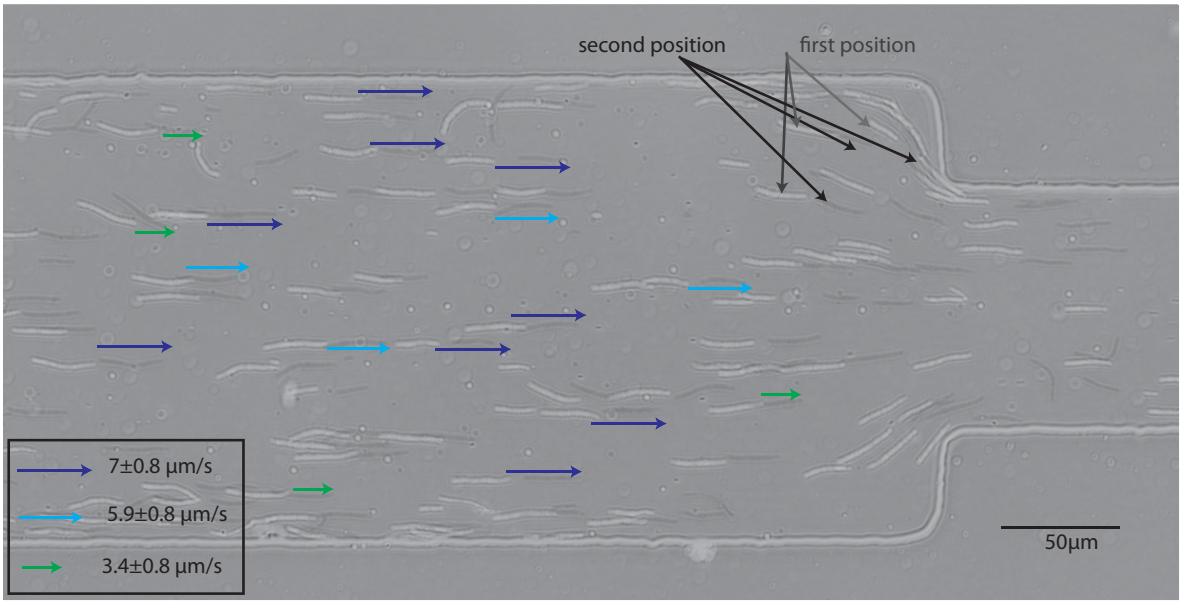

Figure 7.23: *Small variations of fiber velocity in the dilute regime. The variations are due to different vertical positions of particles within the Poiseuille velocity profile.*

At higher concentration of fibers, variations of velocity increase. Three layers seem to be distinct: at the bottom of the channel, some fibers do not flow at all due to adhesion with the bottom slide. Above this layer, fibers flow with an homogeneous velocity field. Finally we observe some isolated fibers positioned further above, towards the center of the channel, flowing faster. The ratio of velocity between the two layers was found to be 10 for three distinct experiments. Figure 7.24 illustrates these two flow regimes with an image constructed from the superposition of three successive frames. The fast fibers are aligned with the flow direction and their traces form a continuous line. Other fibers flowing slowly are not necessarily aligned, one can see their successive traces easily. Note that we observe rotations of some fibers as indicated with the circle. The tip of this rotating fiber is not sharp in the image: it is outside of the depth of field.

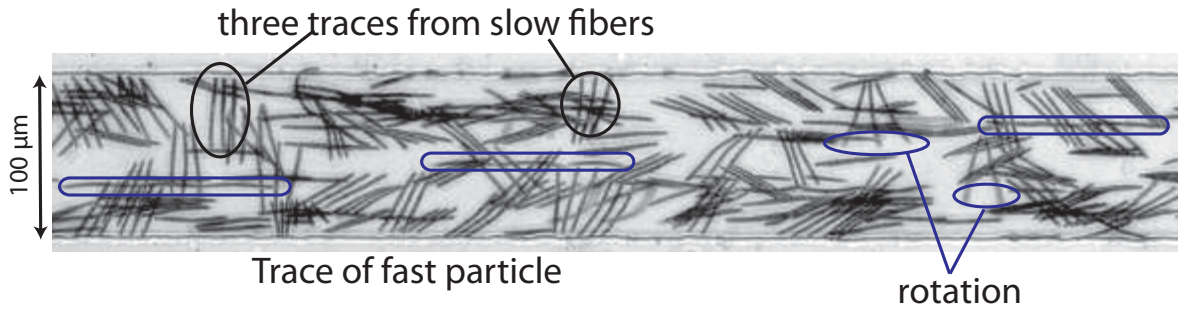

Figure 7.24: *Stack of three successive images extracted from the flow of a concentrated suspension. The traces made of three successive lines correspond to slow fibers. The continuous lines correspond to isolated fibers flowing approximately ten times faster, higher within the channel height. Some isolated lines are visible: they correspond to fibers blocked at the bottom of the channel for which all three frames were identical.*

7.2.2.4 Formation and deformation of aggregates

As the flow starts, the distribution of fibers in the channel is homogeneous (see figure 7.19). When the concentration of fibers is high enough to provoke many collisions between flowing fibers, aggregates of fibers start to form. Contrary to fiber clusters observed in sedimentation, these aggregates are still in the channel and grow in size from fibers flowing into them. We believe that their formation is triggered by slower fibers or fibers adhering on the bottom boundary. In the three examples shown in figure 7.25, a frame before the cluster forms is shown along with a picture of the cluster.

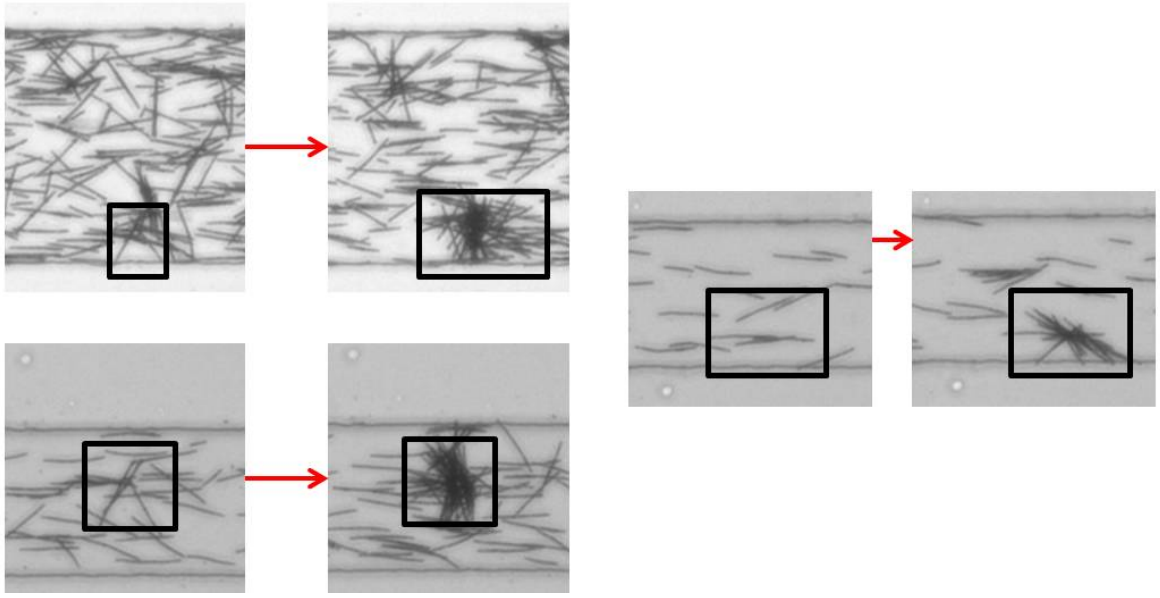

Figure 7.25: *Three cases of fiber clustering. The first picture is taken before the formation of the cluster. One can note the orientations of the fibers in the cluster, mostly perpendicular to the flow direction. Channel width is 100 µm.*

These flocs of fibers are not persistent in the flow. In most observed cases, as one or several fibers flow into a cluster, the strength of the mechanical contacts between fibers is not large enough to overcome the force from the incoming fibers. We observe that many fibers entangled in that cluster leave together, interfiber contacts breaking immediately. A small cluster usually remains, probably due to the fact that one or a few fibers were blocked there prior to the clustering. We illustrate such deformation of clusters in figure 7.26.

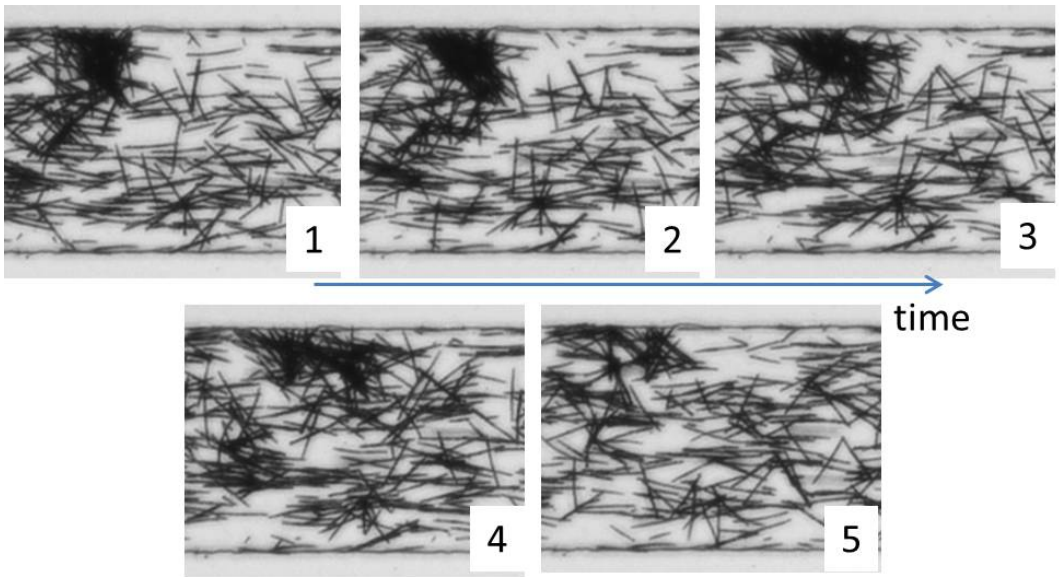

Figure 7.26: *Deformation of a fiber cluster caused by incoming fibers. Channel width is 100 µm.*

At even higher concentrations, we observed the formation of a fiber network flowing downstream at a constant velocity. Some isolated fibers remain in the channel and flow faster than the network, which extends across the channel width. Successive pictures illustrate this behavior in figure 7.27.

7.2.2.5 When very long fibers arrive

The solution of colloids in water and PAA fills the channel entirely as we start making the fibers. Colloids are present in particular inside the tubings connecting the inlet and outlet of the channels. In order to control the imposed pressure difference across the channel, we maintain these tubings vertical. When the vertical magnetic field is applied, the colloids self-assemble also inside the tubings, forming very long filaments. At the end of an experiment when all the fibers fabricated in the channel have flown through the restriction, we start observing the flow dynamics of these very long filaments.

As showed in picture 7.28, the filaments are very flexible and fill the channel in multiple folds. They always flow through the restriction without bridging or plugging permanently thanks to their flexibility. Though it goes beyond our initial goal, it is interesting to see the potential studies of flow such elongated bodies in microfluidic geometries.

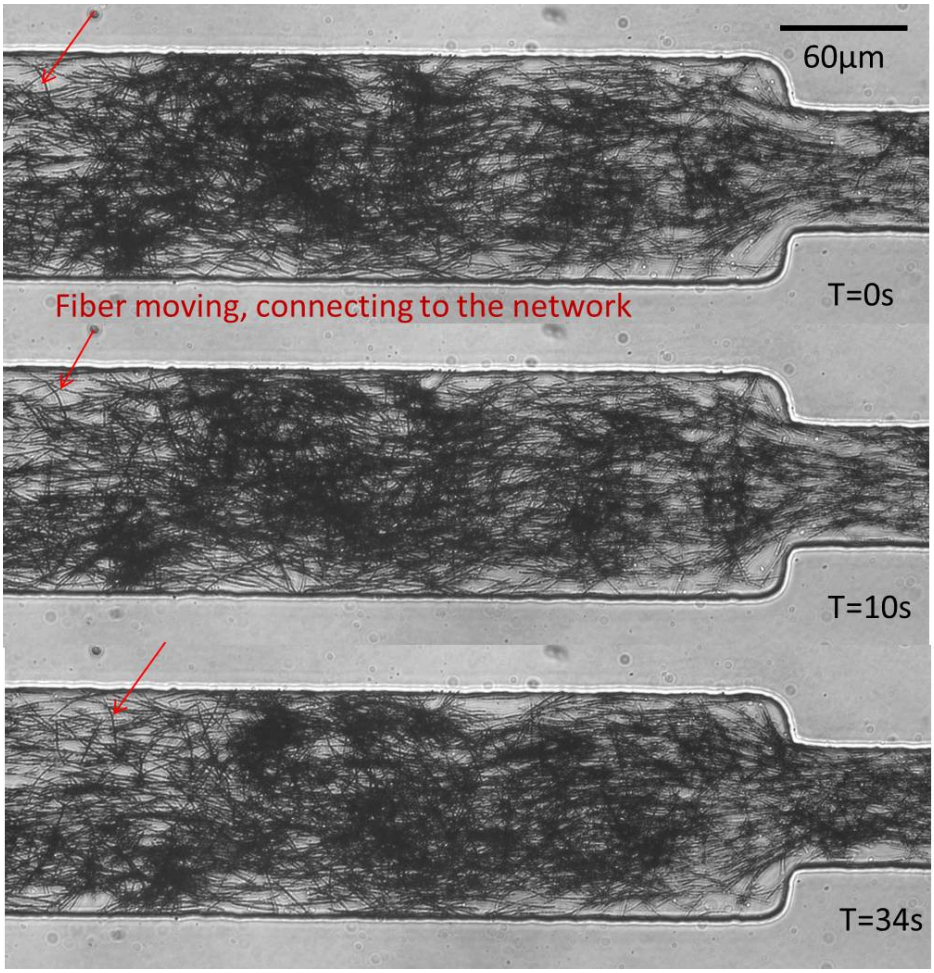

Figure 7.27: *Formation of a network of fibers, all flowing at the same velocity, extending over the channel width. Fiber density fluctuations can be seen between the three pictures, however all fibers have flown by the same distance.*

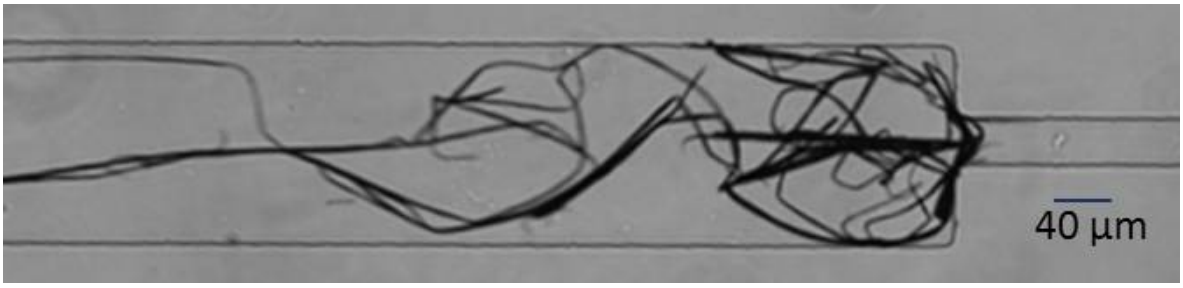

Figure 7.28: *Photograph of a long fiber fabricated in the vertical tube connecting the inlet of the channel to the flow reservoir.*

7.2.2.6 Bridging or no bridging?

We observed rare bridging events in our flow experiments. The magnetic fibers are so flexible that they deform and flow through the restrictions. However, fibers are often capable to temporarily bridge the restriction, taking advantage of the boundaries roughness. Figure 7.29 shows fibers bridging the flow at the restriction and downstream the smaller channel.

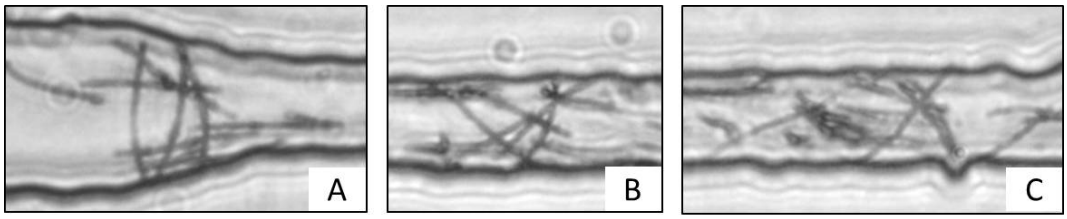

Figure 7.29: *Isolated fibers bridging the channel at the restriction or downstream. Channel width is 20 μm in the restricted portion.*

To illustrate the ability of aggregates of fibers to deform at the restriction without bridging, we show in figure 7.30 the passage of several clusters.

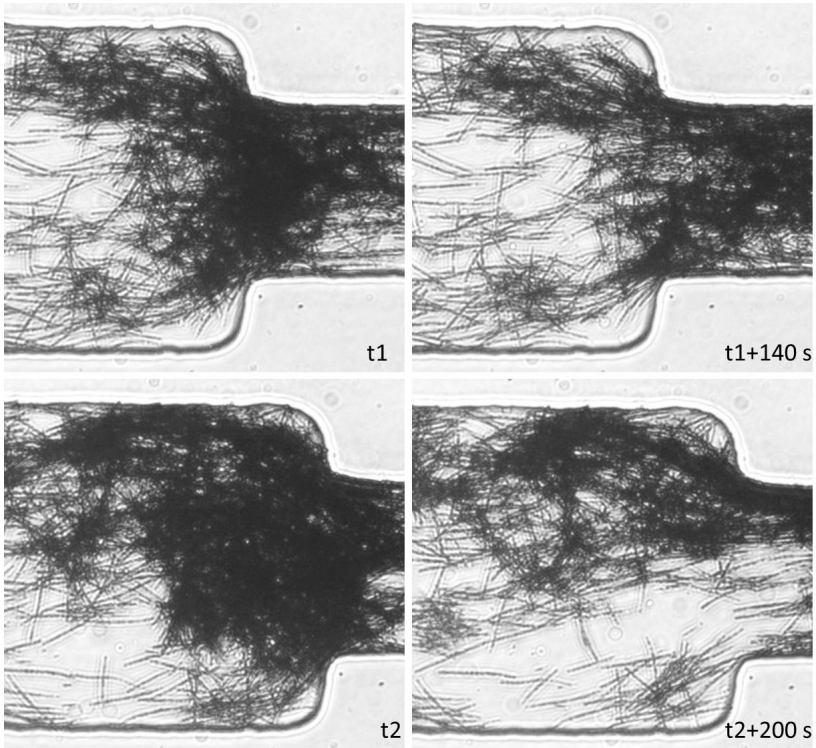

Figure 7.30: *Deformation of a fiber network going through the flow restriction. Channel width is the restriction is 100 μm.*

7.2.3 Image processing

We developed some image processing methods to extract quantitative results from the flow experiments. As we increase the fiber concentration, it becomes difficult to identify and track single fibers. Fibers flow on top of each other with different orientations and form a network of connected traces. The objectives of the tracking methods is mainly focused on fiber flocs: data of their size and position within the channel in time would be ideal to follow their formation and deformation, and detect potential bridging events at the restriction.

The processing technique is described in Appendix C along with some preliminary results of flocs detection.

7.3 Summary

We summarize in table 7.3 the first results of fiber suspensions flows in 2D and 3D geometries.

	Fibers with photo-polymerization method	**Fibers with colloids self-assembly method**
Flow geometry	confined, 2D	3D
Fiber density	Isodensity	Denser than the fluid Fibers sediment in the channel
Concentration	adjustable	adjustable
Initial orientation	adjustable	adjustable
Collective effects	clustering of perpendicular fibers	-clustering at specific locations, not flowing -Formation of fiber network at very high concentrations
Floc persistence	no	no
Bridging **Permanent**	yes yes with parallel fibers	yes no, fibers are too flexible

Table 7.3: *Summary of flow characteristics obtained in our two model systems.*

7.4 Conclusion

We presented our first results of flow of fiber suspensions through microfluidic constrictions. The two fiber-fabrication methods allow us to study two complementary experimental systems. In the first one, ordered suspensions are flowing in two-dimensional confined geometries. Bridging of the restriction if observed when the fibers are parallel to the flow direction. Perpendicular fibers exhibit interesting collective effects that we interpret as a consequence of temporary bridging at the restriction. In the second model system, we were able to fabricate high-concentration suspensions of flexible fibers flowing in 3D geometries. We observed strong alignment of the fibers especially at the restriction where the extensional flow is a limiting factor of bridging. As the fiber concentration is increased, we first observe clustering of the fibers into aggregates. Incoming fibers were however always able to break them back into individual fibers. At even higher concentration, fibers organize into networks extending over the

whole channel width, moving at a constant velocity. Permanent bridging or clogging was never obtained as the fibers can easily deform and flow through the restriction. These preliminary results show the potential of our experimental systems which can be used to study further the mechanisms of fracture bridging.

CHAPTER 8

CONCLUSION

In this thesis, we studied the transport dynamics of single fibers and suspensions of fibers in microfluidic geometries. This collaboration work between Schlumberger and ESPCI-PMMH is motivated by the use of fibers in lost-circulation curing fluids in the oil industry. In this context where fibers are closely interacting with the flow boundaries, the roles of the geometry, flexibility and concentration of fibers as well as the flow geometry need to be understood. We created a microfluidic model system, integrating in a single experiment the fabrication and the flow of tailor-made fibers and suspensions of fibers. Flows are laminar, in well-controlled and adjustable geometries using today's soft-lithography techniques. In this way, we provide with a new experimental system to independently investigate the effect of all flow parameters.

We implemented two techniques to fabricate fibers directly inside microfluidic channels. The first one, based on a photo-polymerization fabrication, allowed us to produce single fibers and fiber suspensions in confined geometries: the channels are Hele-Shaw cells where a two-dimensional flow develops, and the fibers can be confined between the top and lateral boundaries. We can produce fibers of any aspect-ratio and any orientation in the flow. Their flexibility, surface roughness and concentration in suspensions could also be adjusted independently. Fibers were fabricated anywhere in the channel, during a slow-continuous flow or before the flow was started. Then, direct observation of the channel provided with data on fiber transport dynamics.
The second fabrication method is based on the magnetic colloids self-assembly technique developed at PMMH. The dipolar interactions between two super-paramagnetic colloids in the presence of a magnetic field are used to make them assemble in long chains of custom length, forming flexible fibers. We obtained suspensions of fibers that are complementary to the ones made by photo-polymerization. Their concentration in solution can be higher, the flow geometries are now three-dimensional, allowing them to rotate within the channel height.

We developed an *in situ* measurement of the fiber's Young's modulus inspired by the bending-beam experiment. In this way, the mechanical properties of the fibers produced with the polymerization method were characterized in the same flow environment of the micromodel exper-

iment.

We experimentally and numerically investigated the free transport of an isolated fiber in a Hele-Shaw geometry flowing far from the lateral walls. The flow dynamics was found to strongly depend on the confinement of the fiber between the top and bottom walls of the channel. A first regime was defined for confinements smaller than 50%. We found that in this regime, the fiber flows faster than the mean flow velocity, independently of its orientation with the direction of the flow. Its velocity decreases slowly with the confinement: the ratio of the fiber's velocity with the mean flow velocity is 1.5 for a confinement of 10%, decreasing to a value of 1.3 for a confinement of 40%. The orientation of the fiber is constant throughout the flow, far from the lateral walls. The perturbation caused by the fiber on the flow was found to scale with the channel height.
As the confinement between the walls increases over 50%, the fiber's velocity decreases much faster and exhibits an increasing difference between a parallel orientation and a perpendicular one. We found that a parallel fiber flows slower than a perpendicular one. As a consequence, a fiber inclined at an angle different from 0° or 90° drifts towards the lateral wall in the opposite fashion of a sedimenting fiber. The perturbation on the flow increases and depends on the fiber's orientation as well. For a parallel fiber confined at 80 %, it extends over more than one and a half times the channel height. For a perpendicular fiber, it increases to more than half the fiber's length.

When the channel width is reduced to the fiber length, the fiber is confined between the lateral walls. Interactions start to occur, leading to a reproducible oscillatory motion of the fiber from one wall to the other. These oscillations were characterized by fluctuations of the fiber's angle and velocity, leading to a decomposition of the motion in three flow regimes: a contact regime where the fiber is parallel to the walls, a rotation regime where the fiber rotates at constant angular velocity, still in close contact with the wall, and a drift regime where it flows at constant orientation and constant velocities in the center of the channel. We found that the presence of the walls increases the drift velocity compared to the transport of a fiber far from boundaries.

We presented our first results on pressure-driven flows of suspensions of fibers through microfluidic restrictions. The photo-polymerization fabrication method was used to produce ordered suspensions, with fibers either all parallel or perpendicular to the flow direction. In this latter case, reproducible collective effects of fiber clustering were observed. The second fabrication method was used to produce suspensions of fibers at high concentration in 3D geometries. We observed the formation of local flocs which could increase to several fiber-lengths sizes but were not persistent in the flow. At higher concentrations, a network of interconnected fibers was formed, extending over the channel width. Even though the fibers were too flexible to efficiently clog the restrictions, these preliminary results of flocs and temporary bridging show the potential of our model system to study the clogging at restrictions.

In order to extract quantitative results from all these flow experiments, we developed data processing methods. The first technique implements the detection and tracking of isolated fibers in a single MATLAB interface, allowing us to extract in one reference system the position of the fiber, its geometrical features and orientation for all frame of an experiment. It has proven crucial for the investigation of the fiber oscillations between lateral walls where the local fluctuations of these parameters need to be extracted to study the different phases of the motion.

We also proposed a method to quantitatively study the formation and deformation of flocs observed in high-concentration suspensions, and presented preliminary results.

This study led to two publications now under preparation. The first one reviews our technical work on the implementation of the *in situ* fiber fabrication techniques in microfluidic channels, written with O. du Roure. The second one reviews the experimental and numerical results on the free transport of isolated fibers in confined flows, and is written with M. Fermigier.

This work opens many perspective studies. The interaction between a fiber and the flow boundaries needs to be further characterized, exploring for example the effect of fiber elasticity. Our first experiments with more flexible fibers showed promising results to explore the oscillation motion further.
Our model system should now be used to perform systematic studies on the flow of fiber suspensions through the independent variation of the fiber concentration, the flow geometry and its interactions with the fibers. For example, we showed that artificial controlled roughness could be added to the design of the flow boundaries and of the fiber as a way to enhance non-hydrodynamic interactions, linking the study to the more complex environment of rock fractures.
A collaboration has started with E. Climent (IMFT, France) following the numerical study of C.Agbangla on the flow of suspensions of particles through microfluidic restrictions, during his Ph.D (2011). Adapting the study to suspensions of fibers will provide us with a valuable comparison of our experimental results to understand the flow phenomena of fibers at restrictions.
Contacts have also been made with P.Doyle (MIT) through the numerical work of W.E.Uspal on the single fiber's oscillations in confined flows.

APPENDIX A

MICROFLUIDIC DEVICE FABRICATION

A.1 Preparation of channel mold

We use standard soft-lithography methods to prepare the negative mold of the microchannel. The fabrication steps are described in figure A.1. Lithography masks are designed on AUTOCAD 2009 and printed at high resolution (25400 or 50800 dpi) at SELBA S.A (Switzerland). The fabrication then takes place in the clean room of ESPCI. Negative photoresist (SU8 20XX series, MICROCHEM) is spincoated onto a silicon wafer initially cleaned with acetone, isopropanol and ethanol and placed on a hot place (200°C for 10 minutes). Following the spincoating step, the wafer is soft baked on a hot place successively at 65°C and 95°C (baking times given by Microchem) to start curing the thin layer of resin. The wafer is placed in the mask aligner where it will be exposed to a filtered UV-light (365nm) through the lithography mask. It remains to finish the curing of the resin (referred to as the post-exposure bake) on the two hot plates and do the development step: a solution of developper dissolves the resin that was not exposed to UV light, leaving as a positive relief the channels design. The channel height is characterized using a mechanical profilometer (Dektak) providing a measurement of the channel dimension with a precision smaller than 1 μm.

A.2 All-PDMS channels

Fabricating fibers using the lithography method (see chapter 2) requires an all-polydimethylsiloxane channel (PDMS, Sylgard 184) in our experiments to ensure that the fibers don't stick on the walls and can flow downstream. The negative mold of the channel prepared in the clean room is poured with PDMS with an excess of crosslinker (20 wt% of crosslinker) and half cured for 40 minutes at 70°C. In parallel, a microscope glass slide is spincoated with PDMS with a deficit of crosslinker (5 wt%, spincoated 20 s at 500 rpm and 40 s at 3000 rpm) and also partially cured for 40 minutes at 70°C. Individual channels are cut and peeled off the wafer, inlet and outlet holes punched. We place each channel on top of the PDMS-coated glass slide. The final device is left in the oven (70°C) for one day to fully cure.

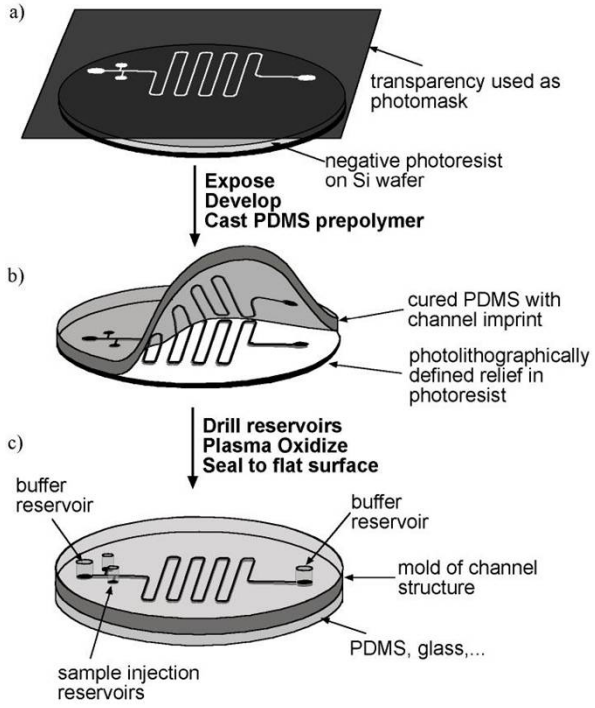

Figure A.1: *Schematic drawing of the three main steps of microchannel fabrication. a: fabrication of the negative channel mold on a silicon wafer. b: making the PDMS channel c: sealing the PDMS channel onto a flat surface. Source: Bdml.stanford.edu*

A.3 PDMS-glass channels

The second fabrication technique with superparamagnetic particles doesn't require all the channel walls to be in PDMS. These flow devices were prepared by pouring PDMS (10 wt% of crosslinker) over the silicon wafer and curing it for one hour at $70°C$. The cured PDMS is peeled off the wafer; individual channels are cut and prepared. We plasma-bond them to microscope glass slides to close them. Finally we place them in the oven for one day at $95°C$ so that they recover their hydrophobicity.

APPENDIX B

SIMULATIONS OF A SINGLE FIBER FLOW

B.1 Two-dimensional simulations in FreeFem++

B.1.1 Fiber parallel to the flow direction

The simulations are done in two steps. The first one consists in solving the Stokes flow equations in its variational form 5.14 assuming a fiber velocity for a given geometry and computing the drag force exerted on the fiber. This computation is iterated until we find the fiber velocity with which we obtain a zero drag force: this corresponds to a fiber advected by the flow. The second step consists in solving the same flow equation now imposing the right velocity condition on the fiber boundaries. We write in the following subsections the corresponding FreeFem codes.

B.1.1.1 Fiber velocity determination

```
// frontieres du domaine
real largeur,hauteur,hfib,vfib,lfib;
cout << " Entrer la largeur du canal  :"; cin >> largeur;
cout << " Entrer la hauteur du canal  :"; cin >> hauteur;
cout << " Entrer l epaisseur de la fibre  :"; cin >> hfib;
cout << " Entrer la largeur de la fibre  :"; cin >> lfib;
//cout << " Entrer la vitesse de la fibre  :"; cin >> vfib;
int C0=98;
int C1=99;
// limites du canal decrites dans le sens trigo
border a(t=0,largeur) {x=t;y=0;label=C0;};
border b(t=0,hauteur) {x=largeur;y=t;label=C0;};
border c(t=0,largeur) {x=largeur-t;y=hauteur;label=C0;};
border d(t=0,hauteur) {x=0;y=hauteur-t;label=C0;};
real xfib,yfib ;
```

```
xfib=0.5*largeur ;
yfib=0.5*hauteur ;
// limites de la fibre decrites dans le sens inverse
border e(t=-0.5*hfib, 0.5*hfib) {x=xfib-0.5*lfib;y=yfib+t;label=C1;};
border f(t=0,lfib) {x=xfib-0.5*lfib+t;y=yfib+0.5*hfib;label=C1;};
border g(t=0.5*hfib, -0.5*hfib) {x=xfib+0.5*lfib;y=yfib+t;label=C1;};
border h(t=0,lfib) {x=xfib+0.5*lfib-t;y=yfib-0.5*hfib;label=C1;};
// maillage
int nlarg,nhaut,nfib,nfib2 ;
nlarg=floor(largeur);
nhaut=floor(hauteur);
nfib=floor(hfib);
nfib2=floor(lfib);
int n=1 ;
cout << " Entrer la resolution du maillage (>1) :"; cin >> n;
mesh th = buildmesh(a(nlarg*n)+b(nhaut*n)+c(nlarg*n)+d(nhaut*n)+e(nfib*n)
+f(nfib2*n)+g(nfib*n)+h(nfib2*n));
plot (th,wait=1,ps="maillage.ps") ;
fespace Vh(th,P2);

Vh u,v,grad=1;
        u=0;
problem Problem1(u,v,solver=LU) =
                int2d(th)(  dx(u)*dx(v) + dy(u)*dy(v))
-int2d(th) (v*grad)
+ on(C0,u=0)
+ on (C1,u=vfib);


// on fait varier la vitesse de la fibre entre deux valeurs vmin et vmax, par pas de dv
real vmin, vmax,dv ;
real ffib;
cout << " Entrer la valeur de v fibre min (>0) :"; cin >> vmin;
cout << " Entrer la valeur de v fibre max (>0) :"; cin >> vmax;
cout << " Entrer la valeur de dv fibre (>0) :"; cin >> dv;
int nit ;
nit = floor((vmax-vmin)/dv) ;
cout << "nb iterations" << nit;
int i,j ;
for (j=0;j<nit;j++)
{
        vfib=vmin+j*dv;
        u=0;
        Problem1 ;
        // trace des isovitesses
        plot (u,value=true,wait=1) ;
        // trace du profil lateral de vitesse
```

```
        real[int] xx(2*largeur), yy(2*largeur) ;

        for (i=0;i<2*largeur;i++)
        {
                x=0.5*i;
                y=0.5*hauteur ;
                xx[i]=x ;
                if ((x > xfib-0.5*lfib) && (x < xfib+0.5*lfib)) {yy[i]=0;}
                else {yy[i]=u ;}
        }
        plot ([xx,yy],wait=1) ;
        // trace du profil vertical de vitesse
        real[int] xv(2*hauteur), yv(2*hauteur) ;
        for (i=0;i<2*hauteur;i++)
        {
                x=0.5*largeur;
                y=0.5*i ;
                xv[i]=y ;
                if ((y > yfib-0.5*hfib) && (y < yfib+0.5*hfib)) {yv[i]=0;}
                else {yv[i]=u ;}
        }
        plot ([xv,yv],wait=1) ;
        // calcul de la force sur la fibre
        ffib=int1d(th,C1) (dx(u)*N.x+dy(u)*N.y)-grad*lfib*hfib;
        cout << "vfib = " << vfib << " force = " << ffib ;
}
```

B.1.1.2 Full planar flow profile

```
// frontieres du domaine
real largeur,hauteur,hfib,vfib,lfib;
cout << " Entrer la largeur du canal  :"; cin >> largeur;
cout << " Entrer la hauteur du canal  :"; cin >> hauteur;
cout << " Entrer l epaisseur de la fibre  :"; cin >> hfib;
cout << " Entrer la largeur de la fibre  :"; cin >> lfib;
cout << " Entrer la vitesse de la fibre  :"; cin >> vfib;
int C0=98;
int C1=99;
// limites du canal decrites dans le sens trigo
border a(t=0,largeur) {x=t;y=0;label=C0;};
border b(t=0,hauteur) {x=largeur;y=t;label=C0;};
border c(t=0,largeur) {x=largeur-t;y=hauteur;label=C0;};
border d(t=0,hauteur) {x=0;y=hauteur-t;label=C0;};
real xfib,yfib ;
xfib=0.5*largeur ;
yfib=0.5*hauteur ;
// limites de la fibre decrites dans le sens inverse
```

```
border e(t=-0.5*hfib, 0.5*hfib) {x=xfib-0.5*lfib;y=yfib+t;label=C1;};
border f(t=0,lfib) {x=xfib-0.5*lfib+t;y=yfib+0.5*hfib;label=C1;};
border g(t=0.5*hfib, -0.5*hfib) {x=xfib+0.5*lfib;y=yfib+t;label=C1;};
border h(t=0,lfib) {x=xfib+0.5*lfib-t;y=yfib-0.5*hfib;label=C1;};
// maillage
int nlarg,nhaut,nfib,nfib2 ;
nlarg=floor(largeur);
nhaut=floor(hauteur);
nfib=floor(hfib);
nfib2=floor(lfib);
int n=1 ;
cout << " Entrer la resolution du maillage (>1) :"; cin >> n;
mesh th = buildmesh(a(nlarg*n)+b(nhaut*n)+c(nlarg*n)+d(nhaut*n)+e(nfib*n)+f(nfib2*n)
+g(nfib*n)+h(nfib2*n));
plot (th,wait=1,ps="maillage.ps") ;
fespace Vh(th,P2);

Vh u,v,grad=1;
        u=0;
problem Problem1(u,v,solver=LU) =
                int2d(th)(  dx(u)*dx(v) + dy(u)*dy(v))
-int2d(th) (v*grad)
+ on(C0,u=0)
+ on (C1,u=vfib);



real vf;
int i;
int j;



        u=0;
        Problem1 ;

real[int] xx(2*largeur+2), yy(2*largeur+2) ;
real[int,int] S(2*largeur+2,2*hauteur+2) ;
real uval ;
        S=0;
        for (i=0;i<=2*largeur;i++)
        {
                x=0.5*i;
                xx[i]=x;
                for (j=0;j<=2*hauteur;j++)
                {
                        y=0.5*j ;
```

```
                yy[j]=y;
                uval=u;
                        S(i,j)=uval ;
                                        }


        }


string yn;
bool sortiev ;
cout << "enregistrement du champ de vitesse ? (oui non)"; cin >> yn;
sortiev = (yn == "oui");
string ufile="correctedFx_u_la_"+largeur+"_ha_"+hauteur+"_fib_"+hfib+lfib+".txt";
{
ofstream uf(ufile,append);
for (i=0;i<=2*largeur;i++)
        {
                for (j=0; j<=2*hauteur;j++)
                {
                        uf << xx[i] << "," << yy[j] << "," << S(i,j) << "\n";
                }
        }

}
```

B.1.2 Fiber perpendicular to the flow direction

We present here a more automatic procedure to compute the fiber velocity corresponding to a zero-force regime. An algorithm written in MATLAB launches FreeFem automatically to run the simulation for a given fiber velocity. It then computes the force exerted on the fiber and iterates the fiber velocity using a bisection code. We copy below the FreeFem code used to simulate the flow in the channel for the case of a perpendicular fiber.

```
//load "medit"
string outputfield= "oui";
// frontieres du domaine
real longueur,hauteur,Lfib,vfib,xfib,yfib,lfib,theta,m,rfib,n,hfib;

vfib=0;
hfib=18;




int C0=98;
int C1=99;
int C2=98;
```

```
longueur=200;
hauteur=20;
lfib=11;

rfib=5;
xfib=0.5*longueur ;
yfib=0.5*hauteur ;

real hmin, hmax, dh;
hmin=1;
hmax=18;
dh=1;
real nit;
nit = floor((hmax-hmin)/dh) ;
cout << "nb iterations" << nit;




n=2;

string ufile1="l="+longueur+"_ha="+hauteur+"_lfib="+lfib+"_hfib=
"+hfib+"_rfib="+rfib+"_vfib="+vfib+"_xfib="+xfib+"_yfib="+yfib+"_FIBER.txt";
string ufile2="l="+longueur+"_ha="+hauteur+"_lfib="+lfib+"_hfib=
"+hfib+"_rfib="+rfib+"_vfib="+vfib+"_xfib="+xfib+"_yfib="+yfib+"_FIELD.txt";



// limites du canal decrites dans le sens trigo

border a(t=0,longueur) {x=t;y=0;label=C0;};
border b(t=0,hauteur) {x=longueur;y=t;label=C2;};
border c(t=0,longueur) {x=longueur-t;y=hauteur;label=C0;};
border d(t=0,hauteur) {x=0;y=hauteur-t;label=C2;};


// limites de la fibre decrites dans le sens inverse


border e(t=-0.5*hfib, 0.5*hfib) {x=xfib-0.5*lfib;y=yfib+t;label=C1;};
border f(t=0,lfib) {x=xfib-0.5*lfib+t;y=yfib+0.5*hfib;label=C1;};
border g(t=0.5*hfib, -0.5*hfib) {x=xfib+0.5*lfib;y=yfib+t;label=C1;};
border h(t=0,lfib) {x=xfib+0.5*lfib-t;y=yfib-0.5*hfib;label=C1;};

// maillage
```

```
int nlong,nhaut,nfib,nfib2 ;
nlong=floor(longueur);
nhaut=floor(hauteur);
nfib=floor(hfib);
nfib2=floor(lfib);

mesh th = buildmesh(a(nlong*n)+b(nhaut*n)+c(nlong*n)+d(nhaut*n)+e(nfib*2*n)
+f(nfib2*2*n)+g(nfib*2*n)+h(nfib2*2*n));
//plot (th,wait=1,ps="maillage.ps") ;

//fespace Vh(th,P2);

fespace Uh(th,P1b);

Uh u,v,uu,vv,sigmaxx,sigmaxy,sigmayy;

fespace Ph(th,P1);

Ph p,pp;
func poiseuille=(-4/hauteur^2)*(y^2-hauteur*y);

u=0; v=0;


problem Problem1([u,v,p],[uu,vv,pp],solver=LU) =
                int2d(th)(  dx(u)*dx(uu) + dy(u)*dy(uu)+dx(v)*dx(vv)+dy(v)*dy(vv)
                                +dx(p)*uu+dy(p)*vv+pp*(dx(u)+dy(v)) -1e-10*p*pp)
+ on(C0,u=0,v=0)
+ on(C1,u=vfib,v=0)
+ on(C2,u=poiseuille,v=0);

//uu vv pp are functions to write variationnal form of Stokes equations
with velocity(u,v) and pressure scalar p


        u=0;v=0;
        Problem1 ;


        sigmaxx=-p+2*dx(u);
        sigmayy=-p+2*dy(v);
        sigmaxy=dy(u)+dx(v);

        real ffibx,ffiby;

        ffibx=int1d(th,C1) ((-p+2*dx(u))*N.x+(dy(u)+dx(v))*N.y);
```

```
        ffiby=int1d(th,C1) ((-p+2*dy(v))*N.y+dy(u)*N.x+dx(v)*N.x);




//Save shear flow values for nodes on the fiber

real[int] xx(50), yy(50) ;
real[int] sxl(2*hfib+2),syl(2*hfib+2),sxyl(2*hfib+2),sxL(2*lfib+2),
syL(2*lfib+2),sxyL(2*lfib+2),pl(2*hfib+2),pL(2*lfib+2);
real sigmavalxx,sigmavalyy,sigmavalxy,pval ;

int i,j;

{
ofstream uf(ufile1,append);

////////////////////////////////////////border e

        sxl=0;syl=0;sxyl=0;pl=0;
        for (i=0;i<=2*hfib;i++)
                {
                        x=xfib-0.5*lfib;
                y=yfib-0.5*hfib+0.5*i;
                        xx[i]=x;
                        yy[i]=y;
                        sigmavalxx=-p+2*dx(u);
                        sigmavalyy=-p+2*dy(v);
                        sigmavalxy=dx(v)+dy(u);
                        pval=p;
                        sxl(i)=sigmavalxx;
                        syl(i)=sigmavalyy;
                        sxyl(i)=sigmavalxy;
                        pl(i)=pval;
                        uf << xx[i] << "," << yy[i] << "," << sxl(i)<< ","
 << syl(i) << ","  << sxyl(i) <<  ","  << pl(i) << ",1" << "\n";
                }


////////////////////////////////////////////border f
        sxL=0;syL=0;sxyL=0;pL=0;
        for (i=0;i<=2*lfib;i++)
        {
            x=xfib-lfib*0.5+i*0.5;
```

```
            y=yfib+hfib*0.5;
                xx[i]=x;
                yy[i]=y;
                sigmavalxx=-p+2*dx(u);
                sigmavalyy=-p+2*dy(v);
                sigmavalxy=dx(v)+dy(u);
                pval=p;
                sxL(i)=sigmavalxx; // same here; the L refers to the fiber width here
                syL(i)=sigmavalyy;
                sxyL(i)=sigmavalxy;
                pL(i)=pval;
                uf << xx[i] << "," << yy[i] << "," << sxL(i)<< ","  << syL(i)
<< ","  << sxyL(i) << ","  << pL(i) << ",2"<<  "\n";
                }
//////////////////////////////////////////border g
        sxl=0;syl=0;sxyl=0;pl=0;
        for (i=0;i<=2*hfib;i++)
        {
                x=xfib+lfib*0.5;
                y=yfib+hfib*0.5-i*0.5;
                xx[i]=x;
                yy[i]=y;
                sigmavalxx=-p+2*dx(u);
                sigmavalyy=-p+2*dy(v);
                sigmavalxy=dx(v)+dy(u);
                pval=p;
                sxl(i)=sigmavalxx;
                syl(i)=sigmavalyy;
                sxyl(i)=sigmavalxy;
                pl(i)=pval;
        uf << xx[i] << "," << yy[i] << "," << sxl(i)<< ","  << syl(i) << ","
 << sxyl(i) << ","  << pl(i)<< ",3" <<  "\n";
        }
//////////////////////////////////////////border h
        sxL=0;syL=0;sxyL=0;pL=0;
        for (i=0;i<=2*lfib;i++)
        {
                x=xfib+lfib*0.5-i*0.5;
                y=yfib-hfib*0.5;
                xx[i]=x;
                yy[i]=y;
                sigmavalxx=-p+2*dx(u);
                sigmavalyy=-p+2*dy(v);
                sigmavalxy=dx(v)+dy(u);
                pval=p;
                sxL(i)=sigmavalxx;
                syL(i)=sigmavalyy;
```

```
                sxyL(i)=sigmavalxy;
                pL(i)=pval;
                uf << xx[i] << "," << yy[i] << "," << sxL(i)<< ","  << syL(i)
 << ","  << sxyL(i) << ","  << pL(i) << ",4"<<  "\n";
        }
}



//SAving the solutions in the center of gravity of the elements

        real[int] xxx(4*longueur+4), yyy(4*longueur+4) ;
        real[int,int] Vx(4*longueur+4,4*hauteur+4), Vy(4*longueur+4,4*hauteur+4),
pressure(4*longueur+4,4*hauteur+4), sigxx(4*longueur+4,4*hauteur+4),sigyy(4*longueur+4,
4*hauteur+4),sigxy(4*longueur+4,4*hauteur+4);

        real uval,vval,sigmaxxval,sigmaxyval,sigmayyval ;
        Vx=0;Vy=0;pressure=0;sigxx=0;sigxy=0;sigyy=0;
pval=0;
        for (i=0;i<=4*longueur;i++)
        {
                x=0.25*i;
                xxx[i]=x;
                for (j=0;j<=4*hauteur;j++)
                {
                        y=0.25*j ;
                yyy[j]=y;



                uval=u;
                vval=v;
                pval=p;
                sigmaxxval=sigmaxx;
                sigmaxyval=sigmaxy;
                sigmayyval=sigmayy;

                Vx(i,j)=uval ;
                Vy(i,j)=vval;
                pressure(i,j)=pval;
                sigxx(i,j)=sigmaxxval;
                sigyy(i,j)=sigmayyval;
                sigxy(i,j)=sigmaxyval;

                }
```

```
        }



if (outputfield=="oui")
{


{

ofstream uf(ufile2,append);

for (i=0;i<=4*longueur;i++)
        {
                for (j=0; j<=4*hauteur;j++)
                {
                        uf << xxx[i] << "," << yyy[j] << "," << Vx(i,j)<< ","
<< Vy(i,j) <<","  << pressure(i,j) << "," << sigxx(i,j) << "," << sigyy(i,j) << "," <<
"\n";
                }
        }

}
}
wait=0;
```

B.2 Three-dimensional simulations in COMSOL

B.2.1 MATLAB code for a typical flow simulation in COMSOL

We used COMSOL coupled with MATLAB to run the 3D flow simulations of a fiber parallel or perpendicular to the flow transported in a confined microchannel. We copy below an example code of such simulations for the case of a fiber perpendicular to the flow. The channel dimensions are 150 μm (length) by 250 μm (width) by 20 μm (height). The fiber is centered in the channel, with a length of 100 μm, a width of 11 μm and a height of 16 μm. A velocity of 100 $\mu m/s$ is applied on the inlet face of the channel. The corresponding zero-force fiber velocity (see next section) is 101.9 $\mu m/s$ (note that all quantities are set with dimensions into COMSOL. The results were made dimensionless to compare with the 2D computations).

```
flclear xfem

% COMSOL version
clear vrsn
vrsn.name = 'COMSOL 3.5';
vrsn.ext = 'a';
```

```
vrsn.major = 0;
vrsn.build = 603;
vrsn.rcs = '$Name:  $';
vrsn.date = '$Date: 2008/12/03 17:02:19 $';
xfem.version = vrsn;

% Geometry 2
g1=rect2(2.4,1.4,'base','corner','pos',[-1.2,-0.6]);
g2=rect2('1.5e-4','2.5e-4','base','center','pos',{'0','0'},'rot','0');
g3=rect2(2.0E-5,1.2E-4,'base','corner','pos',[-2.0E-5,-6.0E-5]);
g4=rect2('11e-6','1e-4','base','center','pos',{'0','0'},'rot','0');
g5=extrude(g2,'distance',[0.00002],'scale',[1;1],'displ',[0;0],'twist',
[0],'face','none','wrkpln',[0 1 0;0 0 1;0 0 0]);
g6=extrude(g4,'distance',[0.000016],'scale',[1;1],'displ',[0;0],'twist',
[0],'face','none','wrkpln',[0 1 0;0 0 1;0 0 0]);

% Geometry 1
g6=move(g6,[0,0,0.000002]);
g7=geomcomp({g5,g6},'ns',{'EXT1','EXT2'},'sf','EXT1-EXT2','face','none','edge','all');
flclear fem

% Analyzed geometry
clear s
s.objs={g7};
s.name={'CO1'};
s.tags={'g7'};

fem.draw=struct('s',s);
fem.geom=geomcsg(fem);

% Initialize mesh for geometry 1
fem.mesh=meshinit(fem, ...
                  'hauto',5, ...
                  'hnumedg',{1,5,2,50,3,60,4,60,5,50,6,5,7,60,8,60,9,9,
                  10,10,11,9,12,10,13,10,14,9,15,9,16,9,17,9,18,8,19,10,
                  20,9,21,5,22,30,23,30,24,5});

% Refine mesh for geometry 1
fem.mesh=meshrefine(fem, ...
                    'mcase',0, ...
                    'rmethod','longest');
%
%% Refine mesh for geometry 1
% fem.mesh=meshrefine(fem, ...
%                     'mcase',0, ...
%                     'rmethod','longest');
xfem.fem{1}=fem;
```

```
% Geometry 2
flclear fem

% Geometry objects
clear s
s.objs={g2,g4};
s.name={'R1','R2'};
s.tags={'g2','g4'};

fem.draw=struct('s',s);
xfem.fem{2}=fem;

% (Default values are not included)

fem=xfem.fem{1};

% Application mode 1
clear appl
appl.mode.class = 'GeneralLaminarFlow';
appl.module = 'MEMS';
appl.gporder = {4,2};
appl.cporder = {2,1};
appl.sshape = 2;
appl.assignsuffix = '_mmglf';
clear prop
prop.analysis='static';
prop.weakcompflow='Off';
prop.inerterm='Off';
appl.prop = prop;
clear bnd
bnd.type = {'walltype','inlet','outlet','walltype'};
bnd.u0 = {0,0.0001,0,0};
bnd.velType = {'U0in','u0','U0in','U0in'};
bnd.walltype = {'noslip','noslip','noslip','lwall'};
bnd.uw = {0,0,0,0.000101957230396709};
bnd.ind = [2,1,1,1,1,4,4,4,4,4,4,3];
appl.bnd = bnd;
clear equ
equ.eta = 53e-3;
equ.gporder = {{1;1;1;2}};
equ.rho = 1.12e3;
equ.cporder = {{1;1;1;2}};
equ.ind = [1];
appl.equ = equ;
fem.appl{1} = appl;
fem.frame = {'ref'};
```

```
fem.border = 1;
clear units;
units.basesystem = 'SI';
fem.units = units;
xfem.fem{1} = fem;

fem=xfem.fem{2};
fem.sdim = {'x','y'};
fem.border = 1;
clear units;
units.basesystem = 'SI';
fem.units = units;
xfem.fem{2} = fem;

% ODE Settings
clear ode
clear units;
units.basesystem = 'SI';
ode.units = units;
xfem.ode=ode;

% Multiphysics
xfem=multiphysics(xfem);

% Extend mesh
xfem.xmesh=meshextend(xfem, ...
                      'geoms',[1]);

% Solve problem
xfem.sol=femstatic(xfem, ...
                   'solcomp',{'w','v','u','p'}, ...
                   'outcomp',{'w','v','u','p'}, ...
                   'blocksize','auto', ...
                   'hnlin','on', ...
                   'linsolver','pardiso', ...
                   'rhob',20, ...
                   'uscale','none');
% Save current fem structure for restart purposes
fem0=xfem;
% Integrate


% Geometry 2
fem=xfem.fem{2};

% Geometry objects
clear s
```

```
s.objs={g2,g4};
s.name={'R1','R2'};
s.tags={'g2','g4'};

fem.draw=struct('s',s);
xfem.fem{2}=fem;


% COMSOL Multiphysics Model M-file
% Generated by COMSOL 3.5a (COMSOL 3.5.0.603, $Date: 2008/12/03 17:02:19 $)

% Geometry 2
fem=xfem.fem{2};

% Geometry objects
clear s
s.objs={g2,g4};
s.name={'R1','R2'};
s.tags={'g2','g4'};

fem.draw=struct('s',s);
xfem.fem{2}=fem;
```

B.2.2 Determination of the fiber velocity

Similarly to the two-dimensional simulations, in order to run the flow simulation in COMSOL, we need to know the fiber velocity at which the fiber is freely transported . For a fiber inclined at any angle with the flow direction, the two components of the force exerted by the fluid on its faces (Fx and Fy, along the flow direction and perpendicular to it) must be zero. We call Vx and Vy the fiber velocity components respectively along the flow direction and perpendicular to the flow direction.

To determine Vx and Vy, we take advantage of the linearity between velocity and force. For a given geometry of the channel and fiber, and an imposed flow, the problem can be written as:

$$Fx = Vx \cdot g11 + Vy \cdot g12 + g13 \tag{B.1}$$

$$Fy = Vx \cdot g21 + Vy \cdot g22 + g23 \tag{B.2}$$

When the coefficients g are known, we can simply solve the above system imposing Fx and Fy to find the velocity corresponding to the zero force, .

$$0 = V0x \cdot g11 + V0y \cdot g12 + g13 \tag{B.3}$$

$$0 = V0x \cdot g21 + V0y \cdot g22 + g23 \tag{B.4}$$

The unknows of the problem, controlling the behaviour of the fiber in the channel for the considered geometry and flow, are the coefficients g. We estimate them computing the force F

(Fx,Fy) for three points in the V plane (Vx,Vy).
We run three simulations for three pairs of Vx and Vy called: (Vx1, Vy1); (Vx2, Vy2); (Vx3, Vy3). Then we compute the three corresponding values of Fx (Fx1, Fx2, Fx3) and of Fy(Fy1, Fy2, Fy3). Considering for Fx the equation B.1, we can write the system of the three corresponding linear equations:

$$Fx1 = g11 \cdot Vx1 + g12 \cdot Vy1 + g13 \tag{B.5}$$
$$Fx2 = g11 \cdot Vx2 + g12 \cdot Vy2 + g13 \tag{B.6}$$
$$Fx3 = g11 \cdot Vx3 + g1 \cdot Vy3 + g13 \tag{B.7}$$

that can be written in matrix form as $Fx = V \cdot G1$ where Fx=[fx1, fx2, fx3]', V=[vx1 vy1 1; vx2 vy2 1; vx3 vy3 1] and G1=[g11 g12 g13];

Now, the unknown G1 can be computed as $G1 = V^{-1} \cdot Fx$ and $G2 = V^{-2} \cdot Fy$ Once the coefficients are known, the system above (eq. B.3 and eq. B.4) is solved and gives F0x and F0y. Finally, a single simulation imposing this obtained fiber velocity is run in order to verify the zero force and to compute the flow profile.

The above procedure has been fully implemented in MATLAB. The three simulations run in COMSOL are launched from MATLAB which then analyzes the force results and compute the coefficients leading to V0. The final simulation is then run with the correct fiber velocity V0 to store additional results of flow. The procedure is repeated automatically varying the geometrical parameters that are being studied such as the angle of the fiber or its position in the flow geometry.

B.2.3 Mesh convergence study

The three-dimensional simulations are costly in computer resources because of the number of nodes involved. Special attention should be paid to the mesh as the confinement of the fiber increases within the channel height: the gap between the fiber surface and the top or bottom wall of the channel should be precisely meshed. A mesh convergence study is carried out by varying the mesh and running the fiber velocity algorithm (parallel fiber) for the highest confinements of the fiber. We present in figure B.1 three refinements around the fiber looking at the channel along the height and width. The number of nodes are given in table B.1.

Mesh	Channel height	Channel length	Channel width	Fiber height	Fiber length	Fiber width
A	5	50	30	10	20	10
B	5	80	60	10	20	10
C	5	80	60	20	40	20

Table B.1: *Number of nodes initially imposed for the mesh of the channel and fiber. The mesh is then refined twice, leading to a denser mesh on and around the fiber. The channel geometry used for the case of a parallel fiber is 250 µm by 100 µm by 20 µm. The fiber length is 100 µm and its width 11 µm.*

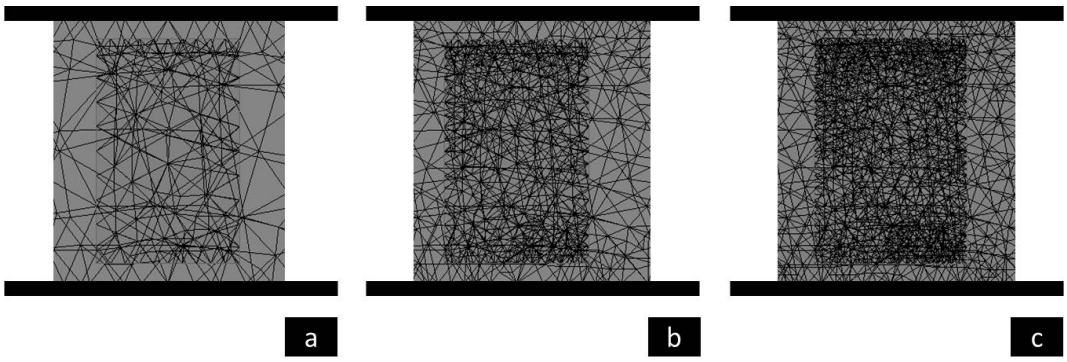

Figure B.1: *View of the channel mesh around the fiber section for three different degrees of refinement. From a to c, the mesh is refined especially inside the gap between the fiber and top and bottom walls.*

We run the flow simulation for these three mesh cases in order to obtain the free-flow fiber velocity. We compare the results of velocity at different degrees of fiber confinement in figure B.2. For low confinements, all three meshes give the same value of fiber velocity. As the fiber height increases over 15 μm (channel height 20 μm), mesh "A" is unable to accurately solve the flow around the fiber. We obtain a plateau of the fiber velocity. Refining it from "A" to "B", then to "C" we can ultimately solve the flow.

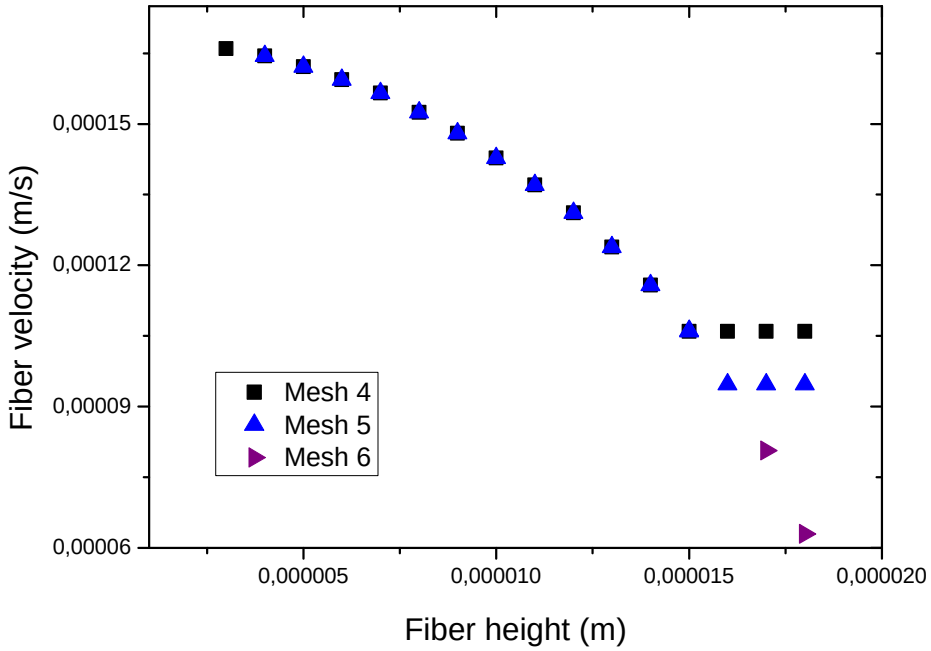

Figure B.2: *Results of fiber velocity obtained with the 3D flow simulations ran on Comsol. We compare different degrees of mesh refinement in particular for the high fiber confinement cases. Mesh "C" is required to accurately obtain the fiber velocity for confinements of 0.8 and 0.9.*

APPENDIX C

DATA PROCESSING METHODS

C.1 Data processing for the flow experiments of single confined fibers

C.1.1 Objectives

We developed a tracking platform in Matlab in order to get the position of the fiber, its geometrical features and orientation from all the images of a given experiment.

To observe the flow of a fiber over a meaningful distance, channels are typically several centimeters long, much more than the size of the field of view (3.3 mm). Long channels are useful for example to study several periods of an oscillating fiber (see 6). A channel longer than the length of the field of view requires the user to regularly move manually or electronically the microscope stage to follow the fiber trajectory. Then, an experiment typically gets divided into **sequences** in which the fiber flows downstream before the user moves the microscope stage to the next sequence of flow.

The detection of fiber position is run for each sequence of frames and extracts the relative position of the fiber within the image. To reconstruct the fiber trajectory as it flows along the whole channel length, the image processing algorithm needs to link all the sequences together, computing the relative position between different viewpoints. This is required to ouput the fiber position information in the reference system of the laboratory.

All the different steps of detection are combined in one graphical interface that we describe in the following sections.

C.1.2 Reference frame

When the fiber flows out of the field of view and once we capture a background image (see C.1.3), we move the microscope stage to the initial frame of the next sequence. This stage movement

gets captured by the camera, leading to blurry images before they stabilize and show the fiber in the next sequence. The initial and final frame of a given sequence is not known. The number of images separating two sequences is also not constant, unless there is a computer-controlled stage and a stable fiber velocity. Finally, if the channel is not perfectly aligned on the glass slide with the microscope stage, a shift in the two directions will occur when the stage is moved.

All these difficulties require user-defined inputs to know which images should not be considered and to compute the shifts in the two directions.

First, the full sequence is displayed on screen along with a table with empty boxes to specify image numbers. The user scrolls through the images, stops at the initial image of a sequence and clicks on the box "initial frame" of the corresponding sequence. The same is done for the last image of the sequence as well as the background image. A screenshot in C.1 shows an experiment with the first two sequences fully analyzed. All frame numbers are stored by the programme once the first step is completed.

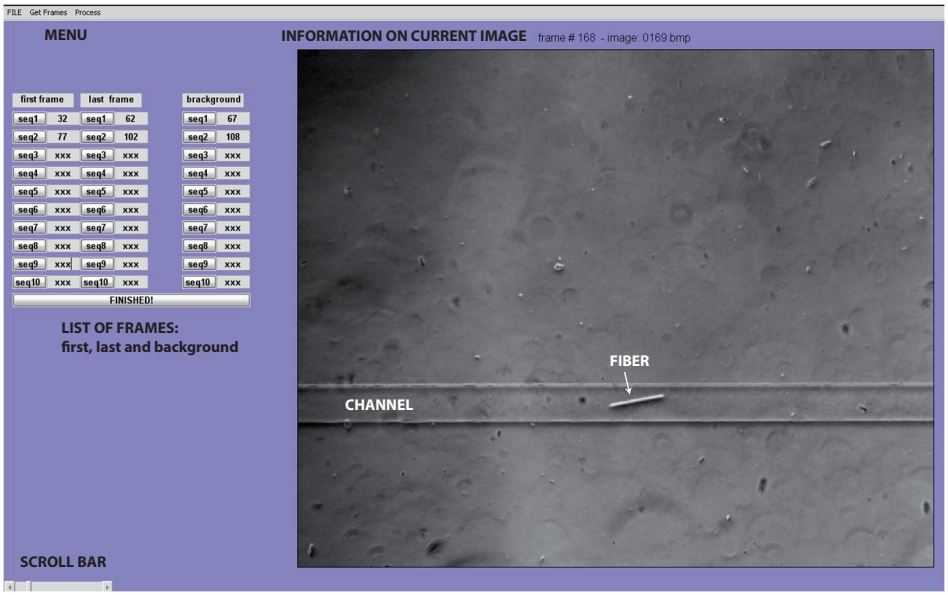

Figure C.1: *Graphical interface of the tracking platform: the full experimental sequence is displayed letting the user to scroll through. The step shown here consists in determining the initial and final frame number of each sequence and the background image number. The table of boxes on the left side is filled as the user clicks on the corresponding icon; here the frames of the first two sequences have been analysed.*

The next step consists in determining the shift in the two horizontal directions from one sequence to the next. This shift between two sequences is estimated computing the relative position of common points within the overlapping portion of the images. To do so, we need to capture common portions of the channel visible in the successive sequences. The same detail inside or outside the channel (dust, marked point) can be detected on both sequences and the corresponding coordinates used to compute the shift. In this step, we display next to each other the last image of the sequence n-1 and the first image of sequence n, for all successive sequences. The user clicks on both images on a particular common point. For each click the point

positions are stored by the programme which computes the successive shifts. A screenshot in C.2 shows two frames being analyzed, the cursor used to select the common point is displayed on the left frame.

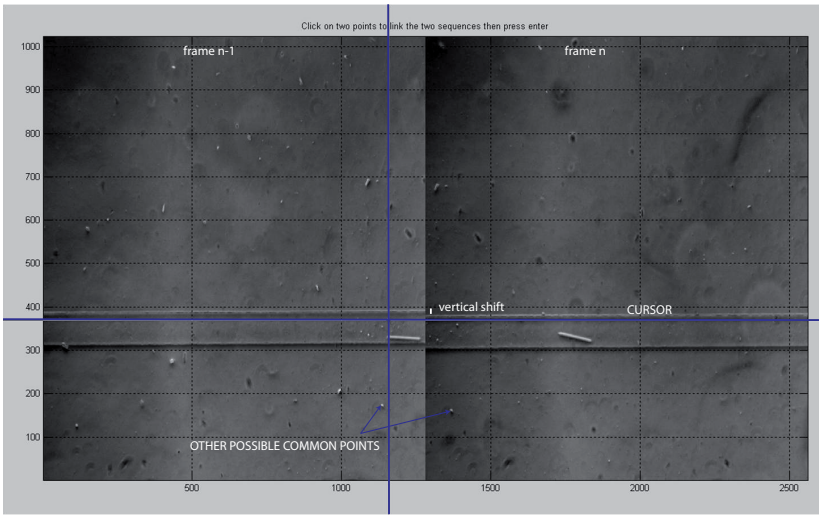

Figure C.2: *Screenshot of the graphical interface for tracking. The last frame of the* $(n-1)^{th}$ *sequence is displayed next to the initial frame of sequence n showing common portions of the channel. In this step, the user clicks on both images on a common point using the cursor. The two positions are stored to get the two-dimensional shift from one sequence to the next. One can see here many points common to the two frames which can be used to determine the vertical and horizontal shift.*

Two more steps required for the tracking algorithm also involve user inputs. The first one is used to position the fiber relative to the channel. It consists in displaying the first image of the first sequence so that the user clicks on two points of the channel bottom lateral border (see screenshot C.3). Then, the programme displays the first frame of all the sequences successively as the user clicks on the center of the fiber. This is used to reduce the detection time.

Once all these user-inputs are performed, the programme is able to position any pixels of any sequence within the laboratory frame (or put more simply, within the first sequence reference frame).

C.1.3 Enhancing the contrast

The image capture of fiber trajectories needs to be done carefully to enhance the detection quality of the image processing. We describe here the several methods and tricks we used in the experiments.
The fiber flows in the oligomer solution used for its fabrication which makes it difficult to be visible with bright field imaging. To see it and improve the contrast with the fluid, we always capture images using a phase contrast filter on the microscope. For any sequence of images we also try to capture a background image. A simple way to do so is to wait for the fiber to leave the field of view at the end of a sequence. When the stage is not moving, the fiber flows over a constant background image, with negligible density variations: substracting each image with

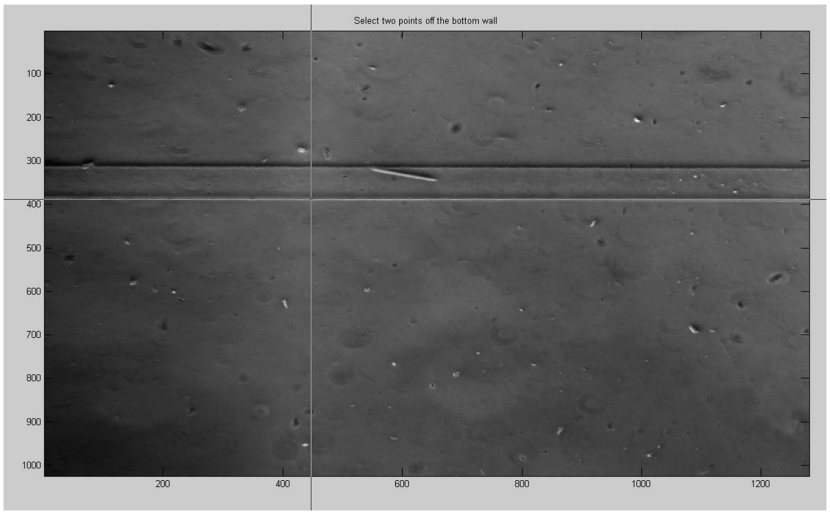

Figure C.3: *Screenshot of the graphical interface for tracking. This step consists in clicking on two points of the bottom lateral wall of the channel so that the programme positions the fiber relative to the channel.The grey cursor is positioned on this wall.*

the background frame provides with a much better contrast as all the portions of the channel not occupied by the fiber will be zeroed. This is illustrated in figure C.4.

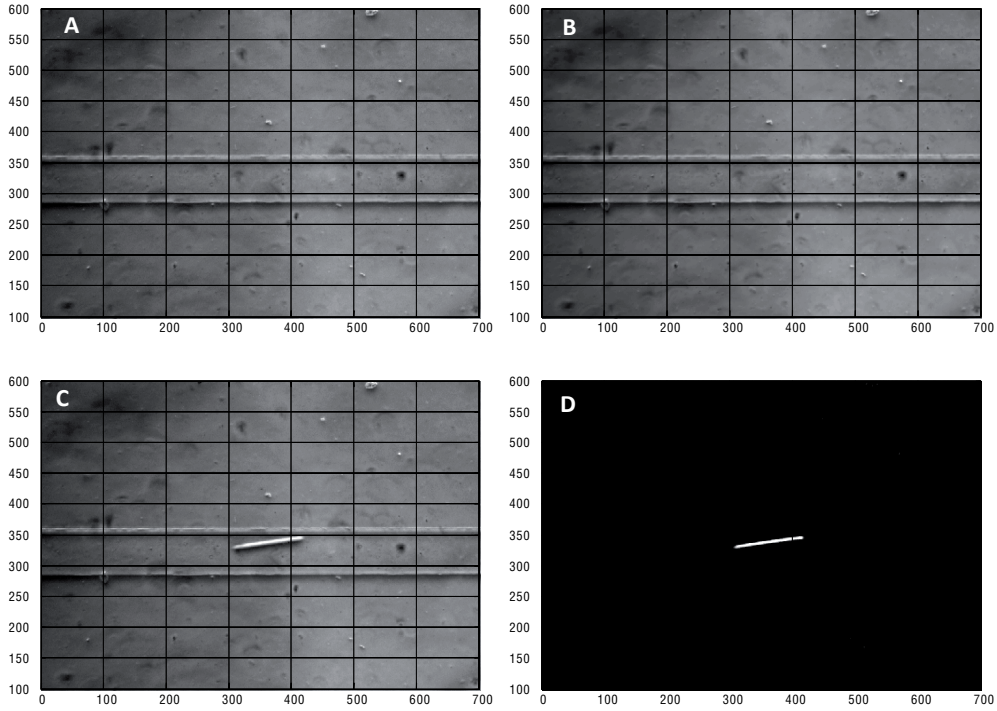

Figure C.4: *Enhancing the contrast using a background image. Image A is a picture of the channel once the fiber left the field of view: "background frame". Image B is a computed background frame from the mean of all the images of the sequence. The result is very similar to Image A. Image C is the original picture of the fiber in the channel. The result of substracting A from C is Image D: the background is in dark pixels, enhancing the contrast of the fiber.*

C.1.4 Algorithm of detection

We describe the main functions of the detection algorithm focusing on a single sequence. The programme is looped through all of them to analyze the full experiment.

Each image is substracted with the background, leading to a black image around a grey fiber. A threshold is applied (the threshold parameter must be adjusted by hand to obtain an efficient filter if no background frame is available) and the region of interest is limited to a box around the fiber. The result of the thresholding step is shown in figure C.5. The area covered by the filtered pixels is compared to the fiber area specified in the programme parameters. If the difference is small, it fits the area with an ellipse and save the center of mass position, the ellipse orientation with the flow direction, its major and minor axis lengths and the distance between the center of mass to the channel lateral wall (see figure C.5). All these parameters will be necessary to study the fiber flow dynamics. As the programme analyses the second and onward sequences, it corrects the fiber position shifted back to the reference frame of the initial sequence. A snapshot of successive positions of the fiber in the channel is displayed in figure C.6 along with the threshold result pictures and its elliptical fit.

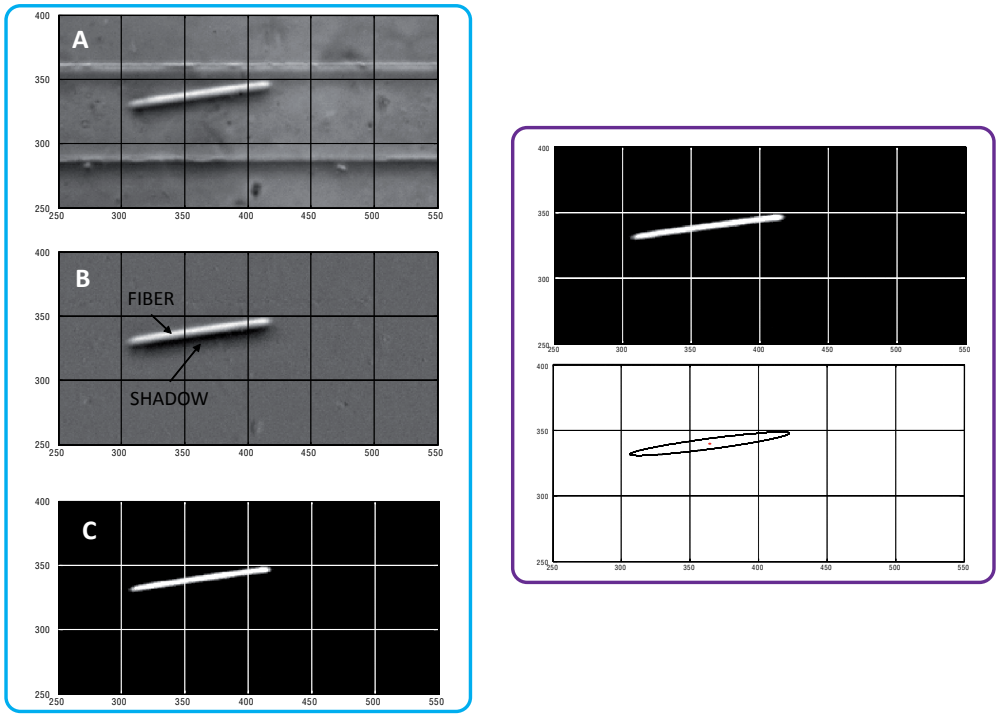

Figure C.5: *The frames of the left panel show the result of the thresholding step. The shadow around the fiber is removed. The images of the right panel show an example of elliptical fit obtained for the detected fiber.*

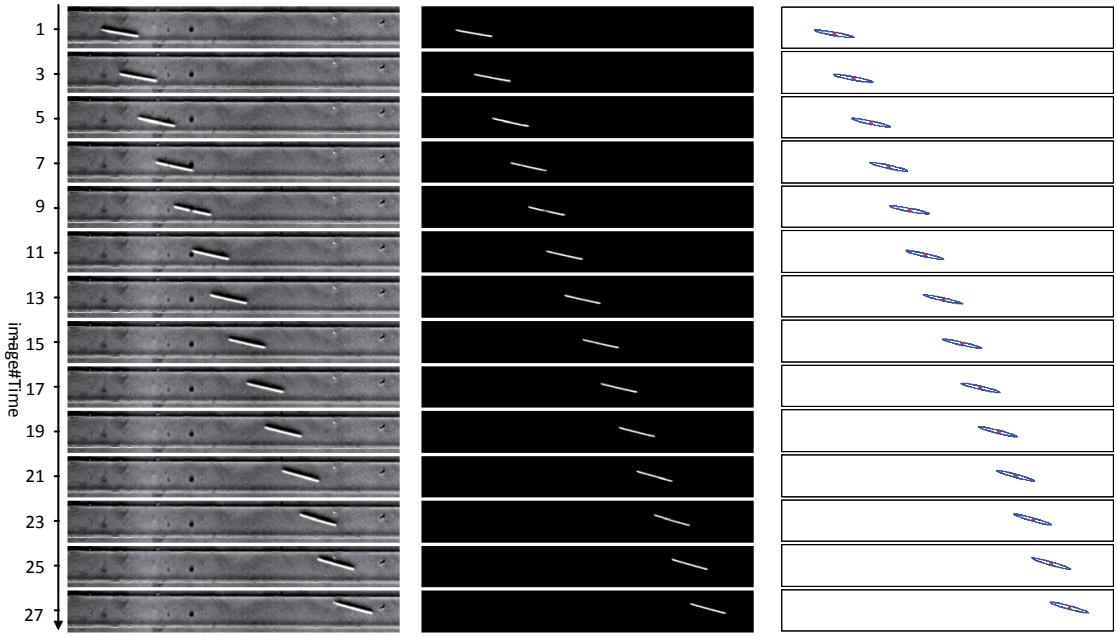

Figure C.6: *Successive positions of a fiber flow in a microchannel. The left panel shows the original frames, the middle one the corresponding thresholded ones. The right panel displays the result of detected and ellipse-fitted fibers with the Matlab detection programme.*

C.2 Image processing for the experiment of fiber suspensions at high concentration

C.2.1 Algorithm principles

We present here our efforts in the development of image processing methods to extract quantitative results from the flow experiments of magnetic fiber suspensions.
The main idea of the image processing is to measure fiber density fluctuations using local variations of greyscales. An image is divided in regions of interest called boxes. Each pixel of the box has a corresponding grayscale value. We average all these values for each box. Then we compute the standard deviation between all the boxes. Figure C.7 shows a series of pictures corresponding to the different steps. The top picture is the original image cropped to show only the inside part of the channel. The second and third images shows two possible sizes of boxes.

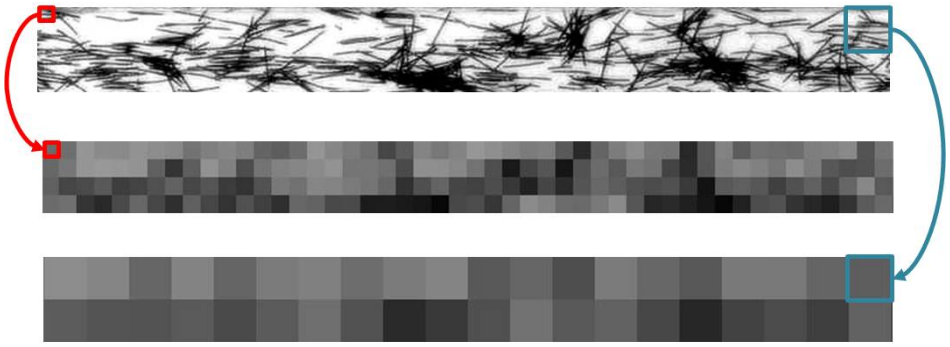

Figure C.7: *Illustration of the image processing method. The top picture is the original frame capturing the flow of a fiber suspensions. It is divided in small domains called boxes. To each box is associated the average grayscale pixels which compose the box. The second picture shows a map of these boxes grayscale-coded with this average, as indicated with the example of the red left-corner box. The third image is similarly constructed from boxes six times larger.*

C.2.2 First results

The box size is critical to capture information on the fiber density fluctuations. We present here a first example obtained for two suspensions of different fiber concentrations, for a box size comparable to a fiber length. The first one (blue curve) is the most dilute one. The fibers are homogeneously distributed in the channel. The intensity of fluctuations is small and does not display strong variations. In the higher-concentration case, the standard-deviation is higher and has several sharp increases which correspond to the capture of flocs.

In the second example, we directly link the sharp increase of fluctuations with the apparition of flocs. The box size is again the fiber length. The large decrease before 6000 s corresponds to the deformation of a floc in the channel. It will be interesting to implement this technique with an iteration over the box size to more precisely capture the steps of its formation. We tried for example to trigger clustering at specific locations in the channel. A first attempt consisted in fabricating pillars anchored at the bottom of the channel with the idea that fibers would form clusters on them.

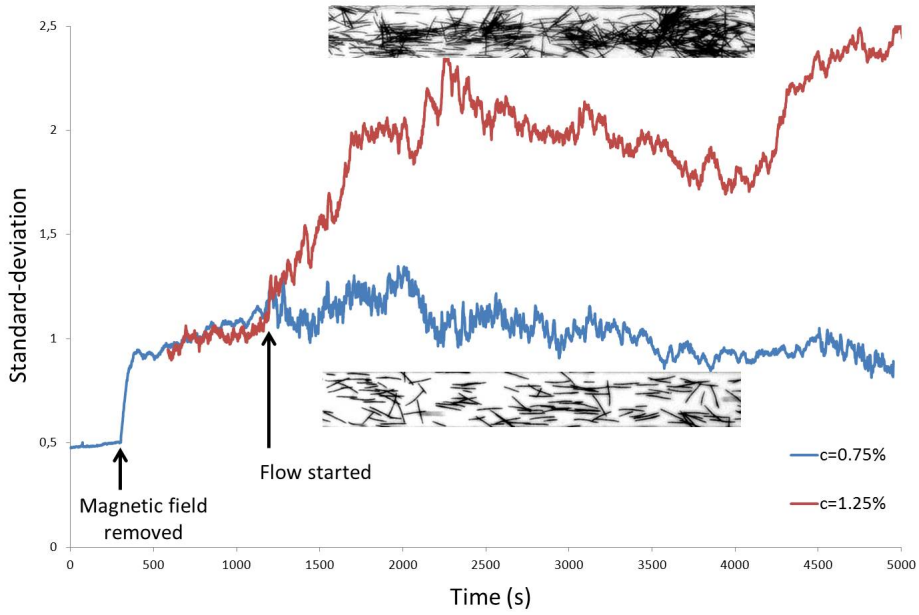

Figure C.8: *Comparison of fiber density fluctuations between two suspensions at different concentrations. The most dilute suspension does not exhibit strong variations as the fibers are well distributed in the channel. In the more concentrated case, fibers start to form aggregate which are captured by the technique.*

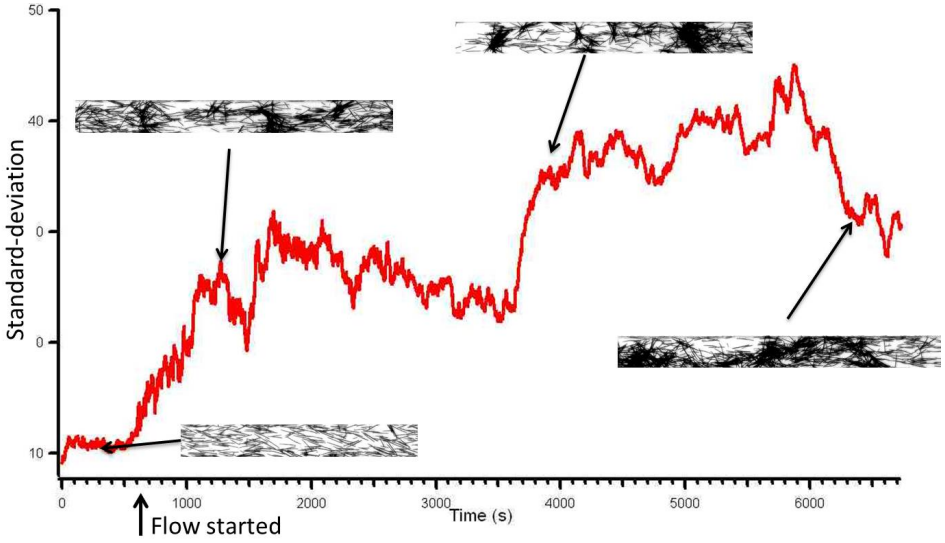

Figure C.9: *Example of a suspension with a high-enough concentration of fibers to observe clustering. Each sharp increase of the fluctuations is due to the formation of a floc.*

APPENDIX D

PARTICLE TRACKING VELOCIMETRY METHODS

Particle Imaging velocimetry (PIV) is a powerful optical technique to quantitatively explore a given flow and provide with an instantaneous measurement of the velocity field [62]. Typically, a PIV experiment begins with seeding the fluid with small particles which will act like local tracers. Then, short time-lapse imaging is done using a video camera (usually fast cameras are needed when the time resolution of the analysis is high). Each image is divided in interrogation areas. Cross-correlation and auto-correlation algorithms analyze the interrogation areas between successive images and compute an instantaneous velocity vector.
The application of the technique to flow in microchannels is complex, but possible [63]. Firstly, particles should be carefully chosen to follow the flow without perturbing it. The scale of the experiment requires them to be typically a few micron-size at maximum and often submicrometric [64]. They also need to be highly visible : fluorescent beads are often used to get an excellent contrast. Since the particles are dispersed in the entire channel, the velocity information is averaged along the depth of view. Some techniques now exist to focus the particles on a given depth [65] but they require a more complex set-up.

We adopted a simple approach to investigate the flow around an advected fiber using particle **tracking** measurements. The fiber is made using the lithography technique. Initially we fill the channel with a suspension of concentrated microspheres (polymer microspheres red fluorescing 1%, 2 μm-diameter, Duke Scientific) in a solution of PEGDA and photo-initiator (PI at 10 wt%, PEGDA Mw=575). Figure D.1 shows a picture of the flow as recorded by the camera. A fast camera (Phantom,V5) was used for the image acquisition (250 im/s or 500 im/s).

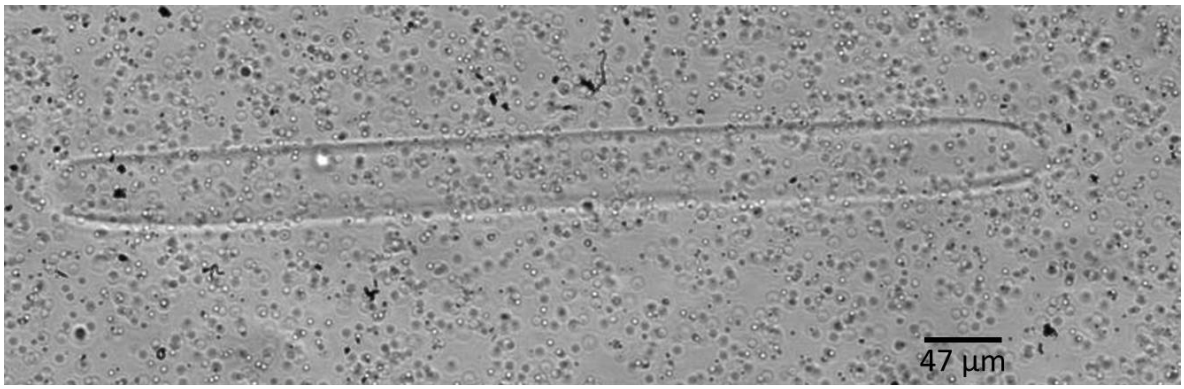

Figure D.1: *Frame extracted from a flow experiment of a fiber parallel to the flow direction. The solution is filled with tracer particles of diameter 2 µm.*

Using commercial softwares to output the velocity field around the fiber is hindered by the motion of the fiber which is slower than the particles. Since we were interested in the regions of the flow close to the fiber edges, we can not simply mask-out the large region covered by the fiber. Instead, we developed an algorithm in MATLAB to modify all the images so that the sequence would be in the reference frame of the fiber. The image processing consists of displaying some selected images from the flow, typiqually an increment of 200 was used over 2000 images to treat. Successively on these 200 images, the user is asked to click on a recognizable point (e.g. the tip of the fiber). The coordinates of these points are stored by the programme which can then compute the velocity of the fiber. Then, all of the images of the flow sequence are shifted so that the fiber remains in the same position throughout the sequence. This is achieved by removing either the left or right pixels of the images. If the original images contain some noise, for example dust in the channel, the image processing will transform it into a moving object in the reference frame of the fiber. In this case, substracting all the images with a background capture will be necessary prior to the other treatment steps.

As a result, the observation now takes place in the reference frame of the fiber in which it

remains still. We can stack all the shifted frames. All particles flowing around the fibers leave a trace indicating their flow path. Particles flowing above the fiber appear sharp on the constructed frame as they are still in the new reference system. Figure D.2 shows the result stack image. We obtain in this way a map of the velocity field around the fiber which can be further analyzed to give quantitative results.

Figure D.2: *Stack of frames shifted in space to be in the reference system of the fiber. The difference of velocity between the particles and the fiber makes the particles leave a path on the image stack. Black marks correspond to dust and defects in the channel.*

APPENDIX E

COLLABORATIONS

E.1 Bending of elastic fibers in viscous flow: Jason Wexler, Princeton University

A collaboration project has started between our group at ESPCI (Anke Lindner, Olivia du Roure, Nawal Quennouz, Helene Berthet) and Jason Wexler and Howard Stone at Princeton University, investigating the bending of elastic fibers in confined viscous flows. The experiment consists in anchoring an elastic fiber in a Hele-Shaw microfluidic channel where a transverse flow is applied. The fiber is fabricated with the photo-polymerization method. The flow is controlled with a syringe pump. As the mean flow velocity increases, the deformation of the fiber (its bending) is measured.

Figure E.1 shows a snapshot of the bending fiber as the fluid velocity increases. During his visit at ESPCI in 2011, Jason learnt the photo-polymerization technique to fabricate *in situ* fibers of controlled geometry in a microfluidic channel.

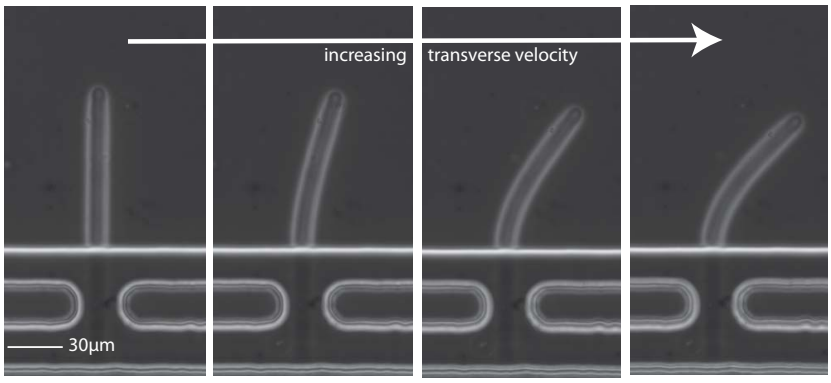

Figure E.1: *Snapshot of successive frames showing an anchored elastic fiber bending under transverse flow. From left to right, the imposed mean flow velocity is increased.*

E.2 Active suspensions: Gaston Mino, ESPCI

A collaboration was done with Gaston Miño (PMMH, ESPCI) to help with the microfabrication side of his PhD project. His study on the rheology of active suspensions consisted in designing an experimental microfluidic system to measure the viscosity of a wild type E. Coli suspension in the dilute and semi-dilute limits. The flow geometry is a monolayer microfluidic channel with a Y-shaped inlet as illustrated in figure E.2. A paper is under preparation.

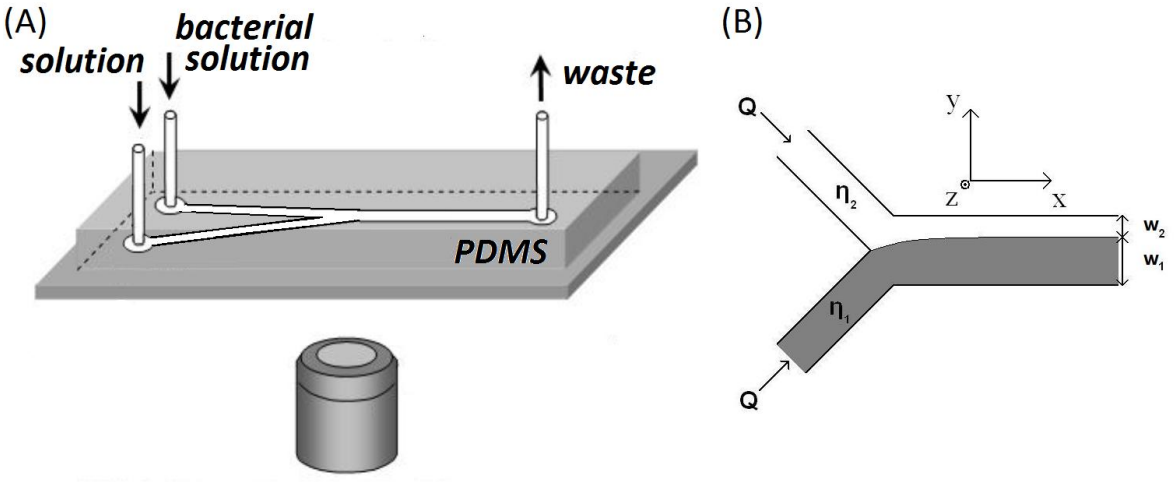

Figure E.2: *Drawing of the microchannel used to study the rheology of E.Coli suspensions. The Y-shape inlet is used to flow two solutions, one containing the bacteria. As indicated on the right drawing, the viscosity difference can be related to the position of the separation lines betwen the two fluids in the main portion of the channel.*

A second collaboration was done with Gastón Miño and Pr. Ernesto Altshuler's group from the University of La Habana in Cuba during his sabbatical at the PMMH laboratory in 2010-2011. They investigated the transport of E-Coli suspensions through a micro-fluidic channel holding a constriction in its middle (the funnel). Figure E.3 illustrates the flow geometry. Using this simple but archetypal geometry, they address the question of the influence of geometry and confinement on the dispersion and transport properties of bacteria in a flow. A paper is in preparation.

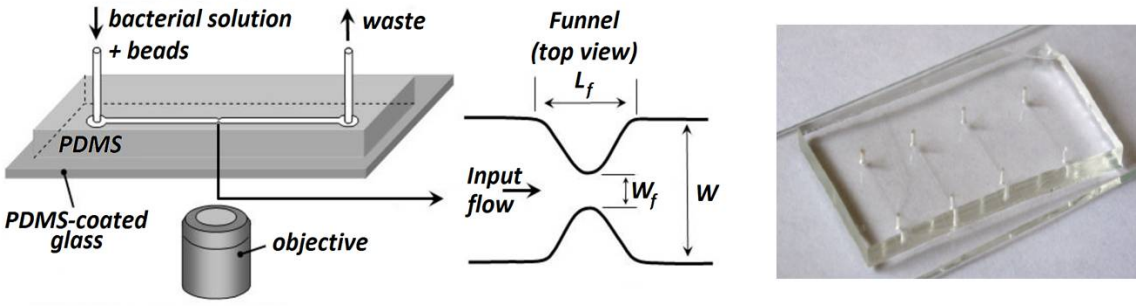

Figure E.3: *Drawing of the microchannel design for the study of E-Coli transport through restrictions. The right picture shows the fabricated channel.*

BIBLIOGRAPHY

[1] N. Low, G. Daccord, and J-P. Bedel. Designing Fibered Cement Slurries for Lost Circulation Applications: Case Histories. *Proceedings of SPE Annual Technical Conference and Exhibition*, October 2003.

[2] S. G. Mason. The Flocculation of Pulp Suspensions and the Formation of Paper. *Tappi Journal*, 33(9):441–444, 1950.

[3] S. G. Mason. Fiber Motions and Flocculation. *Tappi Journal*, 37(11):492–501, 1954.

[4] E. Guazzelli and J. Hinch. Fluctuations and Instability in Sedimentation. *Annual Review of Fluid Mechanics*, 43(1):97–116, January 2011.

[5] M. Haw. Jamming, Two-Fluid Behavior, and "Self-Filtration" in Concentrated Particulate Suspensions. *Physical Review Letters*, 92(18):1–4, May 2004.

[6] G. B. Jeffery. The Motion of Ellipsoidal Particles Immersed in a Viscous Fluid. *Proceedings of the Royal Society A: Mathematical, Physical and Engineering Sciences*, 102(715):161–179, November 1922.

[7] F. P. Bretherton. The motion of rigid particles in a shear flow at low Reynolds number. *Journal of Fluid Mechanics*, (1956):284–304, 1962.

[8] S. G. Mason and R. S. J. Manley. Particle Motions in Sheared Suspensions: Orientations and Interactions of Rigid Rods. *Proceedings of the Royal Society A: Mathematical, Physical and Engineering Sciences*, 238(1212):117–131, December 1956.

[9] K.B. Moses, S. G. Advani, and A. Reinhardt. Investigation of fiber motion near solid boundaries in simple shear flow. *Rheologica Acta*, 40(3):296–306, May 2001.

[10] C. A. Stover and C. Cohen. The motion of rodlike particles in the pressure-driven flow between two flat plates. *Rheologica Acta*, 29(3):192–203, May 1990.

[11] E. Wandersman, M. Fermigier, A. Lindner, and O. du Roure. Buckled in translation. *Soft Matter*, 6(22):5715, 2010.

[12] Y.-N. Young and Michael Shelley. Stretch-Coil Transition and Transport of Fibers in Cellular Flows. *Physical Review Letters*, 99(5):3–6, August 2007.

[13] G. K. Batchelor. Slender-body theory for particles of arbitrary cross-section in Stokes flow. *Journal of Fluid Mechanics*, 44:419–440, 1970.

[14] C.A. Stover, D. L. Koch, and C. Cohen. Observations of fibre orientation in simple shear flow of semi-dilute suspensions. *Journal of Fluid Mechanics*, 238(-1):277, April 2006.

[15] M. Lagomarsino, I. Pagonabarraga, and C. Lowe. Hydrodynamic induced deformation and orientation of a microscopic elastic filament. *Physical review letters*, 94:200, 2005.

[16] M. V. D Angelo, B. Semin, G. Picard, M. E. Poitzsch, J. P. Hulin, and H. Auradou. Single Fiber Transport in a Fracture Slit: Influence of the Wall Roughness and of the Fiber Flexibility. *Transport in Porous Media*, 84(2):389–408, December 2009.

[17] B. Semin, J. P. Hulin, and H. Auradou. Influence of flow confinement on the drag force on a static cylinder. *Physics of Fluids*, (2009):1–9, 2009.

[18] B. Semin. *Interaction d'une fibre et d'un écoulement en géométrie confinée*. PhD thesis, Ecole polytechnique, France, 2010.

[19] S. Champmartin, A. Ambari, and B.R. Abderrahim. Kinematics of a free particle moving between two parallel walls. *Proceedings of the ASME 2010 3rd Joint US-European Fluids Engineering Summer Meeting and 8th International Conference on Nanochannels, Microchannels and Minichannels*, pages 1–9, 2010.

[20] D. Dendukuri, S.S. Gu, D.C. Pregibon, T.A. Hatton, and P.S. Doyle. Stop-flow lithography in a microfluidic device. *Lab on a chip*, 7(7):818–28, July 2007.

[21] C. Goubault, P. Jop, M. Fermigier, J. Baudry, E. Bertrand, and J. Bibette. Flexible Magnetic Filaments as Micromechanical Sensors. *Physical Review Letters*, 91(26):1–4, December 2003.

[22] C. Goubault. *Colloides magnétiques : auto-organisation et applications biologiques*. PhD thesis, 2004.

[23] M. A. Hubbe. Flocculation and redispersion of cellulosic fiber suspensions: a review of effects of hydrodynamic shear and polyelectrolytes. *BioResources*, 2:296–331, 2007.

[24] D. Dendukuri and P.S. Doyle. The Synthesis and Assembly of Polymeric Microparticles Using Microfluidics. *Advanced Materials*, 21(41):4071–4086, November 2009.

[25] E. Guyon, J. P. Hulin, and L. Petit. *Hydrodynamique physique*. 2001.

[26] M. Zurita-Gotor, J. Blawzdziewicz, and E. Wajnryb. Motion of a rod-like particle between parallel walls with application to suspension rheology. *Journal of Rheology*, 51(1):71, 2007.

[27] W. B. Russel, E. J. Hinch, L. G. Leal, and G. Tieffenbruck. Rods falling near a vertical wall. *Journal of Fluid Mechanics*, 83(02):273, April 2006.

[28] N. Champagne, R. Vasseur, A. Montourcy, and D. Bartolo. Traffic Jams and Intermittent Flows in Microfluidic Networks. *Physical Review Letters*, 105(4):2–5, July 2010.

[29] D.L. Koch and E.S.G. Shaqfeh. The instability of a dispersion of sedimenting spheroids. *Journal of Fluid Mechanics*, 209(-1):521, April 2006.

[30] J. E. Butler and E.S.G. Shaqfeh. Dynamic simulations of the inhomogeneous sedimentation of rigid fibres. *Journal of Fluid Mechanics*, 468:205–237, October 2002.

[31] B. Herzhaft and E. Guazzelli. Experimental study of the sedimentation of dilute and semi-dilute suspensions of fibres. *Journal of Fluid Mechanics*, 384:133–158, 1999.

[32] F. Lundell, L. D. Söderberg, and P. H. Alfredsson. Fluid Mechanics of Papermaking. *Annual Review of Fluid Mechanics*, 43(1):195–217, January 2011.

[33] Schlumberger. CemNET Fiber cement additive product sheet. Technical Report 5.

[34] R. J. Kerekes and C. J. Schell. Characterization of fibre flocculation regimes by a crowding factor. *Journal of pulp and paper science*, 18(1):J32–J38.

[35] C.T.J. Dodson. Fibre crowding , fibre contacts and fibre flocculation. *Tappi Journal*, (September):1–9, 1995.

[36] L. Beghello. *The tendency of fibers to build flocs*. PhD thesis, 1998.

[37] C. F. Schmid, L. H. Switzer, and D.J. Klingenberg. Simulations of fiber flocculation: Effects of fiber properties and interfiber friction. *Journal of Rheology*, 44(4):781, 2000.

[38] J. Park and J. E. Butler. Inhomogeneous distribution of a rigid fibre undergoing rectilinear flow between parallel walls at high Péclet numbers. *Journal of Fluid Mechanics*, 630:267, June 2009.

[39] K Takamura, P M Adler, H L Goldsmith, and S G Mason. Particle motions in sheared suspensions: XXXI. Rotations of rigid and flexible dumbbells (experimental). *Journal of Colloid and Interface Science*, 83(2):516–530, October 1981.

[40] R.J. Kerekes. Pulp floc behavior in entry flow to constrictions. *Tappi Journal*, 66(1):88–91, 1983.

[41] K. Higashitani, N. Inada, and T. Ochi. Floc breakup along centerline of contractile flow to orifice. *Colloids and Surfaces A: Physicochemical and Engineering Aspects*, 56:13–23, 1991.

[42] R.C. Sonntag and W. B Russel. Structure and Breakup of Flocs Subjected to Fluid Stresses III. Converging Flow. *Journal of Colloid and Interface Science*, I(2):390–395, 1987.

[43] E. Bertrand, J. Bibette, and V. Schmitt. From shear thickening to shear-induced jamming. *Physical Review E*, 66(6):16–18, December 2002.

[44] D. Dendukuri, D. C. Pregibon, J. Collins, T A. Hatton, and P. S. Doyle. Continuous-flow lithography for high-throughput microparticle synthesis. *Nature materials*, 5(5):365–9, May 2006.

[45] S. Middelhoek. No Title. *IBM Journal of Research and Development*, 14(2):117–127, 1970.

[46] J. C. Love, D. B. Wolfe, H.O. Jacobs, and G.M. Whitesides. Microscope Projection Photolithography for Rapid Prototyping of Masters with Micron-Scale Features for Use in Soft Lithography. *Langmuir*, 17(19):6005–6012, September 2001.

[47] D. Dendukuri, P. Panda, R. Haghgooie, J.M. Kim, T. A. Hatton, and P. S. Doyle. Modeling of Oxygen-Inhibited Free Radical Photopolymerization in a PDMS Microfluidic Device. *Macromolecules*, 41(22):8547–8556, November 2008.

[48] R. Attia, D.C. Pregibon, P.S. Doyle, J-L. Viovy, and D. Bartolo. Soft microflow sensors. *Lab on a chip*, 9(9):1213–8, May 2009.

[49] Rémi Dreyfus, Jean Baudry, Marcus L Roper, Marc Fermigier, Howard a Stone, and Jérôme Bibette. Microscopic artificial swimmers. *Nature*, 437(7060):862–5, October 2005.

[50] A. Babataheri, M. Roper, M. Fermigier, and O. Du Roure. Tethered fleximags as artificial cilia. *Journal of Fluid Mechanics*, 678:5–13, March 2011.

[51] Naïs Coq, Sandrine Ngo, Olivia du Roure, Marc Fermigier, and Denis Bartolo. Three-dimensional beating of magnetic microrods. *Physical Review E*, 82(4):1–10, October 2010.

[52] L. Cohen-Tannoudji, E. Bertrand, L. Bressy, C. Goubault, J. Baudry, J. Klein, J-F. Joanny, and J. Bibette. Polymer Bridging Probed by Magnetic Colloids. *Physical Review Letters*, 94(3):28–31, January 2005.

[53] J. Philip, O. Mondain-Monval, F.L. Calderon, and J. Bibette. Colloidal force measurements in the presence of a polyelectrolyte. *Journal of Physics D: Applied Physics*, 30(20):2798–2803, October 1997.

[54] L. Jing. Field-Induced Structures in Ferrofluid Emulsions. *PRL*, 74(14):2828, 1995.

[55] A. Benrichou. Drag force on a circular cylinder midway between two parallel plates at very low Reynolds numbers. Part 1: Poiseuille flow (numerical). *Chemical Engineering Science*, 59(15):3215–3222, August 2004.

[56] J. M. Gere and S. P. Timoshenko. *Mechanics of Materials*. PWS Publishing Company, 1997.

[57] B Herzhaft, É Guazzelli, Michael B. Mackaplow, and Eric S. G. Shaqfeh. Experimental Investigation of the Sedimentation of a Dilute Fiber Suspension. *Physical review letters*, 77(2):290–293, July 1996.

[58] M. Fermigier. *Hydrodynamique Physique*. 2004.

[59] P. Tabeling. *Introduction à la microfluidique*. Belin edition, 2003.

[60] F. Hecht. *FreeFem++*. 2011.

[61] S. Taneda. Visualization of Separating Stokes Flows. *Journal of the Physical Society of Japan*, 46(6):1935–1946, 1979.

[62] R. Adrian. Particle-Imaging Techniques For Experimental Fluid-Mechanics. *Annual Review of Fluid Mechanics*, 23(1):261–304, January 1991.

[63] J. G. Santiago, S. T. Wereley, C. D. Meinhart, D. J. Beebe, and R. J. Adrian. A particle image velocimetry system for microfluidics. *Experiments in Fluids*, 25(4):316–319, September 1998.

[64] A.K. Singh, E.B. Cummings, and D. J. Throckmorton. Fluorescent liposome flow markers for microscale particle-image velocimetry. *Analytical Chemistry*, 73(5):1057–61, March 2001.

[65] O. Dron, C. Ratier, M. Hoyos, and J-L. Aider. Parametric study of acoustic focusing of particles in a micro-channel in the perspective to improve micro-PIV measurements. *Microfluidics and Nanofluidics*, 7(6):857–867, July 2009.